Electronic Thesis and Dissertation Repository

9-6-2016 12:00 AM

Hydraulic and Electrokinetic Delivery of Remediants for In-situ Remediation

Ahmed I. A. Chowdhury
The University of Western Ontario

Supervisor
Denis M. O'Carroll
The University of Western Ontario

Follow this and additional works at: https://ir.lib.uwo.ca/etd

Part of the Environmental Chemistry Commons, Environmental Engineering Commons, Hydrology Commons, and the Nanoscience and Nanotechnology Commons

Recommended Citation

Abstract

Nano-scale zero valent iron (nZVI) has shown promising mobility and in-situ reactivity with chlorinated volatile organic compounds when injected into saturated porous media. The current study evaluated nZVI mobility and subsequent reactivity with in-situ contaminants in a variably saturated porous media. The nZVI particles, synthesized onsite at subzero temperatures, demonstrated complete trichloroethene (TCE) degradation within the target area. Furthermore, a three dimensional finite difference model (CompSim) was utilized to investigate nZVI mobility in variably saturated zones. Model predicted well head data were in very good agreement with field observations. Simulation results showed that the injected slurry migrated radially outward from the injection well and that nZVI travel distance increases were not proportional to the increase in injected nZVI volume. This study suggested that the numerical simulator can be a practical tool for optimal design of nZVI field applications.

The second study aimed at alleviating back diffusion from low permeability porous media observed at numerous field studies. Experiments were conducted in a two-dimensional sandbox with alternate vertical layers of coarse sand and silt flooded with TCE at aqueous solubility. Electrokinetics (EK) was used to enhance permanganate delivery through the silt layers. The suite of experiments demonstrated that EK was able to drive more permanganate at a faster rate throughout the silt layers in comparison to no-EK experiments. The combined EK and permanganate application resulted in 4.4 orders of magnitude reduction in TCE concentrations compared to a 3.5 orders of magnitude reduction without EK application. This experiment demonstrated that EK coupled with permanganate application can be used to remediate low permeability strata.

The third study investigated a novel approach of EK assisted persulfate delivery followed by electrical resistance heating (ERH) for persulfate activation for low permeability soil remediation. The study showed that EK delivered persulfate throughout the silt. The application of ERH was successfully able to activate the persulfate within the porous matrix leading to complete in-situ tetrachlorothene (PCE) degradation. To the authors' knowledge,

this study was the first to combine EK and ERH for persulfate delivery and activation for low permeability soil remediation.

Keywords

Co-Authorship Statement

The thesis was written in accordance with the guidelines and regulations for an Integrated Article format stipulated by the School of Graduate and Postdoctoral Studies at the University of Western Ontario. The candidate designed, conducted and analyzed all of the experimental and numerical modelling work in this thesis under the supervision of Dr. Denis O'Carroll and Dr. Jason Gerhard. The themes and development of this work were performed in discussions with Dr. Denis O'Carroll and Dr. Jason Gerhard. The candidate wrote three manuscripts that are included as chapters of this thesis. Full details for all chapters given below.

Chapter 2: Literature Review: Background

Contributions:

Ahmed Chowdhury: primary author/writer, developed outline, reviewed references, reviewed/revised chapter, coordinated the other collaborators/co-authors.

Denis O'Carroll: reviewed/revised chapter.

Jason Gerhard: reviewed/revised chapter.

Chapter 3: nZVI Injection into Variably Saturated Soils: Field and Modeling Study

Chowdhury, Ahmed I. A., Krol, Magdalena M., Kocur, Christopher M., Boparai, Hardiljeet K., Weber, Kela P., Sleep, Brent E., O'Carroll, Denis M., (2015), nZVI injection into variably saturated soils: field and modeling study, *Journal of Contaminant Hydrology*., Vol. 183, 16-28.

Contributions:

Ahmed Chowdhury: primary author/writer, designed and developed field work protocol, performed field work, collected field samples, interpreted and analyzed the collected data, developed/modified numerical model, run simulations, analyzed the simulation results.

Magdalena M. Krol: assisted in onsite nZVI synthesis, sample collection, assisted in model development and data interpretation, reviewed and revised chapter.

Christopher M. Kocur: assisted in developing onsite synthesis protocol, field work.

Hardiljeet K. Boparai: assisted in field sample analysis.

Kela P. Weber: assisted in field work, reviewed and revised chapter.

Brent E. Sleep: assisted in model development and data interpretation, reviewed and revised chapter.

Denis M. O'Carroll: initiated work, planning and regulatory approval, grantee of funding, assisted in data interpretation, reviewed and revised chapter.

Chapter 4: Electrokinetic-Enhanced Permanganate Delivery and Remediation of Contaminated Low Permeability Porous Media

Chowdhury, Ahmed I. A., Gerhard, Jason, I., Reynolds, David, Sleep, Brent E., O'Carroll, Denis M., (*in prep*), Electrokinetic-enhanced permanganate delivery and remediation of contaminated low permeability porous media.

Contributions:

Ahmed I. A. Chowdhury: primary author/writer, planned and conducted experiments, interpreted and analyzed the collected data.

David Reynolds: initiated the work, provided formative discussion, reviewed manuscript.

Brent E. Sleep: provided formative discussion, reviewed manuscript.

Jason Gerhard: assisted in image analysis, data interpretation, reviewed and revised chapter.

Denis O'Carroll: grantee of funding, assisted in data interpretation, reviewed and revised chapter.

Chapter 5: Aqueous PCE Remediation in Silt via Persulfate Delivered by Electrokinetics and Activated by Electrical Resistance Heating: Proof of Concept

Chowdhury, Ahmed I. A., Gerhard, Jason, I., Reynolds, David, O'Carroll, Denis M., (*in prep*), Aqueous PCE Remediation in Silt via Persulfate Delivered by Electrokinetics and Activated by Electrical Resistance Heating: Proof of Concept.

Contributions:

Ahmed I. A. Chowdhury: primary author/writer, planned and conducted experiments, interpreted and analyzed the collected data.

David Reynolds: initiated the work, provided formative discussion, reviewed manuscript.

Jason Gerhard: assisted in data interpretation, reviewed and revised chapter.

Denis O'Carroll: grantee of funding, assisted in data interpretation, reviewed and revised chapter.

Acknowledgments

Dedication

To my parents –

Rokhsana Begum

And

Ahmed Amin Chowdhury

Table of Contents

List of Tables

List of Figures

List of Acronyms

1,2, DCA	1,2 Dichloroethane
CFT	Colloidal filtration theory
CompSim	Compositional simulator
CT	Carbon tetrachloride
cVOC	Chlorinated volatile organic compounds
DCM	Dichloromethane
DO	Dissolved oxygen
D_o	Diffusion coefficient at infinite dilution
E_a	Activation energy
EK	Electrokinetics
EM	Electromigration
EO	Electroosmosis
ERH	Electrical resistance heating
ISCO	In-situ chemical oxidation
ISCR	In-situ chemical reduction
k_{obs}	Pseudo-first order rate constant
MCL	Maximum concentration level
nZVI	Nano-scale zero valent iron
OoM	Orders of magnitude
ORP	Oxidation reduction potential
PAH	Poly-aromatic hydrocarbons
PCE	Perchloroethene/Tetrachloroethene
PM	Permanganate
PS	Persulfate
TCE	Trichloroethene

Chapter 1

1   Introduction

1.1   Background

Chlorinated solvents were reported to be first synthesized in Germany during early to mid-nineteenth century (Rossberg et al., 2000). However, widespread use of such solvents began with the rapid industrialization around the world after World War II (Pankow and Cherry, 1996). Chlorinated solvents (e.g., tetrachloroethene (PCE), trichloroethene (TCE), dichloromethane (DCM), 1,2 dichloroethane (1, 2 DCA), carbon tetrachloride (CT)) have been used for a variety of applications including degreasing agents, dry cleaning fluids, heat-transfer fluids, chemical intermediates, paint stripping and adhesives (Kueper et al., 2014; Pankow and Cherry, 1996). Millions of kilograms of these solvents (i.e., 75×10^6 to 5871×10^6 kg for TCE and 1, 2 DCA, respectively), were produced in US alone in 1986. (Pankow and Cherry, 1996). Spills/releases had occurred during the storage, transfer, use, and disposal over the decades of production and use of these chemicals. Improper and/or accidental release of chemicals has resulted in subsurface contamination at many industrial and military sites across the world. An estimated 30,000-50,000 such sites (excluding the underground storage tanks or USTs) exist in the USA alone; of which 48% are contaminated with solvents, such as PCE, TCE, and CT (Kavanaugh et al., 2003). These chemicals are characterized as being denser than water, low water solubility and recalcitrance in the environment as such may persist in the subsurface environment for a very long time and continue to contaminate groundwater.

The production and use of these solvents started declining in the 1970s due to growing concerns of the impact of these chemicals on human and environmental health. By the early to mid-1980s, it was reported that many groundwater supplies in the US were contaminated with chlorinated solvents (Pankow and Cherry, 1996). This led to a call for remediation of contaminated sites. Early treatment strategies (e.g., pump and treat) required prolonged operation (i.e., from years to decades) and showed limited success in cleaning up contaminated sites. As a result researchers have focused on developing in-situ remediation technologies for source zone remediation since the 1990s (Kueper et al., 2014). Examples

of in-situ remediation technologies include chemical oxidation (ISCO), chemical reduction (ISCR), steam flushing, surfactant flushing, electrical resistance heating (ERH), air sparging, and enhanced bioremediation. In-situ chemical oxidation (ISCO) and/or reduction (ISCR) are advanced remediation strategies that have garnered much attention in recent decades. These technologies have shown promising in-situ contaminant degradation in lab-scale as well as field-scale studies. For example, a recent field-scale study with nano-scale zero valent iron (nZVI), a form of ISCR, showed promising nZVI deliverability in the subsurface and reactivity with in-situ contaminants (Kocur et al., 2014; Kocur et al., 2015). Therefore, application of such remediants (both oxidants and reductants) appears to be a viable solution for in-situ remediation. However, field studies so far focused on nZVI transport and remediation of saturated porous media. Contaminants may exist in the unsaturated zones, especially immediately above the water table, given the seasonal fluctuations of groundwater level. Numerical models can be a viable tool for nZVI transport investigations under different scenarios as well as for optimal design of field applications (e.g., injection volume, rate, distance between monitoring wells), but rarely explored. This suggests further studies, both field application and numerical modeling, are required to investigate nZVI transport in such variably saturated systems.

Most of the in-situ remediation technologies perform poorly in reducing aqueous concentrations or contaminant mass removal when low permeability porous media is encountered in the subsurface (NRC, 2005). It is common for contaminants to diffuse into less permeable zones (i.e., forward diffusion) with time (Grathwohl, 1998; Johnson et al., 1989; Parker, 1996). Once a remediant (e.g., oxidants, reductants, bio-amendments) is injected into the subsurface it predominantly travels through permeable zones and degrades contaminants in that zone. However, the less permeable zones remain inaccessible to the injected remediants resulting in incomplete degradation of the contaminants present in these zones. Consequently, the concentration gradient between the less permeable zones and adjacent more permeable zones increases, thereby, slowly releasing the contaminants from the less permeable formation (i.e., back diffusion). Back diffusion was observed at 62% of 71 sites where in-situ chemical oxidation was applied for contaminated groundwater remediation (Krembs et al., 2011). Back diffusion may act as a long term source of contamination even after the removal of the primary source, persisting for

decades to centuries (Ball et al., 1997; Chapman and Parker, 2005; Liu and Ball, 2002; Parker et al., 2008; Sale et al., 2007; Seyedabbasi et al., 2012).

Given the challenges associated with delivering and remediating low permeable zones in the subsurface it was proposed that electrokinetics (EK) can be used to enhance remediant delivery into such low permeability zones (Reynolds et al., 2008; Roach and Reddy, 2006). Several lab-scale studies demonstrated that EK has the potential for enhanced delivery of remediants such as oxidants and nano-iron (Chowdhury et al., 2012; Reddy and Karri, 2007; Reynolds et al., 2008). Therefore, remediation technologies (e.g., ISCO) and EK can be combined to enhance remediant (e.g., permanganate, persulfate) delivery and subsequent in-situ contaminant (e.g., TCE, PCE) degradation to eliminate the extent of back diffusion from low permeable zones.

1.2 Research Objectives

The overall goal of the current study was to evaluate the performance of hydraulic and/or electrokinetic transport of remediants and subsequent in-situ contaminant degradation. More specifically, the transport of nZVI synthesized onsite and in-situ contaminant degradation was studied. This was coupled with development of a numerical model to investigate nZVI transport in variable saturated porous media. The model was further utilized to assess different nZVI injection scenarios. A second theme, electrokinetic assisted oxidant (i.e., permanganate) transport and its ability to degrade in-situ contaminant, was studied as part of the current study. Finally, a novel approach of combining electrokinetics assisted persulfate delivery and electrical resistive heating to activate the delivered persulfate for contaminant degradation was evaluated.

The first objective of the study was to investigate nZVI transport in a variably saturated system. Onsite synthesized monometallic nZVI particles were injected in a variably saturated subsurface and the resulting contaminant (TCE) degradation was monitored. In addition, a three dimensional numerical model was developed to investigate nZVI migration in the variably saturated porous media. The model, in its predictive capacity, was also utilized to assess optimal injection and nZVI migration scenarios in this variably saturated system.

The second objective of the current study was to investigate the ability of EK to deliver permanganate from coarse sand into silt and the resulting contaminant reduction within the silt layer. Experiments were conducted with a heterogeneously packed 2D experimental apparatus contaminated with aqueous TCE. In addition, image analysis was performed to quantify permanganate concentrations in silt and $MnO_{2(s)}$ precipitation in sand layers.

The third objective of this study was to evaluate the novel approach of EK-assisted persulfate delivery through fine grained porous media, followed by electrical resistance heating (ERH) application to activate persulfate. In addition, contaminant degradation resulting from activated persulfate was monitored.

1.3   Thesis Outline

The thesis is written in integrated article format. A brief description of each chapter is listed below.

Chapter 1 provides a brief overview of subsurface contamination by chlorinated solvents and outlines the scope of the thesis.

Chapter 2 reviews the current literature on nZVI transport and reactivity, permanganate and persulfate activation and reactivity. Furthermore, studies related to electrokinetics assisted permanganate and persulfate delivery are also discussed in this chapter.

Chapter 3 titled "nZVI Injection into Variably Saturated Soils: Field and Modeling Study" is a manuscript that evaluates nZVI transport and reactivity in the variably saturated subsurface coupled with numerical simulations to assess optimal injection and nZVI migration scenarios. This chapter was published on October 9th, 2015 in the *Journal of Contaminant Hydrology*. doi:10.1016/j.jconhyd.2015.10.003.

Chapter 4 titled "Electrokinetic-Enhanced Permanganate Delivery and Remediation of Contaminated Low Permeability Porous Media" demonstrates the ability of EK to deliver permanganate through TCE contaminated silt layers and to degrade the TCE in silt. Results were compared to permanganate only and water flushing only experiments. This chapter has been prepared to submit for review in *Environmental Science and Technology*.

Chapter 5 titled "Aqueous PCE Remediation in Silt via Persulfate Delivered by Electrokinetics and Activated by Electrical Resistive Heating: Proof of Concept" is a manuscript that evaluates electrokinetics for persulfate delivery followed by electrical resistive heating of persulfate to degrade PCE. The persulfate was activated at different temperatures to evaluate its decomposition rate and subsequent PCE degradation.

Chapter 6 summarizes the major conclusions of the thesis, discusses the practical and environmental implications of this study. It also suggests areas that require further research.

1.4 References

Rossberg, M. et al., 2000. Chlorinated Hydrocarbons, Ullmann's Encyclopedia of Industrial Chemistry. Wiley-VCH Verlag GmbH & Co. KGaA.

Pankow, J.F. and Cherry, J.A., 1996. Dense chlorinated solvents and other DNAPLs in groundwater: history, behavior, and remediation. Waterloo Press.

Kueper, B., Stroo, H., Vogel, C. and Ward, C.H., 2014. Source Zone Remediation: The State of the Practice. In: B.H. Kueper, H.F. Stroo, C.M. Vogel and C.H. Ward (Editors), Chlorinated Solvent Source Zone Remediation. SERDP ESTCP Environmental Remediation Technology. Springer New York, pp. 1-27.

Kavanaugh, M. et al., 2003. The DNAPL Cleanup Challenge: Is There a Case for Source Depletion? USEPA National Risk Management Research Laboratory, Cincinnati, OH, USA, pp. 129.

Kocur, C.M. et al., 2014. Characterization of nZVI Mobility in a Field Scale Test. Environmental Science & Technology, 48(5): 2862-2869.

Kocur, C.M.D. et al., 2015. Contributions of Abiotic and Biotic Dechlorination Following Carboxymethyl Cellulose Stabilized Nanoscale Zero Valent Iron Injection. Environmental Science & Technology, 49(14): 8648-8656.

NRC, N.R.C., 2005. Contaminants in the subsurface: Source zone assessment and remediation. Committee on Source Removal of Contaminants in the Subsurface. The National Academic Press, Washington, D.C.

Johnson, R.L., Cherry, J.A. and Pankow, J.F., 1989. Diffusive contaminant transport in natural clay: a field example and implications for clay-lined waste disposal sites. Environmental Science & Technology, 23(3): 340-349.

Parker, B.L., 1996. Effects of molecular diffusion on the persistence of dense, immiscible phase organic liquids in fractured porous geologic media.

Grathwohl, P., 1998. Diffusion in natural porous media: Contaminant Transport, Sorption/Desorption and Dissolution Kinetics, 1. Springer Science & Business Media.

Krembs, F.J., Clayton, W.S. and Marley, M.C., 2011. Evaluation of ISCO Field Applications and Performance. In: R.L. Siegrist, M. Crimi and T.J. Simpkin (Editors), In Situ Chemical Oxidation for Groundwater Remediation. SERDP/ESTCP Environmental Remediation Technology. Springer New York, pp. 319-353.

Liu, C. and Ball, W.P., 2002. Back diffusion of chlorinated solvent contaminants from a natural aquitard to a remediated aquifer under well-controlled field conditions: predictions and measurements. Ground Water, 40(2): 175-184.

Parker, B.L., Chapman, S.W. and Guilbeault, M.A., 2008. Plume persistence caused by back diffusion from thin clay layers in a sand aquifer following TCE source-zone hydraulic isolation. Journal of Contaminant Hydrology, 102(1–2): 86-104.

Seyedabbasi, M.A., Newell, C.J., Adamson, D.T. and Sale, T.C., 2012. Relative contribution of DNAPL dissolution and matrix diffusion to the long-term persistence of chlorinated solvent source zones. Journal of Contaminant Hydrology, 134–135: 69-81.

Chapman, S.W. and Parker, B.L., 2005. Plume persistence due to aquitard back diffusion following dense nonaqueous phase liquid source removal or isolation. Water Resources Research, 41(12): n/a-n/a.

Ball, W.P., Liu, C., Xia, G. and Young, D.F., 1997. A diffusion-based interpretation of tetrachloroethene and trichloroethene concentration profiles in a groundwater aquitard. Water Resources Research, 33(12): 2741-2757.

Sale, T.C. et al., 2007. Unpublished report on AFCEE source zone initiative.

Reynolds, D.A., Jones, E.H., Gillen, M., Yusoff, I. and Thomas, D.G., 2008. Electrokinetic migration of permanganate through low permeability media. Ground Water, 46(4): 629-637.

Roach, N. and Reddy, K.R., 2006. Electrokinetic Delivery of Permanganate into Low-Permeability Soils. International Journal of Environment and Waster Management, 1(1): 4-16.

Chowdhury, A.I.A., O'Carroll, D.M., Xu, Y. and Sleep, B.E., 2012. Electrophoresis enhanced transport of nano-scale zero valent iron. Advances In Water Resources, 40(0): 71-82.

Reddy, K.R. and Karri, M.R., 2007. Electrokinetic Delivery of Nanoscale Iron Particles for In-Situ Remediation of Pentachlorophenol-Contaminated Soils, Proceedings of International Symposium on Geo-Environmental Engineering for Sustainable Development, China, pp. 74-79.

Chapter 2

2   Background

2.1   Introduction

Improper and/or accidental release of chemicals has resulted in subsurface contamination at many industrial and military sites across the world. An estimated 30,000-50,000 such sites (excluding the underground storage tanks or USTs) exist in the US alone; of which 60% are contaminated with dense non-aqueous phase liquids (DNAPL) such as perchloroethene (PCE), trichloroethene (TCE), and carbon tetrachloride (CT) (Kavanaugh et al., 2003). These chemicals are characterized by their higher density, lower solubility and recalcitrance in the environment as such they may persist in the subsurface and continue to contaminate the groundwater for very long times. This had led researchers to focus on developing contaminated source zone remediation technologies. Examples of such remediation technologies include, but not limited to, pump and treat, soil excavation, chemical oxidation, chemical reduction, steam flushing, surfactant flushing, electrical resistance heating (ERH), air sparging, and enhanced bioremediation (NRC, 2005). Application of ex-situ treatments (e.g., soil excavation) is limited by several factors such as depth of excavation, necessity of lowering groundwater table, presence of source zone beneath existing infrastructure, potential exposure and release of volatile organic compounds (VOCs) and higher cost associated with treating the excavated soil. Application of in-situ technologies (e.g., steam flushing, oxidation/reduction technologies) eliminates some of the concerns associated with ex-situ treatments. However, the poor source zone delineation, slow reaction with contaminants, moderate to high cost and ineffective delivery due to subsurface heterogeneity pose a limitation on the applicability of these technologies.

In-situ chemical oxidation (ISCO) and/or reduction (ISCR) are advanced remediation strategies that have garnered much attention in recent decades. ISCO involves injecting an oxidant (e.g., sodium/potassium permanganate ($NaMnO_4$/$KMnO_4$), hydrogen peroxide (H_2O_2), persulfate ($Na_2S_2O_8$)) into the subsurface for abiotic transformation (i.e., oxidation in this case) of contaminants (Baciocchi et al., 2014; Siegrist et al., 2011). Advantages of

ISCO include rapid and complete treatment, destruction of a variety of co-contaminants, moderate cost, and compatibility with bioremediation (Siegrist et al., 2011).

ISCR involves use of a reductant, such as, reduced sulfur species (HS^-, $S_2O_4^{2-}$, FeS etc.), ferrous ions (Fe^{2+}), bimetallic materials (Fe/Pd), and (nano/micro scale) zero valent iron (nZVI/mZVI), to reduce subsurface contaminants (Tratnyek et al., 2014). Of these techniques, ISCR with nZVI, and ISCO with permanganate and persulfate have several advantages over other remediation technologies. nZVI has the ability for fast and complete degradation of a wide range of contaminants (e.g., pesticides, chlorinated volatile organic compounds (cVOCs)) (O'Carroll et al., 2013b; Zhang, 2003). A recent study has shown that polymer stabilized nZVI particles were mobile in the subsurface (Kocur et al., 2014). This particular study also demonstrated that nZVI injection resulted in both abiotic and biotic degradation of in-situ cVOCs at a site permeable porous media (Kocur et al., 2015). However, nZVI mobility and reactivity has so far only been studied in the saturated zone. Numerical models can be used for preliminary design of field-scale nZVI applications (e.g., nZVI volume, distance between monitoring wells). Currently, there is a lack of numerical modeling studies for such applications indicating further research is needed.

In-situ remediation technologies have shown promising results in reducing aqueous concentration or contaminant mass from permeable zones in the subsurface. However, these technologies have shown poor performance when low permeability porous media is encountered in the subsurface (NRC, 2005). Contaminants from higher permeability zones diffuse into low permeability zones (e.g., clay lenses, aquitard etc.) (Goodall and Quigley, 1977; Grathwohl, 1998; Johnson et al., 1989; Parker, 1996). As contaminants are removed from high permeability zones, potentially due to aggressive remediation activities, any decrease in contaminant concentrations in the permeable zone results in an increased concentration gradient between high and low permeability zones. This causes contaminant flux from low permeability zones into the permeable zones (i.e., back diffusion). Back diffusion may continue to contaminate the groundwater for decades even after free phase contaminants have been removed from permeable zones, thus posing a long-term threat to groundwater sources. Back diffusion was observed in 73% of the field studies (pilot or full scale) where permanganate was used as an remediant (DNAPL-Test, 2011). Therefore,

remediation techniques aimed to clean up such contamination must be able to deliver remediants throughout the contaminated zones including low permeability zones. Delivery of any remediant into the targeted contaminated zones, especially into the low permeability zones, in the subsurface is one particular concern associated with any remediation technique. Hence, there is significant interest in industry as well as in academia to develop effective remediation technologies to clean-up contaminated sites as such eliminating or limiting the extent of back diffusion from low permeability zones in the subsurface.

2.2 In-Situ Chemical Reduction (ISCR) with Nano-scale Zero Valent Iron (nZVI)

2.2.1 nZVI preparation for field injection

nZVI field applications to date have used both commercially available nZVI (Henn and Waddill, 2006; Krug et al., 2010; Wei et al., 2010) and onsite synthesized nZVI (Bennett et al., 2010; Elliott and Zhang, 2001; He et al., 2010; Johnson et al., 2013; Kocur et al., 2014; Wei et al., 2010; Zhang, 2003). Early field-scale studies used unstabilized or bare nZVI (Elliott and Zhang, 2001; Zhang, 2003) while more recent studies have used polymer coated stabilized (0.10%-0.80%, weight/volume) nZVI to increase suspension stability (Bennett et al., 2010; He et al., 2010; Henn and Waddill, 2006; Kocur et al., 2014; Wei et al., 2010). Such stabilized nZVI particles are more dispersed and reactive than commercially available nZVI particles (Sakulchaicharoen et al., 2010).

He and Zhao (2007) demonstrated that smaller and monodispersed nano-particles are formed at lower temperature (8 °C) compared to those synthesized at higher temperature (30 °C). Lower temperature slows nZVI particle growth rate, forms stable nanoclusters and results in greater stabilizing agent (i.e., carboxy methyl cellulose (CMC)) association to the nZVI surface yielding smaller nano-particles (He and Zhao, 2007). Recently Kocur et al. (2014) synthesized CMC stabilized nZVI at 7 °C during a nZVI field trial. This study reported that the onsite synthesized particles had sizes (86±12 nm, from TEM analysis) and zeta potentials (-49.2±1.5 mV) similar to particles synthesized in controlled laboratory environments. However, no field or laboratory study has been conducted to explore the

possibility of nZVI synthesis at temperatures below 7 °C for field application in cold climate regions.

2.2.2   nZVI injection and transport at the field-scale

Field-scale studies have used both gravity and pressure injection techniques to inject nZVI into the subsurface (Bennett et al., 2010; Elliott and Zhang, 2001; He et al., 2010; Johnson et al., 2013; Kocur et al., 2014; Krug et al., 2010; Zhang, 2003). Pressure injection results in higher nZVI flow rates from the injection well but may cause daylighting (Krug et al., 2010; O'Carroll et al., 2013b). In contrast, flow velocities due to gravity injection are more impacted by subsurface hydraulic conductivity (i.e., injection head cannot be as easily increased under gravity injection). Consequently, injection rates at field trials that have used gravity injection have varied from 1 L/min to as high as 20 L/min, resulting in different transport rates (Elliott and Zhang, 2001; He et al., 2010; Johnson et al., 2013; Kocur et al., 2014; Krug et al., 2010; Wei et al., 2010). Field-scale nZVI travel distances ranging between 0.45 to 2 m have been reported in the literature (O'Carroll et al., 2013b). However, it is difficult to compare the field observed nZVI travel distances due to differences in nZVI formulation, injection method and rate, and the geologic setting where nZVI was applied. More recently, studies have reported nZVI breakthrough at 1 m downstream of the injection well (Johnson et al., 2013; Kocur et al., 2014). Samples collected from a monitoring well 1 m downstream of injection well were analyzed using dynamic light scattering (DLS), transmission electron microscopy (TEM), and Energy dispersive X-ray spectroscopy (EDS) techniques, confirming the presence of nZVI particles (Kocur et al., 2014).

To date most of the field trial studies have investigated nZVI transport in the saturated zone, however, it may be necessary to inject nZVI above the water table to target contamination in the vadose zone, especially in zones immediately above the water table. Contamination immediately above the saturated zone is possible given seasonal fluctuations in the water table. Wei et al. (2010) injected nZVI both in saturated and unsaturated zone where an accumulation of nZVI was observed in the unsaturated zone. It was not evident how much of the nZVI was delivered to the unsaturated zone nor was nZVI transport in this zone

investigated. Therefore, there is a need to assess nZVI transport in variably saturated zones for optimal nZVI application design.

2.2.3   Field-scale modeling of nZVI transport

Travel distances from smaller column experiments are often extrapolated to infer the nZVI travel distances at the field-scale. For this, a steady-state analytical solution based on colloid filtration theory (CFT) are used (He et al., 2009; Johnson et al., 2009; Phenrat et al., 2009; Raychoudhury et al., 2010; Schrick et al., 2004; Tiraferri and Sethi, 2009). Maximum nZVI travel distances, using such analytical methods, are calculated as the distance required to remove 99.9% of the initial nZVI concentration (O'Carroll et al., 2013b). More recent studies have used numerical models incorporating CFT mechanisms in the advection-dispersion transport equation to simulate nZVI migration in 1D columns (Kocur et al., 2013; Tiraferri et al., 2011; Tosco and Sethi, 2010; Tosco et al., 2009). Simulated breakthrough curves in modeling studies were in good agreement with column experiment results when the sticking efficiency (α) (Kocur et al., 2013; Tiraferri and Sethi, 2009) or the attachment rate (K_{att}) (Tiraferri et al., 2011) were used as a fitting parameter. Although nZVI transport has been simulated for small-scale column studies, models capable of simulating large-scale nZVI transport are required to predict nZVI transport, distribution in the subsurface and subsequent remediation (Tosco et al., 2014). Johnson et al. (2013) developed a three-dimensional (3D) model using MT3D-MODFLOW and validated it using pilot scale model aquifer test data. Krol et al. (2013) used a 3D numerical simulator, CompSim, to simulate nZVI transport in the field and validated it using observed field data (Bennett et al., 2010). CFT based equations (Equations 2.1-2.2) were incorporated in CompSim to simulate nanoparticle transport in porous media (Krol et al., 2013):

$$\frac{\partial(\theta_w C)}{\partial t} + \theta_w K_{att} C = \nabla \cdot (\theta_w D \cdot \nabla C) - \nabla \cdot (C\vec{q}) \qquad \text{(Equation 2.1)}$$

where, C is the nZVI concentration in suspension (M/L^3), D is the hydrodynamic dispersion tensor (L^2/T), $\vec{q}$ is the Darcy velocity (L/T), θw is the volumetric water content (-), and K_{att} is the attachment rate coefficient (1/T). K_{att} is defined as:

$$K_{att} = \frac{3(1-\theta_w)}{2d_c}\alpha\eta_o v_p \qquad \text{(Equation 2.2)}$$

where, d_c is the mean collector diameter (L) and v_p is the pore water velocity (L/T). α and η_0 are the sticking efficiency (L) and theoretical single collector contact efficiency (-), respectively. η_0 is calculated using the relationship developed by (Tufenkji and Elimelech, 2004). Krol et al. (2013) showed that CompSim, modified with CFT, could be used to accurately simulate nZVI transport in saturated porous media. However, no study has been conducted to predict nZVI transport in both the saturated and unsaturated zone suggesting that further investigations are necessary for numerical simulation of nZVI transport in variably saturated porous media.

2.2.4   nZVI reactivity

A range of groundwater quality parameters (e.g., pH, oxidation reduction potential (ORP), dissolved oxygen (DO), electrical conductivity (EC), total and dissolved iron, anions (e.g., chloride), and total organic carbon) have been used to assess nZVI arrival at monitoring wells (Bennett et al., 2010; He et al., 2010; Zhang, 2003) based on the geochemical changes induced. For example, nZVI can react with water and DO (Equations 2.4-2.5) in the subsurface resulting in increased groundwater pH (Zhang, 2003):

$$Fe^0_{(s)} + 2H_2O \rightarrow Fe^{2+}_{(aq)} + H_{2(g)} + 2OH^- \qquad \text{(Equation 2.3)}$$

$$Fe^0_{(s)} + 4H^+ + O_2 \rightarrow 2Fe^{2+}_{(aq)} + 2H_2 \qquad \text{(Equation 2.4)}$$

Studies reported an increase of more than 2 pH units following nZVI injection in the subsurface (Elliott and Zhang, 2001). Another geochemical indicator, ORP, is a measure of oxidation or reduction state of a solution where positive and negative ORP indicate oxidizing and reducing conditions, respectively. As nZVI reacts with DO (Equation 2.4) and other oxidants present in groundwater, nZVI donates electrons to these species, decreasing groundwater ORP. For example, He et al. (2010) found that ORP in a monitoring well decreased from -63 to -355 mV in 2 hours following nZVI injection. Thus a decrease in ORP suggests an alteration in groundwater geochemistry and has been used

as an indicator for the presence of nZVI (Bennett et al., 2010; Elliott and Zhang, 2001; He et al., 2010; Wei et al., 2010).

nZVI has been injected at sites contaminated with a range of cVOCs including PCE, TCE, 1,2-dichloroethene (1,2 cis-DCE) and vinyl chloride (VC) (Bennett et al., 2010; He et al., 2010; Wei et al., 2010). At these sites chlorinated ethenes (e.g., TCE) have been reduced to less toxic or environmentally benign compounds such as ethane and chlorides (Elsner et al., 2008; Liu et al., 2005; O'Carroll et al., 2013b):

$$C_2HCl_3 + 4Fe^0 + 5H^+ \rightarrow C_2H_6 + 4Fe^{2+} + 3Cl^- \qquad \text{(Equation 2.5)}$$
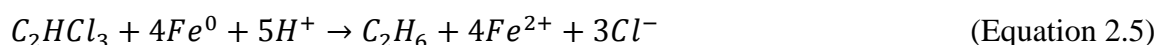
In a recent study Kocur et al. (2015) demonstrated that nZVI injection resulted in rapid abiotic degradation of in-situ cVOCs (Kocur et al., 2015). As shown in Equation (2.4) nZVI injection generates hydrogen and creates a reducing condition that are favorable for biotic degradation of contaminants. Stabilizing polymers (e.g., CMC) also serve as fermentable substrate generating hydrogen that can be utilized by microorganisms (Kocur et al., 2015). The study by Kocur et al. (2015) demonstrated that the *Dehalococcoides* population in the study area increased following CMC stabilized nZVI injection suggesting that injection of nZVI facilitated both abiotic biotic degradation of contaminants.

To increase the reactivity of injected particles with target contaminants, many of the field studies to date have used bimetallic nanoparticles (Pd/Fe) doped with varying amounts (e.g., 0.1%-0.5% by wt) of palladium (Pd) (Bennett et al., 2010; Elliott and Zhang, 2001; He et al., 2010; Wei et al., 2010) leading to very good contaminant degradation. For example, Elliott and Zhang (2001) observed a 7.8%-96.5% decrease in TCE concentration in four weeks at a monitoring well where unstabilized bimetallic nanoparticles were injected into the subsurface. Although many field studies injected bimetallic nZVI there is concern with regards to the use of these particles due to environmental issues associated with injection of noble metals in the subsurface (O'Carroll et al., 2013b). Therefore, there is a need to evaluate the efficacy of monometallic nZVI particles in degrading subsurface contaminants at field sites.

2.3 In-Situ Chemical Oxidation (ISCO) with Permanganate

2.3.1 Permanganate

ISCO is a remediation technology where an oxidant is injected into the subsurface for in-situ oxidation of target contaminants (Baciocchi et al., 2014; Siegrist et al., 2011). Commonly used oxidants include sodium/potassium permanganate ($NaMnO_4$/$KMnO_4$), hydrogen peroxide (H_2O_2), persulfate ($Na_2S_2O_8$), ozone (O_3), or peroxone (H_2O_2 and O_3). Among these oxidants, use of permanganate (PM) for in-situ remediation has garnered significant interest due to its high oxidation-reduction potential (+1.7 volts), stability in aqueous solution, reactivity over a wide range of pH (3.5 to 12), ability to work without an activator, and production of non-toxic by-products after reaction with target contaminants (Kao et al., 2008; Petri et al., 2011b; Siegrist et al., 2011; Waldemer and Tratnyek, 2005). Therefore, it has gained much interest for lab-scale experiments leading to field-scale application.

2.3.2 Permanganate reactivity

Permanganate (PM)-contaminant reaction occurs over a broad pH range (3.5-12) and different permanganate half reactions have been proposed based on the pH of the solution (Petri et al., 2011b; Roach and Reddy, 2006; Yan and Schwartz, 1999), as shown in Equations (2.6-2.8):

$$MnO_4^- + 3e^- + 2H_2O = MnO_{2(s)} + 4OH^-; \qquad [3.5 < \text{pH} < 12] \qquad \text{(Equation 2.6)}$$

$$MnO_4^- + e^- = MnO_4^{2-}; \qquad\qquad [\text{pH} > 12] \qquad\qquad \text{(Equation 2.7)}$$

$$MnO_4^- + 5e^- + 8H^+ = Mn^{2+} + 4H_2O; \qquad [\text{pH} < 3.5] \qquad \text{(Equation 2.8)}$$

$$C_2HCl_3 + 2MnO_4^- \rightarrow 2CO_2 + 2MnO_{2(s)} + 3Cl^- + H^+ \qquad \text{(Equation 2.9)}$$
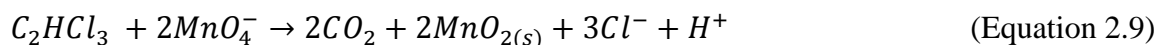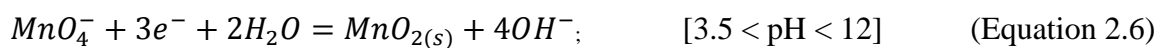
Groundwater pH is expected to vary between 5 and 8 suggesting Equation (2.6) to be the dominating permanganate reaction while Equations (2.7-2.8) are applicable for extreme conditions. Equation (2.9) represents the overall oxidation of TCE by PM although it forms

cyclic hypomanganate ester at the initial step which rapidly degrades to carboxylic acids via different pathways and finally to CO_2 (Yan and Schwartz, 2000).

PM reactivity has been studied in lab-scale experiments with a number of contaminants such as cVOCs, poly aromatic hydrocarbons (PAHs), pesticides and explosives (Siegrist et al., 2008). Among these contaminants cVOCs (e.g., TCE, PCE) mostly in aqueous phase (Huang et al., 2001; Huang et al., 2002c; Kao et al., 2008; Loomer et al., 2010; Waldemer and Tratnyek, 2005; Yan and Schwartz, 2000) or as a DNAPL/residual phase (Crimi and Siegrist, 2005; Huang et al., 2002b; Kim and Gurol, 2005; Schnarr et al., 1998; Schroth et al., 2001), were extensively studied. The laboratory experiments were conducted in reaction vials with aqueous solutions of the target contaminants (e.g., TCE) and PM. The time required for TCE degradation (>99% of initial TCE concentration) in such studies varied depending on initial concentrations of TCE, PM and pH (Huang et al., 2001; Kao et al., 2008; Yan and Schwartz, 1999; Yan and Schwartz, 2000). For example, Kao et al. (2008) reported that the time required for TCE degradation (>99% of initial TCE concentration) were approximately 10, 30 and 125 min when initial TCE concentrations were 100, 20 and 5 mg/L, respectively, with a PM to TCE ratio of 20. Previous TCE treatability studies with PM reported that Equation (2.9) followed a first order reaction kinetics with respect to both TCE and PM; therefore, it followed second order reaction kinetics overall (Huang et al., 2001; Kao et al., 2008; Waldemer and Tratnyek, 2005; Yan and Schwartz, 2000). The reported second order rate constant varied between 0.46 and 1.19 $m^{-1}s^{-1}$ (Huang et al., 2001; Kao et al., 2008; Waldemer and Tratnyek, 2005; Yan and Schwartz, 1999) for a range of pH (4 to 8). Kao et al. (2008) further studied the degradation of TCE by PM in the presence of sand, clayey sand and silty clay. This study reported that more reaction time (250, 330 and 460 min for sand, clayey sand and silty clay. respectively) was necessary for complete TCE degradation (initial TCE concentration of 5 mg/L with PM to TCE ratio of 20) with decreasing soil permeability; however, no explanation for such behavior nor the kinetic rate constant were reported.

A number of column experiments had been conducted to study the effectiveness of PM for in-situ contaminant degradation. Such studies involved different concentrations of PM (0.8 g/L to 10 g/L) and contaminants (aqueous solution to residual phase), porous media (natural

soil, fine to coarse silica sand), and column dimensions (2.54 cm to 95 cm) (Huang et al., 2002b; Li and Schwartz, 2000; Schnarr et al., 1998; Schroth et al., 2001; Struse et al., 2002). These column studies showed that the contaminant reaction was much slower in the presence of any porous matrix consistent with the study by Kao et al. (2008). For example, Li and Schwartz (2000) observed that 96.9% of residual TCE in the column was degraded after 365 hrs of continuous PM (1 g/L) flushing, where 90% of TCE was degraded in first 115 hrs while the last 6.9% was degraded in remaining 250 hrs. In contrast, Huang et al. (2002b) observed complete TCE (5 mL of 1060 mg/L aqueous TCE solution) degradation in 6 hrs resulting from injection of 2.05 g/L PM.

Previous studies showed that PM-TCE interaction was much slower in the presence of a porous media compared to kinetic experiments (in the absence of porous media) requiring more reaction time for TCE (DNAPL or aqueous phase) degradation (Huang et al., 2002b; Li and Schwartz, 2000; Schnarr et al., 1998; Schroth et al., 2001; Struse et al., 2002). Moreover, Kao et al. (2008) observed an increase in TCE reaction time with decreasing soil permeability in reaction vial experiments. PM dispersion decreases due to the presence of soil compared to reaction vials containing only PM solution; therefore, greater PM-TCE contact time is necessary to degrade TCE in soil matrix. The fact that TCE degradation was slower in the presence of a porous media suggests that more reaction time should be allowed for in-situ contaminants (e.g., TCE) degradation.

2.4   In-Situ Chemical Oxidation (ISCO) with Persulfate

2.4.1   Persulfate

Persulfate (PS), also known as peroxydisulfate, for ISCO application is the recent addition to oxidant family and has gained much interest in recent years. The advantages of PS over other oxidants are high reduction potential (2.01 volts), stability in aqueous solution at room temperature and neutral pH, and production of non-toxic by-products after reaction with chlorinated solvent and high solubility (42 wt.% at 25 °C) (House, 1962; Petri et al., 2011a; Tsitonaki et al., 2010). PS can react with the contaminant by direct electron transfer via self-decomposition or free radical (e.g., $SO_4^{-\bullet}$) generation upon activation (Equation 2.10). Direct electron transfer reactions are generally slower than the free radical reactions (Petri

et al., 2011a). Furthermore, $SO_4^{-\bullet}$ (E_o = 2.6 V) is an aggressive oxidant compared to PS itself ($S_2O_8^{2-}, E_o = 2.01\ V$) (Tsitonaki et al., 2010). Therefore, activated PS is generally preferred for ISCO application. PS can first be delivered to the targeted treatment zone followed by activation to degrade the contaminants, thus, making it more suitable for in-situ remediation.

2.4.2   Persulfate activation

Activated PS generates reactive sulfate radicals, $SO_4^{-\bullet}$, that increases the rate of reaction with contaminants compared to self-decomposed PS (Petri et al., 2011a). Activators include heat or ultra-violet (UV) light, high pH (greater than 11), hydrogen peroxide, and dissolved or chelated iron (Fe^{2+}), nano-Fe_3O_4 (Costanza et al., 2010; Petri et al., 2011a; Yang and Yeh, 2011; Yukselen-Aksoy and Reddy, 2012). In a recent study, it was observed that the highest polychlorinated biphenyls (PCBs) degradation was achieved with high pH activation of PS followed by peroxide, chelated Fe^{2+} and zero valent iron activation methods (Fan et al., 2016). However, performance of heat activation was not evaluated as part of the aforementioned study. Delivery of any remediant through contaminated low permeability zones is challenging due to the lower permeability of the porous media as such delivery of activators (e.g., alkaline solution, dissolved or chelated metals) may not be suitable for field application. In contrast, thermal activation does not require delivery of the activator itself through low permeability zones rendering it suitable for subsurface application for PS activation (Petri et al., 2011a). Waldemer et al. (2007) proposed that in-situ thermal remediation (ISTR) can be combined with PS application to activate delivered PS.

Electrical resistance heating (ERH), a form of ISTR, is performed by placing a series of electrodes into the soil in a hexagonal or triangular fashion. An alternating current (AC) is then applied across these electrodes (Krol et al., 2011). The current is conducted through the targeted area and the resistance to current results in heat generation (Krol et al., 2011; Vermeulen and McGee, 2000). ERH has been applied for subsurface remediation, including low permeability zones, where the subsurface is heated to temperatures between 60 and 110 °C (Kingston et al., 2010). However, thermal activation of PS requires low

temperature heating (<60 °C) in contrast to typical ERH. ERH could be a viable solution for PS activation for low permeability soil remediation eliminating the uncertainties associated with activator (e.g., alkaline solution, dissolved or chelated Fe^{2+}) delivery through such porous matrix.

2.4.3   Persulfate decomposition

Thermal activation results in PS decomposition generating reactive $SO_4^{-\bullet}$ (House, 1962; Johnson et al., 2008; Kolthoff and Miller, 1951), as shown in Equation (2.10):

$$S_2O_8^{2-} \xrightarrow{heat} 2SO4^{-\bullet} \hspace{3cm} \text{(Equation 2.10)}$$

The $SO_4^{-\bullet}$ initiates a chain of reactions producing reactive intermediates such as hydroxyl radicals ($HO^{\bullet}$) and peroxymonosulfate (HSO_5^-) (Berlin, 1986; Huang et al., 2002a; Waldemer et al., 2007). Recently, Johnson et al. (2008) performed a series of reaction vial experiments, both in the absence and presence of porous media, to determine the PS decomposition rate at different temperatures. They had observed an increase in PS decomposition rate with increase in temperature in both cases. For example, observed pseudo-first order rate constants, in reaction vial experiments with soil, were 0.053, 1.32 and 13.6 d^{-1} at 30, 50 and 70 °C, respectively. These observed rate constants were consistent with other studies (House, 1962; Kolthoff and Miller, 1951; Santos et al., 1996). The calculated activation energy (E_a) from the reaction vials experiments with soil was 120±7 kJ/mol (Johnson et al., 2008). As a comparison, E_a from reaction vial experiments with water but no soil varied between 118 and 140.2 kJ/mol (House, 1962; Johnson et al., 2008; Kolthoff and Miller, 1951). In contrast, reported E_a for Fe^{2+} activation of PS was 50 kJ/mol (Fordham and Williams, 1951). The similar E_a in the reaction vial experiments with and without the soil matrix as discussed above suggest that E_a for thermal activation of PS is independent of the presence and absence of soil in the reaction vial experiments. This is likely due to the fact that heat can be applied more uniformly in those reaction vials (both with water but no soil and with soil experiments). Application of other activators such as Fe^{2+} or alkaline solution require that both the PS and activator ions must come in contact to activate the PS; however, the presence of soil matrix would affect the dispersion and

mixing of PS and activators. Moreover, heat may also enhance desorption of cVOCs from soils, resulting in faster contaminant removal, therefore, E_a would be different in such cases.

2.4.4   Persulfate reactivity

PS oxidation of contaminant, such as PCE, is given by (Costanza et al., 2010):

$$2C_2Cl_4 + S_2O_8^{2-} + 8H_2O \rightarrow 2SO_4^{-2} + 8Cl^- + 4CO_2 + 10H^+ + 3H_2 \quad \text{(Equation 2.11)}$$
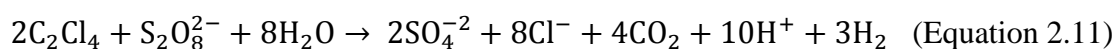
As discussed before activated PS (i.e., $SO_4^{-\bullet}$) is more reactive than slower self-decomposed PS. It should be noted here that the PS needs to be activated (by applying heat) in a manner such that $SO_4^{-\bullet}$ generation is enough to react with contaminant but not too fast to deplete the available PS without reacting with the contaminants. In lab-scale experiments thermally activated PS degraded different organic contaminants (e.g., cVOCs, PAHs, methyl tert-butyl ether) (Costanza et al., 2010; Huang et al., 2002a; Huang et al., 2005; Liao et al., 2014; Waldemer et al., 2007; Xu et al., 2015). However, the studies related to thermal activation for cVOC (e.g., PCE) degradation are discussed in the subsequent section.

Reaction vial experiments, with or without the presence of a soil matrix, were conducted to evaluate the performance of thermally activated PS to degrade PCE (Costanza et al., 2010; Huang et al., 2002a; Huang et al., 2005; Liang et al., 2003; Waldemer et al., 2007). PS concentrations varying between 0.1 and 59 g/L were activated at temperatures ranging from 20 °C to 70 °C to degrade PCE (Costanza et al., 2010; Huang et al., 2005; Liu et al., 2014; Waldemer et al., 2007). For example, Huang et al. (2005) observed 24.3%, 59.3% and 74.9% PCE degradation in reaction vial experiments (with water but no soil) in 72 hrs when 1 g/L PS was activated at 20, 30 and 40 °C, respectively. Higher PCE degradation was achieved when PS, activated at 40 °C, concentration was increased to 5 g/L within same time frame suggesting that increasing PS concentration resulted in faster PCE degradation. The pseudo-first order rate constants, from PCE degradation data, were 0.13, 0.27 and 0.45 d^{-1} at 20, 30 and 40 °C, respectively. However, these rate constants were significantly lower than that obtained by Waldemer et al. (2007) (e.g., 0.96 and 5.8 d^{-1} at 30 and 40 °C, respectively). This difference is likely because Huang et al. (2005) measured the degradation kinetics in a solution of 59 VOCs where the contaminants would compete

for reactive $SO_4^{-\bullet}$; thus, some contaminants might have higher reaction rates than others compared to reactions with single species in solution (Waldemer et al., 2007). The resulting E_a, from PCE degradation kinetics, were 46.4 and 101±4 kJ/mol as reported by Huang et al. (2005) and Waldemer et al. (2007), respectively. More recently Costanza et al. (2010) conducted a series of reaction vial experiments, both with and without the soil in the vials, to observe PCE oxidation by PS. Observed pseudo-first order rate constants varied between 1.9 and 652 d^{-1} (in reaction vials with water but no soil) when the temperature was varied between 31.1 and 70 °C with an E_a of 101.8±4.7 kJ/mol. This E_a was very similar to that obtained by Waldemer et al. (2007). However, the presence of soil slurries in the reaction vial experiments significantly decreased the pseudo-first order rate constants, varying for different types of soils used. For example, the observed rate constants in reaction vials with water, F-70 sand and kaolinite clay were approximately 80, 12 and 3 d^{-1}, respectively, at 50 °C (E_a not available) (Costanza et al., 2010). In general, the studies suggested that thermally activated PS was able to degrade PCE in reaction vials with water (but no soil), and with water and soil experiments. The presence of soil matrix in these reaction vial experiments significantly decreased the kinetics rates (Costanza et al., 2010; Huang et al., 2005; Waldemer et al., 2007). This suggests that in-situ contaminant degradation should be studied in more realistic systems (e.g., column experiments).

2.5   Back Diffusion of Contaminant from Low Permeability Porous Media

Injection of any remediant, oxidants or reductants, aiming for in-situ remediation of contaminated sites would remove the contaminants from the permeable zones but typically has limited accessibility to low permeability zones. The poor remediant delivery into such zones result in inadequate contaminant degradation of such strata in the subsurface. The challenges associated with remediation of low permeability zones and subsequent back diffusion was demonstrated through a series of experiments by Sale et al. (2013). The experiments were conducted in 2D tanks characterized by alternating 5 cm vertical strips of coarse sand (K = 200 m/d) and silt (K = 0.18 m/d) loaded with aqueous TCE (1300 mg/L). All of the 5 remediation efforts tested showed a rebound due to back diffusion of

TCE from the silt layer resulting from inadequate treatment (Figure 2.1). The largest TCE reduction was only 3.8 orders of magnitude (OoM) from the TCE loading, which still represented 1.6 OoM higher than the maximum contaminant level (MCL) permitted for TCE in groundwater (Figure 2.1). This study also showed that diffusive transport of permanganate was limited to 1.3 cm into the silt layers resulting in incomplete remediation. This study, in agreement with many field and modelling studies, accentuated that remediants must be delivered throughout the low permeability zones to treat in-situ contaminants in order for remediation efforts to ultimately be successful.
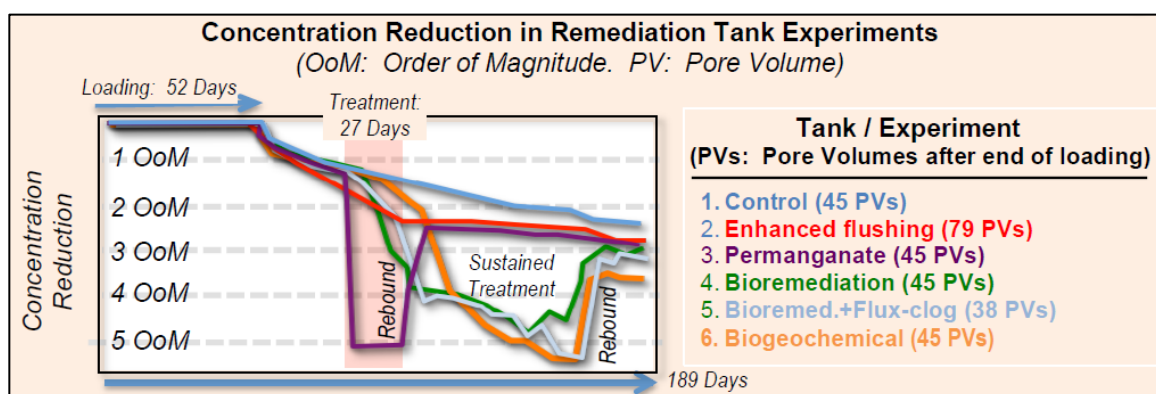
Figure 2.1: TCE concentration reduction in tank experiments by Sale et al. (2013).

Hence, there is a thriving interest in academia as well as in industry to develop effective remediation technologies eliminating, or limiting at the least, the extent of back diffusion from low K zones in the subsurface.

2.6 Electrokinetics

Given the difficulties associated with delivering remediants in low permeability zones, electrokinetics (EK) has been proposed to enhance the delivery in such soil (Reynolds et al., 2008; Roach and Reddy, 2006). EK is the application of a low voltage (DC) across the positively charged (anode) and negatively charged (cathode) electrodes (Acar and Alshawabkeh, 1993; Acar et al., 1997). EK induced migration is insensitive to the hydraulic conductivity of porous media, hence, it is particularly beneficial for low permeability soils where advective transport is very small and often diffusion dominated. EK, therefore, has

been used extensively in low permeability porous media to remediate a wide variety of hazardous wastes, including organic compounds, inorganic species and radionuclides (Acar et al., 1995).

Application of EK results in oxidation and reduction of water at the anode and cathode cells, respectively, decreasing pH at the anode and increasing pH at the (Acar and Alshawabkeh, 1993) according to the following Equations (2.12-2.13):

Oxidation at the anode:

$$2H_2O \rightarrow 4H^+ + O_2 + 4e^-$$ (Equation 2.12)

Reduction at the cathode:

$$2H_2O + 2e^- \rightarrow 2OH^- + H_2$$ (Equation 2.13)

pH at the anode may decrease to less than 2 while cathode pH may increase to higher than 12 depending on the current or the voltage gradient applied (Alshawabkeh, 2009; Yukselen-Aksoy and Reddy, 2012). The oxidative and reductive conditions tend to increase the ORP at the anode and decrease at the cathode. Such non-uniform pH and redox conditions throughout the system complicate EK application and may impact oxidant migration (Hodges et al., 2011). EK-induced mass flux of any species depends on several factors such as soil mineralogy, porosity, tortuosity, pore fluid ionic concentration and the species generated due to EK application (e.g. H^+/OH^-) (Acar and Alshawabkeh, 1993; Alshawabkeh, 2009). These factors affect the EK induced transport mechanisms and rate of migration.

2.6.1   EK-inducted transport mechanisms

The EK-induced migration mechanisms of species can be classified as a) Electrophoresis (EP), b) Electroosmosis (EO), and c) Electromigration (EM). Electrophoresis (EP) is the migration of charged particles or colloids placed within an external electric field (Acar et al., 1997; Masliyah and Bhattacharjee, 2006b). Electroosmosis (EO) is defined as the movement of the bulk pore fluid through the capillary when an external electric field is

imposed (Acar and Alshawabkeh, 1993). Electromigration (EM) is the transport of ions (positive or negative) under a DC electric field (Acar and Alshawabkeh, 1993). It is noted here that under many subsurface conditions (i.e., quartz soil with negative surface charge) EO flow occurs from the anode to the cathode electrode. EM transport direction depends on the valence (positive or negative) of the ions and migrates towards the opposite (to sign of valence) polarity electrode. Therefore, EK induced oxidant transport would be due to EO or EM. Therefore, these two transport mechanisms are discussed in the subsequent sections.
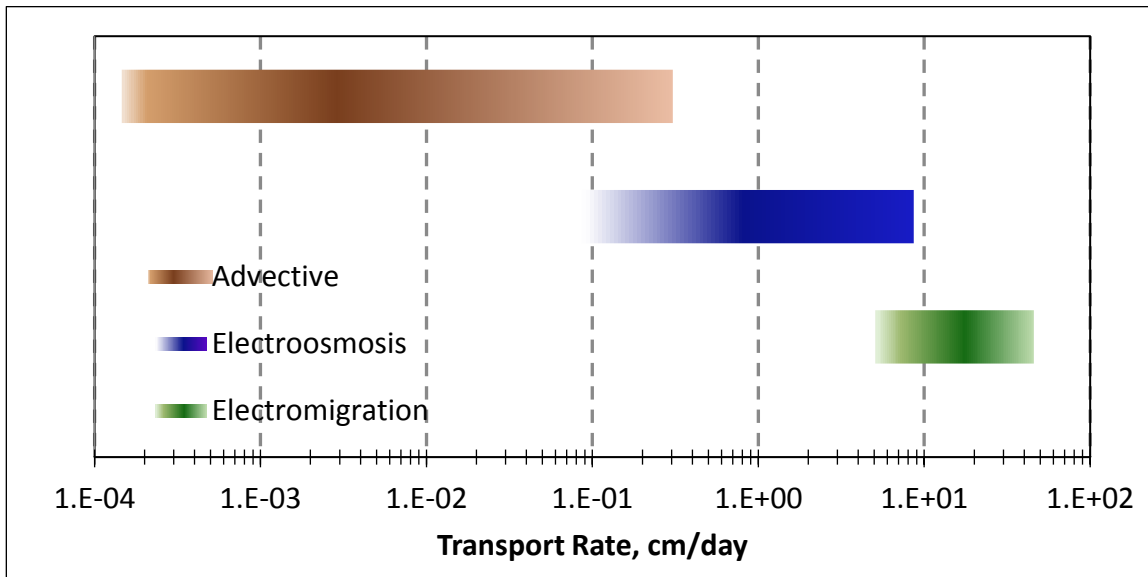
Figure 2.2: Comparison of advective and EK induced transport rates through clayey soil (reproduced after Alshawabkeh (2009)) with k_h between 8.6×10^{-7} and 8.6×10^{-4} m/day (Fetter, 2001); k_{eo} between 8.6×10^{-6} to 8.6×10^{-4} m^2/V-day for all soils (Eykholt and Daniel, 1994; Mitchell and Soga, 2005); calculated u_i^* from 5.0×10^{-4} to 5.0×10^{-3} m^2/V-day for common ions (e.g., H^+, OH^-, HCO_3^-, SO_4^{2-}, Fe^{2+}, PM, PS, lactate, etc.; Table 2.1) (Lide, 2005).

2.6.1.1 Electroosmosis (EO) inducted transport

As defined before that electroosmosis (EO) is the movement of pore fluid relative to the stationary porous media due an external electric field application (Acar and Alshawabkeh, 1993; Masliyah and Bhattacharjee, 2006a). The positively charged ions (i.e., the counter ions) in the diffuse double layer adjacent to the negatively charged porous media move towards the cathode when the external electric field is applied. The counter ions, while migrating, transfer the momentum to the surrounding fluid resulting in EO flow (Q_{EO}) towards the cathode (Acar et al., 1995). This would also result in the migration of the non-ionic species along with the bulk fluid (Cauwenberghe, 1997). Electroosmostic velocity (q_{eo}) is given by Equation (2.14) (Mitchell and Soga, 2005):

$$q_{EO} = \frac{Q_{EO}}{A_{flow}} = k_{EO}i_e = \frac{\epsilon\zeta}{\eta}n\,i_e \qquad \text{(Equation 2.14)}$$

where, k_{EO} is electroosmotic permeability (m^2/V-day), i_e is applied voltage gradient (V/m), ϵ is the dielectric permittivity of the medium (C^{2}V^{-1}m^{-2}), ζ is the zeta potential (V) of the porous media, η is fluid viscosity (Pa.s), and n is porosity (-). k_{EO} is a function of soil ζ potential, as such varies with pH, electrolyte concentration and valence of cations present (Acar et al., 1997). In general, an increase in electrolyte concentration or decrease in pH reduces the k_{EO}, therefore, reduces Q_{EO}. Reported k_{eo} values vary from 8.6x10^{-6} to 8.6x10^{-4} m^2/V-day for all soils (Eykholt and Daniel, 1994; Mitchell and Soga, 2005; Shapiro and Probstein, 1993; Shariatmadari et al., 2009; Weng et al., 2003). This would result in EO transport rates varying between 0.1 and 10 cm/day under a typical voltage gradient of 1 V/cm, as shown in Figure (2.2). In contrast, advective velocity through clay would be at least one order of magnitude lower than EO velocity. This demonstrates that EO has significant potential in driving dissolved species along with the pore fluid through low permeability porous media.

2.6.1.2 Electromigration (EM) inducted transport

Electromigration (EM), or the migration of ionic species due to EK, induced mass flux (J_{EM}) is given by Equation (2.15) (Acar and Alshawabkeh, 1993):

$$J_{EM} = u_i^* c_i i_e = \frac{D_o \tau n z_i F}{RT} c_i i_e \qquad \text{(Equation 2.15)}$$

where, u_i^* is effective ionic mobility of species i (m^2/volt-sec), c_i is concentration (g/m^3), i_e is voltage gradient (V/m), D_o = diffusion coefficient at infinite dilution, (m^2/sec); τ is soil tortuosity [-] that varies between 0.01 and 0.84 (Shackelford and Daniel, 1991), z_i is valence of ionic species i, F is Faraday's constant (96485 C/mol), R is universal gas constant, 8.314 J/mol-K, T is temperature in K. Equation (2.15) implies that for a given porous media, J$_{EM}$ is a function of concentration of ionic species i, diffusion coefficient of species i at infinite dilution, and the valence of species i. The electromigration of a given species depends on applied voltage gradient, porosity and soil tortuosity. Under typical geochemical conditions EM mass transport is at least 10 times higher than EO migration (Acar and Alshawabkeh, 1993). EM is considered to be the dominant ionic migration mechanism in the absence of any advective flow. Equation (2.15) shows that EM mass flux (J$_{EM}$) or the effective ionic velocity (u_i^*) depends on the diffusion coefficient (D$_o$) and valence (z$_i$) of the ions, other parameters being held constant. The D_o and calculated u_i^* values of some selected ions are given in Table 2.1.

Table 2.1: Diffusion coefficient at infinite dilution and effective ionic mobility of selected ions (Lide, 2005)

Ions	Diffusion coefficient at infinite dilution D_o, cm^2/sec	Effective ionic mobility[+] u^*, m^2/V-day
Lactate	1.03×10^{-05}	5.07×10^{-04}
HCO_3^-	1.19×10^{-05}	5.82×10^{-04}
Na^+	1.33×10^{-05}	6.55×10^{-04}
Fe^{2+}	7.19×10^{-06}	7.06×10^{-04}
Ca^{2+}	7.92×10^{-06}	7.78×10^{-04}
Permanganate	1.63×10^{-05}	8.01×10^{-04}
NO_3^-	1.90×10^{-05}	9.34×10^{-04}
Cl^-	2.03×10^{-05}	9.98×10^{-04}
SO_4^{2-}	1.07×10^{-05}	1.05×10^{-03}
Persulfate	1.15×10^{-05}	1.12×10^{-03}
PO_4^{3-}	8.24×10^{-06}	1.21×10^{-03}
OH^-	5.27×10^{-05}	2.59×10^{-03}
H^+	9.31×10^{-05}	4.57×10^{-03}

[+] calculated assuming n = 0.41 [-]; $\tau = = 0.35$ [-]; T= 293K; F = 96485; i_e = 1 V/cm;

Equation (2.15) can be used to calculated theoretical EM transport rates from the known D_o values. Calculated EM velocities for PM and PS are 8.0 and 11.3 cm/day, respectively, with assumed values as shown in Table 2.1. These values suggest that PS migration is 1.4 times faster compared to PM migration. Figure (2.2) suggests that EK induced transport can be beneficial to deliver remediants into low permeability porous media and has gained considerable interest in recent years. Consequently, EK assisted oxidant (e.g., PM, PS)

delivery has been studied in laboratory-scale experiments as discussed in the subsequent sections (Cang et al., 2013; Fan et al., 2014; Hodges et al., 2013; Reynolds et al., 2008; Roach and Reddy, 2006; Robertson, 2009; Thepsithar and Roberts, 2006; Yang and Yeh, 2011; Yukselen-Aksoy and Reddy, 2012).

2.6.2   EK-Permanganate studies

A number of studies reported EM-induced PM migration to be dominant over EO assisted migration in lab-scale experiments (Cang et al., 2013; Hodges et al., 2013; Reynolds et al., 2008; Roach and Reddy, 2006; Thepsithar and Roberts, 2006). However, Roach and Reddy (2006) observed that EO assisted PM migration was the dominant transport mechanism in comparison to EM. All of these studies reported that PM migration stalled during the experiment, limiting further migration. It was hypothesized that a pH gradient between the anode and cathode played a role in stalling PM migration (Hodges et al., 2013; Reynolds et al., 2008; Roach and Reddy, 2006).

Hodges et al. (2013) had demonstrated that PM migration stalled due to the pH gradient resulting from EK application and that eliminating the pH gradient significantly improved PM migration through clayey soil. Hodges et al. (2013) reported a migration rate of 2 cm/day with a 1.7 V/cm voltage gradient (Hodges et al., 2013). However, this rate was smaller than that of Thepsithar and Roberts (2006) who reported 30-45 cm/day under a 1 V/cm voltage gradient. In comparison, Sale et al. (2013) observed a diffusive transport of 1.3 cm over 27 days of PM flushing. Similar diffusive transport was observed (approximately 2.5 cm over 25 days) by Struse et al. (2002). This comparison strengthens the claim that EK can be used to aid PM delivery through low permeability zones in the subsurface.

The aforementioned EK studies were designed to investigate deliverability of PM through lower permeability soil in the absence of contaminants, with the exception of the Cang et al. (2013) and Thepsithar and Roberts (2006) studies. Cang et al. (2013) reported that PM degraded 52% of pyrene after 336 hrs of coupled EK–PM application. Although limited PM migration information was provided degradation results suggest limited PM delivery throughout the soil. Thepsithar and Roberts (2006) studied the effect of PM dosage when

coupled with EK for remediating phenol contaminated soil. Manganese content in the soil at the end of experiment (24 hrs) was higher near the cathode, the PM source, compared to the anode (not detected), suggesting limited PM transport. 91% phenol was removed during 120 hrs coupled EK-PM (9 g/L) application compared to 64% in the control EK only experiment. These results suggested that 64% phenol removal was due to electroosmotic sweeping with only 27% phenol removal due to PM during EK-PM application. These studies suggest that additional work is required to couple EK with PM for successful PM delivery and reactivity with the target contaminant, especially with cVOCs.

2.6.3 EK-Persulfate studies

EK assisted PS delivery and remediation of contaminated porous media has gained much attention in recent years and has been studied by several researchers (Cang et al., 2013; Fan et al., 2014; Fan et al., 2016; Isosaari et al., 2007; Robertson, 2009; Yang and Yeh, 2011; Yuan et al., 2013; Yukselen-Aksoy and Reddy, 2013; Yukselen-Aksoy and Reddy, 2012). Yet, scarce information is available in the literature on EK induced PS transport rates.

Fan et al. (2014) studied PS (200 g/L) transport due to EO and EM through a 0.12 m long column. PS breakthrough was observed due to EM transport only. Estimated transports rates were similar (1.33 cm/day) in both cases, based on appearance of approximately 1 g/L PS at 4 cm from the source (for EO and EM at anode and cathode, respectively), under a 1 V/cm voltage gradient. However, EO delivered more PS (average of 127 g/L) compared to EM migration (44.9 g/L) into the soil at the end of 15 days. In another study, EM induced PS transport was estimated, from the reported data, to be 1.5 cm/day based on appearance of 1 g/L PS at the anode (Robertson, 2009). In this study, PS concentration at the anode was approximately 20% of input PS source (cathode) concentration (4 g/L) under 3.7 V/cm after 650 hrs. Increasing the voltage gradient (3.7 V/cm) increased the PS concentration at the anode cell (by 30%). PS transport information was not available for other studies although the contaminant degradation data suggested PS migrated throughout the soil column (Cang et al., 2013; Yang and Yeh, 2011; Yukselen-Aksoy and Reddy, 2013). In general, all these studies suggested that EK can be used to enhance PS delivery through low permeability soils.

In addition to the EK-assisted PS transport, studies also attempted to activate (via heat, high pH, peroxide, nano-Fe_3O_4 etc.) the delivered PS for in-situ degradation of different contaminants (e.g., PCBs, TCE, PAH etc.) (Fan et al., 2016; Isosaari et al., 2007; Yang and Yeh, 2011; Yukselen-Aksoy and Reddy, 2013). The extent of contaminant removal varied among the studies due to experimental conditions, delivery mechanism, activation method, and type of contaminant used. For example, Fan et al. (2016) observed higher PCB degradation (40.5%) when an alkaline solution was used to activate EK delivered PS compared to other activation methods (i.e., peroxide, chelated Fe^{2+}, and zero valent iron); however, performance of thermally activated PS was not evaluated in this study. In contrast, Yukselen-Aksoy and Reddy (2013) observed similar 2,2',3,5'-tetrachlorobiphenyl (also known as PCB-44, a representative PCB) degradation resulting from heat activated (77.9% at 45 °C) and heat coupled with high pH (12) activated (76.2%) PS (300 g/L) after 7 days. As a comparison, 22.7% and 40.7% PCB-44 was removed in EK only (no PS) and EK-PS (30 g/L PS under 1 V/cm) without activation experiments, respectively, showing significant improvement resulting from PS activation. This study also hypothesized that heat activation alone showed better performance in degrading PCB-44 compared to the contribution of combined high pH and heat activation. This was further explained by the similar PCB-44 degradation at different soil sections (average of 77.9±1.1% removal) in the former case compared to differential degradation across the soil length (85.9%, 86.7% and 56% PCB-44 removal at the anode, central and cathode soil sections, respectively). This study, by Yukselen-Aksoy and Reddy (2013), demonstrated that EK-assisted PS delivery and subsequent thermal activation is a promising technique for in-situ low permeability soil remediation. However, feasible means of heat application to activate the delivered PS needs to be investigated. Electrical resistance heating (ERH) is a technique that has been used for subsurface heating to temperatures between 60 and 110 °C (Kingston et al., 2010). ERH is performed by applying an alternating current (AC) across the electrodes and has been used for subsurface remediation including low permeability zones (Kingston et al., 2010). Therefore, ERH can be a useful technique for thermal activation of the delivered PS.

2.7 Conclusions

The current state of the in-situ remediation technologies suggests that application of nZVI, permanganate or persulfate can degrade a wide range of in-situ contaminants. For example, nZVI application can facilitate both abiotic and biotic degradation of contaminants. However, optimal design (e.g., injection volume and duration, distance between monitoring wells) of field-scale nZVI application is crucial to maximize benefits of remediation efforts and minimize cost. Numerical models can be helpful in this regard but has not been utilized so far. Application of permanganate or persulfate does not require special synthesis procedures, unlike nZVI, and the cost of chemicals is less than that of nZVI. However, any remediant delivery into low permeability is challenging potentially limiting the applicability of these in-situ remediation technologies. Therefore, there is a need for innovative solutions to deliver remediant into such low permeability soil for remediation efforts to be successful.

2.8 References

Acar, Y.B. and Alshawabkeh, A.N., 1993a. Principles of Electrokinetic Remediation. Environmental Science & Technology, 27(13).

Acar, Y.B. and Alshawabkeh, A.N., 1993b. Principles of Electrokinetic Remediation. Environmental Science and Technology, 27: 2638-2647.

Acar, Y.B., Alshawabkeh, A.N. and Parker, R.A., 1997. Theoretical and Experimental Modeling of Multi-Species Transport in Soils Under Electric Fields. United States Environmental Protection Agency, OH, pp. 1-8.

Acar, Y.B. et al., 1995. Electrokinetic remediation: Basics and technology status. Journal of Hazardous Materials, 40: 117-137.

Alshawabkeh, A.N., 2009. Electrokinetic Soil Remediation: Challenges and Opportunities. Separation Science and Technology, 44(10): 2171-2187.

Baciocchi, R., D'Aprile, L., Innocenti, I., Massetti, F. and Verginelli, I., 2014. Development of technical guidelines for the application of in-situ chemical oxidation to groundwater remediation. Journal of Cleaner Production, 77(0): 47-55.

Bennett, P., He, F., Zhao, D., Aiken, B. and Feldman, L., 2010. In situ testing of metallic iron nanoparticle mobility and reactivity in a shallow granular aquifer. Journal of Contaminant Hydrology, 116(4): 35-46.

Berlin, A.A., 1986. Kinetics of radical-chain decomposition of persulfate in aqueous solutions of organic compounds. Kinet. Catalyst, 27(1).

Cang, L., Fan, G.-P., Zhou, D.-M. and Wang, Q.-Y., 2013. Enhanced-electrokinetic remediation of copper–pyrene co-contaminated soil with different oxidants and pH control. Chemosphere, 90(8): 2326-2331.

Cauwenberghe, L.V., 1997. Technology Overview Report: Electrokinetics. Ground-Water Remediation Technologies Analysis Center, Pittsburghe, pp. 1-17.

Costanza, J., Otaño, G., Callaghan, J. and Pennell, K.D., 2010. PCE Oxidation by Sodium Persulfate in the Presence of Solids. Environmental Science & Technology, 44(24): 9445-9450.

Crimi, M.L. and Siegrist, R.L., 2005. Factors Affecting Effectiveness and Efficiency of DNAPL Destruction Using Potassium Permanganate and Catalyzed Hydrogen Peroxide. Journal of Environmental Engineering, 131(12): 1724-1732.

DNAPL-Test, 2011. DNAPL Test. In: Geosyntec Consultants, Queen's University, University of Edinburgh and U. NAVFAC (Editors).

Elliott, D.W. and Zhang, W.X., 2001. Field assessment of nanoscale bimetallic particles for groundwater treatment. Environmental Science & Technology, 35: 4922-6.

Elsner, M., Chartrand, M., VanStone, N., Lacrampe Couloume, G. and Sherwood Lollar, B., 2008. Identifying Abiotic Chlorinated Ethene Degradation: Characteristic Isotope Patterns in Reaction Products with Nanoscale Zero-Valent Iron. Environmental Science & Technology, 42(16): 5963-5970.

Eykholt, G.R. and Daniel, D.E., 1994. Impact of System Chemistry on Electroosmosis in Contaminated Soil, 120. ASCE, 797-815 pp.

Fan, G. et al., 2014. Electrokinetic delivery of persulfate to remediate PCBs polluted soils: Effect of injection spot. Chemosphere, 117(0): 410-418.

Fan, G., Cang, L., Gomes, H.I. and Zhou, D., 2016. Electrokinetic delivery of persulfate to remediate PCBs polluted soils: Effect of different activation methods. Chemosphere, 144: 138-147.

Fetter, C.W., 2001. Applied Hydrogeology. Prentice Hall, NJ.

Fordham, J.W.L. and Williams, H.L., 1951. The Persulfate-Iron(II) Initiator System for Free Radical Polymerizations1. Journal of the American Chemical Society, 73(10): 4855-4859.

Goodall, D.C. and Quigley, R.M., 1977. Pollutant migration from two sanitary landfill sites near Sarnia, Ontario. Canadian Geotechnical Journal, 14(2): 223-236.

Grathwohl, P., 1998. Diffusion in natural porous media: Contaminant Transport, Sorption/Desorption and Dissolution Kinetics, 1. Springer Science & Business Media.

He, F., Zhang, M., Qian, T. and Zhao, D., 2009. Transport of carboxymethyl cellulose stabilized iron nanoparticles in porous media: column experiments and modeling. Journal of colloid and interface science, 334: 96-102.

He, F. and Zhao, D., 2007. Manipulating the Size and Dispersibility of Zerovalent Iron Nanoparticles by Use of Carboxymethyl Cellulose Stabilizers. Environmental Science & Technology, 41: 6216-6221.

He, F., Zhao, D. and Paul, C., 2010. Field assessment of carboxymethyl cellulose stabilized iron nanoparticles for in situ destruction of chlorinated solvents in source zones. Water research, 44(7): 2360-2370.

Heiderscheidt, J.L., Siegrist, R.L. and Illangasekare, T.H., 2008. Intermediate-scale 2D experimental investigation of in situ chemical oxidation using potassium permanganate for remediation of complex DNAPL source zones. Journal of Contaminant Hydrology, 102(1–2): 3-16.

Henn, K.W. and Waddill, D.W., 2006. Utilization of nanoscale zero-valent iron for source remediation—A case study. Remediation Journal, 16(2): 57-77.

Hodges, D., Fourie, A., Reynolds, D. and Thomas, D., 2011. Development of an Apparatus for pH-Isolated Electrokinetic In Situ Chemical Oxidation. Journal of Environmental Engineering, 137(9): 809-816.

Hodges, D., Fourie, A., Thomas, D. and Reynolds, D., 2013. Overcoming Permanganate Stalling during Electromigration. Journal of Environmental Engineering, 139(5): 677-684.

House, D.A., 1962. Kinetics and Mechanism of Oxidations by Peroxydisulfate. Chemical Reviews, 62(3): 185-203.

Huang, K.-C., Couttenye, R.A. and Hoag, G.E., 2002a. Kinetics of heat-assisted persulfate oxidation of methyl tert-butyl ether (MTBE). Chemosphere, 49(4): 413-420.

Huang, K.-C., Hoag, G.E., Chheda, P., Woody, B.A. and Dobbs, G.M., 2001. Oxidation of chlorinated ethenes by potassium permanganate: a kinetics study. Journal of Hazardous Materials, 87(1–3): 155-169.

Huang, K.-C., Hoag, G.E., Chheda, P., Woody, B.A. and Dobbs, G.M., 2002b. Chemical oxidation of trichloroethylene with potassium permanganate in a porous medium. Advances in Environmental Research, 7(1): 217-229.

Huang, K.-C., Hoag, G.E., Chheda, P., Woody, B.A. and Dobbs, G.M., 2002c. Kinetics and mechanism of oxidation of tetrachloroethylene with permanganate. Chemosphere, 46(6): 815-825.

Huang, K.-C., Zhao, Z., Hoag, G.E., Dahmani, A. and Block, P.A., 2005. Degradation of volatile organic compounds with thermally activated persulfate oxidation. Chemosphere, 61(4): 551-560.

Isosaari, P. et al., 2007. Integration of electrokinetics and chemical oxidation for the remediation of creosote-contaminated clay. Journal of Hazardous Materials, 144(1–2): 538-548.

Johnson, R.L., Cherry, J.A. and Pankow, J.F., 1989. Diffusive contaminant transport in natural clay: a field example and implications for clay-lined waste disposal sites. Environmental Science & Technology, 23(3): 340-349.

Johnson, R.L., Johnson, G.O.B., Nurmi, J.T. and Tratnyek, P.G., 2009. Natural Organic Matter Enhanced Mobility of Nano Zerovalent Iron. Environmental Science & Technology, 43(14): 5455-5460.

Johnson, R.L. et al., 2013. Field-Scale Transport and Transformation of Carboxymethylcellulose-Stabilized Nano Zero-Valent Iron. Environmental Science & Technology, 47(3): 1573-1580.

Johnson, R.L., Tratnyek, P.G. and Johnson, R.O.B., 2008. Persulfate Persistence under Thermal Activation Conditions. Environmental Science & Technology, 42(24): 9350-9356.

Kao, C.M., Huang, K.D., Wang, J.Y., Chen, T.Y. and Chien, H.Y., 2008. Application of potassium permanganate as an oxidant for in situ oxidation of trichloroethylene-contaminated groundwater: A laboratory and kinetics study. Journal of Hazardous Materials, 153(3): 919-927.

Kavanaugh, M. et al., 2003. The DNAPL Cleanup Challenge: Is There a Case for Source Depletion? USEPA National Risk Management Research Laboratory, Cincinnati, OH, USA, pp. 129.

Kim, K. and Gurol, M.D., 2005. Reaction of Nonaqueous Phase TCE with Permanganate. Environmental Science & Technology, 39(23): 9303-9308.

Kingston, J.T., Dahlen, P.R., Johnson, P.C., Foote, E. and Williams, S., 2010. Critical evaluation of state-of-the-art in situ thermal treatment technologies for DNAPL source zone treatment.

Kocur, C.M. et al., 2014. Characterization of nZVI Mobility in a Field Scale Test. Environmental Science & Technology, 48(5): 2862-2869.

Kocur, C.M., O'Carroll, D.M. and Sleep, B.E., 2013. Impact of nZVI stability on mobility in porous media. Journal of Contaminant Hydrology, 145(0): 17-25.

Kocur, C.M.D. et al., 2015. Contributions of Abiotic and Biotic Dechlorination Following Carboxymethyl Cellulose Stabilized Nanoscale Zero Valent Iron Injection. Environmental Science & Technology, 49(14): 8648-8656.

Kolthoff, I.M. and Miller, I.K., 1951. The Chemistry of Persulfate. I. The Kinetics and Mechanism of the Decomposition of the Persulfate Ion in Aqueous Medium1. Journal of the American Chemical Society, 73(7): 3055-3059.

Krol, M.M. et al., 2013. A Field-Validated Model for In Situ Transport of Polymer-Stabilized nZVI and Implications for Subsurface Injection. Environmental Science & Technology.

Krol, M.M., Sleep, B.E. and Johnson, R.L., 2011. Impact of low-temperature electrical resistance heating on subsurface flow and transport. Water Resources Research, 47(5).

Krug, T., O'Hara, S. and Watling, M., 2010. Emulsified Zero-Valent Nano-Scale Iron Treatment of Chlorinated Solvent DNAPL Source Areas, ARLINGTON, VA.

Li, X.D. and Schwartz, F.W., 2000. Efficiency Problems Related to Permanganate oxidation Schemes. The Ohio State University, pp. 46-50.

Li, X.D. and Schwartz, F.W., 2004a. DNAPL mass transfer and permeability reduction during in situ chemical oxidation with permanganate. Geophysical Research Letters, 31(6): L06504.

Li, X.D. and Schwartz, F.W., 2004b. DNAPL remediation with in situ chemical oxidation using potassium permanganate: II. Increasing removal efficiency by dissolving Mn oxide precipitates. Journal of Contaminant Hydrology, 68(3–4): 269-287.

Liang, C.J., Bruell, C.J., Marley, M.C. and Sperry, K.L., 2003. Thermally Activated Persulfate Oxidation of Trichloroethylene (TCE) and 1,1,1—Trichloroethane (TCA) in Aqueous Systems and Soil Slurries. Soil & Sediment Contamination, 12(2): 207.

Liao, X., Zhao, D., Yan, X. and Huling, S.G., 2014. Identification of persulfate oxidation products of polycyclic aromatic hydrocarbon during remediation of contaminated soil. Journal of Hazardous Materials, 276: 26-34.

Lide, D.R., 2005. Ionic conductivity and diffusion at infinite dilution. In: D.R. Lide (Editor), CRC handbook of chemistry and physics. CRC Press, Boca Raton, FL.

Liu, J., Gong, X., Song, S., Zhang, F. and Lu, C., 2014. Heat-Activated Persulfate Oxidation of Chlorinated Solvents in Sandy Soil. Journal of Spectroscopy, 2014: 5.

Liu, Y., Majetich, S.A., Tilton, R.D., Sholl, D.S. and Lowry, G.V., 2005. TCE Dechlorination Rates, Pathways, and Efficiency of Nanoscale Iron Particles with Different Properties. Environmental Science & Technology, 39(5): 1338-1345.

Loomer, D.B., Al, T.A., Banks, V.J., Parker, B.L. and Mayer, K.U., 2010. Manganese Valence in Oxides Formed from in Situ Chemical Oxidation of TCE by KMnO4. Environmental Science & Technology, 44(15): 5934-5939.

Masliyah, J.H. and Bhattacharjee, S., 2006a. Electrokinetic Phenomena, Electrokinetic And Colloid Transport Phenomena. John Wiley & Sons, Inc., New Jersey, pp. 221-227.

Masliyah, J.H. and Bhattacharjee, S., 2006b. Electrophoresis, Electrokinetic And Colloid Transport Phenomena. John Wiley & Sons, Inc., pp. 295-361.

Mitchell, J.K. and Soga, K., 2005. Fundamentals of Soil Behavior. John Wiley & Sons, Inc., New Jersey.

NRC, N.R.C., 2005. Contaminants in the subsurface: Source zone assessment and remediation. Committee on Source Removal of Contaminants in the Subsurface. The National Academic Press, Washington, D.C.

O'Carroll, D., Sleep, B., Krol, M., Boparai, H. and Kocur, C., 2013. Nanoscale zero valent iron and bimetallic particles for contaminated site remediation. Advances In Water Resources, 35(0): 104-122.

Parker, B.L., 1996. Effects of molecular diffusion on the persistence of dense, immiscible phase organic liquids in fractured porous geologic media.

Petri, B. et al., 2011a. Fundamentals of ISCO Using Persulfate. In: R.L. Siegrist, M. Crimi and T.J. Simpkin (Editors), In Situ Chemical Oxidation for Groundwater Remediation. SERDP/ESTCP Environmental Remediation Technology. Springer New York, pp. 147-191.

Petri, B.G., Siegrist, R.L. and Crimi, M.L., 2008. Effects of Groundwater Velocity and Permanganate Concentration on DNAPL Mass Depletion Rates during In Situ Oxidation. Journal of Environmental Engineering, 134(1): 1-13.

Petri, B.G., Thomson, N.R. and Urynowicz, M.A., 2011b. Fundamentals of ISCO using Permanganate, In Situ Chemical Oxidation for Groundwater Remediation. SERDP/ESTCP Environmental Remediation Technology. Springer New York, pp. 89-146.

Phenrat, T. et al., 2009. Particle Size Distribution, Concentration, and Magnetic Attraction Affect Transport of Polymer-Modified Fe 0 Nanoparticles in Sand Columns. Environmental Science and Technology, 43: 5079-5085.

Raychoudhury, T., Naja, G. and Ghoshal, S., 2010. Assessment of transport of two polyelectrolyte-stabilized zero-valent iron nanoparticles in porous media. Journal of Contaminant Hydrology, 118(3-4): 143-151.

Reynolds, D.A., Jones, E.H., Gillen, M., Yusoff, I. and Thomas, D.G., 2008. Electrokinetic Migration of Permanganate Through Low-Permeability Media. Ground Water, 46(4): 629-637.

Roach, N. and Reddy, K.R., 2006. Electrokinetic Delivery of Permanganate into Low-Permeability Soils. International Journal of Environment and Waster Management, 1(1): 4-16.

Robertson, T., 2009. Electrokinetic Transport of Persulfate under Voltage Gradients.

Sakulchaicharoen, N., O'Carroll, D.M. and Herrera, J.E., 2010. Enhanced stability and dechlorination activity of pre-synthesis stabilized nanoscale FePd particles. Journal of Contaminant Hydrology, 118(3-4): 117-127.

Sale, T., Parker, B.L., Newell, C.J. and Devlin, J.F., 2013. Management of Contaminants Stored in Low Permeability Zones - A State of the Science Review, SERDP/ESTCP, Alexandria, VA, USA.

Santos, A.M., Vindevoghel, P., Graillat, C., Guyot, A. and Guillot, J., 1996. Study of the thermal decomposition of potassium persulfate by potentiometry and capillary electrophoresis. Journal of Polymer Science Part A: Polymer Chemistry, 34(7): 1271-1281.

Schnarr, M. et al., 1998. Laboratory and controlled field experiments using potassium permanganate to remediate trichloroethylene and perchloroethylene DNAPLs in porous media. Journal of Contaminant Hydrology, 29(3): 205-224.

Schrick, B., Hydutsky, B.W., Blough, J.L. and Mallouk, T.E., 2004. Delivery Vehicles for Zerovalent Metal Nanoparticles in Soil and Groundwater. Chemistry of Materials, 16: 2187-2193.

Schroth, M.H., Oostrom, M., Wietsma, T.W. and Istok, J.D., 2001. In-situ oxidation of trichloroethene by permanganate: effects on porous medium hydraulic properties. Journal of Contaminant Hydrology, 50(1–2): 79-98.

Shackelford, C.D. and Daniel, D.E., 1991. Diffusion in Saturated Soil. I: Background. Journal of Geotechnical Engineering, 117: 467-484.

Shapiro, A.P. and Probstein, R.F., 1993. Removal of contaminants from saturated clay by electroosmosis. Environmental Science & Technology, 27(2): 283-291.

Shariatmadari, N., Weng, C.-H. and Daryaee, H., 2009. Enhancement of Hexavalent Chromium [Cr(VI)] Remediation from Clayey Soils by Electrokinetics Coupled with a Nano-Sized Zero-Valent Iron Barrier, Environmental Engineering Science, pp. 1071-1079.

Siegrist, R., Crimi, M. and Brown, R., 2011. In Situ Chemical Oxidation: Technology Description and Status. In: R.L. Siegrist, M. Crimi and T.J. Simpkin (Editors), In Situ Chemical Oxidation for Groundwater remediation. SERDP/ESTCP Environmental Remediation Technology. Springer New York, pp. 1-32.

Siegrist, R.L. et al., 2008. Chemical Oxidation for Clean Up of Contaminated Ground Water

Methods and Techniques for Cleaning-up Contaminated Sites. NATO Science for Peace and Security Series C: Environmental Security. Springer Netherlands, pp. 45-58.

Struse, A., Siegrist, R., Dawson, H. and Urynowicz, M., 2002. Diffusive Transport of Permanganate during In Situ Oxidation. Journal of Environmental Engineering, 128(4): 327-334.

Thepsithar, P. and Roberts, E.P.L., 2006. Removal of Phenol from Contaminated Kaolin Using Electrokinetically Enhanced In Situ Chemical Oxidation. Environmental Science & Technology, 40(19): 6098-6103.

Tiraferri, A. and Sethi, R., 2009. Enhanced transport of zerovalent iron nanoparticles in saturated porous media by guar gum. Journal of Nanoparticle Research, 11(3): 635-645.

Tiraferri, A., Tosco, T. and Sethi, R., 2011. Transport and retention of microparticles in packed sand columns at low and intermediate ionic strengths: experiments and mathematical modeling. Environmental Earth Sciences, 63(4): 847-859.

Tosco, T., Petrangeli Papini, M., Cruz Viggi, C. and Sethi, R., 2014. Nanoscale zerovalent iron particles for groundwater remediation: a review. Journal of Cleaner Production, 77(0): 10-21.

Tosco, T. and Sethi, R., 2010. Transport of Non-Newtonian Suspensions of Highly Concentrated Micro- And Nanoscale Iron Particles in Porous Media: A Modeling Approach. Environmental Science & Technology, 44(23): 9062-9068.

Tosco, T., Tiraferri, A. and Sethi, R., 2009. Ionic Strength Dependent Transport of Microparticles in Saturated Porous Media: Modeling Mobilization and Immobilization Phenomena under Transient Chemical Conditions. Environmental Science & Technology, 43(12): 4425-4431.

Tratnyek, P.G., Johnson, R.L., Lowry, G.V. and Brown, R.A., 2014. IN SITU Chemical Reduction For Source Remediation. In: H.B. Kueper, F.H. Stroo, M.C. Vogel and H.C. Ward (Editors), Chlorinated Solvent Source Zone Remediation. Springer New York, New York, NY, pp. 307-351.

Tsitonaki, A. et al., 2010. In Situ Chemical Oxidation of Contaminated Soil and Groundwater Using Persulfate: A Review. Critical Reviews in Environmental Science and Technology, 40(1): 55-91.

Tufenkji, N. and Elimelech, M., 2004. Correlation Equation for Predicting Single-Collector Efficiency in Physicochemical Filtration in Saturated Porous Media. Environmental Science and Technology, 38(2): 529-536.

Vermeulen, F. and McGee, B., 2000. In-Situ Electromagnetic Heating for Hydrocarbon Recovery and Environmental Remediation. Journal of Canadian Petroleum Technology, 39(8): 24-28.

Waldemer, R.H. and Tratnyek, P.G., 2005. Kinetics of Contaminant Degradation by Permanganate. Environmental Science & Technology, 40(3): 1055-1061.

Waldemer, R.H., Tratnyek, P.G., Johnson, R.L. and Nurmi, J.T., 2007. Oxidation of Chlorinated Ethenes by Heat-Activated Persulfate: Kinetics and Products. Environmental Science & Technology, 41(3): 1010-1015.

Wei, Y.-T. et al., 2010. Influence of nanoscale zero-valent iron on geochemical properties of groundwater and vinyl chloride degradation: A field case study. Water research, 44(1): 131-140.

Weng, C.-H., Yuan, C. and Tu, H.-H., 2003. Removal of Trichloroethylene from Clay Soil by Series-Electrokinetic Process. Practice Periodical of Hazardous, Toxic, and Radioactive Waste Management, 7(1): 25-30.

Xu, M. et al., 2015. Degradation of carbon tetrachloride in aqueous solution in the thermally activated persulfate system. Journal of Hazardous Materials, 286(0): 7-14.

Yan, Y.E. and Schwartz, F.W., 1999. Oxidative degradation and kinetics of chlorinated ethylenes by potassium permanganate. Journal of Contaminant Hydrology, 37(3-4): 343-365.

Yan, Y.E. and Schwartz, F.W., 2000. Kinetics and Mechanisms for TCE Oxidation by Permanganate. Environmental Science & Technology, 34(12): 2535-2541.

Yang, G.C.C. and Yeh, C.-F., 2011. Enhanced nano-Fe3O4/S2O82− oxidation of trichloroethylene in a clayey soil by electrokinetics. Separation and Purification Technology, 79(2): 264-271.

Yuan, S., Liao, P. and Alshawabkeh, A.N., 2013. Electrolytic Manipulation of Persulfate Reactivity by Iron Electrodes for Trichloroethylene Degradation in Groundwater. Environmental Science & Technology, 48(1): 656-663.

Yukselen-Aksoy, Y. and Reddy, K., 2013. Electrokinetic Delivery and Activation of Persulfate for Oxidation of PCBs in Clayey Soils. Journal of Geotechnical and Geoenvironmental Engineering, 139(1): 175-184.

Yukselen-Aksoy, Y. and Reddy, K.R., 2012. Effect of soil composition on electrokinetically enhanced persulfate oxidation of polychlorobiphenyls. Electrochimica Acta, 86(0): 164-169.

Zhang, W.-x., 2003. Nanoscale iron particles for environmental remediation: An overview. Journal of Nanoparticle Research, 5: 323-332.

Chapter 3

3 nZVI Injection into Variably Saturated Soils: Field and Modeling Study

Ahmed I. A. Chowdhury[a], Magdalena M. Krol[b], Christopher M. Kocur[a], Hardiljeet K. Boparai[a], Kela P. Weber[c], Brent E. Sleep[d], Denis M. O'Carroll[e] [*]

[a]Department of Civil and Environmental Engineering, The University of Western Ontario, 1151 Richmond Street, London, ON, Canada, N6A 5B9; [b]Department of Civil Engineering, Lassonde School of Engineering, York University, 4700 Keele St., Toronto, ON, Canada, M3J 1P3; [c]Department of Chemistry and Chemical Engineering, Royal Military College of Canada, Kingston, ON, Canada, K7K 7B4; [d]Department of Civil Engineering, University of Toronto, 35 St. George St., Toronto, ON, Canada, M5S 1A4;

[e*]Department of Civil and Environmental Engineering, The University of Western Ontario, 1151 Richmond Street, London, ON, Canada, N6A 5B9, e-mail: docarroll@eng.uwo.ca, Phone: (+1) 519-661-2111x 82193.

3.1   Abstract

Nano-scale zero valent iron (nZVI) has been used at a number of contaminated sites over the last decade. At most of these sites, significant decreases in contaminant concentrations have resulted from the application of nZVI. However, limited work has been completed investigating nZVI field-scale mobility. In this study, a field test was combined with numerical modelling to examine nZVI reactivity along with transport properties in variably saturated soils. The field test consisted of 142 L of carboxymethyle cellulose (CMC) stabilized monometallic nZVI synthesized onsite and injected into a variably saturated zone. Periodic groundwater samples were collected from the injection well, as well as, from two monitoring wells to analyze for chlorinated solvents and other geochemistry indicators. This study showed that CMC stabilized monometallic nZVI was able to decrease tricholorethene (TCE) concentrations in groundwater by more than 99% from the historical TCE concentrations. A three dimensional, three phase, finite difference numerical simulator, (CompSim) was used to further investigate nZVI and polymer (used as stabilizer for nZVI particles) transport at the variably saturated site. The model was able to accurately predict the field observed head data without parameter fitting. In addition, the numerical simulator estimated the mass of nZVI delivered to the saturated and unsaturated zones and distinguished the nZVI phase (i.e. aqueous or attached). The simulation results showed that the injected slurry migrated radially outward from the injection well, and therefore nZVI transport was governed by injection velocity and viscosity of the injected solution. A suite of sensitivity analyses was performed to investigate the impact of different injection scenarios (e.g. different volume and injection rate) on nZVI migration. Simulation results showed that injection of a higher nZVI volume delivered more iron particles at a given distance; however, the travel distance was not proportional to the increase in volume. Moreover, simulation results showed that using a 1D transport equation to simulate nZVI migration in the subsurface may overestimate the travel distance. This is because the 1D transport equation assumes a constant velocity while pore water velocity radially decreases from the well during injection. This study suggests that onsite synthesized nZVI particles are mobile in the subsurface and that a numerical simulator can be a valuable tool for optimal design of nZVI field applications.

3.2   Introduction

Nano-scale zero valent iron (nZVI) has generated considerable interest for remediation of brownfield sites due to its ability to degrade a wide range of contaminants (O'Carroll et al., 2013a). Due to this increase in popularity, nZVI has been the subject of numerous studies focusing on injection media, preparation, and coating substances. To date, nZVI has been injected into a range of subsurface environments (e.g. bedrock (Zhang, 2003), coarse-medium sand (Wei et al., 2010), silty sand (Bennett et al., 2010), and stiff clay with sand and gravel deposits (He et al., 2010)). Early field-scale studies used unstablized or bare nZVI (Elliott and Zhang, 2001; Zhang, 2003) while more recent studies have used polymer coated nZVI (0.10% - 0.80%, weight/volume) to increase suspension stability (Bennett et al., 2010; He et al., 2010; Henn and Waddill, 2006; Kocur et al., 2014; Wei et al., 2010). Lastly, field applications have used both commercially available nZVI (Henn and Waddill, 2006; Krug et al., 2010; Wei et al., 2010) and onsite synthesized nZVI (Bennett et al., 2010; Elliott and Zhang, 2001; He et al., 2010; Johnson et al., 2009; Kocur et al., 2014; Wei et al., 2010; Zhang, 2003). Presynthesis stabilized nZVI particles are more dispersed and reactive than commercially available nZVI particles (Sakulchaicharoen et al., 2010) and therefore are preferred for field injection applications. Although multiple field studies have been performed to date, uncertainties about field-injected nZVI remain. These include synthesis temperature, performance of monometallic nanometals in variably saturated soils, and ideal injection strategies to maximize nZVI migration.

nZVI synthesis temperature has been reported ranging between 7 ^{o}C to 25 ^{o}C (Bennett et al., 2010; Henn and Waddill, 2006; Kocur et al., 2014; Zhang, 2003). A lab-scale study found that smaller and monodispered particles are formed at lower temperature (8 ^{o}C) compared to those synthesized at higher temperature (30 ^{o}C) (He and Zhao, 2007). Lower temperature slows nZVI growth rate, forms stable nanoclusters and results in greater carboxymethyle cellulose (CMC) association to the nZVI surface, all resulting in smaller particles (He and Zhao, 2007). Recently Kocur et al. (2014) synthesized CMC stabilized nZVI at 7 ^{o}C during a nZVI field trial and reported that the particles had sizes (86±12 nm, from transmission electron microscopy (TEM) analysis) and zeta potentials (-49.2±1.5 mV) similar to particles synthesized in controlled laboratory environments and that 50% of the

A version of this chapter has been published (Chowdhury et al., 2015)

nZVI particles remained in suspension for 24-32 hrs after synthesis. Therefore lowered synthesis temperatures may be beneficial to nZVI injection. However, no field or laboratory study has been conducted to explore the possibility of nZVI synthesis at temperatures below 7 °C for field applications in cold climate regions.

In addition, most of the field trial studies have investigated nZVI transport in the saturated zone, however, it may be necessary to inject nZVI above the water table to target contamination in the vadose zone. Contamination immediately above the saturated zone is possible given seasonal fluctuations in the water table. To date, only Wei et al. (2010) has reported nZVI injecting into a variably saturated zone. The layer was 5 m thick with the water table at 4 m and part of the injected nZVI volume was delivered in the unsaturated zone (from 3 to 4 m, bgs). Wei et al. (2010) observed an accumulation of nZVI in the top layer. The authors also observed a decrease in nZVI concentration in this top layer after 66 days, following a storm event, and inferred that nZVI was mobile in this variably saturated layer. However, it is not clear how much of the nZVI was actually delivered to the unsaturated zone or the nZVI distance travelled. Therefore there is a need to assess nZVI transport in variably saturated zones for nZVI application design.

nZVI can be injected into the subsurface using gravity feed methods (Elliott and Zhang, 2001; He et al., 2010; Johnson et al., 2013; Kocur et al., 2014; Zhang, 2003) or pressure injection techniques (Bennett et al., 2010; He et al., 2010; Krug et al., 2010). Pressure injection enhances nZVI flow rates from the injection well but may cause daylighting (Krug et al., 2010; O'Carroll et al., 2013a) while flow velocities under gravity injection are largely influenced by subsurface hydraulic conductivity. Injection rates at field trials using gravity injection have been reported to range from 1 L/min to as high as 20 L/min, depending on the formation (Elliott and Zhang, 2001; He et al., 2010; Johnson et al., 2013; Kocur et al., 2014; Krug et al., 2010; Wei et al., 2010). Injection velocities (i.e. ratio of injection rate to surface area of injection well screen) in these studies varied between 7.3 to 45.8 m/day with the injection well screen length varying between 0.5 and 15 m (Bennett et al., 2010; Elliott and Zhang, 2001; He et al., 2010; Henn and Waddill, 2006; Kocur et al., 2014; Wei et al., 2010) (assuming a standard 5 cm diameter injection well where data was not available). In comparing injection velocities they should be normalized to the same screen diameter. The

A version of this chapter has been published (Chowdhury et al., 2015)

higher injection velocity achieved by Johnson et al. (2013) (i.e. 146.7 m/day) would correspond to 73.3 m/day if a larger diameter (0.05 m instead of 0.025 m) was used, thus, might impact the nZVI travel distance.

Field-scale nZVI travel distances ranging from 0.45 to 2 m have been reported in the literature (O'Carroll et al., 2013a). However, it is difficult to compare the field observed nZVI travel distances due to differences in nZVI formulations, injection methods and rates, and geologic settings. He et al. (2010) reported normalized iron concentrations (i.e., total iron concentration normalized to tracer data but did not definitively quantify nZVI breakthrough) of CMC stabilized Fe/Pd nanoparticles, injected via gravity and pressure injection, respectively, in a stiff silty clay formation with sand and gravel. The monitoring well, where the iron was detected, was 1.5 m away from the injection well, representing the travel distance. Bennett et al. (2010) estimated travel distances of 0.54 m to 1.3 m through poorly graded coarse sand and silty-sand during three push-pull tests. More recently, studies have reported nZVI breakthrough due to visual presence of a black solution at 1 m downstream of the injection well (Johnson et al., 2013; Kocur et al., 2014). Samples collected by Kocur et al. (2014) were analyzed using dynamic light scattering (DLS), TEM, and Energy dispersive X-ray spectroscopy (EDS) techniques all of which confirmed the presence of nZVI particles after being transported to a monitoring well. The travel distance observed by Johnson et al. (2013) might be due to the higher injection velocity, as discussed earlier. It is reported that nZVI travel distance is a function of both velocity and viscosity of the injected solution (Krol et al., 2013). Viscosity of the solution can be manipulated by increasing the polymer concentration (Krol et al., 2013) while the velocity depends on the injection method and rate.

A number of column studies have been conducted to explore nZVI migration through porous media (Berge and Ramsburg, 2009; He et al., 2009; Johnson et al., 2009; Kim et al., 2009; Kocur et al., 2013; Phenrat et al., 2009; Raychoudhury et al., 2010; Saleh et al., 2008; Tiraferri and Sethi, 2009; Vecchia et al., 2009). Many of these studies found polymer stabilized nZVI to be mobile in shorter (5-15 cm) length 1D column experiments despite aggregation and sedimentation (He et al., 2009; Kocur et al., 2013; Phenrat et al., 2009; Raychoudhury et al., 2010; Raychoudhury et al., 2014; Schrick et al., 2004; Tiraferri and

A version of this chapter has been published (Chowdhury et al., 2015)

Sethi, 2009). However, many column studies were completed at higher pore water velocities (15-260 m/day) than experienced in the field, although these velocities could occur near the injection well (He et al., 2009; Johnson et al., 2009; Kim et al., 2009; Phenrat et al., 2009; Saleh et al., 2008; Vecchia et al., 2009). The length of the columns used in these studies varied between 0.125 and 0.613 m. Higher groundwater velocities would result in less attachment to soil surfaces, as such, column experiments completed at higher velocities could overestimate field-scale nZVI travel distances (Kocur et al., 2013). More recent studies have been completed at representative groundwater velocities (0.25-11 m/day) (Berge and Ramsburg, 2009; Kocur et al., 2013; Raychoudhury et al., 2010; Tiraferri and Sethi, 2009) allowing for a better comparison between field and lab-scale investigations.

In column studies, field-scale nZVI travel distances are often inferred using a steady state analytical solution based on 1D colloid filtration theory (CFT) (He et al., 2009; Johnson et al., 2009; Phenrat et al., 2009; Raychoudhury et al., 2010; Schrick et al., 2004; Tiraferri and Sethi, 2009). In such cases, maximum nZVI travel distances are calculated as the distance required to remove 99.9% of the initial nZVI concentration (O'Carroll et al., 2013a). Numerical models can also be used that incorporate CFT mechanisms in the advection-dispersion transport equation and simulate 1D nZVI migration (Kocur et al., 2013; Tiraferri et al., 2011; Tosco and Sethi, 2010; Tosco et al., 2009). In these studies, simulated breakthrough curves are typically in good agreement with column experiment results when the sticking efficiency (α) (Kocur et al., 2013; Tiraferri and Sethi, 2009) or the attachment rate (K_{att}) (Tiraferri et al., 2011) is used as a fitting parameter.

Although nZVI transport has been simulated for small-scale column studies, very limited work has been completed to develop models for the simulation of field-scale nZVI transport (Tosco et al., 2014). Johnson et al. (2013) developed a 3D model using MT3D-MODFLOW and validated it using pilot scale model aquifer test data. In their study, a constant viscosity (approx. 3.2 cP) was used since no shear thinning behavior was observed in separately conducted experiments over a range of velocities. Krol et al. (2013) modified a 3D numerical simulator, CompSim, to simulate nZVI transport in the field and validated it using observed field data (Bennett et al., 2010). Krol et al. (2013) showed that CompSim,

A version of this chapter has been published (Chowdhury et al., 2015)

modified with CFT, could be used to simulate nZVI transport in saturated porous media. Unlike the Johnson et al (2013) model, variable viscosity was simulated corresponding to the injection of polymer-modified nZVI. Models capable of simulating large-scale contaminant transport are required to predict contaminant distribution in the subsurface to aid in remediation activities (Tosco et al., 2014). For example, O'Carroll and Sleep (2009) used CompSim to assess the utility of hot water flooding for coal tar recovery at the field scale. Similarly, West and Kueper (2012) used a numerical model to investigate source zone remediation using in-situ chemical oxidation (ISCO) at the field scale. Therefore, the development of numerical models with the ability to accurately simulate different injection scenarios (e.g. optimal volume and nZVI injection rate, nZVI spatial distribution, location of injection and monitoring wells, depth and length of well screens, and manipulation of flow filed to enhance nZVI travel distance) would aid in the design of nZVI field applications.

This study describes an nZVI field trial at a variably saturated TCE contaminated site. Groundwater samples were collected over a year and analyzed for cVOCs to evaluate the performance of monometallic nZVI particles in degrading TCE. In order to better understand nZVI migration and subsequent contaminant degradation in the subsurface, the injection was modeled using a 3D computational simulator (CompSim). Specific study objectives were to: a) assess the effectiveness of stabilized monometallic nZVI, synthesized onsite below 0 $^{\circ}$C, in degrading VOC at the field-scale, b) investigate nZVI transport in a variably saturated system, and c) assess optimal injection and nZVI migration scenarios using CompSim as a predictive model.

3.3   Site Description, Methods and Materials

3.3.1   Site description

The field study site was situated in London, Ontario, Canada at a former military vehicle assembly facility that was used as a maintenance depot after World War II. Chlorinated solvents, primarily TCE, were used in a degreasing tank and in other cleaning activities during military vehicle maintenance. The cross-section of the study area is reconstructed using the borehole logs from previous site investigation reports (DCC, 2007), as shown in

A version of this chapter has been published (Chowdhury et al., 2015)

Figure (3.1a). The top layer is a sand and gravel fill or brown reworked silty sand extending to a depth of approximately 1.3 to 1.7 m (bgs). This layer also contains about 0.75 m thick sand and silt and/or clay silt and acts as an aquitard. The third layer consists of inter-bedded sand or sand and silt to depths of approximately 5.4 to 8.75 m (bgs) and represents a shallow aquifer. A glacial silt/clay till beneath the third layer has significantly lower permeability than the upper sand/silt and is assumed to be an aquitard. The groundwater in the shallow sandy-silt aquifer has a velocity of approximately 0.3 m/day (DCC, 2007). The ambient water table in the study area is located at 2.76 m (bgs).

nZVI was injected into an existing well (injection well, IW) while geochemical parameters were monitored at two nearby monitoring wells (MW1 and MW2) (Figure 3.1a). The wells were 0.05 m in diameter and were screened at 2.1-3.75 m, 4.2-5.9 m and 1.2-3.0 m (bgs), for IW, MW1 and MW2, respectively. Well screen depths suggest that the IW and MW2 partially penetrated the shallow aquifer and that the top of the MW1 well screen was 0.45 m below the bottom of the IW well screen (Figure 3.1a). This gap in well screens may negatively impact the injection-extraction phases and thus, affect nZVI transport in the subsurface.
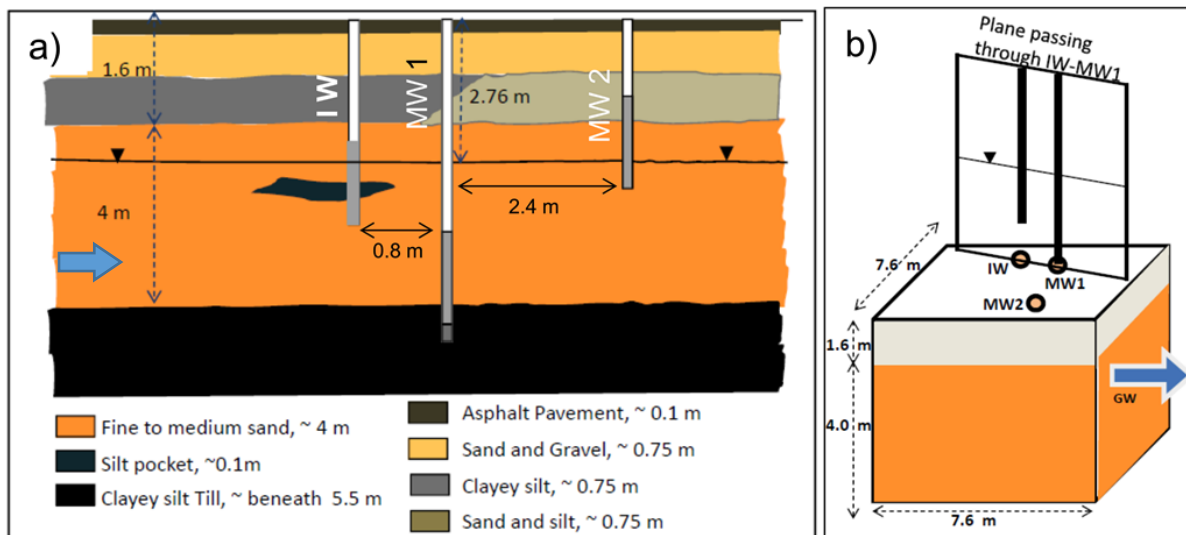
Figure 3.1: Site schematic showing: (a) cross-section of study area (b); model domain with volumetric section or plane passing through IW-MW1. Blue arrow represents the regional groundwater flow direction.

A version of this chapter has been published (Chowdhury et al., 2015)

3.3.2   Onsite nZVI synthesis

nZVI was synthesized using the borohydride reduction method in the presence of a stabilizer (sodium carboxymethyle cellulose, Na-CMC) (He and Zhao, 2007) dissolved in de-oxygenated de-ionized (DI) water. The synthesis was completed in a 190 L vessel closed at the top except for inlet tubing for chemical addition, gas venting, and nitrogen gas purging (Kocur et al., 2014). A pneumatic hand drill mounted on the synthesis vessel was used to ensure uniform mixing. Commercially available ferrous sulfate (A&K Petrochem Ind. Ltd, ON, CA) and sodium borohydride (GFS Chemicals, USA) was used to synthesize 142 L of 1.0 g/L nZVI slurry in the presence of 0.8% (wt/Vol.) commercially available CMC (Molecular Weight = 90,000 g/mol) (Cellogen HP-8A, Dai-Ichi Kogyo Seiyaki Co.). Similar iron concentrations were used in other field studies, but with lab-grade reagents and tap water (Bennett et al., 2010; He et al., 2010) or commercially available reagents (Kocur et al., 2014). The nZVI slurry in the synthesis vessel was continuously mixed and purged with nitrogen (Grade 5.0, Praxair Inc., CA) to disperse the particles in solution and to maintain anoxic conditions to prevent nZVI oxidation. It is important to note that the nZVI was not doped with a catalyst (i.e., a palladium (Pd) catalyst was not used). The maximum air temperature during the synthesis process was -15°C. The nZVI solution temperature was not measured, however, the groundwater temperature was 6 °C.

3.3.3   nZVI injection and monitoring

nZVI injection was completed in three phases. In phase 1 (P1) 142 L of freshly synthesized 1 g/L nZVI suspension was gravity fed into IW on February 8th, 2011 using a peristaltic pump (110-43E, ERE Inc.). Details of the injection schedule for the field application (Field case) are given in Table 3-1.

In phase 2 (P2), 110 L of de-oxygenated DI water was injected for 33 min into IW immediately after nZVI injection at the same rate as P1. Finally, in phase 3 (P3), groundwater was re-circulated from MW1 to IW at 5 L/min for 50 min. pH, dissolved oxygen (DO), oxidation reduction potential (ORP), and electrical conductivity (EC) were monitored with a field multi-parameter probe (Horiba U-22) at MW1 during the injection and at IW, MW1 and MW2 after the injection. In addition, groundwater samples from the

A version of this chapter has been published (Chowdhury et al., 2015)

three wells were collected following nZVI injection. No tracer salt was used during the field application of nZVI since increased ionic strength may affect the size, stability and hence, the reactivity of nZVI (Saleh et al., 2008).

Table 3-1: Field injection schedule (FC) and additional model simulations

Case	Phase 1 (P1)	Phase 2 (P2)	Phase 3 (P3)
Field case (FC)[a]	nZVI at 3.3 L/min (142 L) for 43 min	DI water at 3.3 L/min (110 L) for 33 min	Groundwater recirculation at 5.0 L/min for 50 min
Groundwater only (GW)[b]	nZVI at 3.3 L/min (142 L) for 43 min	Groundwater at ambient velocity (0.3 m/day) for 33 min	Groundwater at ambient velocity (0.3 m/day) for 50 min
Viscous DI water injection (VC)[b]	nZVI at 3.3 L/min (142 L) for 43 min	DI water at 3.3 L/min with a higher viscosity (7cP, 110 L) for 33 min	Groundwater recirculation at 5.0 L/min for 50 min
Large Volume injection (LV)[b]	nZVI at 3.3 L/min (2000L) for 606 min	DI water at 3.3 L/min (110 L) for 33 min	Groundwater recirculation at 5.0 L/min for 50 min
Location of Well screen Case (WS)[b]	nZVI at 3.3 L/min (142 L) and extraction from MW1 at the same rate for 43 min	Polymer solution at 3.3 L/min (110 L) and extraction from MW1 at the same rate for 33 min	Groundwater recirculation at 3.3 L/min for 50 min

[a] Real case as conducted in the field; [b] Hypothetical model simulations

3.3.4   Methods of analysis

The groundwater samples for TCE analysis were collected in 40-mL glass vials with zero headspace. TCE concentrations were determined by transferring 250 µl aliquots to 2-mL GC vials containing 1 mL hexane for TCE extraction. The extracted samples were then analyzed using an Agilent 7890 GC equipped with an Electron Capture Detector and a DB-624 capillary column (75m x 0.45mm, 2.55µm) following a modified EPA 8021 method. Analysis of anions (chloride and sulfate) was performed using a high performance liquid chromatography (HPLC) equipped with a conductivity detector (Model 432, Waters, Milford, MA) and a 4.6x50 cm IC-Pak Anion column. Total iron concentration was measure using the Ferrozine method (Chowdhury et al., 2012; Stookey, 1970).

A version of this chapter has been published (Chowdhury et al., 2015)

3.4 Numerical Modeling

Compositional Simulator (CompSim), developed and verified by Sleep and Sykes (1993), a three dimensional, three phase, finite difference numerical simulator, was used to simulate nZVI and CMC transport. CompSim has been used in a number of studies to simulate groundwater flow and contaminant transport, including hot water flushing for NAPL displacement (O'Carroll and Sleep, 2007; O'Carroll and Sleep, 2009), and LNAPL accumulation and recovery from wells (Sleep et al., 2000a). Most recently, CFT based equations (Equations 3.1, 3.2) were incorporated in CompSim to simulate nanoparticle transport in porous media (Krol et al., 2013):

$$\frac{\partial(\theta_w C)}{\partial t} + \theta_w K_{att} C = \nabla \cdot (\theta_w D \cdot \nabla C) - \nabla \cdot (C\vec{q}) \qquad \text{(Equation 3.1)}$$

where, C is the nZVI concentration in suspension (M/L^3), D is the hydrodynamic dispersion tensor (L^2/T), $\vec{q}$ is the Darcy velocity (L/T), Θ_w is the volumetric water content (-), and K_{att} is the attachment rate coefficient (1/T). K_{att} is defined as:

$$K_{att} = \frac{3(1 - \theta_w)}{2d_c} \alpha \eta_o v \qquad \text{(Equation 3.2)}$$

where, d_c is the mean collector diameter (L) and v_p is the pore water velocity (L/T). α and η_0 are the sticking efficiency (-) and theoretical single collector contact efficiency (-), respectively. η_0 is calculated using the relationship developed by (Tufenkji and Elimelech, 2004). The Θ_w in Equation (3.2) was substituted for porosity to account for the nZVI attachment in the unsaturated condition (Bradford and Torkzaban, 2008). Water saturations and relative permeability were calculated using Brook-Corey relationship (parameters listed in Table 3-2) and capillary pressure – relative permeability relationship described by Lenhard and Parker (1987). The detailed processes are outlined by Sleep and Sykes (1993). CMC was modeled as a conservative species following Krol et al. (2013) as such, nZVI and CMC transport were modeled as individual species. CMC viscosity was calculated using the Grunberg and Nissan equation (Poling et al., 2001). Compsim was used to predict nZVI transport in both the saturated and unsaturated zone. CFT has been used in previous studies of colloid transport through unsaturated porous media (Gargiulo et al., 2007;

A version of this chapter has been published (Chowdhury et al., 2015)

Torkzaban et al., 2008; Zhang et al., 2010), therefore CFT is applicable in both zones and feasible in CompSim since the program uses multiphase flow equations with air and water modeled as separate phases (O'Carroll and Sleep, 2009).

3.4.1   Model setup

To simulate the field study, a 7.6 m by 7.6 m by 5.6 m domain was used (Figure 3.1b) with a 0.2 m grid size in all directions. The upper 1.6 m and lower 4.0 m layers of the domain were modeled as clayey-silt and sandy silt soil, respectively, consistent with site conditions (Figure 3.1 a-b). Both layers were assumed to be homogeneous and isotropic. Borehole logs showed a clayey soil layer below 5.6 m (bgs) therefore, the bottom of the domain was modeled as a no flow boundary. The left and right sides were modeled using prescribed constant head boundaries yielding a regional groundwater velocity of 0.23 m/day, consistent with site conditions. Since the water table is located at 2.8 m (bgs), an unsaturated layer was included in the model domain. Model parameters are summarized in Table 3-2.

Table 3-2: Summary of field and modeling parameters

Parameters	Top clayey soil layer	Bottom sandy-silt soil layer
Porosity[a]	0.30	0.30
Hydraulic conductivity, m/s[a]	8.8×10^{-6}	3.2×10^{-5}
Hydraulic gradient, m/m[a]	-	0.025
Collector size[b], d_{50}, m	5.4×10^{-5}	1.0×10^{-4}
Attachment efficiency[c], α	1.0×10^{-2}	1.0×10^{-2}
Longitudinal Dispersivity[c], α_L m	-	0.07
Displacement pressure[d], P_d, m	0.7223	0.3774
Brooks Corey parameter[e], λ	5.94	5.94

[a] Site investigation report (DCC, 2007) [b] calculated using Carmen-Kozeny equation, [c] based on literature values (Johnson et al., 2013; Krol et al., 2013), [d] calculated using Leverett scaling; [e] assumed based on literature values (O'Carroll et al., 2004).

A version of this chapter has been published (Chowdhury et al., 2015)

Injection and extraction wells were modeled using the stratified wellbore formulation presented in Sleep et al., (2000b). This allowed for variable wellbore-formation flow rates for different wellbore sections and accommodated wellbore storage. This formulation also implicitly calculated changes in water levels in the wellbore and soil by accounting for fluid stratification (i.e. water in the lower section of the wellbore, air at the top). The wellbore diameters were 0.05 m for both injection and extraction wells. Injection and extraction rates used in the model were consistent with the field study (Table 3-1). One goal of the current study was to evaluate the predictive capabilities of CompSim for nZVI field applications. As such, model parameters were not fitted or calibrated; the regional groundwater velocity and gradient was given as input (i.e., taken from site conditions) and attachment efficiency (α) was assumed based on the study by Krol et al. (2013).

3.5   Results and Discussion

3.5.1   Field observed changes in head at the IW

Injection of nZVI caused a significant increase in water level in IW during the first phase of the injection (Appendix A, Figure 7.1a). The water level in IW during phase 1 (P1) increased from 2.76 m (bgs) to 0.99 m (bgs) after 43 min (end of P1). The total IW screen length was 1.65 m with 0.66 m of the well screen lying above the ambient water table (at 2.76 m (bgs)) (Figure 3.1a). Thus, a portion of the fluid was injected above the water table. The water level in the MW1 remained unaffected by the injection (data not shown here). The water level at IW dropped to ambient levels one day after groundwater recirculation was stopped (Figure 7.1a).

3.5.2   Changes in groundwater geochemistry

Water quality parameters (e.g., pH, ORP and DO) were measured at MW1 during nZVI injection and at IW, MW1 and MW2 after injection (Figures 7.2 and 7.3). These parameters have been used in other studies as an indirect indication of injected fluid arrival at the target locations (Johnson et al., 2013; Kocur et al., 2014). pH in the IW increased from 6.3 to 6.8 and then to 8.1, 1 and 3 days following injection, respectively, as expected with nZVI oxidation. Similarly, pH in MW1 increased from 6.9 (pre-injection) to 7.8 after 3 days.

A version of this chapter has been published (Chowdhury et al., 2015)

Similar increases in pH have been observed in other nZVI field trials (Elliott and Zhang, 2001; Kocur et al., 2014). Changes in pH in MW1 suggest that the injection solution reached the vicinity of MW1.

ORP at MW1 decreased from 305 mV to 63 mV 43 minutes after nZVI injection (end of P1), ORP decreases have been observed in other field studies (Bennett et al., 2010; Elliott and Zhang, 2001; He et al., 2010; Johnson et al., 2013). DO at the IW decreased from 9.8 mg/L to 0.85 mg/L three days after injection (Figure 7.3) suggesting that nZVI reduced DO. Similar behavior was observed in MW1 where DO decreased from 8.9 mg/L to 0.17 and 1.6 mg/L after 45 min and 3 days, respectively, following injection (Figure 7.3). He et al. (2010) observed a similar drop in DO (e.g., 4 mg/L to 0 mg/L following injection). These changes in geochemical parameters indicate that the injection fluid reached MW1 but is not a direct indication of nZVI arrival since dissolved species, associated with nZVI oxidation, could have migrated to MW1 (Johnson et al., 2013; Kocur et al., 2014). These indicators do, however, suggest that the injection fluid is distributed in the treatment area (i.e., at the vicinity of the injection and monitoring wells).

3.5.3   Field observed total iron and sulfate concentration results

At the IW, limited iron was detected one day after nZVI injection (0.12 mg/L), however, the iron concentration increased by two orders of magnitude after three days (10.1 mg/L) (Figure 3.2a). This was due to the radial flow from the IW which delivered fluid downstream as well as upstream of the IW during the nZVI, DI water and groundwater injections. Therefore species present in the injection fluid would migrate with the ambient groundwater flow back towards the IW when injection ceased. For this reason, iron concentrations increased at the IW three days following injection. Sulfate, which was part of the injection solution (i.e., addition of iron sulfate as nZVI precursor) can also be used to assess aqueous phase transport. Similar to Fe^0, sulfate concentration at the IW increased from 2.9 mg/L to 395.5 mg/L at 1 and 3 days, respectively (Figure 3.2b). MW1, which was 1 m away from IW, showed a gradual increase in sulfate concentration (e.g. 2.9 and 47.7 mg/L at 1 and 365 days, respectively) after which it decreased to 23 mg/L at 477 days (Figure 3.2b). It is likely that sulfate could be reduced to sulfides under the reducing

A version of this chapter has been published (Chowdhury et al., 2015)

conditions resulting from nZVI injection, decreasing sulfate concentration. The gradual increase in sulfate concentration at MW1 during the first 365 days suggests that the injected fluid was distributed in the study area, however, nZVI did not migrate to MW1 along with the injection fluid likely due to attachment to the soil surface which is discussed in section 3.5.5. Flushing with DI water and re-circulated groundwater transported the nZVI suspension away from the injection well which is further discussed in the modeling section.
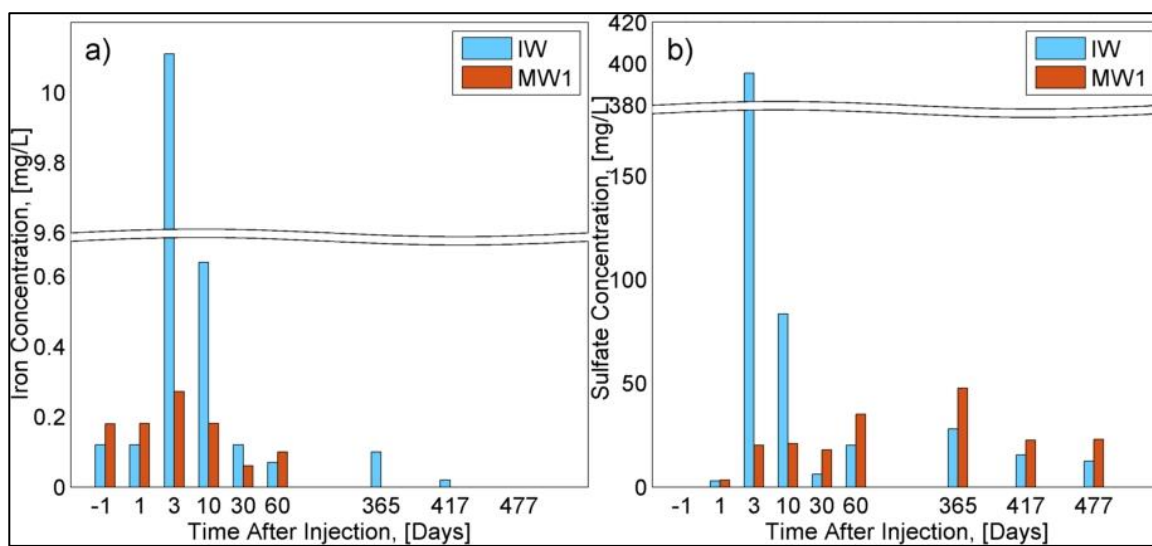
Figure 3.2: Observed a) Total iron and b) sulfate concentration in IW and MW1.

3.5.4   Monitoring contaminant degradation

TCE and chloride concentrations in IW, MW1 and MW2 are shown in Figures 3.3 (a, b), respectively. TCE and chloride concentrations immediately prior to nZVI injection were not available due to inadequate preservation methods during the field trial (a maximum air temperature of $-15^{o}C$ resulted in sample vials freezing and breaking). Therefore, historic TCE concentrations (from samples collected between July, 2003 and April, 2006) were averaged and presented for comparison. TCE concentrations decreased by 55%, 94%, and by 73% at MW1, MW2, and IW, respectively, 30 days after nZVI injection, with continued long term decreases in concentration in the subsequent 477 days (Figure 3.3a). TCE concentration decreased at all locations by more than 99%, compared to historic concentrations. Chloride concentrations increased at the three monitoring locations (Figure 3.3b) as chloride is a TCE degradation by-product (Equation 7.1). Molar chloride evolution is higher than moles of TCE degraded, as shown in the Figures (3.3 a,b). The aqueous phase

TCE concentration decreased from 239.5 to 0.05 (method detection limit for TCE) microg/L at the IW between day 1 and 60 that corresponded to a molar concentration decrease of 1.44 uM. Degradation of 1.44 uM of TCE in the aqueous phase to ethane would produce 4.3 uM of chloride (Equation 7.1). In contrast, the increase in chloride concentration at the IW was 2654 uM over the same time period. One possible explanation for this stoichiometric disparity could be the contribution from sorbed TCE. Assuming sorbed TCE is responsible for the additional chloride evolution would suggest that 0.03 to 0.07 mg TCE/kg soil was degraded. Kocur et al. (2015) also observed higher chloride molar concentrations than expected from the cVOCs degraded. The observed decrease in TCE concentration suggested that synthesizing nZVI at temperature below $0^{\circ}C$ did not impact nZVI reactivity. The study of Kocur et al. (2014) confirmed that low temperature synthesized particles had nano-scale dimensions. The present study, therefore, suggests that onsite synthesized monometallic nZVI could be used for subsurface remediation in cold climate regions (i.e. below 7 $^{\circ}C$).

The initial observed TCE concentration decrease was likely due to abiotic reaction with nZVI while enhanced microbial activity was likely responsible for the long-term degradation. It has been reported that CMC, in the presence of hydrogen gas produced from the nZVI corrosion as well as from the CMC fermentation, may enhance microbial activity resulting in enhanced TCE biodegradation (He et al., 2010). In addition, Kirschling et al. (2010) found that polyaspartate coated nZVI resulted in increased bacterial populations (compared to the control test) where the polymer served as a carbon and nitrogen source. Furthermore, a recent field study have shown that *Dehalococcoides* spp. population increased in the study area following CMC-nZVI injection and that both abiotic and biotic degradation occurred following the nZVI injection (Kocur et al., 2015). It is important to note that the site under investigation has been contaminated with cVOCs for many years. Previous site investigations reported that TCE at this site was subjected to microbial mediated reduction at a moderate rate (TSH, 2007). As such, based on the discussion above, it is believed that nZVI application in the current study resulted in short-term abiotic TCE degradation and created conditions favorable for long-term enhanced microbial activity in the treatment area.

A version of this chapter has been published (Chowdhury et al., 2015)
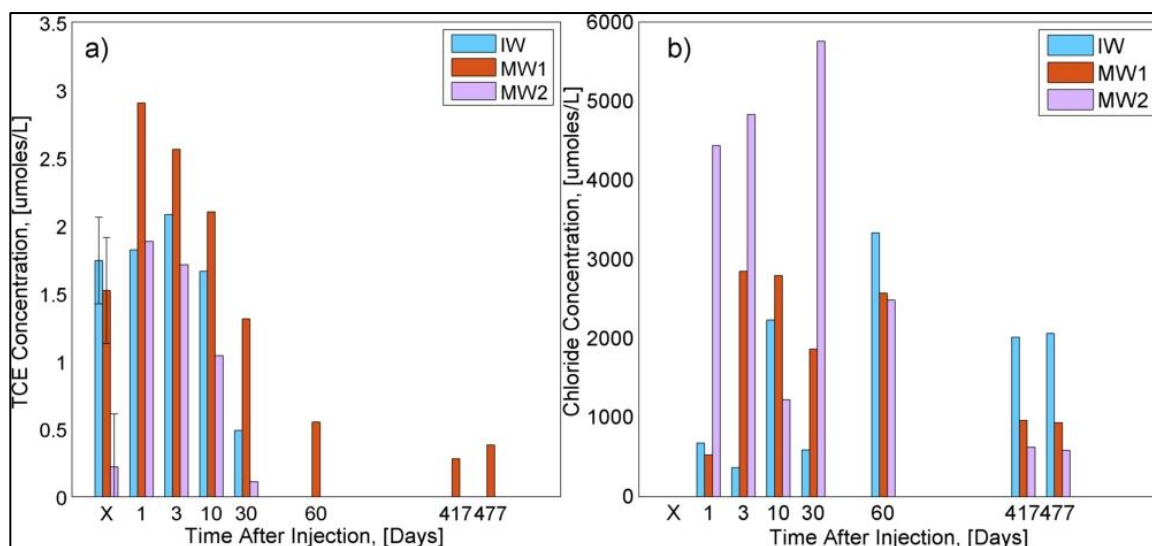
Figure 3.3: Concentration of: (a) TCE and (b) chloride in IW, MW1 and MW2; X denotes the average concentration for samples collected between July, 2003 and April, 2006 (i.e., prior to the current study). Error bars represent one standard deviation for samples collected between 2003 and 2006.

3.5.5   Description of numerical simulations

The numerical simulator CompSim was used to simulate the nZVI injection suspension to explore nZVI mobility in this field study. Simulation results also helped interpret the extent of nZVI delivery and injection fluid distribution that resulted in TCE degradation at the site. Finally the numerical simulator was used to explore design changes that could be used to improve mobility and also limitations associated with typical nZVI field trials. Results are presented for the plane passing through IW and MW1 for ease of presentation (shown in Figure 3.1b). This plane had a thickness of 0.2 m and therefore represents a volumetric section. It's important to note that these results are predictive and that model parameters were not fitted. A summary of the modeling parameters are given in Table 3-2.

3.5.5.1   Predicted changes in water level

The ambient water table at the site was located at 2.76 m (bgs) as shown in Figure 3.1a. However, the simulated water table was assumed to be at 2.8 m (bgs) due to the grid size used in the numerical simulations. The model predicted that the water level in IW increased to 0.94 m (bgs) at the end of P1 (Figure 7.1a), consistent with that observed in the field

A version of this chapter has been published (Chowdhury et al., 2015)

(i.e., 0.99 m). The simulated water level then decreased to 2.1 m (bgs) at the end of P2 (Figure S1), due to injection of DI water that is less viscous than the nZVI suspension injected during P1. The Reynolds number (Re) was calculated along the x direction using the spatially varying velocity and viscosity at different phases of the Field Case simulation, as shown in the Figure (7.1b). Calculated Re at all the locations were less than 0.01 suggesting darcy-compatible flow around the injection well and elsewhere, at the end of P1, P2 and P3. At the end of P3, the predicted water level at IW further increased from 2.1 m (bgs) at the end of P2 to 1.9 m (bgs) (Figure 7.1) due to the increased injection rate during this phase (5 L/min in P3 versus 3.3 L/min at P1 and P2). These changes are in good agreement with field observations (Figure 7.1). These results suggest that CompSim gave good predictions of the hydraulics associated with nZVI suspension injection at this site. No parameter fitting was required for these simulations and sources of relevant data are presented in Table 3-2.

The well screen length of the IW was 1.65 m with 0.66 m of the well screen lying above the ambient water table (at 2.76 m (bgs)) (Figure 3.1a). Figure (3.4 a-c) shows the predicted water saturation in the model domain including the unsaturated zone. Model predictions confirm that the injection fluid was delivered to the unsaturated zone causing a significant increase in the water content around the IW. This means that nZVI would have been delivered to the formerly unsaturated zone (Figure 3.4, a-c) and would also have resulted in nZVI attachment to soil grains (Figure 3.4, a-i).
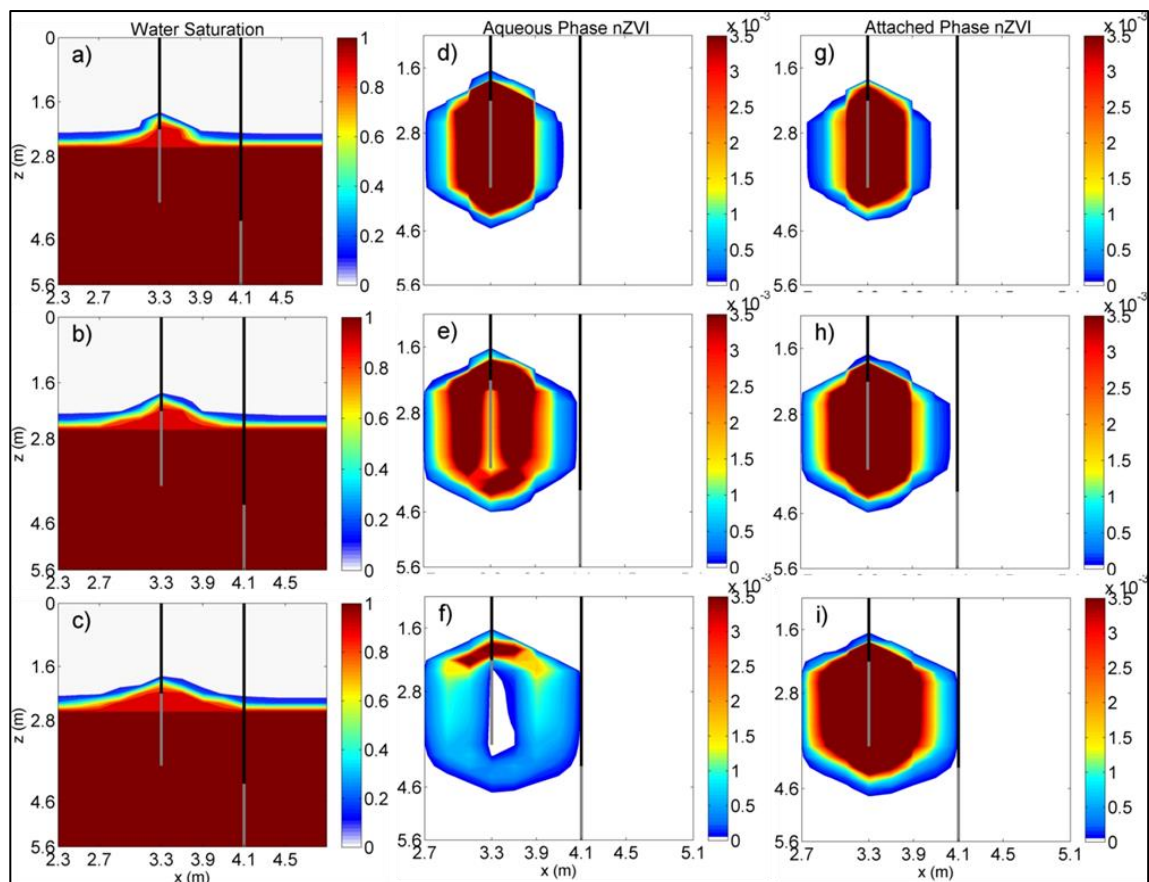
Figure 3.4: Simulated changes in water saturation a) t = 43 min (end of P1); b) t = 76 min (end of P2); c) t = 126 min (end of P3); Aqueous nZVI mass (in moles) at: d) t = 43 min; e) t = 76 min; f) t = 126 min; Attached nZVI mass (in moles) at: g) t = 43 min; h) t = 76 min; i) t = 126 min for Field case simulation.

3.5.5.2   Predicted changes in nZVI concentration

nZVI injection and subsequent flushing at the site were completed in three phases (P1, P2 and P3, respectively), as discussed above, and were modeled accordingly (referred to as Field Case, FC, Table 3-1). CompSim simulations predicted that approximately 75%, 39% and 13% of the injected nZVI (total of 2.66 moles) was in the aqueous phase in the domain at the end of P1, P2 and P3, respectively, with the remaining mass attached to the soil. The injection of DI water during P2 transported nZVI aqueous mass away from the IW, as shown by the dip in aqueous phase nZVI, as well as the increased spreading (Figure 3.5). Figure (3.4, d-i) also shows that re-circulating groundwater increased the spread of nZVI in the aqueous phase at the end of P3. Attached nZVI mass increased (Figure 3.5) along the

A version of this chapter has been published (Chowdhury et al., 2015)

section as injected nZVI migrated radially outwards and experienced decreasing groundwater velocities. About 0.97, 0.76 and 0.72 moles of nZVI (total mass) were present within the volumetric section at the end of P1, P2 and P3, respectively. About 28.5% (0.76 moles, total nZVI mass) of the injected nZVI mass remained between 2.7 m and 3.9 m in the x direction (IW at 3.3 m) along the section at the end of P2 indicating that nZVI was delivered to 0.60 m upstream and downstream of the IW (Figure 3.5).
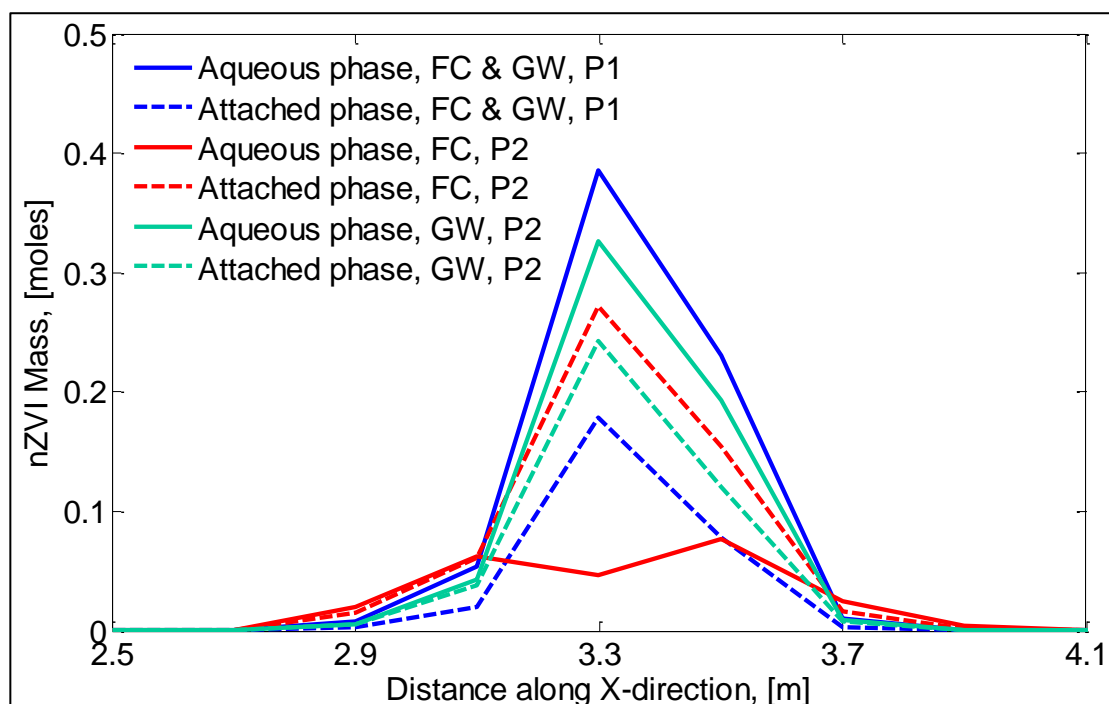
Figure 3.5: nZVI mass with distance (along the x direction) for different times (on the plane through IW (located at 3.3 m) and MW1 (located at 4.2 m)); Groundwater was flowing from left to the right resulting in slight asymmetry in the curve; P1 and P2 represents 43, and 76 minutes following nZVI injection. Field case (FC) and groundwater (GW) simulations are shown (refer to Table 3-2).

Aqueous phase nZVI mass in the unsaturated zone gradually decreased (Figure 3.4 (d-f)), and the attached mass increased with the DI flushing and groundwater re-circulation phases in the FC simulation (Figure 3.4, g-i). Total nZVI mass in the unsaturated zone varied between 18% and 20% for FC at the end of P1, P2 and P3. In the unsaturated zone the decrease in aqueous nZVI mass between P1 and P2 (0.10 moles) is almost equal to the increase in attached nZVI mass (0.14 moles) between these two phases. Similarly, the decrease in aqueous nZVI mass (0.16 moles) is equal to the increase in attached nZVI mass

A version of this chapter has been published (Chowdhury et al., 2015)

(0.16 moles) between P2 and P3. These results suggest that aqueous phase nZVI mass in the unsaturated zone that was removed between P1 and P2 did not travel to the saturated zone but was attached to the unsaturated zone soil. Therefore, nZVI injected into the unsaturated zone would not be available for degradation of contaminants present in the saturated zone. However, injection into the unsaturated zone could be advantageous in places where water table fluctuates over time or if the capillary fringe contains contaminants of concern. In such cases, immobile nZVI could act as a permeable reactive barrier (PRB) to remediate the contaminants in the unsaturated zone. It is assumed here that nZVI in the attached phase (onto the soil grains) within the capillary fringe would be surrounded by immobile water. So the atmospheric oxygen would need to slowly diffuse into the water and then to nZVI surface. As the diffused oxygen reacts with nZVI, an outer oxide layer would grow onto the nZVI core. This outer oxide layer could limit reaction with target contaminants (Farrell et al., 2000; Liu and Lowry, 2006; Sarathy et al., 2008).

The radius of gyration (and center of mass) is calculated to quantify the spread of nZVI mass following Dekker and Abriola (2000). For the FC simulation the radius of gyration in the x-direction, or the spread of aqueous nZVI, increased from 0.13 m at the end of P1 to 0.25 m and 0.36 m at the end of P2 and P3, respectively (Figure 3.6a and Table 7-1). The polymer radius of gyration (simulated as a conservative species with respect to reaction and attachment) shows a similar trend (0.15, 0.27 and 0.39 m, at the end of P1, P2 and P3, respectively) (Figure 3.6b). However, the radius of gyration of aqueous phase nZVI in the z-direction for the saturated zone increases as time progresses (i.e. 0.45 m, 0.50 m and 0.56 m, at the end of P1, P2 and P3, respectively) moving in a downward direction. This is expected since the nZVI suspension (55.96 moles/L) has a slightly higher molar density than water (55.46 mole/L) and therefore would sink with time. In the unsaturated zone, the radius of gyration of the aqueous phase nZVI does not change much in the z-direction (i.e. 0.15 m, 0.16 m and 0.17 m, at the end of P1, P2 and P3, respectively). The change in spread of aqueous nZVI mass in the x and z-directions can be seen in Figure 3.4 (d-f). These simulation results further support the discussion above that injection of DI water and groundwater recirculation helped in transporting the nZVI despite an increase in attached nZVI mass. It is further noted here that reaction of nZVI with the in-situ contaminants would consume nZVI. However, nZVI reaction with contaminants is slower compared to

A version of this chapter has been published (Chowdhury et al., 2015)

the nZVI migration rate in the presence of the flushing scheme. Therefore, the predicted nZVI concentration is not expected to decrease much. This current study was not focused on incorporating nZVI-Contaminant reaction and is an area that requires further investigation.
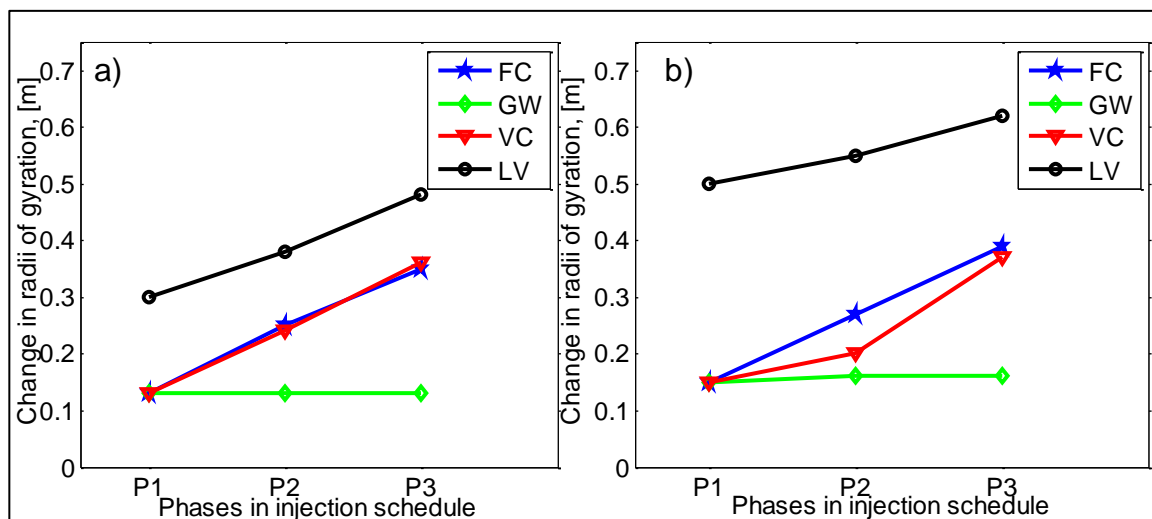
Figure 3.6: Radius of gyration for a) aqueous nZVI and b) polymer mass, for different cases at the end of P1, P2 and P3.

The FC simulation results predicted that nZVI was delivered to 0.60 m around the IW and that the injection fluid was able to reach MW1 (Figure 7.4). It is expected that injected nZVI would degrade the TCE within the distance travelled i.e. an area covered by 0.6 m radius; and nZVI that was attached to the soil created a PRB which degraded incoming TCE within the study area such that little TCE would reach MW1 and MW2. These simulation results therefore support the field observed decrease in TCE concentration (> 99%) in the study area resulting from nZVI injection, compared to historic data. The model also predicted that injection fluid containing CMC should have reached MW1 (Figure 7.4). Therefore, the long term decreases in concentration at MW1 in the subsequent 477 days was probably due to the enhanced biodegradation resulting from the delivery of CMC as nutrient carbon source for microorganisms as suggested in other studies (Elliott and Zhang, 2001; He et al., 2010; Kocur et al., 2015).

A version of this chapter has been published (Chowdhury et al., 2015)

3.5.6   Sensitivity analysis

A series of simulations were conducted to assess the factors controlling nZVI transport and assess methods to maximize transport distances. The details of these simulations are summarized in Table 3-1 and the results are discussed below.

3.5.6.1   Transport due to groundwater only (GW case)

The first simulation was conducted to assess the utility of the DI water injection (P2, for 33 min) and groundwater re-circulation (P3, for 50 min), following nZVI injection (P1). This simulation is referred to as GW where active pumping was stopped after P1, leaving only the background groundwater flow of approximately 0.23 m/day. As such, neither DI water injection nor groundwater re-circulation was simulated in the GW case. A comparison between the FC and GW cases is shown in Figure (3.5). Each of these cases had the same nZVI profile at the end of P1 since the same nZVI amount was injected at the same rate in these two cases. Approximately 37% (0.99 moles) of the injected nZVI mass was delivered between 2.7 m and 3.9 m (IW at 3.3 m) along the section at the end of P2 for the GW case compared to 28% (0.76 moles) in the FC case over the same distance.

Aqueous nZVI mass at the end of P2 is higher in the GW scenario (0.58 moles) compared to FC (0.23 moles) between 2.7 m and 3.9 m (IW at 3.3 m) along the section with less attachment to soil (0.42 and 0.52 moles in GW and FC simulations, respectively). There is also less spreading of aqueous phase nZVI mass in the GW case (Figure 3.5). The smaller amount of attached nZVI (0.42 moles) in GW compared to FC (0.52 moles) is somewhat counter intuitive considering that lower groundwater velocity should result in higher K_{att}, and thus, greater attached nZVI mass in GW compared to FC. However, DI water injection at P2 during the FC causes dilution of the previously injected viscous solution (7 cp). Figure (3.7) shows that for the FC simulation, the viscosity of the solution is much lower at the end of P2 (1.2 cP) and P3 (1 cP) compared to P1 (6.1 cP) at the IW location due to dilution by injected DI water (P2) and groundwater (P3). Lower solution viscosity increases the η_o and results in increased K_{att} (Equation 3.2), decreasing nZVI mass in the aqueous phase. This is further shown in Figure (3.7) where K_{att} at the IW location increases as the viscosity decreases at the end of P1, P2 and P3. Similar increase in attached phase nZVI mass

A version of this chapter has been published (Chowdhury et al., 2015)

resulting from lower viscosity was shown in Krol et al. (2013). In the absence of the DI flushing and groundwater recirculation phases the GW case has almost no increased lateral spreading for both the aqueous phase nZVI and CMC during the P2 and P3 phases, as shown in Figure 3.6 (a,b), respectively. Consequently, in the GW case, solution viscosity is larger leading to less nZVI attachment. Although continued flushing was found to increase the radial nZVI travel distance compared to the no flushing case, it is expected that injection of a viscous solution, instead of water, could further increase radial nZVI travel distance.
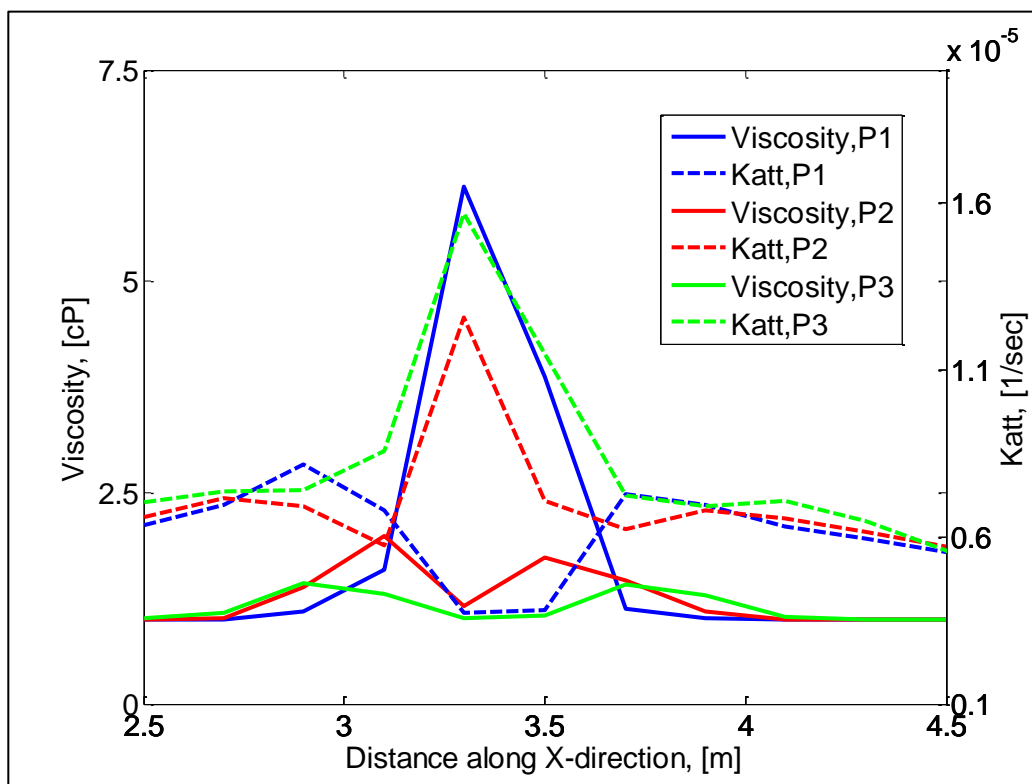
Figure 3.7: Changes in viscosity and attachment to soil (K_{att}) at different phase of the injection schedule, along the volumetric section for the Field Case (FC).

3.5.6.2   Effect of viscosity on nZVI transport and attachment (VC case)

The next simulation (referred to as VC) investigated the injection of water (i.e., nZVI free) with the same viscosity (7 cP) as the nZVI suspension injected during P2 to investigate the

A version of this chapter has been published (Chowdhury et al., 2015)

impact of viscosity on aqueous nZVI concentrations. The result of the VC case was compared to FC and GW cases.

Injecting a viscous solution resulted in slightly higher nZVI mass in the aqueous phase (9.6% and 8.6% of total injected mass in VC and FC cases, respectively, at the end of P2) due to increased viscosity (6.7 cP compared to 1.2 cP in VC and FC cases, respectively). However, increasing the viscosity of the solution resulted in decreased velocity (4.4 m/day in VC case compared to 4.9 m/day in FC) near the IW, similar to a previous modeling study (Krol et al., 2013). The symmetrical mass distributions around the IW in both FC and VC simulations suggest that nZVI transport in the porous matrix is governed by the radially decreasing groundwater velocity from the IW. Although the VC case predicted more nZVI mass in the aqueous phase at the end of P2 (0.3 moles in VC compared to 0.2 moles in FC simulations) nZVI did not travel further compared to FC simulation. Hence, injection of viscous slurry alone may not be enough to increase nZVI delivery area unless the velocity is manipulated. Therefore, increasing both injection velocity and viscosity, where possible, is recommended to increase nZVI distribution in the study area.

3.5.6.3   Effect of large volume injection (LV case)

The next simulation (referred to LV) assessed the effect of larger nZVI volume injection to increase nZVI travel distance from the injection well. This consisted of injecting 2000 L of nZVI solution in the LV case (P1), compared to 142 L in the FC, but at the same injection rate as the FC (i.e. 3.3 L/min). Similar higher volume injections have been used in field studies (Elliott and Zhang, 2001; He et al., 2010; Wei et al., 2010; Zhang, 2003). Conditions during P2 and P3 were the same as the FC. A total of 36 moles of nZVI were delivered into the domain in the LV case compared to 2.66 moles in FC. Approximately 7.5 moles were in the aqueous phase in the domain at the end of P1 in the LV case (606 min) compared to 2 moles of nZVI for FC (at 43 min) (Figure 7.5). However, more nZVI mass was attached to the solid phase in the LV case compared to the FC. For example, approximately 79% (28.5 moles) of injected mass was attached in the LV case in the domain while 25% (0.67 moles) of injected nZVI was attached in the FC at the end of P1. In the FC and LV cases the velocity profiles are similar, moving radially outwards from the IW (due to same

A version of this chapter has been published (Chowdhury et al., 2015)

injection rate); thus, these cases should have similar K_{att} at any point in the domain. Therefore, the higher mass of attached nZVI at the end of P1 in the LV case, compared to FC, resulted from the longer injection duration, and greater mass injected, in the LV case as attachment rates are similar in both cases. The model predicted 24.3% (8.75 moles), 23.5% (8.45 moles) and 23.1% (8.31 moles) of injected nZVI mass (total nZVI) migrated to 0.80 m (location of MW1) upstream and downstream of the IW along the section in LV case at the end of P1, P2 and P3, respectively. In comparison, the FC simulation predicted that nZVI did not migrate beyond 0.60 m from the IW. Although injecting a larger volume of nZVI resulted in greater travel distance (0.80 m in the LV case compared to 0.60 m in the FC), a large proportion of the nZVI was in the attached phase (79%) and therefore a larger injection volume may not be cost effective considering the 14 times greater volume that was used to achieve the increased (approx. 1.3 times) travel distance. However, a larger volume would deliver more nZVI mass within the distance travelled (i.e. 0.80 m in this case) which might be beneficial for source zone remediation where more nZVI mass is required to degrade a large mass of target contaminant.

3.5.6.4   Impact of location of injection and monitoring wellscreen (WS case)

The comparison of FC, GW and VC simulations above suggests that nZVI transport is dependent on both velocity and the viscosity of injected solution. Therefore, another suite of simulations was conducted to investigate the impact of injection of a viscous solution, as well as, the location of injection and monitoring/recirculation well screens on nZVI delivery. In this case (referred to as WS case) IW and MW1 well screens were assumed to be located at the same depth (between 4.2 m and 5.6 m, bgs) as opposed to FC simulation where wells were screened at 2.1-3.75 m and 4.2-5.9 m (bgs) for IW and MW1, respectively. In the FC case, there was a zone of low flow between the depth of IW and MW1 screens, as such, extraction from the MW1 had almost no influence on nZVI transport. Therefore, in WS case, the MW1 and IW screens are located at the same depth to investigate if MW1 extraction influences nZVI transport. The nZVI/polymer/groundwater was injected at 3.3 L/min, (equivalent to the FC case). A summary of injection schedules used for this suite of simulations is given in Table 3-1. A

A version of this chapter has been published (Chowdhury et al., 2015)

comparison of Figures 3.4 (d-i), 7.4 and 7.6 show that the WS case yielded greater nZVI travel distance compared to FC simulation at the end of P1. Figure 7.6 also shows that trace amounts of both nZVI and the polymer mass migrated past MW1 at the end of P2 and P3. The radius of gyration for WS case was 0.16 m, 0.28 m and 0.40 m in the x direction compared to 0.13 m, 0.25 m and 0.35 m in FC case at the end of P1, P2 and P3, respectively indicating that the aqueous phase nZVI travelled a greater distance in the WS case simulation. As an objective comparison, the radii of gyration for CMC in the WS case simulation were 0.18 m, 0.25, and 0.40 m in the x direction compared to 0.15 m, 0.27 m, and 0.39 m in FC case at the end of P1, P2 and P3, respectively. Moreover, 31.7% of total nZVI travelled a distance of 0.80 m (i.e. location of MW1) along the section through IW-MW1 in WS case at the end of P1 compared to 36.4% of total nZVI delivered to 0.60 m in FC. Simulated nZVI mass that has reached MW1 would have been removed due to the extraction and thus may have resulted in lower mass in WS case (31.7%) over FC case (36.4%). This WS simulation suggests that greater nZVI travel distance would be achieved if the injection and monitoring/extraction well screens were located at the same depth as opposed to the field setup used in this study.

In addition to the aforementioned analyses, another suite of sensitivity analysis (results not shown) was conducted to evaluate the sensitivity of dispersion and grid size of the model domain on nZVI migration. For this purpose two more simulations were conducted with dispersivity values of 0.20 m (which is equal to the current meshsize) and 0.70 m (which is 10 times higher than the base case dispersivity of 0.07 m). The results showed that the nZVI spreading, along the volumetric section through the injection well and monitoring well, for both saturated and unsaturated zones, did not change at the end of the nZVI injection phase. Hence, it was anticipated that the model results for the simulations conducted in this study are not sensitive to dispersivity (and to gridsize) for the range of the dispersivity values investigated (i.e., 0.70 to 0.07 m).

3.5.7   1D and 3D results comparison

The 1D CFT equation is commonly used to explore nZVI mobility (O'Carroll et al., 2013a; Tiraferri and Sethi, 2009), however, the 1D CFT equation does not include the complicated

A version of this chapter has been published (Chowdhury et al., 2015)

flow field present at typical field sites (i.e., pore water velocity radially decreases from the well, finite well screen length, dilution of CMC). Another suite of simulations was therefore performed to compare simulation results generated from the 1D assumption to those generated from a scenario more typical of a 3D field scale. For the 1D case, CompSim was used to generate the flow field, the associated pressure head distribution, and predict nZVI transport. The injection fluxes per well block were the same for both the 1D and 3D cases and the travel distance was compared. The domain setup for these two cases is shown in Figure (7.7) and the results are shown in Figure (3.8) and Figure (7.8).
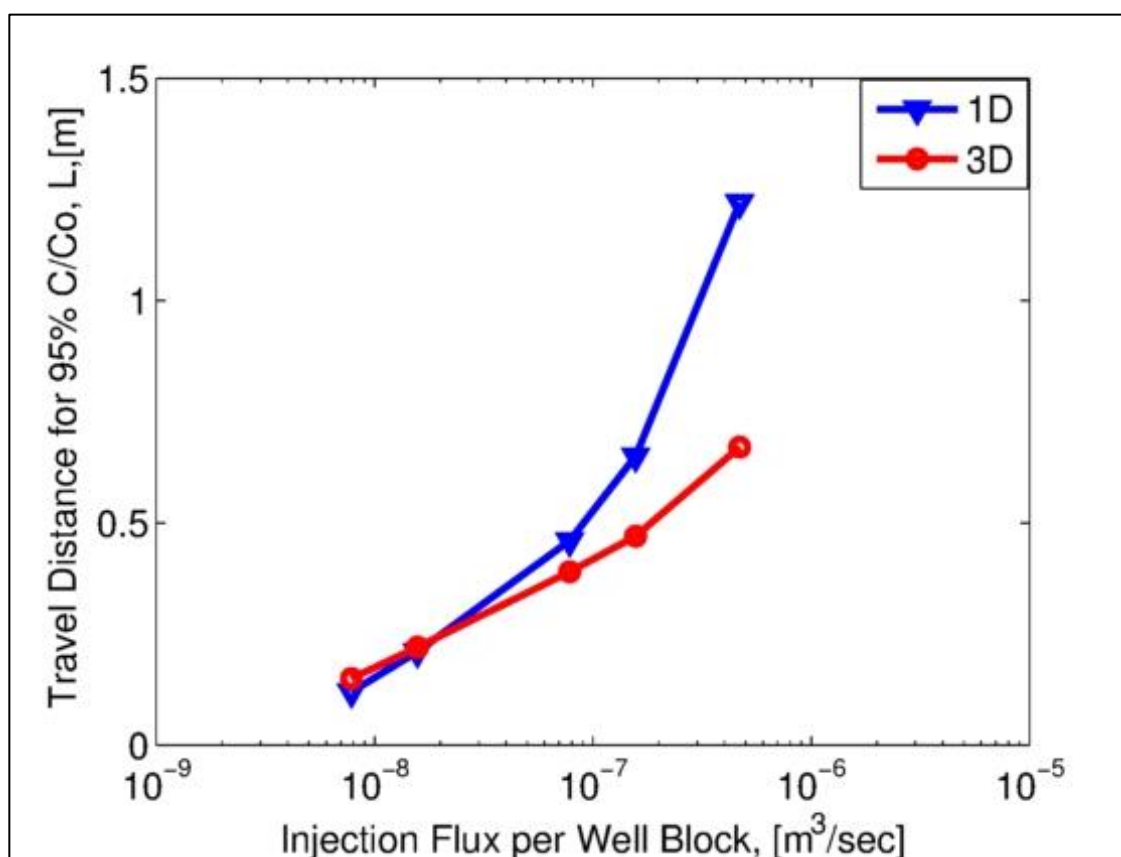
Figure 3.8: Interpolated nZVI travel distances for 95% aqueous nZVI concentration removal for different injection fluxes for 1D and 3D CompSim simulations.

As shown in Figure (3.8) the travel distance before 95% of the nZVI mass is removed from solution increases more rapidly in the 1D case (0.21 to 1.22 m) compared to 3D case (0.22 to 0.67 m) as the flux per injection node is increased from 1.57×10^{-8} to 4.7×10^{-7} m^3/sec per well block. In the 1D case, the travel distance increases exponentially with velocity as the

A version of this chapter has been published (Chowdhury et al., 2015)

velocity term in the first order sink term in Equation (3.2) drops out (i.e., it is divided by the velocity in the advective flux term) (Equation 7.3). Since this velocity term is removed, the first order sink term decreases with velocity (due to functional form of η_o). The same occurs in the 3D case, however this is counterbalanced by the radially decreasing velocity away from the injection well. Additionally, pore water velocity is the same at all locations in the 1D case. The simulation results also show that 1D cases resulted in higher water head compared to 3D cases for a given injection flux. Figure (7.8) demonstrated that water head at the injection location is very high (25.5 m) for the 1D case at the higher injection flux ($4.7x10^{-7}$ m^3/sec). Given the model domain (5.6 m deep) a water head of approximately 6 m can be accommodated at the site (the depth in the model domain is 5.6 m in the z-direction). However, water heads of 8.9 to 25.46 m are unrealistic for any practical scenario. The 3D case, on the contrary, lowered water heads (5.6 - 6.3 m) over the range of injection fluxes were simulated given that velocity decreases radially away from the well.

These results suggest that 1D simulation would overestimate nZVI travel distance if used to predict nZVI migration in the subsurface. The higher water head associated with the higher travel distances at a given flux would also be impractical. The nZVI travel distances, as predicted by 3D CompSim, are very similar to the field observed nZVI travel distance (O'Carroll et al., 2013a). This again suggests that 3D simulations are more appropriate than 1D simulations for the prediction of nZVI travel distance in the subsurface.

3.6 Conclusion

In this study, the lab-scale nZVI synthesis process was scaled up for onsite nZVI synthesis and injection into a field-scale contaminated subsurface. Although nZVI was not detected in any of the monitoring wells because of the injection schedule used in this study, indirect measurements such as pH, ORP, DO as well as sulfate concentration data suggest that the injection fluid was able to travel at least 0.8 m away from the injection well. Additionally TCE concentrations in the treatment area decreased by more than 99% from the historical TCE concentrations. These results suggested that synthesising nZVI at lower temperature did not impact nZVI reactivity and that monometallic nZVI was able to degrade the target contaminant. To further assess nZVI mobility, CompSim was used to model the field study

A version of this chapter has been published (Chowdhury et al., 2015)

as well as to evaluate a range of injection scenarios. Simulations predicted that in the field trial, nZVI was mobile in the subsurface to at least 0.60 m, radially, from the injection well. The simulations also showed that the injected fluid could be delivered to MW1, consistent with field observed changes in geochemical parameters. Therefore, the simulation results complement the field observed contaminant degradation resulting from this nZVI injection.

The modeling sensitivity analyses showed that injection of higher volumes of nZVI delivered more nZVI mass, up to 0.80 m radial distance from the IW. CompSim simulations predicted that injecting a higher volume of nZVI suspension (14 times greater) resulted in a 1.3 times increase in travel distance which may not be a cost effective solution to increasing nZVI travel distance. Model predictions also showed that nZVI travel distance was dependent on the injection velocity and viscosity of the water flushing consistent with previous modeling findings by Krol et al. (2013). Therefore, nZVI delivery to a targeted zone can be enhanced by flushing the IW with a higher viscosity solution at a higher injection rate. Simulation results also indicated that installing the injection and monitoring well screens at the same depth resulted in greater nZVI travel distance due to the influence of extraction from monitoring well compared to a case where the well screens were located at different depths. Finally a comparison of 1D and 3D simulation results suggest that travel distances generated from the simplified 1D CFT solution should be used with caution as they could over predict nZVI travel distance.

Acknowledgements

A version of this chapter has been published (Chowdhury et al., 2015)

3.7 References

Bennett, P., He, F., Zhao, D., Aiken, B. and Feldman, L., 2010. In situ testing of metallic iron nanoparticle mobility and reactivity in a shallow granular aquifer. Journal of Contaminant Hydrology, 116(4): 35-46.

Berge, N.D. and Ramsburg, C.A., 2009. Oil-in-Water Emulsions for Encapsulated Delivery of Reactive Iron Particles. Environmental Science & Technology, 43(13): 5060-5066.

Bradford, S.A. and Torkzaban, S., 2008. Colloid Transport and Retention in Unsaturated Porous Media: A Review of Interface-, Collector-, and Pore-Scale Processes and Models. Vadose Zone Journal, 7(2): 667-681.

Chowdhury, A.I.A., O'Carroll, D.M., Xu, Y. and Sleep, B.E., 2012. Electrophoresis enhanced transport of nano-scale zero valent iron. Advances In Water Resources, 40(0): 71-82.

DCC, D.C.C., 2007. Detailed Testing Program for Highbury Complex, Defence Construction Canada, London.

Dekker, T.J. and Abriola, L.M., 2000. The influence of field-scale heterogeneity on the infiltration and entrapment of dense nonaqueous phase liquids in saturated formations. Journal of Contaminant Hydrology, 42(2–4): 187-218.

Elliott, D.W. and Zhang, W.X., 2001. Field assessment of nanoscale bimetallic particles for groundwater treatment. Environmental Science & Technology, 35: 4922-6.

Farrell, J., Kason, M., Melitas, N. and Li, T., 2000. Investigation of the Long-Term Performance of Zero-Valent Iron for Reductive Dechlorination of Trichloroethylene. Environmental Science & Technology, 34(3): 514-521.

Gargiulo, G. et al., 2007. Bacteria transport and deposition under unsaturated conditions: The role of the matrix grain size and the bacteria surface protein. Journal of Contaminant Hydrology, 92(3–4): 255-273.

He, F., Zhang, M., Qian, T. and Zhao, D., 2009. Transport of carboxymethyl cellulose stabilized iron nanoparticles in porous media: column experiments and modeling. Journal of colloid and interface science, 334: 96-102.

He, F. and Zhao, D., 2007. Manipulating the Size and Dispersibility of Zerovalent Iron Nanoparticles by Use of Carboxymethyl Cellulose Stabilizers. Environmental Science & Technology, 41: 6216-6221.

He, F., Zhao, D. and Paul, C., 2010. Field assessment of carboxymethyl cellulose stabilized iron nanoparticles for in situ destruction of chlorinated solvents in source zones. Water research, 44(7): 2360-2370.

Henn, K.W. and Waddill, D.W., 2006. Utilization of nanoscale zero-valent iron for source remediation—A case study. Remediation Journal, 16(2): 57-77.

Johnson, R.L., Johnson, G.O.B., Nurmi, J.T. and Tratnyek, P.G., 2009. Natural Organic Matter Enhanced Mobility of Nano Zerovalent Iron. Environmental Science & Technology, 43(14): 5455-5460.

Johnson, R.L. et al., 2013. Field-Scale Transport and Transformation of Carboxymethylcellulose-Stabilized Nano Zero-Valent Iron. Environmental Science & Technology, 47(3): 1573-1580.

Kim, H.-J., Phenrat, T., Tilton, R.D. and Lowry, G.V., 2009. Fe0 Nanoparticles Remain Mobile in Porous Media after Aging Due to Slow Desorption of Polymeric Surface Modifiers. Environmental Science & Technology, 43: 3824-3830.

A version of this chapter has been published (Chowdhury et al., 2015)

Kirschling, T.L., Gregory, K.B., Minkley, J.E.G., Lowry, G.V. and Tilton, R.D., 2010. Impact of Nanoscale Zero Valent Iron on Geochemistry and Microbial Populations in Trichloroethylene Contaminated Aquifer Materials. Environmental Science & Technology, 44(9): 3474-3480.

Kocur, C.M. et al., 2014. Characterization of nZVI Mobility in a Field Scale Test. Environmental Science & Technology, 48(5): 2862-2869.

Kocur, C.M., O'Carroll, D.M. and Sleep, B.E., 2013. Impact of nZVI stability on mobility in porous media. Journal of Contaminant Hydrology, 145(0): 17-25.

Kocur, C.M.D. et al., 2015. Contributions of Abiotic and Biotic Dechlorination Following Carboxymethyl Cellulose Stabilized Nanoscale Zero Valent Iron Injection. Environmental Science & Technology, 49(14): 8648-8656.

Krol, M.M. et al., 2013. A Field-Validated Model for In Situ Transport of Polymer-Stabilized nZVI and Implications for Subsurface Injection. Environmental Science & Technology.

Krug, T., O'Hara, S. and Watling, M., 2010. Emulsified Zero-Valent Nano-Scale Iron Treatment of Chlorinated Solvent DNAPL Source Areas, ARLINGTON, VA.

Liu, Y. and Lowry, G.V., 2006. Effect of Particle Age (Fe0 Content) and Solution pH On NZVI Reactivity: H2 Evolution and TCE Dechlorination. Environmental Science & Technology, 40(19): 6085-6090.

O'Carroll, D., Sleep, B., Krol, M., Boparai, H. and Kocur, C., 2013. Nanoscale zero valent iron and bimetallic particles for contaminated site remediation. Advances In Water Resources, 51: 104-122.

O'Carroll, D.M., Bradford, S.A. and Abriola, L.M., 2004. Infiltration of PCE in a system containing spatial wettability variations. Journal of Contaminant Hydrology, 73(1–4): 39-63.

O'Carroll, D.M. and Sleep, B.E., 2007. Hot water flushing for immiscible displacement of a viscous NAPL. Journal of Contaminant Hydrology, 91(3-4): 247-266.

O'Carroll, D. and Sleep, B., 2009. Role of NAPL Thermal Properties in the Effectiveness of Hot Water Flooding. Transport in Porous Media, 79(3): 393-405.

Phenrat, T. et al., 2009. Particle Size Distribution, Concentration, and Magnetic Attraction Affect Transport of Polymer-Modified Fe 0 Nanoparticles in Sand Columns. Environmental Science and Technology, 43: 5079-5085.

Poling, B.E., Prausnitz, J.M. and O'Connell, J.P., 2001. The Properties of Gases and Liquids. McGraw-Hill, Toronto.

Raychoudhury, T., Naja, G. and Ghoshal, S., 2010. Assessment of transport of two polyelectrolyte-stabilized zero-valent iron nanoparticles in porous media. Journal of Contaminant Hydrology, 118(3-4): 143-151.

Raychoudhury, T., Tufenkji, N. and Ghoshal, S., 2014. Straining of polyelectrolyte-stabilized nanoscale zero valent iron particles during transport through granular porous media. Water Research, 50(0): 80-89.

Sakulchaicharoen, N., O'Carroll, D.M. and Herrera, J.E., 2010. Enhanced stability and dechlorination activity of pre-synthesis stabilized nanoscale FePd particles. Journal of Contaminant Hydrology, 118(3-4): 117-127.

Saleh, N. et al., 2008. Ionic Strength and Composition Affect the Mobility of Surface-Modified Fe 0 Nanoparticles in Water-Saturated Sand Columns. Environmental Science and Technology, 42: 3349-3355.

A version of this chapter has been published (Chowdhury et al., 2015)

Sarathy, V. et al., 2008. Aging of Iron Nanoparticles in Aqueous Solution: Effects on Structure and Reactivity. The Journal of Physical Chemistry C, 112(7): 2286-2293.

Schrick, B., Hydutsky, B.W., Blough, J.L. and Mallouk, T.E., 2004. Delivery Vehicles for Zerovalent Metal Nanoparticles in Soil and Groundwater. Chemistry of Materials, 16: 2187-2193.

Sleep, B.E., Sehayek, L. and Chien, C.C., 2000a. A Modeling and experimental study of light nonaqueous phase liquid (LNAPL) accumulation in wells and LNAPL recovery from wells. Water Resour. Res., 36(12): 3535-3545.

Sleep, B.E., Sehayek, L. and Chien, C.C., 2000b. Modeling wells in variably saturated soil with wellbore fluid gravity segregation. Advances In Water Resources, 23(7): 689-697.

Sleep, B.E. and Sykes, J.F., 1993. Compositional simulation of groundwater contamination by organic compounds: 1. Model development and verification. Water Resour. Res., 29(6): 1697-1708.

Stookey, L.L., 1970. Ferrozine-A New Spectrophotometric Reagent for Iron. Analytical Chemistry, 42(7): 779-781.

Tiraferri, A. and Sethi, R., 2009. Enhanced transport of zerovalent iron nanoparticles in saturated porous media by guar gum. Journal of Nanoparticle Research, 11(3): 635-645.

Tiraferri, A., Tosco, T. and Sethi, R., 2011. Transport and retention of microparticles in packed sand columns at low and intermediate ionic strengths: experiments and mathematical modeling. Environmental Earth Sciences, 63(4): 847-859.

Torkzaban, S., Bradford, S.A., van Genuchten, M.T. and Walker, S.L., 2008. Colloid transport in unsaturated porous media: The role of water content and ionic strength on particle straining. Journal of Contaminant Hydrology, 96(1–4): 113-127.

Tosco, T., Petrangeli Papini, M., Cruz Viggi, C. and Sethi, R., 2014. Nanoscale zerovalent iron particles for groundwater remediation: a review. Journal of Cleaner Production, 77(0): 10-21.

Tosco, T. and Sethi, R., 2010. Transport of Non-Newtonian Suspensions of Highly Concentrated Micro- And Nanoscale Iron Particles in Porous Media: A Modeling Approach. Environmental Science & Technology, 44(23): 9062-9068.

Tosco, T., Tiraferri, A. and Sethi, R., 2009. Ionic Strength Dependent Transport of Microparticles in Saturated Porous Media: Modeling Mobilization and Immobilization Phenomena under Transient Chemical Conditions. Environmental Science & Technology, 43(12): 4425-4431.

TSH, 2007. Detailed Testing Program: Highbury Complex, London, ON. Project No. 52-27811, Defence Construction Canada, London, ON.

Tufenkji, N. and Elimelech, M., 2004. Correlation Equation for Predicting Single-Collector Efficiency in Physicochemical Filtration in Saturated Porous Media. Environmental Science and Technology, 38(2): 529-536.

Vecchia, E.D., Luna, M. and Sethi, R., 2009. Transport in Porous Media of Highly Concentrated Iron Micro- and Nanoparticles in the Presence of Xanthan Gum. Environmental Science & Technology, 43(23): 8942-8947.

A version of this chapter has been published (Chowdhury et al., 2015)

Wei, Y.-T. et al., 2010. Influence of nanoscale zero-valent iron on geochemical properties of groundwater and vinyl chloride degradation: A field case study. Water research, 44(1): 131-140.

West, M.R. and Kueper, B.H., 2012. Numerical simulation of DNAPL source zone remediation with in situ chemical oxidation (ISCO). Advances In Water Resources, 44(0): 126-139.

Zhang, W.-x., 2003. Nanoscale iron particles for environmental remediation: An overview. Journal of Nanoparticle Research, 5: 323-332.

Zhang, W. et al., 2010. Colloid Transport and Retention in Unsaturated Porous Media: Effect of Colloid Input Concentration. Environmental Science & Technology, 44(13): 4965-4972.

Chapter 4

4 Electrokinetic-Enhanced Permanganate Delivery and Remediation of Contaminated Low Permeability Porous Media

Ahmed I. A. Chowdhury[a], Jason I. Gerhard[a], David Reynolds[b], Brent E. Sleep[c], Denis M. O'Carroll[a,*]

[a] Department of Civil and Environmental Engineering, Western University, 1151 Richmond St., London, ON, Canada. N6A 5B9

[b] Geosyntec Consultants, 130 Stone Road W., Guelph, ON, Canada. N1G 3Z2

[c] Department of Civil Engineering, University of Toronto, 35 St. George St., Toronto, ON, Canada. M5S 1A4.

4.1 Abstract

Back diffusion of contaminants from low permeability strata has inhibited site remediation and closure due to an inability to deliver remediants into these strata. This study demonstrates the potential of electrokinetics (EK) to facilitate remediation of low permeability porous media contaminated by chlorinated solvents. Experiments were conducted in a two-dimensional sandbox packed with vertical layers of coarse sand and silt contaminated with aqueous trichloroethene (TCE). Nine experiments, each approximately 40 days in duration, were conducted to compare EK-enhanced in situ chemical oxidation (EK-ISCO) to EK or ISCO alone. EK-ISCO successfully delivered the oxidant (permanganate, PM) throughout the silt cross-section while ISCO without EK resulted only in PM delivery to the edges of the silt layer fringes. EK-ISCO resulted in a 4.4 order-of-magnitude (OoM) reduction in TCE concentrations in the coarse sand compared to a 3.5 OoM reduction from ISCO alone. EK-ISCO with a 25 mA current was found to be more effective than with 300 mA current. Overall, this study suggests that electrokinetics coupled with an appropriate in situ remediation technique, such as ISCO, can achieve enhanced remediation of lower permeability strata.

4.2   Introduction

Contaminant mass sequestered in low permeability zones has recently been identified as an issue limiting site closure (Seyedabbasi et al., 2012). Low permeability, in this context, means below approximately 1.0×10^{-14} m^2 (e.g., silt, clay) such that flow via advection is negligible (Fetter, 2001; Hodges, 2010; NRC, 2005). These zones can store significant contaminant mass, and this mass can diffuse into adjacent permeable zones (termed 'back diffusion'), acting as a long term source of contamination (Ball et al., 1997; Chapman and Parker, 2005; Liu and Ball, 2002; Parker et al., 2008; Sale et al., 2007; Seyedabbasi et al., 2012). This form of groundwater contamination sometimes becomes apparent, and even dominates, after aggressive remediation of the permeable zones (termed 'rebound') (Chapman and Parker, 2005; Gerhard et al., 2014; Sale et al., 2013). Remediating both high and low permeability zones is now recognized as necessary to prevent rebound at sites and ensure compliance with regulatory standards (Sale et al., 2013).

A range of technologies have been developed to target contaminant mass in permeable zones, including injection of oxidants (e.g., sodium/potassium permanganate (KMnO$_4$/ NaMnO$_4$) and sodium persulfate (Na$_2$S$_2$O$_8$)) (Baciocchi et al., 2014; Siegrist et al., 2011). Use of permanganate (PM) as an in-situ chemical oxidation (ISCO) remediation technology has garnered significant interest due to its high oxidation-reduction potential (+1.7 volts), stability in aqueous solution, reactivity over a wide range of pH (3.5 to 12), ability to work without an activator, and production of non-toxic by-products after reaction with chlorinated solvents (Kao et al., 2008; Petri et al., 2011a; Siegrist et al., 2011; Waldemer and Tratnyek, 2005). PM reacts to degrade trichloroethylene (TCE) as follows (Yan and Schwartz, 2000):

$$TCE + 2MnO_4^- \rightarrow 2CO_2 + 2MnO_{2(s)} + 3Cl^- + H^+ \qquad\qquad \text{(Equation 4.1)}$$
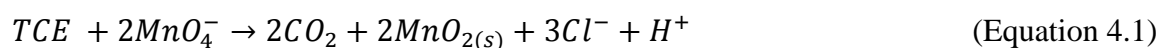
MnO$_{2(s)}$ precipitate, a brown to black product of PM reduction (Equation 4.1) (Li and Schwartz, 2004a; Li and Schwartz, 2004b; Schnarr et al., 1998; Schroth et al., 2001), can limit PM transport in the long term via pore clogging, reduced permeability, and rind formation at the edges of contaminated regions. Limited PM transport may result in

inefficient mixing between TCE and PM. Nevertheless, PM application has generally demonstrated success in controlled, laboratory-scale experiments, and field studies focused on remediating permeable strata. However, subsurface heterogeneity is a significant impediment to field applications. In particular, successful delivery of oxidants, or any remediant, into low permeability zones or uniformly throughout heterogeneous zones, is an unresolved challenge (Sale et al., 2013; Yeung, 2011).

This challenge was clearly shown in a series of 2D laboratory experiments by Sale et al. (2013). In this study, ISCO was applied to tanks characterized by alternating 5 cm vertical strips of coarse sand (K = 200 m/d) and silt (K = 0.2 m/d) flooded with aqueous TCE (1300 mg/L) for 52 d (17 pore volumes, PV). PM (2000 mg/L) was flooded through the permeable zones for 27 d (9 PV) and TCE concentrations were measured at the tank effluent for the following 82 d (27 PV). $MnO_{2(s)}$ precipitation was inhibited by the addition of sodium hexametaphosphate (2000 mg/L), thereby maximizing the chances of success. During the PM injection period, TCE was non-detect at the outlet, due to destruction of TCE diffusing out of the silt by PM in the permeable zones. However, TCE concentrations rebounded as soon as PM injection stopped; this occurred because back-diffusion continued while PM was swept out of the system by continuing groundwater flow. At the end of the post-PM treatment period the final TCE concentration was reduced by 3.1 orders of magnitude (OoM) from the initial concentration, showing some improvements on the 2.6 OoM reduction observed in the no-treatment control. Photographs revealed that PM was only able to penetrate a maximum of 1.3 cm into the edges of the silt layers, underscoring that remediation of the silt itself was ineffective. Of the 5 remediation methods tested, the largest TCE reduction was only 3.8 OoM, leaving concentrations that were 1.6 OoM higher than the maximum contaminant level (MCL) permitted for TCE in groundwater. Overall, this study emphasized, in agreement with many field and modelling studies (Ball et al., 1997; Chapman and Parker, 2005; Gerhard et al., 2014; Liu and Ball, 2002; Parker et al., 2008; Seyedabbasi et al., 2012), that remediants must be effectively delivered into contaminated low permeability zones in order for remediation efforts to ultimately be successful.

Electrokinetics (EK) has been proposed for increasing the effectiveness of remediant (nano-scale zero valent iron, permanganate, persulfate) delivery into low permeability soils (Chowdhury et al., 2012; Hodges et al., 2013; Reynolds et al., 2008; Roach and Reddy, 2006; Robertson, 2009). EK involves the application of a low voltage direct current (DC) across two or more electrodes (positive/anode and negative/cathode) (Acar and Alshawabkeh, 1993). Electromigration (EM), an EK migration mechanism, results in the transport of ionic species in the bulk solution. The EM-induced transport direction depends on the valence of the ions; for example, PM ions migrate from cathode to anode due to the negative charge on the ions. Since EM is independent of intrinsic permeability, EK has significant potential for delivering ionic remediants into low permeability zones (Hodges et al., 2013; Reynolds et al., 2008; Robertson, 2009).

EM-induced migration of PM has been examined in a number of laboratory studies (Cang et al., 2013; Hodges et al., 2013; Reynolds et al., 2008; Roach and Reddy, 2006; Thepsithar and Roberts, 2006). Overall these studies confirmed that PM penetration into low permeability zones could be enhanced with EK. With the exception of two, these studies were conducted in the absence of contaminants and were therefore unable to determine if EK induced PM transport would reduce contaminant mass in low permeability media. Cang et al. (2013) reported that PM degraded 52% of pyrene after 336 hrs of EK–PM (9 g/L) application. Thepsithar and Roberts (2006) reported 91% of phenol was removed during 120 hrs of EK-PM (9 g/L) compared to 64% in the control (EK only) experiment suggesting that phenol removal was primarily due to electroosmotic sweeping (i.e., bulk fluid movement) and not from oxidation. These two studies suggest that PM penetrated into low permeability zones due to EK application, but the extent of PM penetration was small therefore limiting contaminant destruction. Sale and McWhorter (2001) suggests that removing most of the contaminant mass in low permeability zones is required to achieve remedial objectives. From existing research, it is unknown whether the extent of contaminant mass destruction from EK-enhanced ISCO is adequate to improve groundwater quality in adjacent permeable media (i.e., limit the extent of back diffusion).

The goal of this work was to close this knowledge gap; specifically, to quantify EK-enhanced ISCO remediation of a system characterized by both low and high permeability

porous media contaminated with a chlorinated solvent. This was accomplished by (a) measuring the extent to which EK to delivered PM from coarse sand into silt, and (b) quantifying the contaminant concentration reductions resulting from EK-enhanced oxidant delivery. Nine (9) experiments were conducted with a heterogeneously packed 2D experimental apparatus contaminated with aqueous TCE. Experiments, including a control (i.e., hydraulic flushing), EK-only, and EK-ISCO, were carefully delineated over 40 days of treatment and post-treatment rebound. The suite of analyses included contaminant concentrations, image analysis for PM concentration in silt and $MnO_{2(s)}$ precipitation in sand, and the geochemical properties pH and oxidation-reduction potential (ORP). This study represents a major step forward in our understanding of the ability for EK-ISCO to remediate low permeability zones and provides valuable information for pilot field trials as the next step for this innovative remediation approach.

4.3   Materials and Methods

4.3.1   Experimental setup

All experiments were conducted in a custom built 2D sandbox (working area of 50 cm x 35.5 cm x 1.75 cm) made of aluminum with a 1.2 cm thick front glass panel (Figure 4.1a). The metal back plate was covered with chemical resistant Viton glue (Pelseal® 2078: Zero-VOC, Pelseal Technologies, LLC, Bensalem, PA, USA) to avoid current short circuiting. Nine sampling ports with luer lock valves were installed on the back plate to collect water samples from the coarse sand (Figure 4.1a-b). In addition, the sandbox contained one inlet and one effluent port arranged so that advective flow was vertically upwards (Figure 4.1, a-b).

The sandbox was carefully packed (in 1 cm, individually compacted lifts) with coarse sand (F32, Barco Silica sand, $d_{50} = 0.475$ mm, K = 42 m/day) and fine silt (Sil-Co-Sil 106, US Silica, $d_{50} = 0.045$ mm, K = 0.2 m/day). The heterogeneity pattern consisted of alternate vertical layers of the sand (27.5 cm long x 6.5 cm wide) and the silt (27.5 cm long x 8 cm wide) (Figure 4.1a-b). The left and right silt layers are referred to as Silt-1 and Silt-2 hereafter, and the three vertical coarse sand channels are referred to as Channel 1, Channel

2, and Channel 3 from left to right (Figure 4.1a-b). The setup was conceptually similar to that used by Sale et al. (2013). Sampling ports P1, P4 and P7 were located in Channel 1, P2, P5, P8 in Channel 2, and P3, P6, P9 were in Channel 3 (Figure 4.1b). Gradational horizontal layers at the inlet and outlet locations ensured that injected fluid was well distributed across the width and advective flow was primarily vertically upwards. The inlet was located within a 2.75 cm thick horizontal layer of glass beads (1.5 mm diameter, VWR International, Canada) followed by a 2.5 cm thick coarse sand and a 2 cm thick fine sand (d_{50} = 0.12 mm, K = 4.8 m/day, F110, Barco Silica sand) layers. The outlet was located within a 5.5 cm thick coarse sand horizontal layer above a 2 cm thick fine sand layer (Figure 4.1a-b). The upper, open end of the sandbox was sealed with a 5 cm thick layer of kaolinite clay (PSH, Oakville, Ontario, Canada).
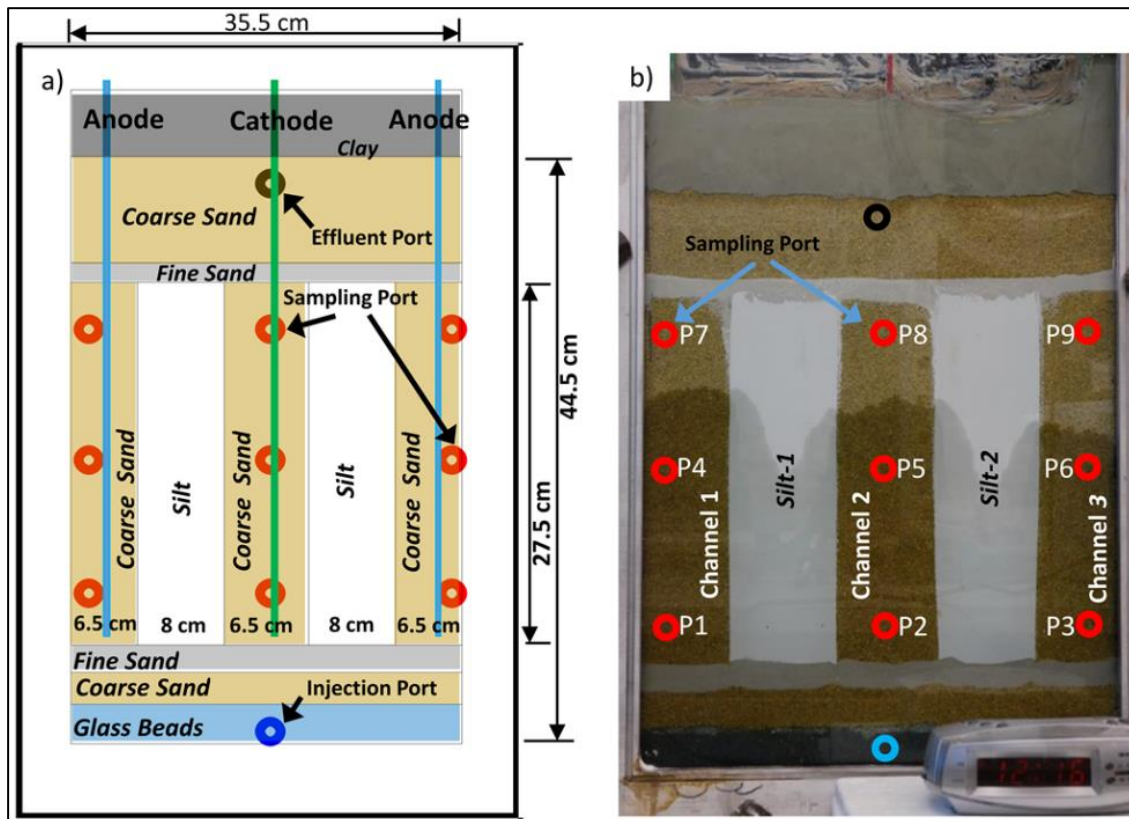
Figure 4.1: a) Schematic of experimental setup; b) actual sandbox packed with dry sand during the TCE solution flushing phase; red circles represent locations of sampling ports at the backside of the setup. Blue and black circles represent the injection and effluent ports, respectively.

The sandbox was packed twice in an identical manner, referred to as "a" and "b", in the experiment number (Table 4-1). The sandbox was packed an additional time to quantify geochemical changes (e.g., pH and ORP) due to EK. Calculated porosities were 0.30, 0.31 and 0.33 for sand packings a, b and the third packing, respectively. Two mixed metal oxide (MMO) anode electrodes (Titanium Electrode Products Inc, Stafford, Texas) were inserted into the left and right coarse sand channels while one MMO cathode electrode was inserted into the middle coarse sand channel (Figure 4.1a). The distance between each anode-cathode pair was 14 cm. The electrodes were connected to a DC power supply (BK Precision–1623A, USA).

4.3.2   Experimental methodology

A summary of the nine experiments performed is presented in Table 4-1. The "a" sand pack was employed for seven consecutive experiments without repacking; the order is noted in the experiment number because $MnO_{2(s)}$ precipitation slightly altered the in situ conditions between cases. The main experiment was ISCO+EK-25mA, in which 25 mA direct current (DC) was applied during PM injection. Hydraulic flushing experiments (no PM, no EK) were conducted before and after, as well as in packing "b". ISCO (no EK) experiments were also conducted both before and after, and again in packing "b", for comparison purposes.

A similar experimental procedure was used for each experiment. The dry packed sandbox was flushed with carbon dioxide (CO_2) gas for four hours. A stock solution with TCE at solubility (~900 mg/L) was prepared by equilibrating free phase TCE (Alfa Aesar, USA) with de-ionized (DI) water (EASYpure II, Model: D7401, Barnstead International, Iowa, USA) for at least three weeks prior to each experiment. In Phase 1 of each experiment (Table 4-1), the TCE solution was pumped into the dry sandbox through the bottom inlet port using a gear pump (Model no: 75211-30, Barnant Co., IL, USA) for 8 hrs (5.5 to 7 pore volumes (PV)) to ensure that the silt layers were water saturated and contaminated. In Phase 2 of each experiment, DI water was flushed for 10 hrs (Table 4-1) to sweep TCE from the coarse sand. Phases 3 and 4, the treatment stages, were different for each experiment.

Table 4-1: Injection schedule for all experiments

Experiment	TCE flush, Phase 1	DI flush, Phase 2	DI/PM flush, Phase 3	DI/PM/EK flush, Phase 4	DI flush, Phase 5	DI/PM flush, Phase 6	DI/PM/EK flush, Phase 7	DI/PM flush, Phase 8	No Flow, Phase 9	DI flush, Phase 10	No Flow, Phase 11	Purpose of the experiment
1a/b. Hydraulic flushing (Pre-EK, b)	8	10	4	8	138	148	96					Effect of hydraulic flushing i.e., dilution
6a. Hydraulic flushing (Post-EK)	8	10	4	50	263	1	76	4	160	192	120	
2a. ISCO(Pre-EK)+	8	10	4	8	138	148	96					Diffusive transport of PM and resulting TCE degradation
7a. ISCO(Post-EK)*	8	10	4	50	263	1	76	4	160	192	120	
3a. ISCO+EK-25mA*	8	10	4	50	263	1	76	4	160	192	120	EK enhanced PM delivery and resulting TCE degradation
2b. ISCO+EK-300mA+	8	10	4	24	138	136	96					
4a. EK-25mA	8	10	4	8	138	96						Effect of EK application on TCE degradation
5a. EK-300mA	8	10	4	20	138	12						

Green cells represent duration (hrs) of TCE flushing; blue cells represent durations (hrs) of DI water flushing; purple cells represent durations (hrs) of PM flushing; grey boxes represent durations (hrs) of no flow condition and black boxes represent durations (hrs) of EK application. +experiments with 10 g/L PM concentration; *experiment with 30 g/L PM concentration. Letter beside experiment number indicates sandbox packing (i.e., a or b).

In the hydraulic flushing experiments, Phases 3 to 7 involved flushing DI water at a specified flow rate to assess the extent of TCE rebound in the absence of any treatment (details in Tables 4-1 and 4-2). In the ISCO experiments with no EK, diffusive PM transport into the silt layers and impact on TCE concentrations in the absence of EK were evaluated. PM solution (10 or 30 g/L) was prepared by dissolving PM powder (Anachemia, Canada) in 30 °C DI water under continuous mixing with a magnetic stirrer at 200 rpm and stored in the dark until used. The PM stock concentration was measured before injecting into the sandbox. In ISCO and ISCO+EK experiments Phases 3 and 4 involved PM injection for 12 or 54 hrs without EK, while Phase 5 involved DI water flushing for specified durations (Table 4-1). A second PM injection was applied in several cases (see Tables 4-1 and 4-2 and further discussed below).

Phase 3 for the ISCO+EK-25mA experiment involved PM solution (30 g/L) flushing for 4 hrs without EK application. Phase 3 was followed by 50 hrs of PM flushing with EK enhanced transport (i.e., Phase 4) under a 25 mA (5.1 A/m^2 current density) current (Phase 4, Table 4-1). Following Phase 5 (263 hr DI water flushing), Phase 6 applied a second pulse of PM (30 g/L) for 1 hr without EK, 76 hrs with EK (Phase 7), and 4 hrs without EK (Phase 8), as listed in Table 4-1. Phase 9 then had no flow for 160 hrs. Phases 10, 11 and 12 involved alternating DI water flushing and no flow conditions (see Table 4-1). The experiment in total was 984 hrs, including 126 total hours of EK application and injection of 18 pore volumes of PM.

Typically, PM injection volumes comprising less than 10% of the treatment area pore volume are preferred to limit cost and avoid contaminant plume displacement (Stroo and Ward, 2010). The higher volume of remediant in the current study (18 PVs), resulting from the choice to continuously inject PM, was utilized for two purposes. First, it ensured that TCE was removed from the coarse sand layers so that the extent of TCE back diffusion from the silt layers could be quantified. Second, it minimized the geochemical changes resulting from applying EK application, ensuring that TCE degradation by PM could be quantified independently from geochemical impacts. It is acknowledged that injecting such large volumes of PM is atypical of field applications. In the field, only the electrode wells would be continuously purged with buffer solution to maintain a stable pH while PM would

be delivered through constant head supply wells. It should be noted that the ambient water flow in the current study was in the vertical direction (flowing from bottom to the top at an average pore water velocity of 10.8 m/day through the sandbox) and the PM migration into the silt layers was in the transverse direction due to EK application. This configuration is analogous to emplacement of horizontal electrodes for remediant delivery (Wu et al., 2013).

Experiment ISCO(Post-EK), reproduced the entirety of the ISCO+EK-25mA experiment but without EK application. Differences between ISCO(Pre-EK) and ISCO(Post-EK), were PM dosages (10 g/L for 12 hrs vs 30 g/L for 50 or 76 hrs, respectively) and flow conditions (e.g., single pulse vs two pulses, length of experiment, etc.) as shown in Tables 4-1. An additional experiment, ISCO+EK-300mA, was conducted to observe the impact of the much higher applied current on PM delivery and subsequent remediation. In this experiment, EK application caused gas formation (due to electrolysis of water) near the cathode, which blocked PM transport into the cathode channel. Therefore, the Channel 2 sampling ports were opened for 2 hrs after the PM+EK phase while DI water flushing was continued to remove the gas bubbles. In experiment ISCO+EK-25mA, gas formation was not observed.

Two additional experiments (EK-25mA and EK-300mA) were conducted in a manner similar to experiment ISCO+EK-25mA, except that DI water was used instead of PM to assess if contaminant removal was solely due to EK and not reaction with PM.

Previous studies have shown that EK application resulted in geochemical changes (including pH) of the solution (Acar and Alshawabkeh, 1993; Acar et al., 1995). Given that pH/ORP measurements require a finite sample volume (approximately 20 mL) to be removed from each sampling location, disrupting the flow field in the sandbox, no pH/ORP measurements were taken during the ISCO+EK experiment. Hence, an additional experiment was completed in which pH and ORP changes were monitored with a multimeter (Orion 5 Star, Thermo Scientific, USA) for 6 hrs while an electrolyte solution of sodium bromide (3.7 g/L) was continuously injected and EK was applied at two different currents (25 mA and 300 mA). No PM or TCE was present in the system, therefore, any geochemical changes were due to EK.

For all of the experiments, periodic water samples were collected with a gas tight syringe from the nine sampling ports within the coarse sand layers (Figure 4.1 a,b) to analyse for TCE concentration. The initial 0.35 mL sample was discarded to remove any residual liquid. From the second 0.35 mL sample collected from each location, 0.25 mL was immediately injected into a 1 mL hexane-filled GC vial. The vial was then mixed using a vortex mixer for 1 min and allowed to equilibrate for 2 hrs. The hexane was then collected using glass pipettes and TCE concentrations were analysed using a GC-ECD system (Agilent 7890A, Agilent, Santa Clara, CA). The method detection limit for TCE was 0.02 mg/L.

Image analysis was used to quantify the rate and mass of PM migration into the silt in all experiments and the extent of $MnO_{2(s)}$ precipitation in the coarse sand channels in select experiments. Details related to the image analysis procedure can be found in the supplementary information section (Appendix B, section 8.2).

4.4   Results and Discussion

4.4.1   Contaminant removal for hydraulic flushing experiments

The two hydraulic flushing experiments, hydraulic flushing a (Pre-EK) and hydraulic flushing b, involving TCE loading and then water flushing only, showed high reproducibility in the TCE concentration over time as indicated by the mean and 95% confidence interval (CI) of 18 sampling locations (nine from each experiment) (Figure 8.1). TCE concentrations throughout the coarse sand channels rapidly decreased during the first 48 hrs of DI water flushing and then showed lengthy tailing due to TCE diffusion from the silt layers. The average TCE concentration of the hydraulic flushing a (Pre-EK) experiment decreased from 571±74 mg/L (mean and 95% CI hereafter) at 8 hours to 4.4±1.8 mg/L at 48 hrs and finally to 0.89±0.25 mg/L at 408 hrs, representing a 2.8 OoM reduction in TCE concentrations between 8 hours and 408 hours. In this study all OoM reductions are benchmarked to the respective TCE concentrations at 8 hours (i.e., the end of TCE flushing phase for all experiments) in a given experiment as there were slight variations in TCE concentrations at 8 hours. TCE concentrations from the hydraulic flushing-b experiment

were similar to hydraulic flushing-a (Pre-EK) experiment. It is noted here that no sample was collected from the silt layers due to experimental setup limitations (e.g., silt removal through the sampling ports); therefore, a TCE mass balance could not be performed.

4.4.2   Permanganate delivery

PM migration into the silt layers during ISCO experiments was limited in the absence of EK (Figure 4.2, a,b). Image analysis shows that a sharp, high concentration PM front diffused approximately 1.5 cm into the silt after 12 hrs in the ISCO(Pre-EK) experiment, followed by a thin low concentration band, and then moving towards the sandbox center leaving approximately 4 cm of silt with no PM (Figure 4.3b, Figure 8.2). The ISCO(Post-EK) experiment, which ran much longer, achieved 2 cm and 3 cm of diffusive transport into the silt after 24 and 50 hrs of PM application, respectively (Figure 4.3c). This results in a diffusion rate of approximately $1.5 - 2$ cm/day. In comparison, Sale et al. (2013) observed a maximum of 1.3 cm PM penetration into silt over 27 days of flushing while Struse et al. (2002) observed diffusion of approximately 2.5 cm through silty-clayey soil over approximately 25 days. As expected, diffusion was approximately symmetrical on both sides of the silt layers. Continued forward PM diffusion as well as back diffusion into the coarse sand was observed during water flushing in these two experiments. The advective transport of PM into the silt was assumed to be negligible given the low hydraulic conductivity of the silt.
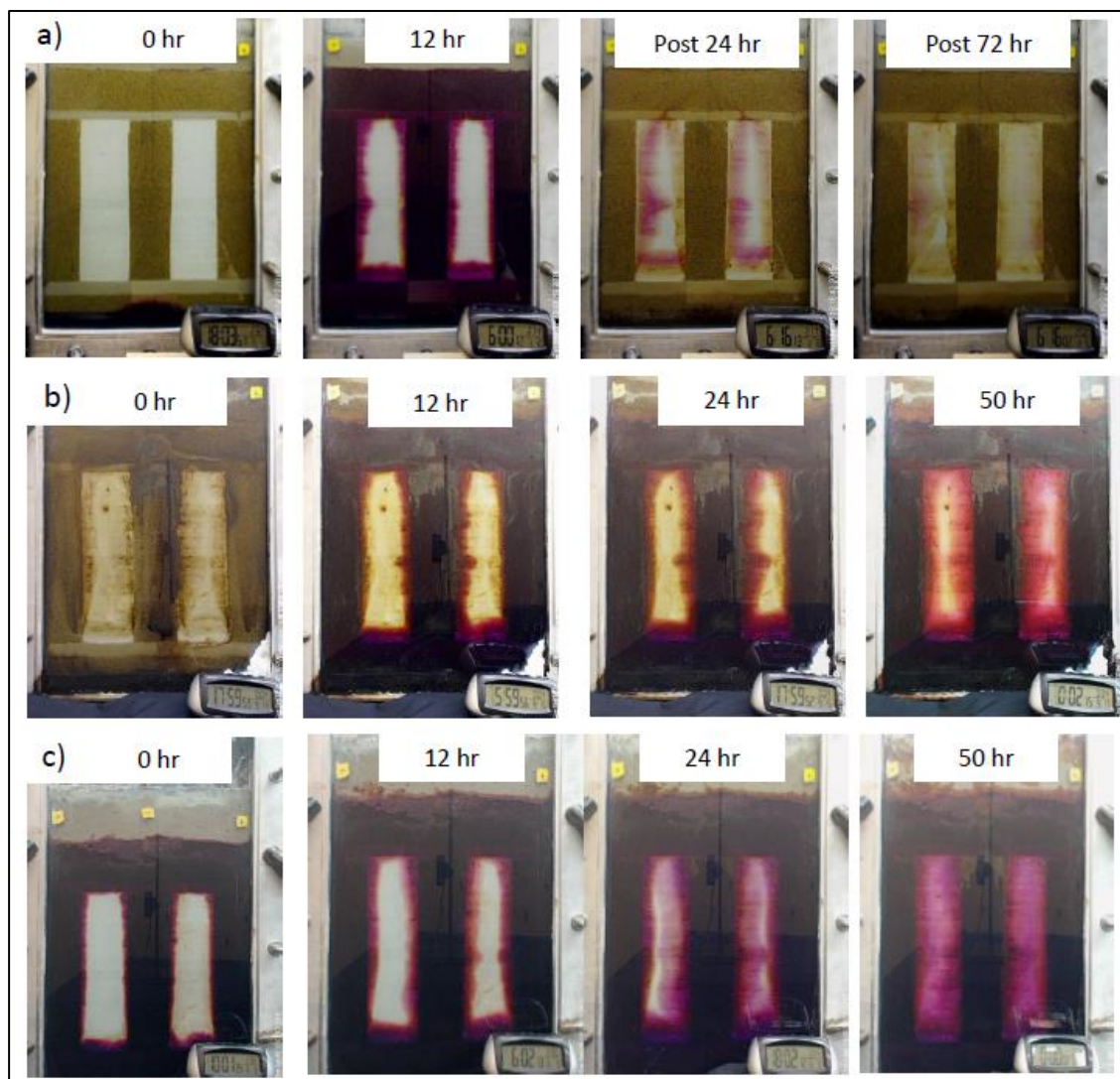
Figure 4.2: Visual observations of PM migration into the silt layers during a) ISCO(Pre-EK), b) ISCO(Post-EK) – Phase 4, and c), ISCO+EK-25mA – Phase 4; 0 hrs refers to the time when PM or EK+PM application started. Post hours refer to time after PM application stopped.

PM migration in the silt was faster and more extensive (from visual observation as well as image analysis data) when EK was applied (experiment ISCO+EK-25mA in Figure 4.2c). Silt layers from two sacrificial experiments conducted in a manner similar to those presented here were dissected providing visual evidence that PM migration was limited to the peripheral 1-2 cm in an ISCO only (i.e., PM flushing only) experiment while PM migration was observed to be more uniform and throughout the cross-section of silt layers

in a coupled EK+PM application (Figure 8.3). PM migrated as a sharp front primarily due to EM (i.e., from the cathode to the anode) similar to that observed in previous studies (Cang et al., 2013; Hodges et al., 2013; Hodges, 2010; Reynolds et al., 2008; Roach and Reddy, 2006; Thepsithar and Roberts, 2006). Image analysis shows that the PM front, at the injected concentration, travelled approximately 3.2 cm from the cathode side of the silt layer to the anode side in 12 hrs (Figure 4.3d); this corresponds to a migration rate of 6.4 cm/day (under a 0.3 V/cm voltage gradient with a constant current of 25 mA) but the migration rate slowed with time. The PM migration rate observed in the present study was higher than that of Hodges et al. (2013) who reported a migration rate of 2 cm/day with a 1.7 V/cm voltage gradient but smaller than that of Thepsithar and Roberts (2006) who reported 30-45 cm/day under a 1 V/cm voltage gradient. The higher transport rate in the present study might be due to application of a constant current (25 mA) as opposed to the constant voltage applied by Hodges et al. (2013) that resulted in decreasing current with time (from 14.6 mA to 9.2 mA in 12.9 days). Similar decreases in PM migration with time during EK application were observed by (Hodges et al., 2013; Roach and Reddy, 2006). Hodges et al. (2013) observed that PM migration stalled due to the pH gradient created by EK application and that eliminating the pH gradient significantly improved PM migration through clayey soil.
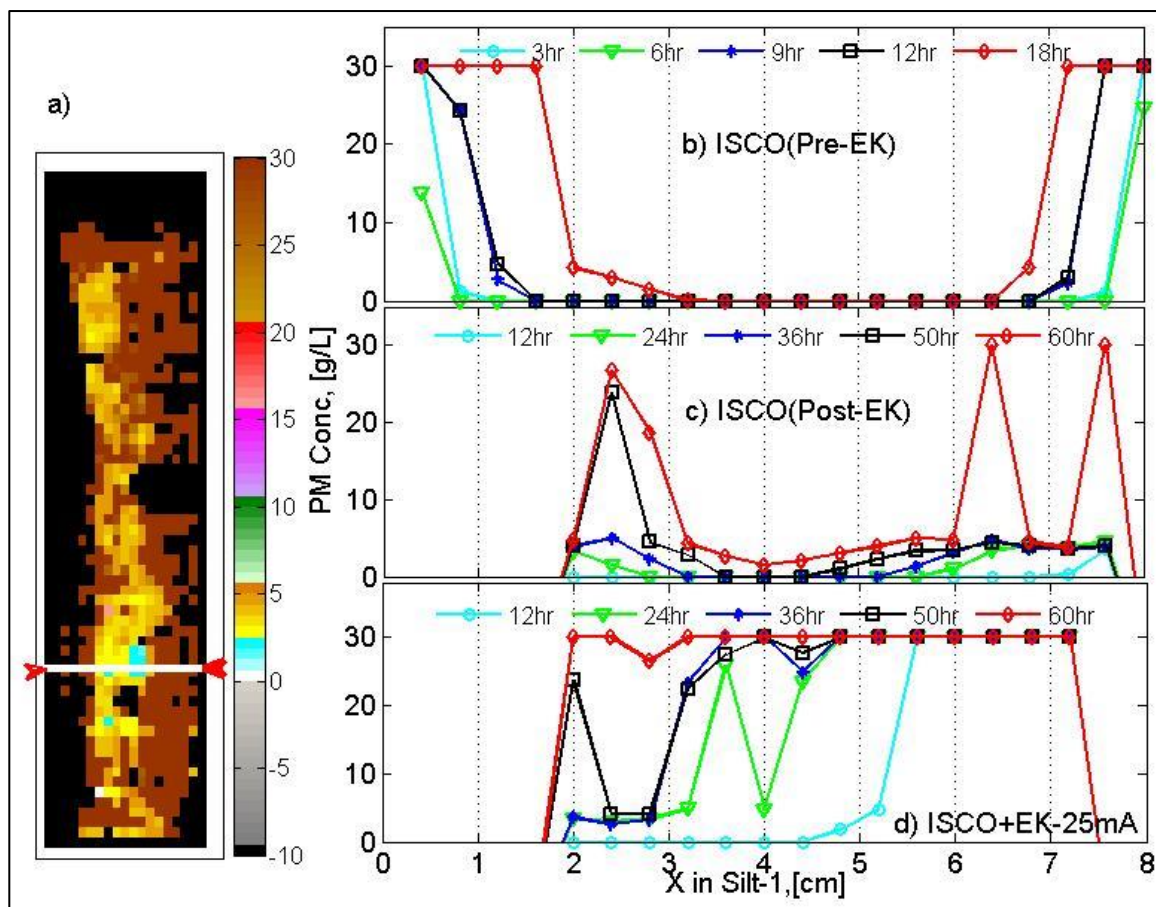
Figure 4.3: a) reconstructed image of left silt layer (Silt-1) after 50 hrs of EK+PM application during ISCO+EK-25mA experiment (original image shown in Figure (4.2b, 50 hrs)) where the color bar represents the PM concentrations in [g/L] as obtained from image analysis and related calibration. PM concentration profiles were created from such reconstructed images at a height of 7.5 cm (identified by the "white" horizontal line with red arrows) of this silt layer as shown in (a); b) PM concentration profile for ISCO(Pre-EK) experiment where 18 hrs refer to 6 hrs of DI flushing following 12 hrs of EK+PM application; c) PM concentration profile for Phase 4, ISCO(Post-EK) experiment; and d) PM concentration profile for Phase 4, ISCO+EK-25mA experiment. The negative PM concentration (-10 g/L) represents the areas with $MnO_{2(s)}$ precipitates that interfered with PM analysis, hence excluded from the analysis; 0 to 30 g/L in the color bar represents image analysis calibrated PM concentration. Timescale represents the time since PM/EK+PM application started.

Image analysis demonstrates that substantially more PM mass was delivered into the silt when EK was applied. Phase 4 of ISCO+EK-25mA delivered 1.2±0.1 g PM to each of the silt layers compared to 0.35±0.1 g for Phase 4 of ISCO (Post-EK) after 50 hrs (Figure 8.4).

This represents a 240% increase in PM mass delivery due to EK application relative to no EK experiment (i.e., ISCO alone).

The ISCO+EK-300mA experiment showed that PM migration was due to EO (i.e., from anodes towards the cathode at the center) as opposed to EM (i.e., from cathode towards the anodes on the sides) observed during the ISCO+EK-25mA experiment (Phase 4 and 7, Table 4-1). Such EO-induced transport was observed in a previous study by Roach and Reddy (2006). The different EK induced migration mechanisms observed in the ISCO+EK-300mA experiment were attributed to the application of a higher current (300 mA vs 25 mA in ISCO+EK-300mA and ISCO+EK-25mA experiments, respectively).

4.4.3   TCE concentration

In the ISCO experiments in the absence of EK, average TCE concentrations (of nine sampling locations) in the coarse sand channels decreased to below the method detection limit (MDL) throughout PM injection as the TCE in the coarse sand was oxidized and flushed out of the system (Figure 4.4). However, TCE concentrations rebounded, similar to observations of Sale et al. (2013), when PM injection stopped and DI water flushing resumed (Figure 4.4). For example, maximum TCE rebound concentrations were 1.9 mg/L (at 60 hrs) and 1.6 mg/L (at 120 hrs) for ISCO(Pre-EK) and ISCO(Post-EK), respectively. ISCO(Pre-EK) and ISCO(Post-EK) resulted in 3.1 and 3.2 OoM reductions in TCE concentration from the end of TCE loading (at 8 hrs), respectively, measured after 312 hrs. By comparison, the average TCE concentration of the hydraulic flushing(Pre-EK) experiment was reduced by 2.8 OoM after the same amount of time.

Results from ISCO(Post-EK) are used as a baseline to assess the performance of ISCO+EK-25mA as these experiments had similar experimental conditions (PM concentration, flushing duration, multiple PM injections, etc.). Similar to other ISCO experiments, during PM delivery in ISCO+EK 25mA (Figure 4.4) TCE concentrations decreased to non-detect followed by TCE concentration rebound when PM application ceased. However, given that EK delivered more PM into the silt layers (Section 4.4.2), it is not surprising that the maximum TCE rebound concentration after the 1st PM injection was much lower (0.70±0.1 mg/L at 108 hrs for ISCO+EK-25mA versus 1.6±0.3 mg/L at 120 hrs ISCO(Post-EK)).

Final TCE concentrations at the end of Phase 5 water flush (335 hrs) for ISCO+EK-25mA and ISCO(Post-EK) were 0.17±0.05 and 0.44±0.14 mg/L, respectively. However, these concentrations were still 1.5 and 1.9 OoM higher than MCL, respectively, suggesting further treatment was necessary.
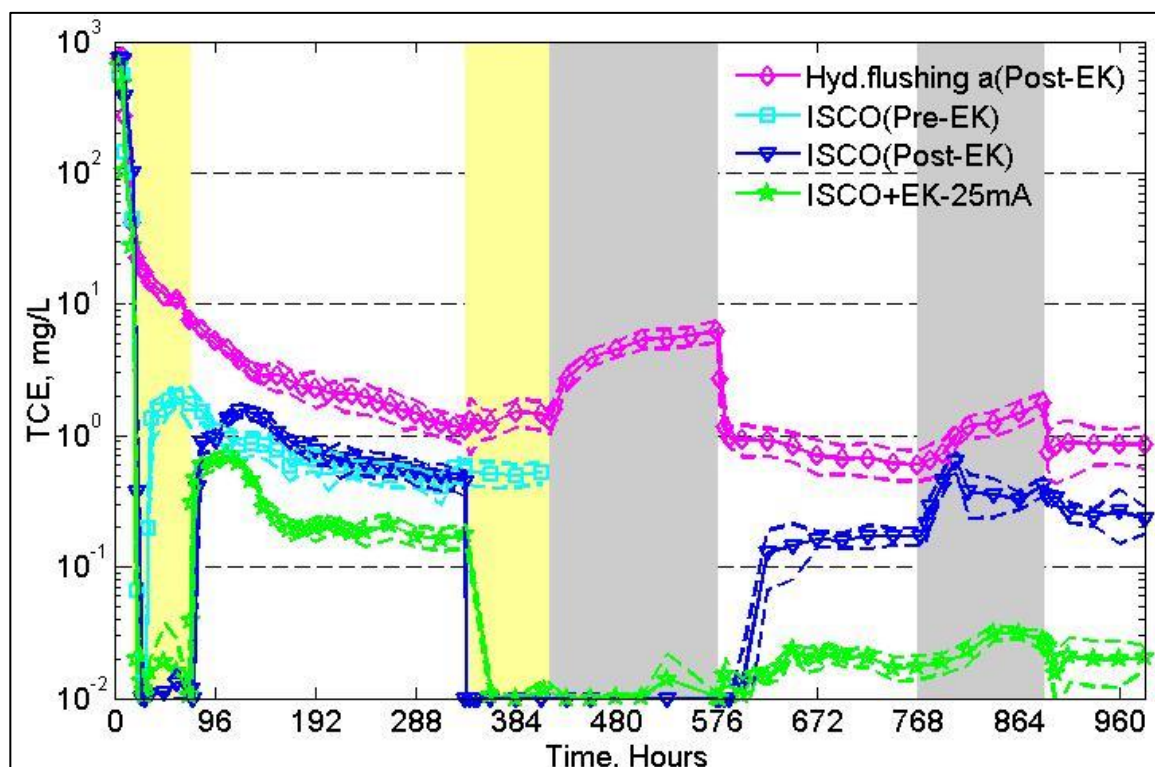
Figure 4.4: Observed average TCE concentrations (with 95% CI) of the nine (9) sampling ports located within the coarse sand (in Figure 4.1a, b) with time for different experiments Regions marked within yellow boxes represent "PM/PM+EK" applications except for ISCO(Pre-EK) experiment while regions within gray boxes represent "no flow" conditions.

To pursue aggressive treatment, a 2nd PM pulse (i.e., Phase 7) was applied including a 160 hr no flow period for both ISCO(Post-EK) and ISCO+EK-25mA, the latter with EK applied throughout (Tables 4-1). Applying a second PM pulse and including a no-flow period in the ISCO(Post-EK) experiment increased the reaction time between PM and TCE. Following this, when DI water flow was resumed, the TCE concentration rebounded to much lower levels for ISCO+EK-25mA (0.024±0.002 mg/L at 648 hr) while rebound was much higher for ISCO(Post-EK) (0.16±0.02 mg/L at 672 hrs) (Figure 4.4). A second no flow condition, between 768 and 888 hrs, (Table 4-1) was imposed during water flushing

to assess maximum TCE rebound. At the end of the experiment, at 984 hrs (41 days), ISCO+EK-25mA had TCE concentrations of 0.021±0.004 mg/L which corresponds to a 4.4 OoM reduction in TCE concentration. By comparison ISCO(Post-EK) resulted in a 3.5 OoM reduction in TCE concentration. Sale et al. (2013) observed a 3.1 OoM reduction in TCE concentration during the chemical oxidation experiment after 189 days. The current results show a further 0.9 OoM reduction in TCE concentration due to EK enhanced PM transport. It is acknowledged that pore water velocities and pore volumes flushed differ between this and the Sale et al. (2013) studies (3-11 m/d and 670 PVs compared to 0.33 m/d and 82 PVs, respectively). The higher pore water velocity and pore volume flush was used in the current study to observe the impact of aggressive hydraulic flushing schemes on TCE concentration reduction.

$MnO_{2(s)}$ precipitate was formed during ISCO+EK-25mA in both the sand and silt channels. Image analysis on the sand (Figure 8.6a) indicates that 16%, 13% and 11% (areal coverage) of Channels 1, 2 and 3, respectively, contained precipitate at the end of Phase 4. This increased to 26%, 31% and 22%, respectively, at the end of Phase 7 (Figure 8.6b). To evaluate the impact of $MnO_{2(s)}$ on TCE transport an additional hydraulic flushing experiment was conducted, hydraulic flushing(Post-EK), following ISCO+EK-25mA and with its precipitated $MnO_{2(s)}$ present. Average TCE concentrations in this hydraulic flushing experiment were similar to the average of the two other hydraulic flushing experiments including at late times (between 120 and 408 hrs) (Figure 4.4 and Figure 8.5). These results suggest that $MnO_{2(s)}$ had negligible impact on TCE transport, and the additional TCE concentration reductions observed for ISCO+EK-25mA were due to remediation of the silt.

ISCO+EK-300mA was conducted in a new similar sand packing, with a higher current (300 mA) and lower PM concentration (10 g/L), compared to ISCO+EK-25mA (25 mA and 30 g/L), to assess the impact of PM concentration and EK current on TCE degradation. TCE concentrations at the anode locations (mean of Channel 1 and 3 – Figure 8.5) in ISCO+EK-300mA experiment were much higher than that at the cathode location. For example, the average TCE concentration was 2.2±1.4 mg/L at the anode locations compared to 0.17±0.05 mg/L at the cathode location after 336 hours in this experiment. Interestingly, TCE concentrations at the cathode in ISCO+EK-300mA were similar to ISCO+EK-25mA

at the end of Phase 4 (Figure 4.4 and 8.5). As shown in Figure (8.6c) 60% and 39% of the Channel 1 and 3 (anodic) sand layers, respectively, had measureable $MnO_{2(s)}$ precipitate at 408 hours in ISCO+EK-300mA. By comparison only 9% of Channel 2 (cathodic) sand had measureable $MnO_{2(s)}$ precipitate, potentially leading to observed differences in TCE concentration (Figure 8.5). Channel 2 had less precipitate due to gas evolution during EK application (due to electrolysis of water) blocking PM flow, a precursor to $MnO_{2(s)}$ precipitate formation.

The precipitation at the anodic sand layers likely impacted the flow field, reducing the permeability of the coarse sand (Heiderscheidt et al., 2008; Henderson et al., 2009; Hood, 2000; Mahinthakumar and West, 1997; Reitsma and Dai, 2001; West et al., 2008; West and Kueper, 2012; Zhang and Schwartz, 2000). As such less fresh water flux would be expected through Channels 1 and 3 in comparison to Channel 2. This would result in less TCE dilution in Channels 1 and 3 relative to the Channel 2, potentially explaining the observed TCE concentration results. As discussed in Section 4.4.2, this more aggressive EK application resulted in low pH/high ORP and high pH/low ORP conditions at the anode and cathode locations, respectively. H^+ ions (i.e., low pH front) would have migrated towards the cathode through the silt layer due to EM as well as EO. Such low pH/high ORP (i.e., oxidizing) conditions might have impacted PM-TCE reactivity or might have inactivated PM. Evaluation of this hypothesis is beyond the scope of current study and merits further investigation. Less $MnO_{2(s)}$ precipitation was observed during ISCO+EK-25mA experiment compared to ISCO+EK-300mA experiment. It is also noted that TCE concentrations at the anode and cathode locations in the ISCO+EK-25mA experiment (Phase 4) were similar potentially due to limited precipitation of $MnO_{2(s)}$.

Two additional experiments, EK-25mA and EK-300mA, were conducted to evaluate the possibility of TCE degradation or TCE migration due only to applied current. The average TCE concentrations, as measured from the nine sampling locations for each of these two experiments, were similar to the average of two hydraulic flushing experiments (Figure 8.5). Additionally, similar TCE concentrations were observed at the cathode and anode locations for these two experiments. This suggests that the degradation observed during the ISCO+EK-25mA experiment was due to EK enhanced PM delivery, and subsequent

reaction, and not due to the EK application alone. Moreover, it suggests that EK application did not lead to concentration differences at the anode and cathode locations.

4.4.4   EK-induced geochemical changes

Two experiments were conducted to evaluate changes in pH and ORP due to EK application. Since no PM or TCE was present, all geochemical changes were associated with EK. The average pH at the anodes (Channels 1 and 3) decreased from 6.5 to 3.1 in the first hour following EK initiation while pH at the cathode (Channel 2) increased from 7 to 11.6.   These changes were consistent at both currents examined (i.e., 25 and 300 mA) (Figure 8.7). ORP increased from 210 mV to 1244 mV at the anode for both currents while it decreased to -235 mV in the 25 mA case and -615 mV in the 300 mA case. These results are consistent with previous EK studies (Acar and Alshawabkeh, 1993; Acar et al., 1995; Chowdhury et al., 2012).

4.5   Conclusions

Remediation of contaminants in low permeability zones remains an unresolved challenge limiting attainment of remediation endpoints and site closure. This study supports previous work in demonstrating that EK can significantly enhance PM delivery into low permeability strata. This study is unique in demonstrating that EK-enhanced PM delivery resulted in improved treatment of TCE mass in these strata, thereby reducing back diffusion and decreasing TCE concentrations in the higher permeability strata in the long term. Final TCE concentrations were only 0.6 OoM above the MCL for the EK-enhanced ISCO experiments compared to 1.7 OoM above MCL for ISCO alone. This work demonstrate that TCE concentrations can be lowered by application of multiple EK+PM pulses. Further work is required to determine optimal remediation designs. For example, application of the 300 mA current appeared to cause excessive $MnO_{2(s)}$ precipitate formation whereas 25 mA avoided excessive precipitation. The most appropriate current, as well as numerous other implementation parameters (e.g., PM dose, electrode arrangement) need to be assessed in a pilot field test, which is planned.

The current study implies that EK can be used to enhance permanganate mass delivery through low permeability soils. The higher permanganate mass delivered by EK can significantly reduce contaminant concentrations sequestered in low permeability soils, limiting the extent of back diffusion from such soils. Moreover, multiple pulses of EK-induced permanganate transport can potentially aid the achievement of site closure requirements that otherwise would not be practical.

Acknowledgements

4.6 References

Acar, Y.B. and Alshawabkeh, A.N., 1993. Principles of Electrokinetic Remediation. Environmental Science & Technology, 27(13).

Acar, Y.B. et al., 1995. Electrokinetic remediation: Basics and technology status. Journal of Hazardous Materials, 40: 117-137.

Baciocchi, R., D'Aprile, L., Innocenti, I., Massetti, F. and Verginelli, I., 2014. Development of technical guidelines for the application of in-situ chemical oxidation to groundwater remediation. Journal of Cleaner Production, 77(0): 47-55.

Ball, W.P., Liu, C., Xia, G. and Young, D.F., 1997. A diffusion-based interpretation of tetrachloroethene and trichloroethene concentration profiles in a groundwater aquitard. Water Resources Research, 33(12): 2741-2757.

Cang, L., Fan, G.-P., Zhou, D.-M. and Wang, Q.-Y., 2013. Enhanced-electrokinetic remediation of copper–pyrene co-contaminated soil with different oxidants and pH control. Chemosphere, 90(8): 2326-2331.

Chapman, S.W. and Parker, B.L., 2005. Plume persistence due to aquitard back diffusion following dense nonaqueous phase liquid source removal or isolation. Water Resources Research, 41(12).

Chowdhury, A.I.A., O'Carroll, D.M., Xu, Y. and Sleep, B.E., 2012. Electrophoresis enhanced transport of nano-scale zero valent iron. Advances In Water Resources, 40(0): 71-82.

Fetter, C.W., 2001. Applied Hydrogeology. Prentice Hall, NJ.

Gerhard, J.I., Kueper, B.H. and Sleep, B.E., 2014. Modeling source zone remediation. In: H.B. Kueper, F.H. Stroo, M.C. Vogel and H.C. Ward (Editors), Chlorinated Solvent Source Zone Remediation. Springer New York, New York, NY, pp. 113-144.

Heiderscheidt, J.L., Crimi, M., Siegrist, R.L. and Singletary, M.A., 2008. Optimization of Full-Scale Permanganate ISCO System Operation: Laboratory and Numerical Studies. Ground Water Monitoring & Remediation, 28(4): 72-84.

Henderson, T.H., Mayer, K.U., Parker, B.L. and Al, T.A., 2009. Three-dimensional density-dependent flow and multicomponent reactive transport modeling of chlorinated solvent oxidation by potassium permanganate. Journal of Contaminant Hydrology, 106(3-4): 195-211.

Hodges, D., Fourie, A., Thomas, D. and Reynolds, D., 2013. Overcoming Permanganate Stalling during Electromigration. Journal of Environmental Engineering, 139(5): 677-684.

Hodges, D.J., 2010. Permanganate Electromigration in Low Permeability Media, The University of Western Australia, 243 pp.

Hood, E.D., 2000. Permanganate Flushing of DNAPL Source Zones: Experimental and Numerical Investigation, University of Waterloo, Waterloo, Ontario, Canada.

Kao, C.M., Huang, K.D., Wang, J.Y., Chen, T.Y. and Chien, H.Y., 2008. Application of potassium permanganate as an oxidant for in situ oxidation of trichloroethylene-contaminated groundwater: A laboratory and kinetics study. Journal of Hazardous Materials, 153(3): 919-927.

Li, X.D. and Schwartz, F.W., 2004a. DNAPL mass transfer and permeability reduction during in situ chemical oxidation with permanganate. Geophysical Research Letters, 31(6): L06504.

Li, X.D. and Schwartz, F.W., 2004b. DNAPL remediation with in situ chemical oxidation using potassium permanganate: II. Increasing removal efficiency by dissolving Mn oxide precipitates. Journal of Contaminant Hydrology, 68(3–4): 269-287.

Liu, C. and Ball, W.P., 2002. Back Diffusion of Chlorinated Solvent Contaminants from a Natural Aquitard to a Remediated Aquifer Under Well-Controlled Field Conditions: Predictions and Measurements. Ground Water, 40(2): 175-184.

Mahinthakumar, G. and West, O.R., 1997. High Resulation Numerical Simulations in Support of ISCOR Experiment at Portsmouth, Oak Ridge National Laboratory, Oak Ridge, Tenn.

NRC, N.R.C., 2005. Contaminants in the subsurface: Source zone assessment and remediation. Committee on Source Removal of Contaminants in the Subsurface. The National Academic Press, Washington, D.C.

Parker, B.L., Chapman, S.W. and Guilbeault, M.A., 2008. Plume persistence caused by back diffusion from thin clay layers in a sand aquifer following TCE source-zone hydraulic isolation. Journal of Contaminant Hydrology, 102(1–2): 86-104.

Petri, B. et al., 2011. Fundamentals of ISCO Using Persulfate. In: R.L. Siegrist, M. Crimi and T.J. Simpkin (Editors), In Situ Chemical Oxidation for Groundwater Remediation. SERDP/ESTCP Environmental Remediation Technology. Springer New York, pp. 147-191.

Reitsma, S. and Dai, Q.L., 2001. Reaction-enhanced mass transfer and transport from non-aqueous phase liquid source zones. Journal of Contaminant Hydrology, 49(1–2): 49-66.

Reynolds, D.A., Jones, E.H., Gillen, M., Yusoff, I. and Thomas, D.G., 2008. Electrokinetic Migration of Permanganate Through Low-Permeability Media. Ground Water, 46(4): 629-637.

Roach, N. and Reddy, K.R., 2006. Electrokinetic Delivery of Permanganate into Low-Permeability Soils. International Journal of Environment and Waster Management, 1(1): 4-16.

Robertson, T., 2009. Electrokinetic Transport of Persulfate under Voltage Gradients.

Sale, T., Parker, B.L., Newell, C.J. and Devlin, J.F., 2013. Management of Contaminants Stored in Low Permeability Zones - A State of the Science Review, SERDP/ESTCP, Alexandria, VA, USA.

Sale, T.C. et al., 2007. Unpublished Report on AFCEE Source Zone Initiative.

Schnarr, M. et al., 1998. Laboratory and controlled field experiments using potassium permanganate to remediate trichloroethylene and perchloroethylene DNAPLs in porous media. Journal of Contaminant Hydrology, 29(3): 205-224.

Schroth, M.H., Oostrom, M., Wietsma, T.W. and Istok, J.D., 2001. In-situ oxidation of trichloroethene by permanganate: effects on porous medium hydraulic properties. Journal of Contaminant Hydrology, 50(1–2): 79-98.

Seyedabbasi, M.A., Newell, C.J., Adamson, D.T. and Sale, T.C., 2012. Relative contribution of DNAPL dissolution and matrix diffusion to the long-term persistence of chlorinated solvent source zones. Journal of Contaminant Hydrology, 134–135: 69-81.

Siegrist, R., Crimi, M. and Brown, R., 2011. In Situ Chemical Oxidation: Technology Description and Status. In: R.L. Siegrist, M. Crimi and T.J. Simpkin (Editors), In Situ Chemical Oxidation for Groundwater remediation. SERDP/ESTCP Environmental Remediation Technology. Springer New York, pp. 1-32.

Struse, A., Siegrist, R., Dawson, H. and Urynowicz, M., 2002. Diffusive Transport of Permanganate during In Situ Oxidation. Journal of Environmental Engineering, 128(4): 327-334.

Thepsithar, P. and Roberts, E.P.L., 2006. Removal of Phenol from Contaminated Kaolin Using Electrokinetically Enhanced In Situ Chemical Oxidation. Environmental Science & Technology, 40(19): 6098-6103.

Waldemer, R.H. and Tratnyek, P.G., 2005. Kinetics of Contaminant Degradation by Permanganate. Environmental Science & Technology, 40(3): 1055-1061.

West, M.R., Grant, G.P., Gerhard, J.I. and Kueper, B.H., 2008. The influence of precipitate formation on the chemical oxidation of TCE DNAPL with potassium permanganate. Advances in Water Resources, 31(2): 324-338.

West, M.R. and Kueper, B.H., 2012. Numerical simulation of DNAPL source zone remediation with in situ chemical oxidation (ISCO). Advances In Water Resources, 44(0): 126-139.

Yan, Y.E. and Schwartz, F.W., 2000. Kinetics and Mechanisms for TCE Oxidation by Permanganate. Environmental Science & Technology, 34(12): 2535-2541.

Yeung, A.T., 2011. Milestone developments, myths, and future directions of electrokinetic remediation. Separation and Purification Technology, 79(2): 124-132.

Zhang, H. and Schwartz, F.W., 2000. Simulating the in situ oxidative treatment of chlorinated ethylenes by potassium permanganate. Water Resources Research, 36(10): 3031-3042.

Chapter 5

5   Aqueous PCE Remediation in Silt via Persulfate
     Delivered by Electrokinetics and Activated by Electrical
     Resistance Heating: Proof of Concept

Ahmed I. A. Chowdhury[a], Jason I. Gerhard[a], David Reynolds[b], Denis M. O'Carroll[a,*]

[a] Department of Civil and Environmental Engineering, Western University, 1151 Richmond St., London, ON, Canada. N6A 5B9

[b] Geosyntec Consultants, 130 Stone Road W., Guelph, ON, Canada. N1G 3Z2

Keywords: electrokinetics, persulfate, ISCO, thermal activation, electrical resistance heating, ERH, low permeable zone, PCE, remediation.

5.1 Introduction

Transport of constituents in low permeability zones is dominated by diffusion-limited mass transport. As such, low permeability zones can store significant contaminant mass over extended periods (i.e., since a historical release) and slowly release that mass into adjacent, more permeable zones (i.e., back diffusion). Low permeability zones can therefore act as long term sources of contamination even after adjacent permeable media has been remediated (Ball et al., 1997; Chapman and Parker, 2005; Liu and Ball, 2002; Parker et al., 2008; Sale et al., 2007; Seyedabbasi et al., 2012). Traditional remediation technologies that target permeable strata via injection (i.e., advection) of fluids (e.g., in-situ chemical oxidation (ISCO)) are unable to adequately penetrate, and therefore remediate, low permeability zones (Sale et al. (2013). Therefore, it is necessary to develop methods to remediate low permeability zones to comply regulatory standards at contaminated sites (Sale et al., 2013).

ISCO is a remediation technology where an oxidant is injected into the subsurface to intercept and react with the contaminant (Baciocchi et al., 2014; Siegrist et al., 2011). Use of persulfate (PS) ($S_2O_8^{2-}$) has gained much interest due to its high reduction potential ($E_o = 2.01\ V$), its stability in aqueous solution at neutral pH, and the production of non-toxic by-products after reaction with chlorinated solvents (House, 1962; Petri et al., 2011a; Tsitonaki et al., 2010). PS can react with the contaminant by direct electron transfer via self-decomposition or, after activation, can produce free radicals (e.g., $SO_4^{-\bullet}$); the latter reactions are faster (Petri et al., 2011a) since $SO_4^{-\bullet}$ is a more aggressive oxidant ($E_o = 2.6$ V) (Tsitonaki et al., 2010). It is noted here that PS self-decomposition should be able to degrade contaminants at a very slow rate; therefore activated PS is preferred.

PS can activated using heat, ultra-violet light, high pH (>11), hydrogen peroxide, or dissolved or chelated metals (e.g., Fe^{2+}) (Costanza et al., 2010; Petri et al., 2011a; Yukselen-Aksoy and Reddy, 2012). Some studies examine activation effectiveness by quantifying contaminant degradation. For example, Fan et al. (2016) observed more polychlorinated biphenyls (PCBs) degradation from high pH activation of PS compared to other methods. Heat activation of PS was not evaluated in this study. Other studies quantify

PS activation by measuring PS disappearance in the absence of contaminants. Additionally, most studies examine PS activation in ideal systems, using continuously stirred reactors with no soil (Costanza et al., 2010; Huang et al., 2002a; Huang et al., 2005; Liang et al., 2003; Waldemer et al., 2007; Zhao et al., 2013). At elevated temperatures PS decomposes to reactive sulfate radicals (SO_4^-•) (House, 1962; Kolthoff and Miller, 1951):

$$S_2O_8^{2-} \xrightarrow{heat} 2SO_4^{-•} \qquad\qquad \text{(Equation 5.1)}$$

SO_4^-• initiates a chain of reactions producing reactive intermediates (e.g., hydroxyl radicals ($OH^•$) and peroxymonosulfate (HSO_5^-)) (Berlin, 1986; Dahmani et al., 2006; Huang et al., 2002a; Waldemer et al., 2007). The activation energy (E_a) for PS decomposition is reported to be between 118 and 140.2 kJ/mol in systems with just water and 120±7 kJ/mol in systems that included soil (House, 1962; Johnson et al., 2008; Kolthoff and Miller, 1951). Similar E_a in systems with and without soil suggest that E_a for thermal activation of PS is independent of the presence of soil. Dissolved phase activators such as Fe^{2+} or alkaline solutions require that both the PS and activator ions come into contact to activate PS. The presence of soil would affect mixing and collisions between PS and activators, resulting in different rate constants and E_a. In contrast, application of heat is relatively more uniform in comparison to other activation methods.

Thermally activated PS has been employed to degrade a number of contaminants in batch experiments (Costanza et al., 2010; Huang et al., 2002a; Huang et al., 2005; Liang et al., 2003; Waldemer et al., 2007; Zhao et al., 2013). For example PS has been proposed to degrade tetrachloroethene (PCE) as follows (Costanza et al., 2010):

$$S_2O_8^{2-} + 2C_2Cl_4 + 8H_2O \rightarrow 2SO_4^{-2} + 8Cl^- + 4CO_2 + 10H^+ + 3H_2 \qquad \text{(Equation 5.2)}$$
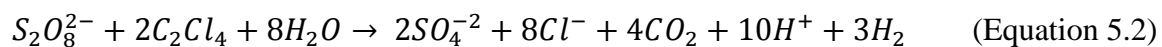
It is noted here that the reaction given by Equation (5.2) involves the generation of reactive sulfate radicals (SO_4^-•) that reacts with PCE. Therefore, the reaction is dependent on the availability of SO_4^-• upon activation. Previous studies demonstrated that the observed rate constants (determined from PCE concentration data after PS- PCE reaction for 80 min) in stirred reaction vials with water, F-70 sand and kaolinite clay were approximately 80, 12 and 3 d^{-1}, respectively, at 50 °C (Costanza et al., 2010). Therefore, it is reasonable to expect

that PS-contaminant reaction kinetics will be slower in the subsurface in comparison to constantly stirred-reactor conditions. Although PS has the potential to degrade contaminants difficulties in transporting any remediant (e.g., oxidants) through low permeability soil has to date limited remedial success in low permeability zones.

The use of electrokinetics (EK) for enhanced remediant delivery to low permeability zones has been investigated in the literature (Chowdhury et al., 2012; Hodges et al., 2013; Reynolds et al., 2008; Roach and Reddy, 2006; Robertson, 2009). EK is the application of a low voltage direct current (DC) across two or more electrodes (positive/anode and negative/cathode) inducing two important transport mechanisms (Acar and Alshawabkeh, 1993). Electromigration (EM) is the transport of ionic species in bulk solution. For example, PS will be repelled by the cathode and migrate to the anode through EM due to its negative charge. Electroosmosis (EO) results in bulk pore fluid, including dissolved species, migration in the opposite direction (i.e., anode to cathode) (Acar and Alshawabkeh, 1993). EK-induced transport mechanisms are independent of the intrinsic permeability of a porous medium. Therefore, EK has significant potential for delivering remediants into low permeability zones. As such it has generated considerable interest for the EM of PS into low permeability soils.

EK-induced PS transport has been examined in a number of laboratory-scale studies (Cang et al., 2013; Fan et al., 2014; Fan et al., 2016; Robertson, 2009; Yang and Yeh, 2011; Yukselen-Aksoy and Reddy, 2013; Yukselen-Aksoy and Reddy, 2012). Robertson (2009) reported an EM-induced transport rate of 1.5 cm/day through clayey soil based on the appearance of approximately 1 g/L PS at the anode. Similar transport rate (1.3 cm/day) was observed by Fan et al. (2014) suggesting that EK can deliver PS into low permeability zones. However, delivery of aqueous-based PS activators (e.g., alkaline solution, dissolved or chelated metals) into low permeability zones poses an additional challenge. Hence, thermal activation, with temperatures between 30-60 °C, is a promising alternative for activating EK-delivered PS to low permeability zones (Petri et al., 2011a) since heat transport is not influenced by intrinsic permeability. This has been examined to a limited extent by Yukselen-Aksoy and Reddy (2013) who used EK-induced PS transport and then heated their experimental system using silicone heating tape. This heating approach,

however, cannot be used in the field. Waldemer et al. (2007) proposed thermal activation of PS using in-situ thermal remediation (ISTR). Electrical resistance heating (ERH), a form of ISTR, applies an alternating current (AC) across electrodes with soil resistance causing in situ heating (Krol et al., 2011; Vermeulen and McGee, 2000). ERH has been applied for subsurface remediation, including low permeability zones, where the subsurface is heated to temperatures between 60 and 110 °C (Kingston et al., 2010). In those studies, ERH was used to volatilize contaminants. To the author's knowledge, ERH has never been used for thermal activation of PS. Here, it is proposed that low temperature ERH can thermally activate PS delivered by EK.

This work presents a proof-of-concept of PS oxidation of chlorinated solvent-contaminated low permeability soil where EK was used to deliver the PS followed by ERH for heat activation. The specific objectives were to: (i) investigate the extent of EK-assisted PS delivery through fine grained porous media, (ii) evaluate the ability of ERH to activate PS, and (iii) quantify the resulting PCE degradation. To this end a two-dimensional, multi-stage, 90 days long bench-top experiment was conducted. This study provides the basis for up-scaling this novel technology for remediation of contaminated low permeability zones.

5.2 Experimental Methodology

All experiments were conducted in a custom built 2D sandbox (workable area of 36 cm × 15 cm × 10 cm) made of acrylic (1.5 cm thick) panels with a water-tight top cap (Figure 5.1). The porous medium was contained in the central part of the sandbox and was attached to two cells, the "anode" (left) and "cathode" (right) cells, each having 5L liquid capacity (Figure 5.1). The left and right ends of the soil compartment were fitted with 0.45 µm polypropylene filters with O-rings. PVC tubing (0.64 cm inner diameter) connected to the bottom of the anode and cathode cells provided constant head in the cells and allowed delivery of aqueous solutions.

Six sampling ports, with luer lock valves (Figure 5.1) were installed on the front panel of the central soil compartment to collect aqueous samples from the soil. In addition, four thermocouples (Dial Thermometers, Taylor, NM, USA) were installed. The exposed metal portions outside the soil were insulated with silicon.

A stock solution with dissolved PCE (~70 mg/L) was prepared by equilibrating free phase PCE (Alfa Aesar, MA, USA) in buffered de-ionized (DI) water (EASYpure II, Model: D7401, Barnstead International, Iowa, USA) for two weeks prior to the experiment. 1.3 g/L of mono and di-basic phosphate salts (Anachemia, Canada) were dissolved into the DI water to prepare the buffer solution.
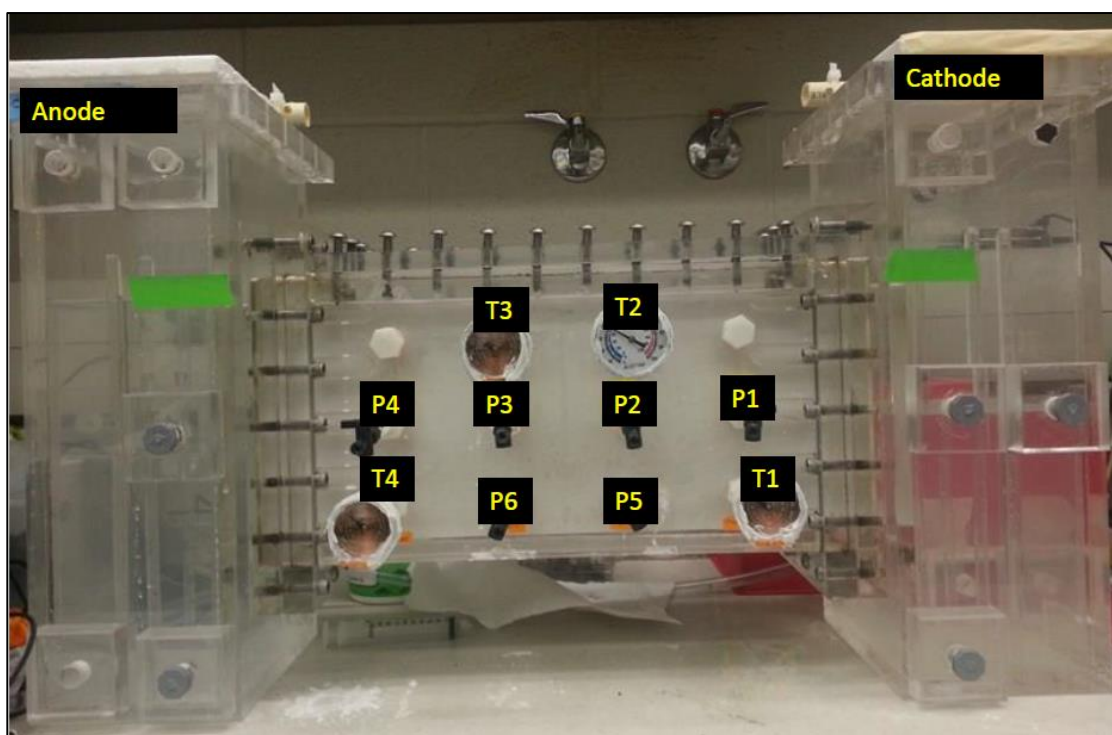
Figure 5.1: Photograph of 2D experimental setup where P1 to P6 refer to sampling ports and T1 to T4 represent the installed thermocouples.

The sandbox was filled using a wet packing method. Dry fine silt (Sil-Co-Sil 106, US Silica, $d_{50} = 0.045$ mm, K = 0.2 m/day) was added to the soil compartment in approximately 2 cm height increments. A gear pump (Model no: 75211-30, Barnant Co., IL, USA) was used to inject aqueous PCE stock solution into the silt layer to a height of approximately 4 cm. The silt was then allowed to settle in the aqueous PCE solution for two hours and gently tapped with a custom built Teflon hammer to further compact the silt layer. These steps were repeated until the soil compartment was full. Additional dry silt was added before the top cap was compressed into place to ensure no void space in the systems. Estimated soil porosity was 0.41.

A stock buffer solution with no PCE was constantly injected into the anode and cathode cells while packing the soil compartment. However, the solution levels in the anode/cathode cells were maintained below the silt height in the soil compartment. This minimized infiltration of the buffer solution into the soil compartment which would have diluted PCE in the silt. The head in the anode and cathode cells was raised to 2 cm above the silt once the soil compartment was sealed as such there was no head gradient. This head was maintained throughout the experiment. The sandbox was allowed to equilibrate for 5 days following packing.

A 22L buffer solution (same recipe as above) was prepared in a 26L container (referred to as the anode reservoir) and 22L persulfate (98%, Alfa Aesar, MA, USA) (10 or 40 g/L) with phosphate buffer solution was prepared in a separate container (referred to as the cathode reservoir). At the start of the experiment, previously injected buffer solution (i.e., during PCE loading) from the anode and cathode cells was syphoned out and approximately 4L of buffer and PS solution was added to anode and cathode cells, respectively. Two mixed metal oxide (MMO) electrodes (Titanium Electrode Products Inc, Stafford, Texas) were inserted into the anode and cathode cells. The electrodes were connected to either a DC power supply (BK Precision–1623A, USA) or to a variable voltage controller (Startco Energy Products Co., Model: 3PN1010B, OH, USA). In the latter case, constant power was supplied and AC voltage and current varied with time due to changes in electrical conductivity.

The experiment was divided into 8 phases as summarized in Table 5-1. Phase 1, as mentioned above, was an equilibration stage of 5 days, the end of which was established as time = 0 days for the experiment. The experiment began with 21 days of EK-assisted PS delivery (Phase 2). The constant head (with 4L solution) in the cathode reservoir was maintained with a 10 g/L buffered PS solution. A similar approach was followed for the anode cell using the buffer solution in the anode reservoir. A constant current (25mA) was applied throughout this phase to enhance PS migration through the silt. pH was monitored in the anode and cathode cells. These cells, and the reservoirs feeding them, were completely replaced with new solutions every 4 to 6 days of EK application to maintain buffering capacity.

Phase 3 involved activating the PS. For this, the DC power source was disconnected and the voltage controller was attached to the electrodes. In a separate experiment with the same setup but no PCE, target temperatures were correlated to the applied current. In this phase, the voltage controller output was adjusted to reach approximately 50 °C in the system by applying 78% full power for 8 days. At the end of Phase 3 the system was allowed to cool down to room temperature for 4 days (Phase 4) followed by 3 days of EK-only application with DC 25 mA constant current (Phase 5) without further PS injection (i.e., PS solution was removed from cathode cell). This EK-only phase was conducted to evaluate the impact of EK application on PCE and PS concentrations.

Table 5-1: Different phases during the experiment

Phases	Phase duration [days]	Persulfate Conc. [g/L]
1. PCE equilibrium	0-5	-
2. EK-PS delivery (EK-PS Period 1)	5-21	10
3. Activation (Heating Period 1)	21-29	-
4. Cooling Period (No EK, No PS)	29-33	-
5. EK-only (No PS)	33-36	-
6. EK-PS delivery (EK-PS Period 2)	36-61	40
7. Activation (Heating Period 2)	61-91	-
8. Cooling period (No EK, No PS)	91-122	-

PCE remained in the system at the end of Phase 5. Consequently, Phase 6 of the experiment involved a 2nd Period of EK-assisted PS delivery for 25 days with a higher dose of PS (40 g/L) but the same applied DC current (25 mA) (Table 5-1). Phase 7 involved activating the PS, but with a target of 35 °C. The rate of temperature change was reduced relative to Phase 3 by carefully controlling the voltage controller output power (starting with 10% power and increasing in 5% increments on days 61.5, 62.5, 64 and 64.5 and then decreasing to 18% on day 80). This provided a means to evaluate the impact of temperature on PS

decomposition and PCE degradation. This activation phase continued for 30 days followed by a 21 days Cooling Period (Phase 8), which ended the experiment.

Water samples were collected regularly (approximately every 12 hrs) with a gas tight syringe from the 6 sampling locations (Figure 5.1). The initial 0.20 mL sample was discarded to remove any residual liquid within the luer lock system. Thereafter, 0.10, 0.10 and 0.25 mL samples were collected from each port to analyse for PS, sulfate and PCE, respectively. Aqueous PS concentrations were determined using the UV-spectrometer method at 352 nm (Liang et al., 2008). The PCE sample was immediately injected into a 1 mL hexane-filled GC vial. The hexane was extracted after two hours and PCE concentrations were analysed using a GC-ECD system (Agilent 7890A, Agilent, Santa Clara, CA). The method detection limit (MDL) for PCE was 0.02 mg/L. In addition, thermal images were taken during Phase 7 using Infra-red camera (A320, FLIR Systems Ltd., Burlington, ON, Canada). No gas evolution was visually observed.

5.3   Results and Discussion

5.3.1   Persulfate migration

PS migrated from the cathode to P1 (6.5 cm from cathode) in 1 day, gradually migrating to P4 (29 cm from cathode) after 4 days of applied EK during Phase 2 (Figure 5.2a). An average transport rate of 2.8±0.5 cm/day was estimated based on the arrival times of 1 g/L PS concentration (i.e., 10% of the source concentration) at all locations. During the second EK induced PS transport period (Phase 6) the observed average PS transport rate was 1.6±0.4 cm/day using breakthrough of 10% of the source concentration as the benchmark. PS migrated to the anode cell, 36 cm from the cathode, 5.5 days into EK induced PS transport suggesting that EK was able to deliver PS across the full width of the silt. The transport rates observed in the current study were similar to that observed by Fan et al. (2014) (1.3 cm/day) and Robertson (2009) (1.5 cm/day). It is noted here that the anode cell in the current study was replenished with new buffer solution (to maintain the pH above 6) after 4 days of Phase 6. As such PS breakthrough data at this location is not available.

Maximum PS concentrations differed at the sampling locations with a gradual decreasing trend from P1 (5.5 g/L; near the source) towards P4 (2.5 g/L) at the end of Phase 2 (Figure 5.2a). It is noted here that PS decomposition was not expected during this phase since the setup was at room temperature (20 °C). This assumption is corroborated by no sulfate evolution from PS decomposition. These sampling locations (P1-P4) were located in the same horizontal plane (Figure 5.1). A similar trend (i.e., decreasing towards P4) was observed in Phase 6 (Figure 5.2a). Concentrations were similar along the same vertical transect (e.g., sampling ports P2 and P5 as well as P3 and P6).

PS concentration in the source reservoir was increased to 40 g/L during the Phase 6 to evaluate the impact of higher PS dosage on EK assisted PS migration and subsequent remediation. Maximum PS concentrations at the observation ports were approximately 60% and 29%, when normalized to source concentrations, during Phases 2 and 6, respectively. The lower normalized maximum PS concentrations during Phase 6 in comparison to Phase 2 suggests that injection at higher PS dosages does not necessarily translate to a proportional increase in mass transport when normalized to injection concentration. Fan et al. (2014) observed an average of 45 g/L PS transported into the soil, due to EM of PS, which was 22.5% of injected PS concentration (200 g/L). Similar higher PS source concentrations, ranging from 100 to 400 g/L, were used in previous EK-PS studies (Cang et al., 2013; Fan et al., 2014; Isosaari et al., 2007; Yukselen-Aksoy and Reddy, 2013). The use of higher PS source concentration but relatively lower mass delivery would increase the reagent cost without additional benefit to increased mass delivery. Further work is therefore required to optimize PS injection concentrations to balance the mass delivered, within a given time, and the cost associated with oxidant loss (i.e., PS) in the porous media during migration for field applications.

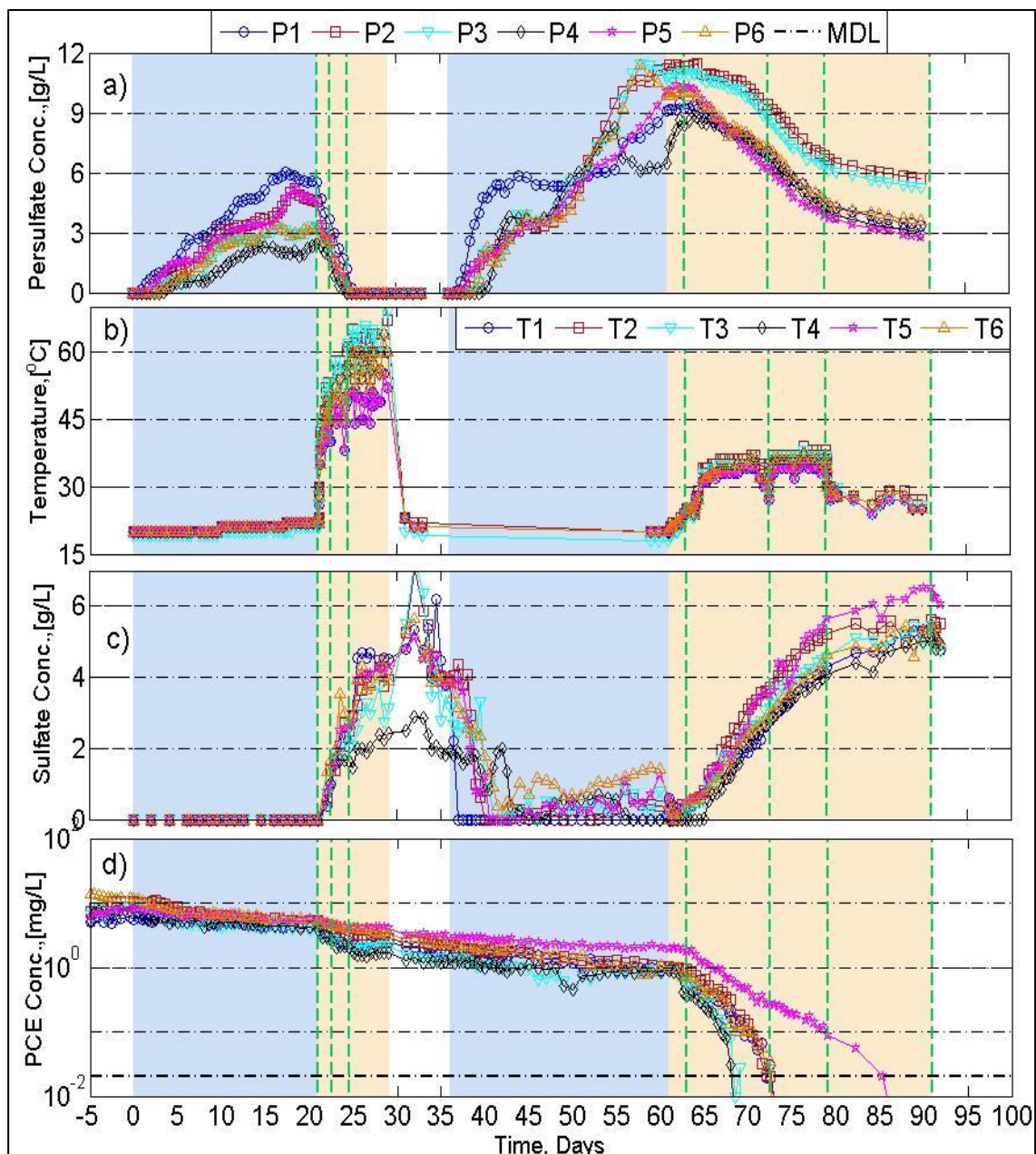Figure 5.2: Observed data for a) aqueous persulfate concentrations; b) temperature with T5 = T1 and T6 = T4; c) sulfate concentrations, and d) PCE concentrations at different sampling locations; "blue boxes" represent EK-PS periods while "orange boxes" represent thermal activation periods, respectively; the region bounded between vertical green lines represent the TG1 to TG5 temperature regimes from left to right.

5.3.2   Thermal activation and persulfate decomposition

PS that was delivered to the silt during Phases 2 and 6 was heat activated during Phases 3 and 7, respectively. Application of a higher current (i.e., 190 mA of AC source) resulted in rapid increase in temperature at all four thermocouple locations (Figure 5.2b). For example, the temperature increased at 13 °C/day, averaged from the 4 thermocouples locations, during the first 1.5 days of Phase 3 and decreased to 5 °C/day until the end of this phase. The final temperature at the end of Phase 3 (i.e., 29th day) was 62±7 °C. For Phase 7, when power was increased gradually, temperature increased at 2.3 °C/day during the first 11.5 days. The rate of temperature increase then decreased to 0.6 °C/day to achieve the targeted temperature (35 °C) between 72.5 and 79 days. The average temperature was then decreased from 36±1 °C, at 79 days, to 27±2 °C at 91 days to further evaluate the PS decomposition at lower temperature. Temperatures in the upper part of the cell were consistently higher than the lower part of the cell (e.g., at T3 72 °C and 55 °C at T1 on day 28.5) (Figure 5.2b). A similar trend was observed during Phase 7. Thermal images taken during Phase 7 confirm this temperature distribution (Appendix C, Figure 9.1). Similar temperatures across a horizontal plane, and the variations in the vertical plane, may be due to buoyancy with water at higher temperature migrating vertically upwards (Krol et al., 2011).

Based on the rates of temperature increase, the heating periods (Phases 3 and 7) were divided into five temperature groups (referred to as TG1 to TG5). The average temperatures of all temperature measurement locations during TG1, TG2, TG3, TG4 and TG5 were 42±5 (21-22.5 days), 53±6 (22.5-24.5 days), 32±4 (63-72.5 days), 36±1 (72.5-79 days), and 27±2 °C (79-91 days), respectively (Table 5-2). Increased temperature resulted in PS concentration decrease due to decomposition (Figure 5.2a,b) with faster PS decomposition during Phase 3 in comparison to Phase 7 due to higher temperatures during Phase 3. For example, complete PS decomposition was observed in 4 days following heat activation in Phase 3 whereas in Phase 7 considerable PS was observed at the end of experiment (i.e., an average of 10% of the source concentration at 91 days). Consistent with literature studies these data suggest that PS decomposition rate was a function of temperature (Johnson et al., 2008; Waldemer et al., 2007).
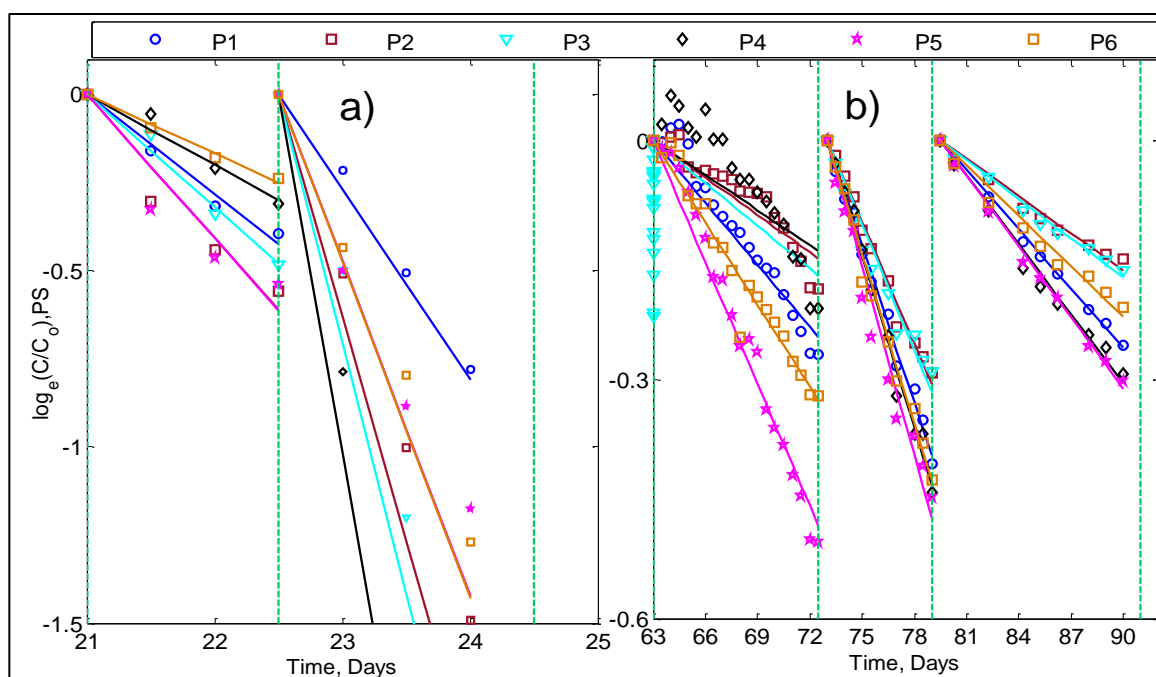
Figure 5.3: logarithm of normalized observed and fitted data for a) aqueous PS during TG1-2; b) aqueous PS during TG3-5; green vertical lines represent the durations of different temperature groups.

Pseudo-first order rate constants ($k_{obs,PS}$), fitted to observed PS concentration at each sampling location, were between 0.023 ± 0.006 at 27 °C and 1.19 ± 0.47 day^{-1} at 52 °C (Table 5-2, Figure 5.3a,b). Activation energy (E_a) for thermal PS decomposition was calculated using fitted $k_{obs,PS}$ values and observed temperatures measured at the nearest thermocouple (Table 5-2, Figure 9.2a). E_a for PS decomposition ranged between 126 to 154 kJ/mol at the different measurement locations with an average of 142 ± 10 kJ/mol (Table 5-2). This value is similar to that obtained by Johnson et al. (2008) for continuously stirred reactors with soil (i.e., 120 kJ/mol). To the author's knowledge, the cited study is the only other study to quantify E_a for PS decomposition with soil present and the current study is the only one to provide an in-situ value. Literature values for E_a from batch experiments with water, and no soil, varied between 118 to 140 kJ/mol (House, 1962; Johnson et al., 2008; Kolthoff and Miller, 1951). Similar E_a in the batch experiments, both with and without the soil, as well

as in the current study suggest that presence of soil matrix may have less impact on thermal activation of PS compared to other activators. Activators such as Fe^{2+} or high pH requires that the PS and the activator ion come into contact for PS activation. Mixing processes would be affected by the presence of soil, thus, E_a might differ for systems with and without soil. In contrast heat can be applied more uniformly in a system resulting in homogeneous PS activation.

Table 5-2: Temperature groups (TG) and calculated $k_{obs,PS}$ at different sampling locations

Location	TG5 (79-91 days)		TG3 (63-72.5 days)		TG4 (72.5-79 days)		TG1 (21.2-22.5 days)		TG2 (22.5-24.5 days)		$E_{a,PS}$ (kJ/mol)
	T^*	$k_{obs,PS}$	T^*	$k_{obs,PS}$	T^*	$k_{obs,PS}$	T^*	$k_{obs,PS}$	T^*	$k_{obs,PS,}$	
P1 (T1)	26±1	0.025	31±3	0.026	34±1	0.066	38±3	0.28	46±5	0.54	141
P2 (T2)	28±1	0.016	33±4	0.016	37±1	0.051	44±5	0.41	56±5	1.27	142
P3 (T3)	27±1	0.016	32±4	0.018	37±1	0.053	43±5	0.32	57±5	1.42	135
P4 (T4)	27±1	0.029	32±3	0.015	36±0	0.072	42±4	0.20	52±4	2.04	154
P5 (T1)	26±1	0.030	31±3	0.051	34±1	0.079	38±3	0.41	46±5	0.95	151
P6 (T4)	27±1	0.021	32±4	0.034	36±0	0.072	42±4	0.17	52±4	0.95	126
Avg.	27	0.023	32	0.027	36	0.065	42	0.30	52	1.19	142
Std. Dev.	1	0.006	4	0.013	1	0.010	5	0.09	6	0.47	10

* reported temperature (in °C) is averaged over the TG durations for a given location with one standard deviations; the final average temperature represents the average temperatures of all locations at a given TG.

Sulfate (SO_4^{-2}) concentrations increased during Phases 3 and 7 due to PS decomposition (Figure 5.2c). Theoretically, each mole of PS decomposes to 2 moles of $SO_4^{-\bullet}$, ultimately resulting in 2 moles of SO_4^{-2} (Equation 5.1). Observed and theoretical SO_4^{-2} concentrations were in good agreement at all locations (Figure 5.4). As discussed earlier PS rapidly decomposed during Phase 3 due to the high temperatures, resulting in rapid increases in SO_4^{2-} which reached a plateau when PS concentration was depleted (Figure 5.2a). SO_4^{2-} concentration increased more gradually during Phase 7 due to the lower temperatures and did not reach a plateau due to excess PS. SO_4^{2-} concentrations decrease during Phase 5 (EK-only phase; days 33 to 36) as SO_4^{2-} migrates to the anode cell due to EM, thus, removing SO_4^{2-} ions from the soil compartment. EM mass transport is at least 10 times higher than EO migration (Acar and Alshawabkeh, 1993) as such electroosmotic sweeping of SO_4^{2-} ions would be small compared to EM. SO_4^{2-} concentration was not quantified in the anode/cathode cells as these cells were completely replenished periodically.
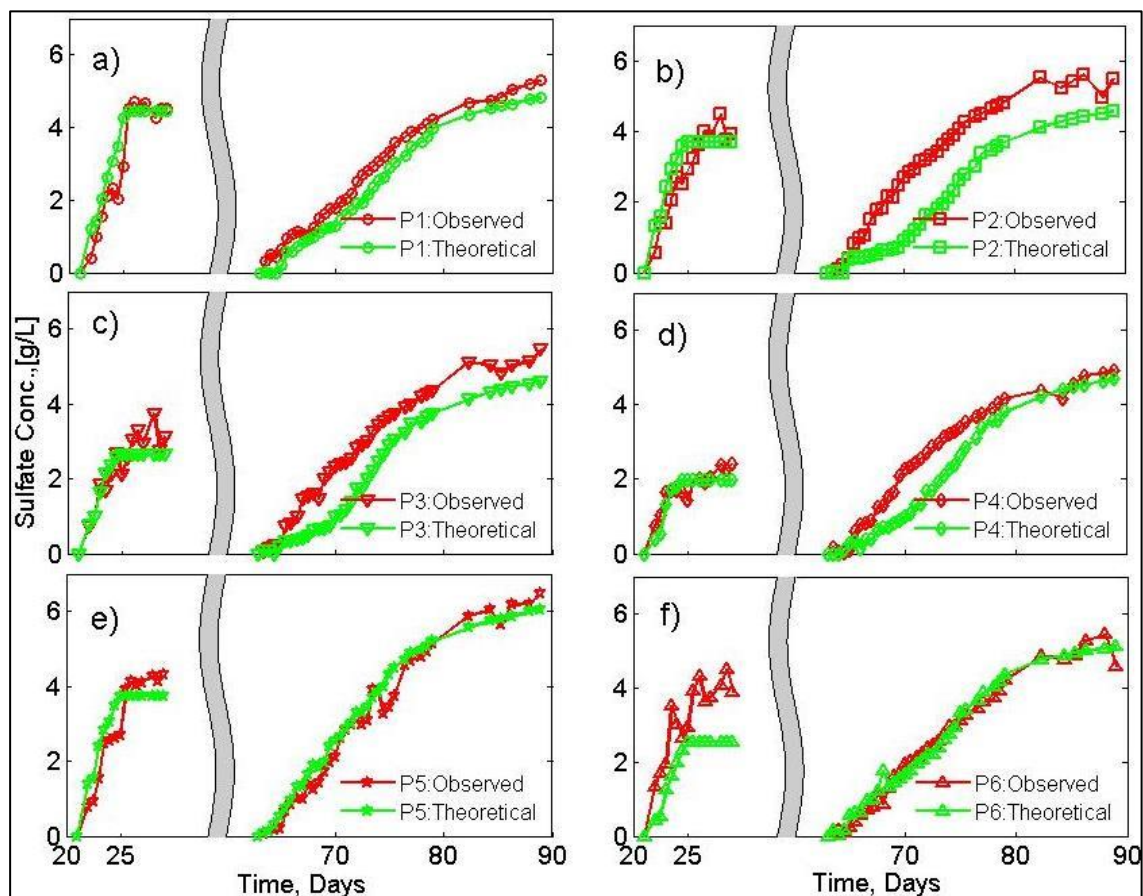

Figure 5.4: Observed and theoretical sulfate concentrations for different sampling locations.

5.3.3 PCE degradation

After packing, the sandbox was left idle for 5 days (-5 to 0 days in Figure 5.2d and Phase 1, Table 5-1), allowing the PCE to equilibrate within the silt. Average PCE concentrations were 7.4 ± 3 mg/L and 8.7 ± 2 mg/L at the beginning and end of this phase, respectively (Figures 5.2d and 9.3). This suggest that the system was sealed (e.g., no volatile losses). PCE concentrations decreased during EK-PS periods (Phases 2 and 6), when no degradation is expected. The average PCE concentration decreased from 8.7 ± 2 mg/L to 4 ± 1 mg/L during the 21 days of Phase 2 and from 2 ± 0.5 mg/L to 1.1 ± 0.4 mg/L during the 25 days of Phase 6 (Figures 5.2d and 9.3), likely due to electroosmotic sweeping. Contaminant (e.g., phenol, TCE) removal due to EO sweeping has been observed in previous studies (Thepsithar and Roberts, 2006; Weng et al., 2003). From the observed PCE concentrations it was estimated that approximately 10 and 2 mg PCE were lost during Phase 2 and Phase 6, respectively, due to EO sweeping. Based on these observations the EO sweeping rate was calculated to be 0.50 and 0.08 mg/day, during these two phases, respectively. As a comparison the theoretical EO sweeping rate is also calculated. The in-situ electroosmotic permeability (k_{EO}) could not be measured in the current study due to limitations associated with the experimental setup used. Reported EO permeability (k_{EO}) values vary from 4×10^{-10} to 1×10^{-8} m^2/V-s for all soils (Eykholt and Daniel, 1994; Mitchell and Soga, 2005; Shapiro and Probstein, 1993). This range of k_{EO} values would results in EO-induced PCE migration rates, using Equation 9.1, varying between 0.13 and 0.60 mg/day which are a good match to observed EO sweeping rates. EO-induced flow would be towards the cathode cell. Unfortunately PCE was not detected in the cathode cell likely due to dilution in the large reservoir.

The good match between the observed EO sweeping rate and calculated EO-induced PCE migration rate suggests that the loss in PCE mass during the EK-PS delivery phases was due to EO migration of PCE and not due to PS-PCE reaction. To further support this hypothesis, PS decomposition was modelled at different temperatures (Figure 5.5) using the Arrhenius equation and the parameters obtained from the PS decomposition data of the current work. Figure 5.5 also demonstrates that PS decomposition would be very slow (approximately 1% decomposition after 15 days) at the average ambient groundwater

temperature (approximately 10 °C for Canada). Application of ERH to increase the temperature to 20, 32 and 50 °C would result in 6%, 45% and 100% PS decomposition, respectively, in 15 days. This further suggests that PS, at the room temperature (20 °C), was not activated during the EK-PS delivery phases and that the observed decrease in PCE concentration during Phases 2 and 6 was due to EO sweeping of PCE.
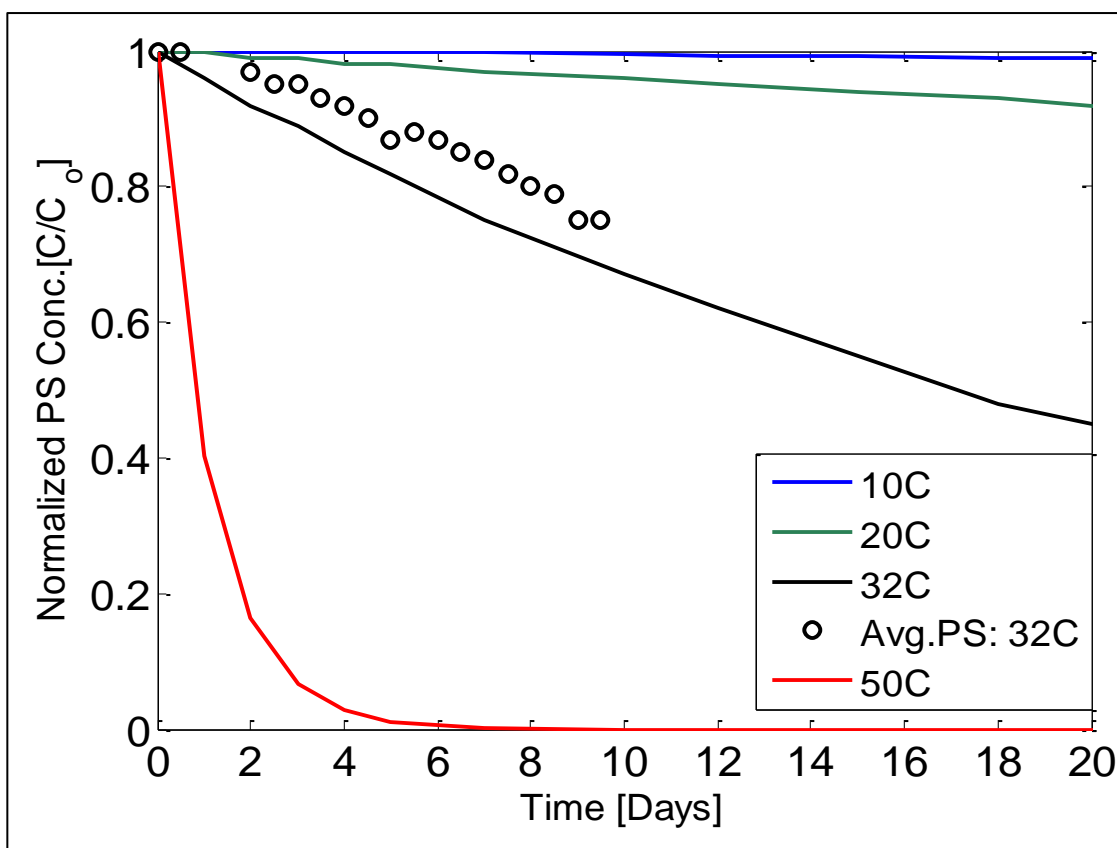
Figure 5.5: Observed and predicted normalized PS concentrations at different temperatures. The solid lines were plotted using the Arrhenius equation using the parameters (E_a = 142 kJ/mol; A = 7.5×10^{22} per day) obtained from PS decomposition data of the current study. The difference between the observed normalized average PS concentrations and the predicted concentrations has resulted because of using average temperature observed during TG3 (32±4 °C, Table 5-2).

Thermal activation of PS produces reactive sulfate radicals $SO_4^{-\bullet}$ that oxidize PCE (Equations 5.1 and 5.2). PCE concentrations decreased more rapidly at the onset of PS activation (Phases 3 and 7) in comparison to any PCE loss before activation (EO sweeping only) or afterwards (Figures 5.2d and 9.3) suggesting PCE reaction with PS. This is further

supported by increases in sulfate concentrations and decreases in PS concentrations (Figure 5.2a,c). As expected, the rapid decrease in PCE concentration stopped after 24.5 days at most of the sampling locations when PS was depleted (Figure 5.2a,d).

The rate of temperature increase was much slower during Phase 7 resulting in slower PS decomposition and more sustained and complete PCE degradation. During the first two days of Phase 7 (61-63 days) the rate of temperature increase was very low with negligible SO_4^{-2} generation due to very limited PS decomposition. As temperature further increased after 63 days, PCE degradation was observed (Figure 5.2a,d). PCE concentrations at P3 and P4 decreased to below the MDL at 68.5 days and at 73 days at P1, P2, and P6 (Figure 5.2d). The PCE concentration at P5 decreased to MDL after 85.5 days (Figure 5.2d). Consistently higher PCE concentrations, and slower degradation, were observed at P5, likely due to its lower temperatures (at T1) compared to the other locations (Figure 5.2b,d). PCE concentrations decreased sharply at all locations 1-2 days before reaching the MDL. This behaviour has been observed in previous studies (Liang et al., 2003; Waldemer et al., 2007). Waldemer et al. (2007) proposed that this distinct downward curvature at low contaminant concentrations could be due to combined reactivity of $SO_4^{-\bullet}$ and other reactive species (e.g., $Cl^{\bullet}$) resulting from oxidation of chlorinated ethenes.

Pseudo-first order rate constants ($k_{obs,PCE}$) for PCE degradation for the different temperature regimes, TG1-TG4, decreased with increasing temperature at all sampling locations (Figure 9.2b). For example, $k_{obs,PCE}$ for location P5 were 0.20, 0.15, 0.097, and 0.092 d^{-1} at 31, 34, 38 and 46 °C, respectively. The decrease in observed first order rate constants with increase in temperature is counter intuitive, suggesting that the PS-PCE reaction might not be following first order kinetics. It is noted here that $SO_4^{-\bullet}$ generated from the thermal activation of PS reacts with PCE, not the PS itself. It is not possible to determine if the PS-PCE reaction is following first order reaction kinetics as $SO_4^{-\bullet}$ could not be measured.

Average pseudo-first order rate constants ($k_{obs,PCE}$) values obtained in the current study (0.48±0.28 d^{-1} to 0.14±0.05 d^{-1} between 32 and 52 °C, respectively) were 1 to 2 orders of magnitude (OoM) lower than those reported in batch experiments in the presence of sand (12 d^{-1}) or kaolinite (3 d^{-1}) at 50 °C (Costanza et al., 2010). The cited study also reported

that PS decomposition varied between 0.9% and 6.4% in the aforementioned experiments. This suggests that the reaction, in the cited study, was not limited by availability of reactive $SO_4^{-\bullet}$. The difference in the observed rate constants compared to the cited study was not surprising considering that current study was performed in conditions more representative of field applications whereas the literature study was conducted under ideal conditions with continuous mixing. In the current study, complete PS decomposition was observed at the higher temperature (TG2) compared to low temperature activation phases. It is therefore possible that the PS-PCE reaction was limited by the availability of reactive $SO_4^{-\bullet}$ as well as proper mixing and collision of PS-PCE molecules. Activating PS at a higher temperature would rapidly consume PS without allowing for PS-PCE reaction. Activating PS at a slower rate might limit the rate of PS-PCE reaction due to insufficient availability of reactive $SO_4^{-\bullet}$. These results suggest that the PS needs to be activated in a manner as such $SO_4^{-\bullet}$ generation is enough to react with contaminant but not too fast to deplete the available PS without reacting with the contaminants.

5.4 Environmental Implications

Oxidant delivery and subsequent remediation of low permeability porous media is challenging given inaccessibility of these soils. The current study employed a novel combination of EK-assisted PS delivery and low temperature ERH activation of the delivered PS. Electromigration was shown to successfully deliver the PS at a rate between 2.8 and 1.6 cm/day through the silt, during the two EK assisted PS delivery phases. Low temperature ERH was successful in activating PS homogenously throughout the silt, resulting in the complete destruction of PCE in silt within 18 days after activation. This combination of technologies has never been previously demonstrated and can likely easily be scaled-up for field application. Both techniques use the same equipment, a pair of commonly available electrodes, and requires only switching from DC current (for PS delivery) to AC current (for activation). This study suggests that a pilot test of the approach for treating chlorinated solvent-contaminated low permeability zones is warranted.

This study demonstrated that increasing the source PS concentration resulted in increased PS mass transport rate, delivering more mass at a given distance within a given time.

However, increased source PS concentration does not necessarily result in proportional increase in pore fluid PS concentration. In a field setting it is always desirable to deliver higher oxidant mass at a faster rate that can be achieved within the limited budget. Therefore the optimum PS source concentration needs to be investigated to balance the PS mass transport and cost of excess chemicals. The results of the current study suggest that PS would slowly decompose at the room temperature (20 °C) or at the ambient groundwater temperature (10 °C in Canada). This suggests PS can be delivered to the targeted contaminated zone, without any appreciable loss due to PS decomposition, where it can be thermally activated to degrade in-situ contaminants. This study also suggests that PS activation temperatures around 30 °C would be more effective than the high temperatures ($\geq$40 °C) applied in most lab-scale studies with heat assisted PS activation. Application of higher temperatures (>40 °C) rapidly decomposed the available PS compared to low temperature (<40 °C) application. The estimated activation energy (E_a) for thermally activated PS decomposition was similar to the literature values obtained from continuously mixed and controlled reaction vial (both with water only but no soil and with soil) experiments. It is inferred that the presence of a porous matrix may have less impact on thermal activation of PS compared to the use of other activators. This was due to the fact that heat can be applied uniformly even in the presence of soil where the mixing between other activators (e.g., Fe^{2+}, alkaline solution) and PS are impacted by the presence of soil. Finally, the estimated PCE degradation rate constants revealed that the PS-PCE reaction was rate limited by the availability of reactive $SO_4^{-\bullet}$. Activating the PS at higher temperature would rapidly consume the PS without allowing for PS-PCE reaction. While activating PS at a slower rate might limit the rate of PS-PCE reaction due to insufficient availability of reactive $SO_4^{-\bullet}$. Therefore, current study suggests that the optimum PS source concentration and temperature would likely best be evaluated in field pilot tests.

5.5 References

Acar, Y.B. and Alshawabkeh, A.N., 1993. Principles of Electrokinetic Remediation. Environmental Science & Technology, 27(13).

Baciocchi, R., D'Aprile, L., Innocenti, I., Massetti, F. and Verginelli, I., 2014. Development of technical guidelines for the application of in-situ chemical oxidation to groundwater remediation. Journal of Cleaner Production, 77(0): 47-55.

Ball, W.P., Liu, C., Xia, G. and Young, D.F., 1997. A diffusion-based interpretation of tetrachloroethene and trichloroethene concentration profiles in a groundwater aquitard. Water Resources Research, 33(12): 2741-2757.

Berlin, A.A., 1986. Kinetics of radical-chain decomposition of persulfate in aqueous solutions of organic compounds. Kinet. Catalyst, 27(1).

Cang, L., Fan, G.-P., Zhou, D.-M. and Wang, Q.-Y., 2013. Enhanced-electrokinetic remediation of copper–pyrene co-contaminated soil with different oxidants and pH control. Chemosphere, 90(8): 2326-2331.

Chapman, S.W. and Parker, B.L., 2005. Plume persistence due to aquitard back diffusion following dense nonaqueous phase liquid source removal or isolation. Water Resources Research, 41(12).

Chowdhury, A.I.A., O'Carroll, D.M., Xu, Y. and Sleep, B.E., 2012. Electrophoresis enhanced transport of nano-scale zero valent iron. Advances In Water Resources, 40(0): 71-82.

Costanza, J., Otaño, G., Callaghan, J. and Pennell, K.D., 2010. PCE Oxidation by Sodium Persulfate in the Presence of Solids. Environmental Science & Technology, 44(24): 9445-9450.

Dahmani, M.A., Huang, K. and Hoag, G.E., 2006. Sodium Persulfate Oxidation for the Remediation of Chlorinated Solvents (USEPA Superfund Innovative Technology Evaluation Program). Water, Air, & Soil Pollution: Focus, 6(1): 127-141.

Eykholt, G.R. and Daniel, D.E., 1994. Impact of System Chemistry on Electroosmosis in Contaminated Soil, 120. ASCE, 797-815 pp.

Fan, G. et al., 2014. Electrokinetic delivery of persulfate to remediate PCBs polluted soils: Effect of injection spot. Chemosphere, 117(0): 410-418.

Fan, G., Cang, L., Gomes, H.I. and Zhou, D., 2016. Electrokinetic delivery of persulfate to remediate PCBs polluted soils: Effect of different activation methods. Chemosphere, 144: 138-147.

Fordham, J.W.L. and Williams, H.L., 1951. The Persulfate-Iron(II) Initiator System for Free Radical Polymerizations1. Journal of the American Chemical Society, 73(10): 4855-4859.

Hodges, D., Fourie, A., Thomas, D. and Reynolds, D., 2013. Overcoming Permanganate Stalling during Electromigration. Journal of Environmental Engineering, 139(5): 677-684.

House, D.A., 1962. Kinetics and Mechanism of Oxidations by Peroxydisulfate. Chemical Reviews, 62(3): 185-203.

Huang, K.-C., Couttenye, R.A. and Hoag, G.E., 2002. Kinetics of heat-assisted persulfate oxidation of methyl tert-butyl ether (MTBE). Chemosphere, 49(4): 413-420.

Huang, K.-C., Zhao, Z., Hoag, G.E., Dahmani, A. and Block, P.A., 2005. Degradation of volatile organic compounds with thermally activated persulfate oxidation. Chemosphere, 61(4): 551-560.

Johnson, R.L., Tratnyek, P.G. and Johnson, R.O.B., 2008. Persulfate Persistence under Thermal Activation Conditions. Environmental Science & Technology, 42(24): 9350-9356.

Kingston, J.T., Dahlen, P.R., Johnson, P.C., Foote, E. and Williams, S., 2010. Critical evaluation of state-of-the-art in situ thermal treatment technologies for DNAPL source zone treatment.

Kolthoff, I.M. and Miller, I.K., 1951. The Chemistry of Persulfate. I. The Kinetics and Mechanism of the Decomposition of the Persulfate Ion in Aqueous Medium1. Journal of the American Chemical Society, 73(7): 3055-3059.

Kosmulski, M. and Dahlsten, P., 2006. High ionic strength electrokinetics of clay minerals. Colloids and Surfaces A: Physicochemical and Engineering Aspects, 291(1-3): 212-218.

Krol, M.M., Sleep, B.E. and Johnson, R.L., 2011. Impact of low-temperature electrical resistance heating on subsurface flow and transport. Water Resources Research, 47(5).

Liang, C., Huang, C.-F., Mohanty, N. and Kurakalva, R.M., 2008. A rapid spectrophotometric determination of persulfate anion in ISCO. Chemosphere, 73(9): 1540-1543.

Liang, C.J., Bruell, C.J., Marley, M.C. and Sperry, K.L., 2003. Thermally Activated Persulfate Oxidation of Trichloroethylene (TCE) and 1,1,1—Trichloroethane (TCA) in Aqueous Systems and Soil Slurries. Soil & Sediment Contamination, 12(2): 207.

Liu, C. and Ball, W.P., 2002. Back Diffusion of Chlorinated Solvent Contaminants from a Natural Aquitard to a Remediated Aquifer Under Well-Controlled Field Conditions: Predictions and Measurements. Ground Water, 40(2): 175-184.

Mitchell, J.K. and Soga, K., 2005. Fundamentals of Soil Behavior. John Wiley & Sons, Inc., New Jersey.

Parker, B.L., Chapman, S.W. and Guilbeault, M.A., 2008. Plume persistence caused by back diffusion from thin clay layers in a sand aquifer following TCE source-zone hydraulic isolation. Journal of Contaminant Hydrology, 102(1–2): 86-104.

Petri, B. et al., 2011. Fundamentals of ISCO Using Persulfate. In: R.L. Siegrist, M. Crimi and T.J. Simpkin (Editors), In Situ Chemical Oxidation for Groundwater Remediation. SERDP/ESTCP Environmental Remediation Technology. Springer New York, pp. 147-191.

Reynolds, D.A., Jones, E.H., Gillen, M., Yusoff, I. and Thomas, D.G., 2008. Electrokinetic Migration of Permanganate Through Low-Permeability Media. Ground Water, 46(4): 629-637.

Roach, N. and Reddy, K.R., 2006. Electrokinetic Delivery of Permanganate into Low-Permeability Soils. International Journal of Environment and Waster Management, 1(1): 4-16.

Robertson, T., 2009. Electrokinetic Transport of Persulfate under Voltage Gradients.

Sale, T., Parker, B.L., Newell, C.J. and Devlin, J.F., 2013. Management of Contaminants Stored in Low Permeability Zones - A State of the Science Review, SERDP/ESTCP, Alexandria, VA, USA.

Sale, T.C. et al., 2007. Unpublished Report on AFCEE Source Zone Initiative.

Seyedabbasi, M.A., Newell, C.J., Adamson, D.T. and Sale, T.C., 2012. Relative contribution of DNAPL dissolution and matrix diffusion to the long-term persistence of chlorinated solvent source zones. Journal of Contaminant Hydrology, 134–135: 69-81.

Shapiro, A.P. and Probstein, R.F., 1993. Removal of contaminants from saturated clay by electroosmosis. Environmental Science & Technology, 27(2): 283-291.

Siegrist, R., Crimi, M. and Brown, R., 2011. In Situ Chemical Oxidation: Technology Description and Status. In: R.L. Siegrist, M. Crimi and T.J. Simpkin (Editors), In Situ Chemical Oxidation for Groundwater remediation. SERDP/ESTCP Environmental Remediation Technology. Springer New York, pp. 1-32.

Thepsithar, P. and Roberts, E.P.L., 2006. Removal of Phenol from Contaminated Kaolin Using Electrokinetically Enhanced In Situ Chemical Oxidation. Environmental Science & Technology, 40(19): 6098-6103.

Tsitonaki, A. et al., 2010. In Situ Chemical Oxidation of Contaminated Soil and Groundwater Using Persulfate: A Review. Critical Reviews in Environmental Science and Technology, 40(1): 55-91.

Vermeulen, F. and McGee, B., 2000. In-Situ Electromagnetic Heating for Hydrocarbon Recovery and Environmental Remediation. Journal of Canadian Petroleum Technology, 39(8): 24-28.

Waldemer, R.H., Tratnyek, P.G., Johnson, R.L. and Nurmi, J.T., 2007. Oxidation of Chlorinated Ethenes by Heat-Activated Persulfate: Kinetics and Products. Environmental Science & Technology, 41(3): 1010-1015.

Weng, C.-H., Yuan, C. and Tu, H.-H., 2003. Removal of Trichloroethylene from Clay Soil by Series-Electrokinetic Process. Practice Periodical of Hazardous, Toxic, and Radioactive Waste Management, 7(1): 25-30.

Yang, G.C.C. and Yeh, C.-F., 2011. Enhanced nano-Fe3O4/S2O82− oxidation of trichloroethylene in a clayey soil by electrokinetics. Separation and Purification Technology, 79(2): 264-271.

Yukselen-Aksoy, Y. and Reddy, K., 2013. Electrokinetic Delivery and Activation of Persulfate for Oxidation of PCBs in Clayey Soils. Journal of Geotechnical and Geoenvironmental Engineering, 139(1): 175-184.

Yukselen-Aksoy, Y. and Reddy, K.R., 2012. Effect of soil composition on electrokinetically enhanced persulfate oxidation of polychlorobiphenyls. Electrochimica Acta, 86(0): 164-169.

Zhao, D. et al., 2013. Effect and mechanism of persulfate activated by different methods for PAHs removal in soil. Journal of Hazardous Materials, 254–255: 228-235.

Chapter 6

6 Conclusions and Recommendations

6.1 Summary and Conclusions

This thesis explores the transport of remediants due to hydraulic or electrokinetic transport for subsurface remediation. Three manuscripts were prepared as part of this thesis investigating performance of these delivery methods for remediants transport and the resulting clean-up of the contaminated porous media.

Field-scale studies with Nano-scale zero valent iron (nZVI) has demonstrated that these particles are mobile and capable of degrading in-situ contaminants. However, nZVI mobility and reactivity has so far only been studied in the saturated zone. Seasonal fluctuations of the groundwater table may cause subsurface contamination in the vadose zone, especially, immediately above the water table. However, no study has been conducted so investigate nZVI mobility and reactivity in variably saturated porous media. Numerical models can be used to design field-scale nZVI applications (e.g., nZVI volume, distance between monitoring wells). Currently, there is a lack of numerical modeling studies that have focused on this. The first manuscript titled "nZVI injection into variably saturated soils: field and modeling study" addressed the aforementioned concerns. Onsite synthesized nZVI was injected at a TCE contaminated site. Moreover, a three-dimensional model was developed and utilized for further investigation of nZVI migration in the subsurface. The major conclusions from this study are:

❖ Onsite synthesized monometallic nZVI particles were reactive and complete TCE degradation was achieved at the site.
❖ The developed numerical model, CompSim, accurately predicted water head at the injection and monitoring wells without any model calibration.
❖ CompSim, in its predictive capacity, simulated that nZVI was mobile in the both saturated and unsaturated zone in the subsurface but did not transport further from the unsaturated zone to saturated zone.

❖ Model results suggested that increasing the injected nZVI volume increased the nZVI travel distance, however, the net increase in travel distance was not proportional to increase in injection volume.

❖ Finally, the model results showed that use of the simplified 1D colloidal filtration theory (CFT) solution, commonly used to predict nZVI travel distances, could over predict nZVI migration, as such it should be used with caution.

Field-scale studies have demonstrated remediants (e.g., nZVI, oxidants) are capable of cleaning up a contaminated target zone. However, most of these studies were conducted in homogeneous porous media. Delivery of any remediants into low permeability porous media is challenging and can result in poor contaminant removal. This has often led to back diffusion of contaminants from low permeability zones. Electrokinectics (EK) has been proposed and used to enhance remediants (e.g., permanganate) delivery through such soil in laboratory experiments. However, limited contaminant removal was observed in such studies. No studies, so far, has attempted to demonstrate the ability of EK to enhance permanganate transport through contaminated low permeability porous media to limit back diffusion. The second study of the current thesis, "Electrokinetics-enhanced permanganate delivery and remediation of contaminated low permeability porous media" investigated the EK enhanced permanganate transport in a two-dimensional sandbox with heterogeneous contaminated sand and silt layers. This study, for the first time, studied the ability of EK delivered permanganate to degrade TCE within the silt layers. In addition, image analysis was used to quantify permanganate mass in the silt layers. The major conclusions from this study were:

❖ Image analysis revealed that EK delivered permanganate transport rate (6.4 cm/day) was higher than the transport rate without EK application (1.5-2 cm/day).

❖ In addition, image analysis demonstrated that more permanganate mass was delivered when EK was coupled with permanganate application (1.2 and 0.35 g of permanganate for EK and no-EK experiments, respectively).

❖ EK enhanced permanganate delivery resulted in 1.1 orders of magnitude (OoM) reduction in TCE concentration compared to experiments without EK application.

❖ Results revealed that TCE concentration was 1.7 OoM higher than the maximum concentration level (MCL) when permanganate was delivered with no electrokinetic application. By comparison, final TCE concentrations for the EK enhanced permanganate transport experiment were only 0.6 OoM higher than MCL, thus, limiting the extent of back diffusion.

The second study demonstrated EK enhanced permanganate delivery through the contaminated low permeability soil, limiting the extent of TCE back diffusion. However, $MnO_2(s)$ precipitation, as observed in that study, may reduce permeability impacting the permanganate delivery in the targeted zone. Therefore, persulfate was used in the third study to investigate EK enhanced persulfate delivery, activation and subsequent PCE degradation. The combination of EK assisted persulfate delivery and electrical resistance heating (ERH) to activate the persulfate is a novel approach for oxidant delivery and activation. The experiment was conducted in a two-dimensional sandbox packed with PCE contaminated silt. The major conclusions from this third study were:

❖ EK was able to deliver unactivated persulfate through the entire soil compartment (36 cm).

❖ Persulfate was not the activated during the EK assisted delivery phase at the room temperature (20 °C).

❖ ERH successfully activated the delivered persulfate.

❖ Application of higher temperature (>40 °C) rapidly depleted the available persulfate limiting reaction with PCE.

❖ Application of low temperature ERH (<40 °C) activated the available persulfate at a slower rate, therefore, complete PCE degradation was observed in this case.

❖ The estimated activation energy for thermal activation of persulfate (142±10 kJ/mol) was similar to literature values and suggested that thermal activation is independent of the presence of porous media.

6.2 Implications

- ❖ The up-scaled onsite nZVI synthesis protocol was successful at subzero temperatures.

- ❖ In-situ TCE degradation results suggested that nZVI synthesized at subzero temperatures was reactive. Therefore this technology can be used in cold climate regions.

- ❖ The numerical model, CompSim, was used in its predictive capacity and showed a very good match to field observed well head data. Therefore, this robust model can be used with minimum site data.

- ❖ The developed model can be utilized for preliminary design of nZVI field applications. For example, it can be used to determine nZVI injection volume and rate, maximum travel distance and distance between monitoring wells. Such information would be helpful for practitioners to minimize cost and remediation performance monitoring.

- ❖ The EK enhanced permanganate delivery and subsequent remediation study suggested that EK delivered permanganate can significantly reduce contaminant mass sequestrated in low permeability.

- ❖ This contaminant mass destruction would reduce back diffusion of contaminants. Thus, this technology would help to achieve site closure requirements.

- ❖ The EK assisted persulfate delivery study demonstrated that EK can successfully drive unactivated persulfate through contaminated low permeability porous media. Therefore, persulfate can be delivered to the targeted treatment zone without significant loss due to self-decomposition. Once sufficient persulfate mass is delivered throughout the targeted zone persulfate can be activated.

- ❖ The thermal activation of the delivered persulfate at the field-scale would be more beneficial as it eliminates the requirement of delivering activators through low permeability soils.

- ❖ Low temperature ERH for thermal activation can be easily up-scaled for field application. EK and ERH applications use the same electrodes but need to be switched from DC to AC voltages when heat activation is required.

❖ Low temperature ERH would activate persulfate at a slower rate allowing the reactive sulfate radical ($SO_4^{-\bullet}$) to react with contaminants. This would consume less power for low temperature ERH application, thus, would be energy efficient.

6.3   Research Needs and Future Work

❖ Field-scale nZVI application has been studied in relatively homogeneous permeable soils. nZVI transport and in-situ contaminant removal performance needs to be evaluated in heterogeneous soil system.

❖ nZVI-contaminant reactivity needs to be added to the numerical model to predict contaminant degradation and should be verified from field observations.

❖ For EK-permanganate system, more experiments are needed to optimize permanganate concentration, duration of permanganate injection, magnitude of applied current, and electrode configuration.

❖ In this study two EK pulses with permanganate were applied. However, the performance should be further evaluated under a single longer pulse and multiple pulses.

❖ Precipitation of $MnO_{2(s)}$ can possibly be minimized using a phosphate buffer as such future studies should combine a phosphate buffer with permanganate solution.

❖ The TCE concentration in the silt layers could not be measured due to experimental setup limitations. Therefore a numerical model can be used to fit TCE concentrations in the sand layers. The fitted data can then be used to predict TCE concentrations within the silt layers. Once calibrated and validated against the experimental results this model can be used further for investigation for different scenario (e.g., impact of different permanganate concentration).

❖ Future experiments need to be conducted with different types of low permeability porous media to determine the impact of electromigration and electroosmosis on persulfate migration.

❖ An increase in persulfate source concentration resulted in an increased in EK-assisted mass delivery although the resulting increase in pore fluid persulfate concentration was not proportional to increased source concentration. Therefore,

more experiments should be conducted to determine the optimal persulfate source concentration.

❖ The current study demonstrated that PCE degradation was rate limited by the availability of reactive sulfate radical ($SO_4^{-\bullet}$). Therefore, future studies should optimize persulfate activation and resulting PCE degradation.

❖ The rate of temperature increase in this study was shown to correlate to applied voltages. However, further studies are required to confirm rates that can be used for up-scaling this technology for field application.

7   Appendix A: Supplementary Material for "nZVI Injection into Variably Saturated Soils: Field and Modeling Study"
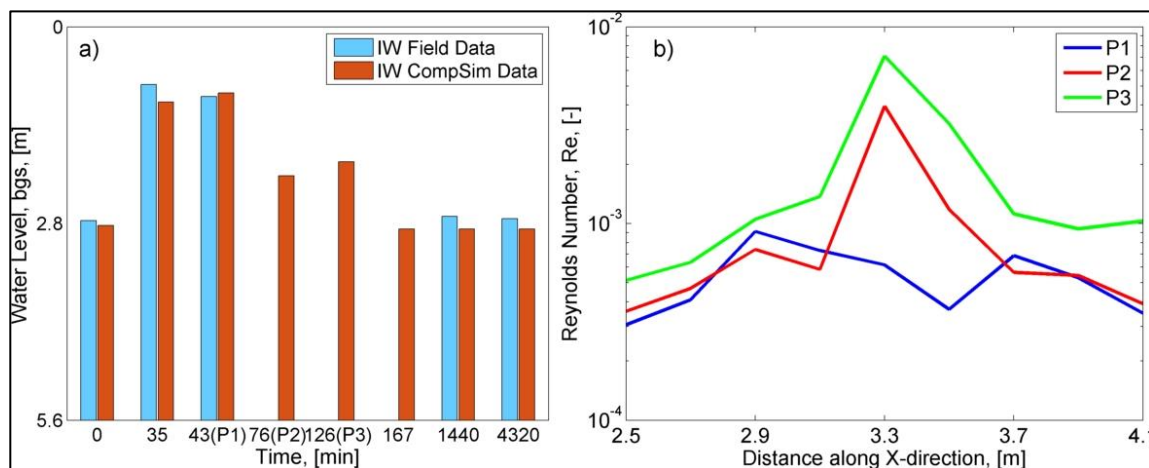

Figure 7.1: a) Observed change in water level at IW; b) Calculated Reynolds Number (R_e) for the Field Case (FC) simulation.
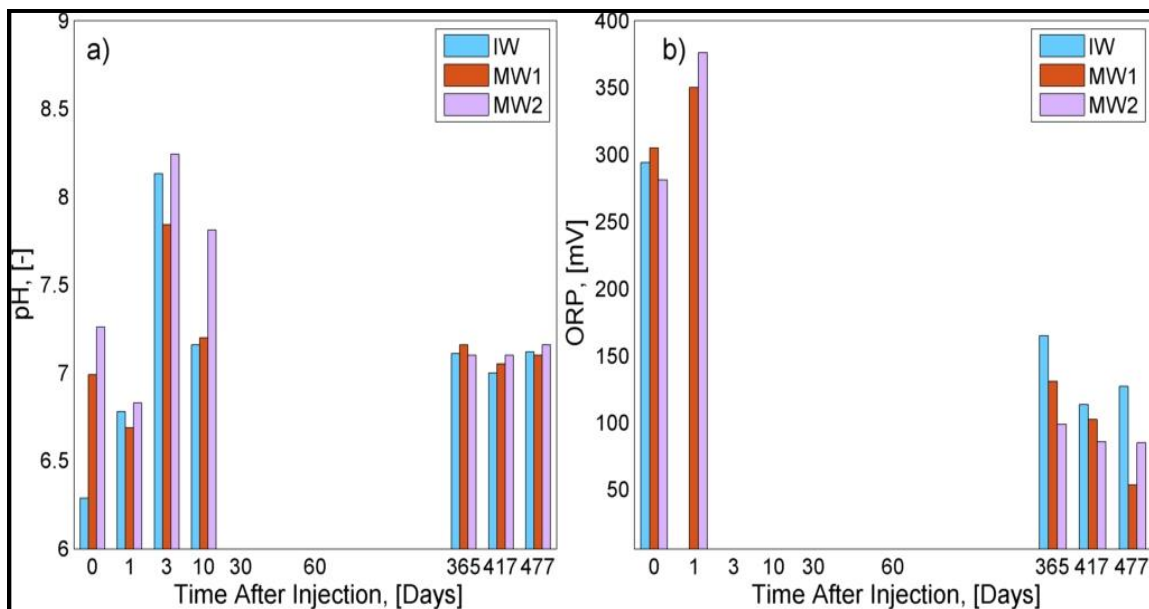

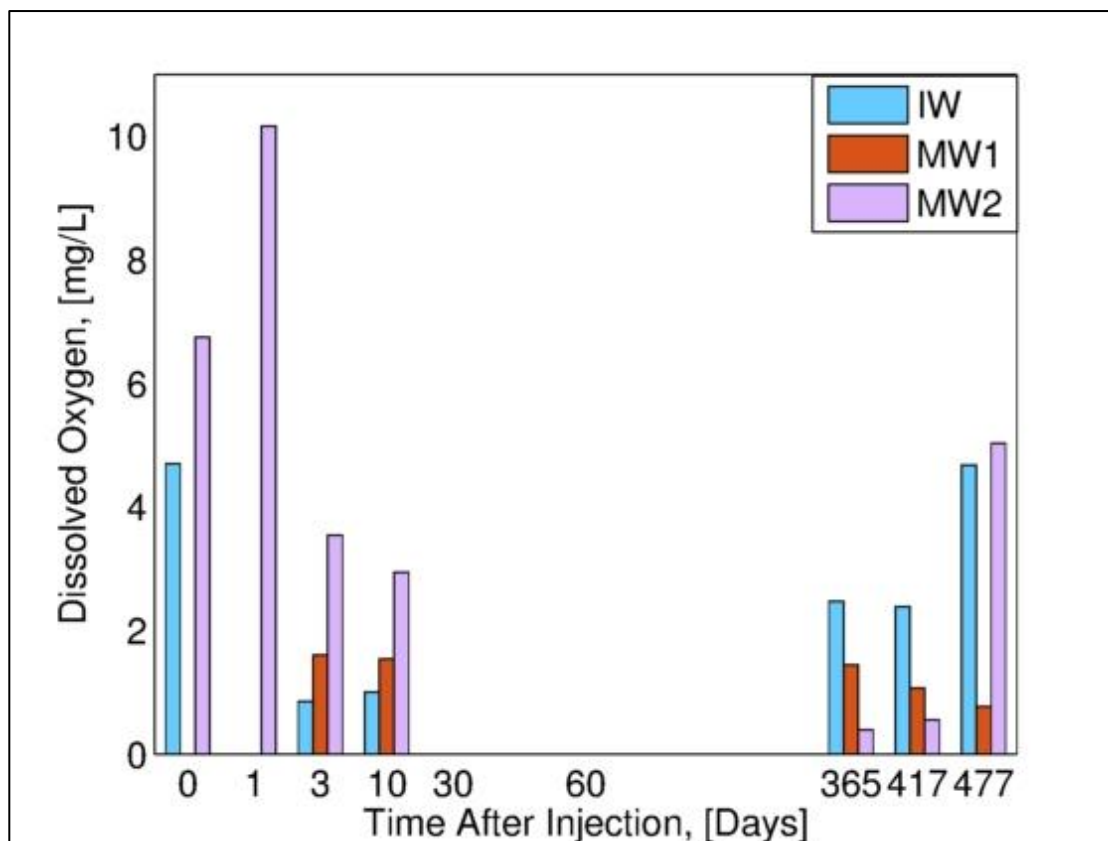Figure 7.2: Observed (a) pH and (b) ORP data for IW, MW1 and MW2.

Figure 7.3: Dissolve oxygen concentration in IW, MW1 and MW2.

7.1 TCE Degradation Reaction

nZVI has been injected at sites contaminated with a range of chlorinated volatile organic compounds *(*cVOCs) including tetrachloroethene (PCE), trichloroethene (TCE), 1,2-dichloroethene (1,2 cis-DCE) and vinyl chloride (VC) (Bennett et al., 2010; He et al., 2010; Wei et al., 2010). At these sites chlorinated ethenes (e.g., TCE) have been reduced to less toxic or environmentally benign compounds such as ethane and chlorides (Elsner et al., 2008; Liu et al., 2005; O'Carroll et al., 2013a):

$$C_2HCl_3 + 4Fe^0 + 5H^+ \rightarrow C_2H_6 + 4Fe^{2+} + 2Cl^- \hspace{2cm} \text{(Equation 7.1)}$$
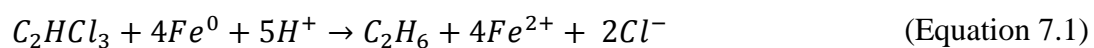
7.2 Equation for Theoretical Single Collector Contact Efficiency (η_o) (Tufenkji and Elimelech, 2004)

$$\eta_o = 2.4 A_S^{1/3} N_R^{-0.081} N_{Pe}^{-0.715} N_{vdW}^{0.052} + 0.55 A_S N_R^{1.675} N_A^{0.125} \quad \text{(Equation 7.2)}$$
$$+ 0.22 N_R^{-0.24} N_G^{1.11} N_{vdW}^{0.053}$$

where, $A_S = \dfrac{2(1-\gamma^5)}{2-3\gamma+3\gamma^5-2\gamma^6}$;

$\gamma = (1-f)^{\frac{1}{3}}$; f is the porosity;

$N_R = \dfrac{d_p}{d_c}$; d_p and d_c are particle and collector diameter, respectively;

$N_{Pe} = \dfrac{U d_c}{D_\alpha}$; U and D_α are fluid approach velocity and bulk diffusion coefficient;

$N_{vdW} = \dfrac{A}{kT}$; A is the Hamaker constant; k is Boltzmann constant and T is fluid absolute temperature;

$N_A = \dfrac{A}{12\pi\mu a_P^2 U}$; μ is the absolute fluid viscosity;

$N_G = \dfrac{\frac{2}{9} a_P^2 (\rho_P - \rho_f) g}{\mu U}$; ρ_P and ρ_f are particle and fluid densities;

7.3 Equation for 1D – 3D Velocity vs Concentration Relationship

$$\frac{\partial \theta_w C}{\partial t} = \frac{\partial}{\partial x}\left\{\theta_w D \frac{\partial C}{\partial x}\right\} - \frac{\partial}{\partial x}(C\vec{q}) - \theta_w K_{att} C \qquad \text{(Equation 7.3)}$$

where, C is the nZVI concentration in suspension (M/L^3), D is the hydrodynamic dispersion tensor (L^2/T), $\vec{q}$ is the Darcy velocity (L/T), Θ_w is the volumetric water content (-), and K_{att} is the attachment rate coefficient (1/T). K_{att} is defined as:

$$K_{att} = \frac{3(1 - \theta_w)}{2d_c}\alpha\eta_o v \qquad \text{(Equation 7.4)}$$

where, d_c is the mean collector diameter (L) and v is the pore water velocity (L/T). α and η_0 are the sticking efficiency (-) and theoretical single collector contact efficiency (-), respectively. η_0 is calculated using the relationship developed by (Tufenkji and Elimelech, 2004).

Neglecting the terms at steady state, substituting $\vec{q} = \theta_w v$ and K_{att} in Equation (7.3):

$$\frac{\partial}{\partial x}(C\theta_w v) = -\theta_w \left\{\frac{3(1-\theta_w)}{2d_c}\alpha\eta_o v\right\} C$$

dividing by both sides by $\theta_w v$, we have:

$$\frac{\partial}{\partial x}(C) = -\left\{\frac{3(1 - \theta_w)}{2d_c}\alpha\eta_o\right\} C \qquad 7.5$$

Figure 7.4 shows the mass (moles) of the polymer mass migrating along the section through IW-MW1. A total of 0.013 moles of polymer has been injected at this site during the current study. Figure 7.4 also shows that polymer mass migrated a radial distance of about 0.40, 0.75 and 0.85 m during P1, P2 and P3, respectively. This model prediction supports the initial hypothesis that part of the injection fluid was able to intercept the MW1 which might have resulted in long term degradation of the contaminant.

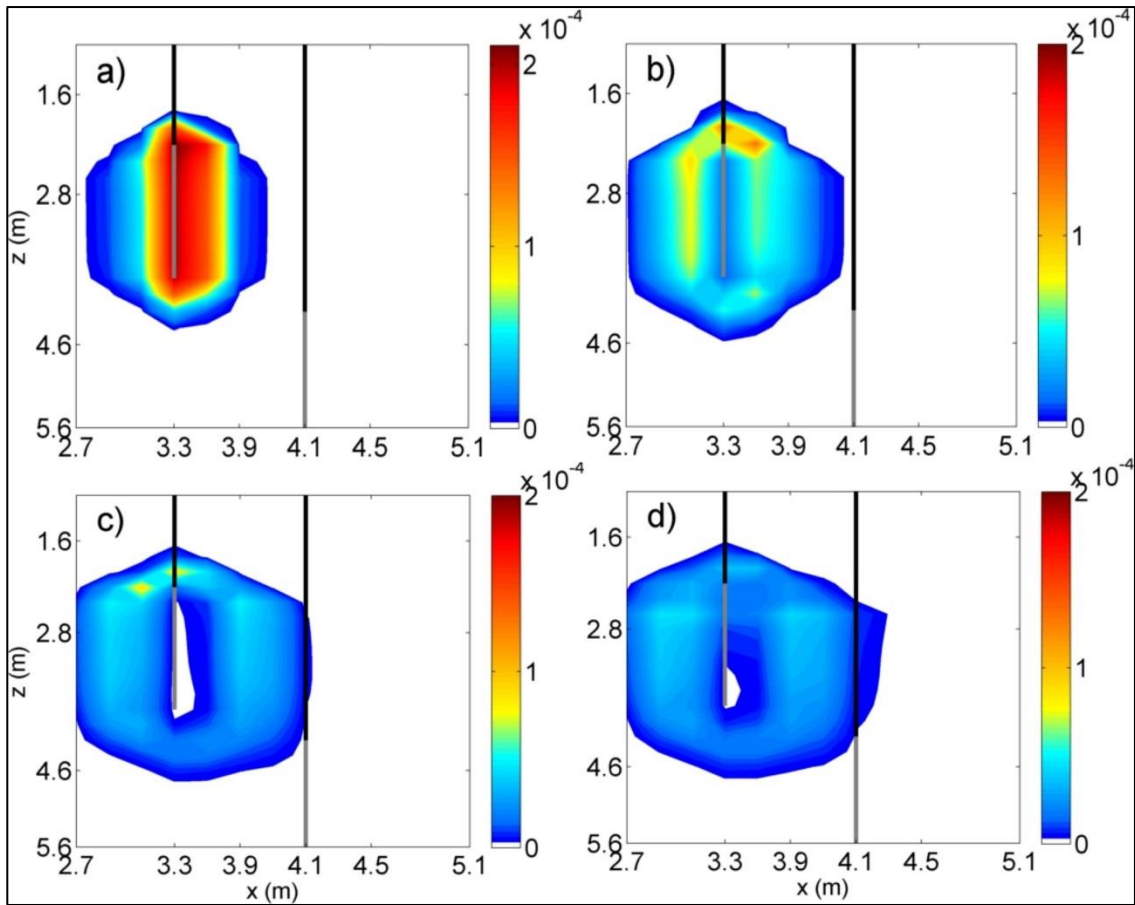Figure 7.4 : Changes in polymer concentration at different times: a) t = 43 min (end of P1); b) t = 76 min (end of P2); c) t = 126 min (end of P3); d) t = 150 min.
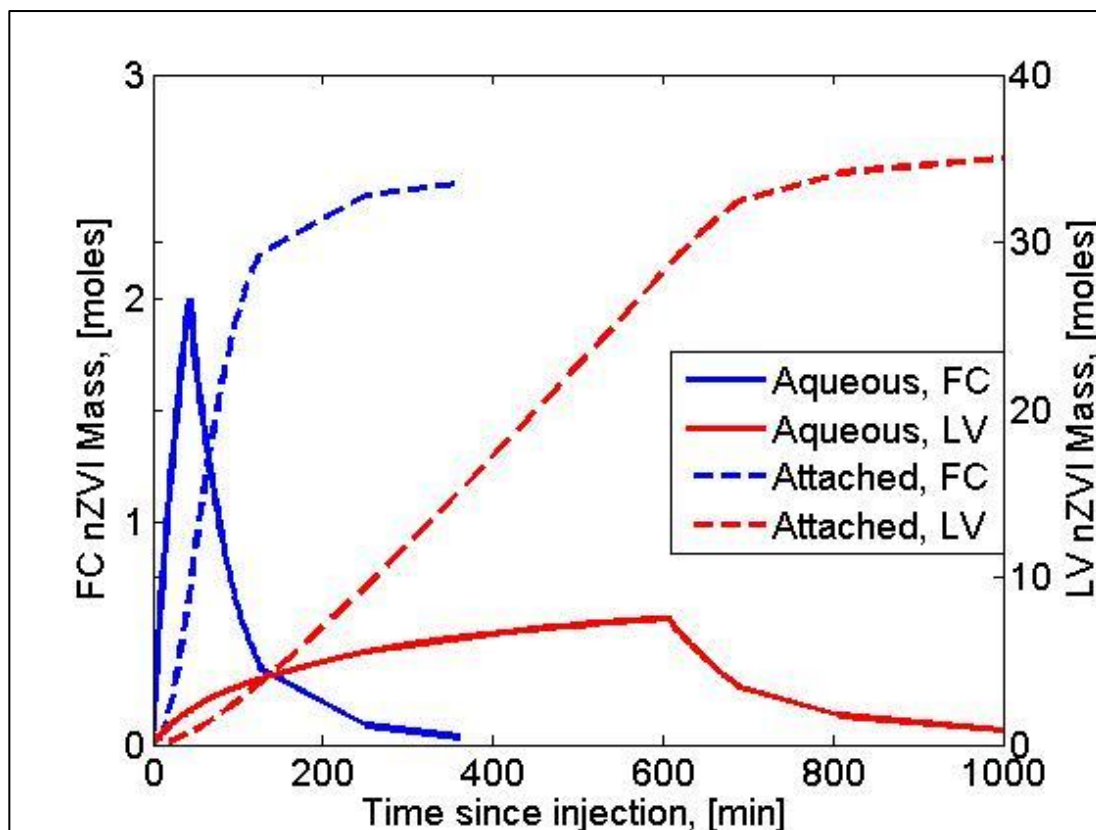
Figure 7.5 : Comparison of nZVI mass for base case (FC) and for large volume injection (LV) case for the domain; P1, P2 and P3 represent 43, 76 and 126 min for FC and 606, 639 and 689 min, respectively, for LV case following nZVI injection.

Table 7-1: Radius of gyration of nZVI and polymer mass

Case	Phase	Radius of gyration, X direction, m, Aqueous nZVI	Radius of gyration, Z direction, m, Aqueous nZVI	Radius of gyration, X direction, m, Attached nZVI	Radius of gyration, Z direction, m, Attached nZVI	Radius of gyration, X direction, m, Polymer	Radius of gyration, Z direction, m, Polymer
FC	P1	0.13	0.59	0.12	0.55	0.15	0.59
FC	P2	0.25	0.67	0.16	0.57	0.27	0.65
FC	P3	0.35	0.74	0.2	0.59	0.39	0.72
GW	P1	0.13	0.59	0.12	0.55	0.15	0.59
GW	P2	0.13	0.58	0.14	0.56	0.16	0.58
GW	P3	0.13	0.57	0.15	0.57	0.16	0.58
VC	P1	0.13	0.59	0.12	0.55	0.15	0.59
VC	P2	0.24	0.66	0.17	0.57	0.2	0.61
VC	P3	0.36	0.72	0.21	0.59	0.37	0.7
LV	P1	0.3	0.68	0.25	0.64	0.5	0.76
LV	P2	0.38	0.74	0.25	0.64	0.55	0.79
LV	P3	0.48	0.79	0.26	0.65	0.62	0.84
WS	P1	0.16	0.46	0.15	0.47	0.18	0.47
WS	P2	0.28	0.5	0.2	0.48	0.25	0.49
WS	P3	0.4	0.51	0.25	0.49	0.4	0.53

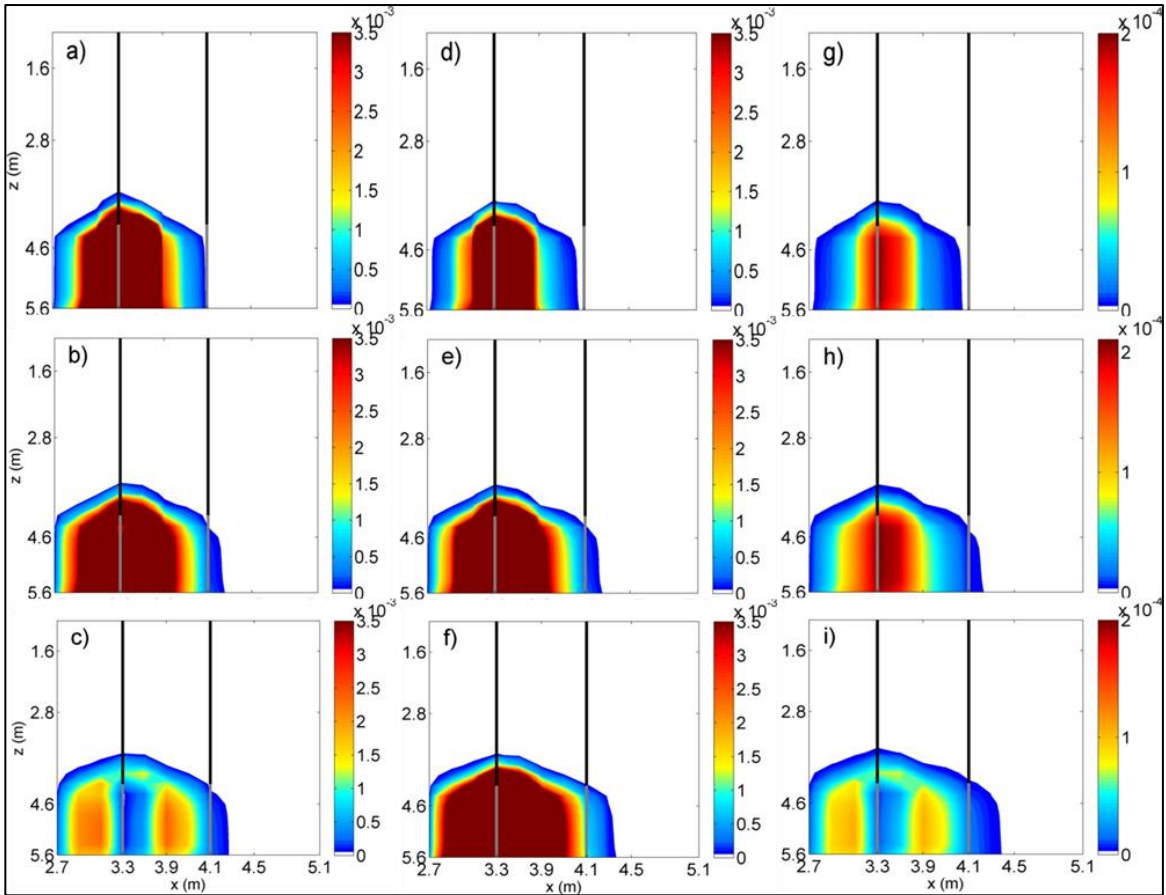In this table, the locations of the radii of gyration in x and z directions are calculated following (Dekker and Abriola, 2000).

Figure 7.6: Aqueous nZVI mass (in mol) at a) t = 43 min (end of P1); b) t = 76 min (end of P2); c) t = 126 min (end of P3); Changes in attached nZVI mass (in mol) at: d) t = P1; e) t = P2; f) t = P3; Polymer mass (in mol) at: g) t = P1; h) t = P2; i) t = P3, for WS case simulation.
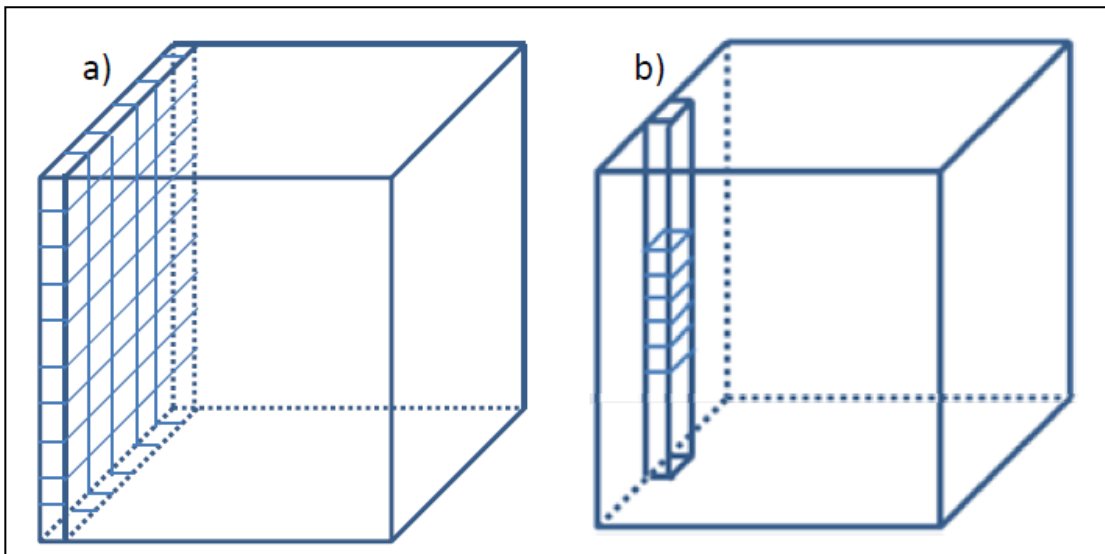
Figure 7.7: Domain setup for a) 1D CompSim simulation where nZVI is injected from the left boundary through 38 injection wells along the y-direction with 28 injection blocks

along the z-direction in each well such that the resulting flow is 1D in nature; and b) 3D CompSim simulation where nZVI is injected from the left boundary through one injection well with 10 injection blocks at the center of y-direction such that the resulting flow is 3D in nature.
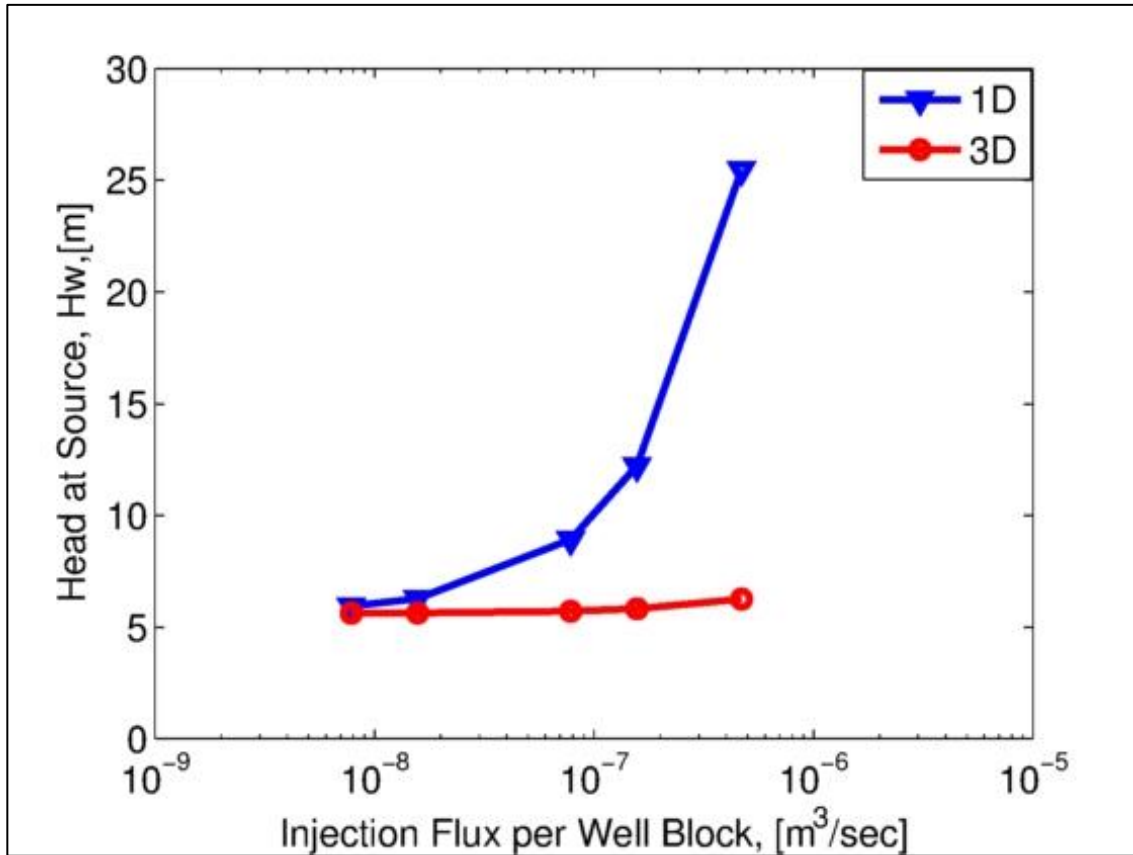

Figure 7.8: Water head data for 1D and 3D CompSim cases.

7.4 References

Acar, Y.B. and Alshawabkeh, A.N., 1993. Principles of Electrokinetic Remediation. Environmental Science & Technology, 27(13).

Acar, Y.B., Alshawabkeh, A.N. and Parker, R.A., 1997. Theoretical and Experimental Modeling of Multi-Species Transport in Soils Under Electric Fields. United States Environmental Protection Agency, OH, pp. 1-8.

Acar, Y.B. et al., 1995. Electrokinetic remediation: Basics and technology status. Journal of Hazardous Materials, 40: 117-137.

Alshawabkeh, A.N., 2009. Electrokinetic Soil Remediation: Challenges and Opportunities. Separation Science and Technology, 44(10): 2171-2187.

Baciocchi, R., D'Aprile, L., Innocenti, I., Massetti, F. and Verginelli, I., 2014. Development of technical guidelines for the application of in-situ chemical oxidation to groundwater remediation. Journal of Cleaner Production, 77(0): 47-55.

Ball, W.P., Liu, C., Xia, G. and Young, D.F., 1997. A diffusion-based interpretation of tetrachloroethene and trichloroethene concentration profiles in a groundwater aquitard. Water Resources Research, 33(12): 2741-2757.

Bennett, P., He, F., Zhao, D., Aiken, B. and Feldman, L., 2010. In situ testing of metallic iron nanoparticle mobility and reactivity in a shallow granular aquifer. Journal of Contaminant Hydrology, 116(4): 35-46.

Berge, N.D. and Ramsburg, C.A., 2009. Oil-in-Water Emulsions for Encapsulated Delivery of Reactive Iron Particles. Environmental Science & Technology, 43(13): 5060-5066.

Berlin, A.A., 1986. Kinetics of radical-chain decomposition of persulfate in aqueous solutions of organic compounds. Kinet. Catalyst, 27(1).

Bradford, S.A. and Torkzaban, S., 2008. Colloid Transport and Retention in Unsaturated Porous Media: A Review of Interface-, Collector-, and Pore-Scale Processes and Models. Vadose Zone Journal, 7(2): 667-681.

Cang, L., Fan, G.-P., Zhou, D.-M. and Wang, Q.-Y., 2013. Enhanced-electrokinetic remediation of copper–pyrene co-contaminated soil with different oxidants and pH control. Chemosphere, 90(8): 2326-2331.

Cauwenberghe, L.V., 1997. Technology Overview Report: Electrokinetics. Ground-Water Remediation Technologies Analysis Center, Pittsburghe, pp. 1-17.

Chapman, S.W. and Parker, B.L., 2005. Plume persistence due to aquitard back diffusion following dense nonaqueous phase liquid source removal or isolation. Water Resources Research, 41(12): n/a-n/a.

Chowdhury, A.I.A. et al., 2015. nZVI injection into variably saturated soils: Field and modeling study. Journal of Contaminant Hydrology, 183: 16-28.

Chowdhury, A.I.A., O'Carroll, D.M., Xu, Y. and Sleep, B.E., 2012. Electrophoresis enhanced transport of nano-scale zero valent iron. Advances In Water Resources, 40(0): 71-82.

Costanza, J., Otaño, G., Callaghan, J. and Pennell, K.D., 2010. PCE Oxidation by Sodium Persulfate in the Presence of Solids. Environmental Science & Technology, 44(24): 9445-9450.

Crimi, M.L. and Siegrist, R.L., 2005. Factors Affecting Effectiveness and Efficiency of DNAPL Destruction Using Potassium Permanganate and Catalyzed Hydrogen Peroxide. Journal of Environmental Engineering, 131(12): 1724-1732.

Dahmani, M.A., Huang, K. and Hoag, G.E., 2006. Sodium Persulfate Oxidation for the Remediation of Chlorinated Solvents (USEPA Superfund Innovative Technology Evaluation Program). Water, Air, & Soil Pollution: Focus, 6(1): 127-141.

DCC, D.C.C., 2007. Detailed Testing Program for Highbury Complex, Defence Construction Canada, London.

Dekker, T.J. and Abriola, L.M., 2000. The influence of field-scale heterogeneity on the infiltration and entrapment of dense nonaqueous phase liquids in saturated formations. Journal of Contaminant Hydrology, 42(2–4): 187-218.

DNAPL-Test, 2011. DNAPL Test. In: Geosyntec Consultants, Queen's University, University of Edinburgh and U. NAVFAC (Editors).

Elliott, D.W. and Zhang, W.X., 2001. Field assessment of nanoscale bimetallic particles for groundwater treatment. Environmental Science & Technology, 35: 4922-6.

Elsner, M., Chartrand, M., VanStone, N., Lacrampe Couloume, G. and Sherwood Lollar, B., 2008. Identifying Abiotic Chlorinated Ethene Degradation: Characteristic Isotope Patterns in Reaction Products with Nanoscale Zero-Valent Iron. Environmental Science & Technology, 42(16): 5963-5970.

Eykholt, G.R. and Daniel, D.E., 1994. Impact of System Chemistry on Electroosmosis in Contaminated Soil, 120. ASCE, 797-815 pp.

Fan, G. et al., 2014. Electrokinetic delivery of persulfate to remediate PCBs polluted soils: Effect of injection spot. Chemosphere, 117(0): 410-418.

Fan, G., Cang, L., Gomes, H.I. and Zhou, D., 2016. Electrokinetic delivery of persulfate to remediate PCBs polluted soils: Effect of different activation methods. Chemosphere, 144: 138-147.

Farrell, J., Kason, M., Melitas, N. and Li, T., 2000. Investigation of the Long-Term Performance of Zero-Valent Iron for Reductive Dechlorination of Trichloroethylene. Environmental Science & Technology, 34(3): 514-521.

Fetter, C.W., 2001. Applied Hydrogeology. Prentice Hall, NJ.

Fordham, J.W.L. and Williams, H.L., 1951. The Persulfate-Iron(II) Initiator System for Free Radical Polymerizations1. Journal of the American Chemical Society, 73(10): 4855-4859.

Gargiulo, G. et al., 2007. Bacteria transport and deposition under unsaturated conditions: The role of the matrix grain size and the bacteria surface protein. Journal of Contaminant Hydrology, 92(3–4): 255-273.

Gerhard, J.I., Kueper, B.H. and Sleep, B.E., 2014. Modeling source zone remediation. In: H.B. Kueper, F.H. Stroo, M.C. Vogel and H.C. Ward (Editors), Chlorinated Solvent Source Zone Remediation. Springer New York, New York, NY, pp. 113-144.

Goodall, D.C. and Quigley, R.M., 1977. Pollutant migration from two sanitary landfill sites near Sarnia, Ontario. Canadian Geotechnical Journal, 14(2): 223-236.

Grathwohl, P., 1998. Diffusion in natural porous media: Contaminant Transport, Sorption/Desorption and Dissolution Kinetics, 1. Springer Science & Business Media.

He, F., Zhang, M., Qian, T. and Zhao, D., 2009. Transport of carboxymethyl cellulose stabilized iron nanoparticles in porous media: column experiments and modeling. Journal of colloid and interface science, 334: 96-102.

He, F. and Zhao, D., 2007. Manipulating the Size and Dispersibility of Zerovalent Iron Nanoparticles by Use of Carboxymethyl Cellulose Stabilizers. Environmental Science & Technology, 41: 6216-6221.

He, F., Zhao, D. and Paul, C., 2010. Field assessment of carboxymethyl cellulose stabilized iron nanoparticles for in situ destruction of chlorinated solvents in source zones. Water research, 44(7): 2360-2370.

Heiderscheidt, J.L., Crimi, M., Siegrist, R.L. and Singletary, M.A., 2008. Optimization of Full-Scale Permanganate ISCO System Operation: Laboratory and Numerical Studies. Ground Water Monitoring & Remediation, 28(4): 72-84.

Henderson, T.H., Mayer, K.U., Parker, B.L. and Al, T.A., 2009. Three-dimensional density-dependent flow and multicomponent reactive transport modeling of chlorinated solvent oxidation by potassium permanganate. Journal of Contaminant Hydrology, 106(3-4): 195-211.

Henn, K.W. and Waddill, D.W., 2006. Utilization of nanoscale zero-valent iron for source remediation—A case study. Remediation Journal, 16(2): 57-77.

Hodges, D., Fourie, A., Reynolds, D. and Thomas, D., 2011. Development of an Apparatus for pH-Isolated Electrokinetic In Situ Chemical Oxidation. Journal of Environmental Engineering, 137(9): 809-816.

Hodges, D., Fourie, A., Thomas, D. and Reynolds, D., 2013. Overcoming Permanganate Stalling during Electromigration. Journal of Environmental Engineering, 139(5): 677-684.

Hodges, D.J., 2010. Permanganate Electromigration in Low Permeability Media, The University of Western Australia, 243 pp.

Hood, E.D., 2000. Permanganate Flushing of DNAPL Source Zones: Experimental and Numerical Investigation, University of Waterloo, Waterloo, Ontario, Canada.

House, D.A., 1962. Kinetics and Mechanism of Oxidations by Peroxydisulfate. Chemical Reviews, 62(3): 185-203.

Huang, K.-C., Couttenye, R.A. and Hoag, G.E., 2002a. Kinetics of heat-assisted persulfate oxidation of methyl tert-butyl ether (MTBE). Chemosphere, 49(4): 413-420.

Huang, K.-C., Hoag, G.E., Chheda, P., Woody, B.A. and Dobbs, G.M., 2001. Oxidation of chlorinated ethenes by potassium permanganate: a kinetics study. Journal of Hazardous Materials, 87(1–3): 155-169.

Huang, K.-C., Hoag, G.E., Chheda, P., Woody, B.A. and Dobbs, G.M., 2002b. Chemical oxidation of trichloroethylene with potassium permanganate in a porous medium. Advances in Environmental Research, 7(1): 217-229.

Huang, K.-C., Hoag, G.E., Chheda, P., Woody, B.A. and Dobbs, G.M., 2002c. Kinetics and mechanism of oxidation of tetrachloroethylene with permanganate. Chemosphere, 46(6): 815-825.

Huang, K.-C., Zhao, Z., Hoag, G.E., Dahmani, A. and Block, P.A., 2005. Degradation of volatile organic compounds with thermally activated persulfate oxidation. Chemosphere, 61(4): 551-560.

Isosaari, P. et al., 2007. Integration of electrokinetics and chemical oxidation for the remediation of creosote-contaminated clay. Journal of Hazardous Materials, 144(1–2): 538-548.

Johnson, R.L., Cherry, J.A. and Pankow, J.F., 1989. Diffusive contaminant transport in natural clay: a field example and implications for clay-lined waste disposal sites. Environmental Science & Technology, 23(3): 340-349.

Johnson, R.L., Johnson, G.O.B., Nurmi, J.T. and Tratnyek, P.G., 2009. Natural Organic Matter Enhanced Mobility of Nano Zerovalent Iron. Environmental Science & Technology, 43(14): 5455-5460.

Johnson, R.L. et al., 2013. Field-Scale Transport and Transformation of Carboxymethylcellulose-Stabilized Nano Zero-Valent Iron. Environmental Science & Technology, 47(3): 1573-1580.

Johnson, R.L., Tratnyek, P.G. and Johnson, R.O.B., 2008. Persulfate Persistence under Thermal Activation Conditions. Environmental Science & Technology, 42(24): 9350-9356.

Kao, C.M., Huang, K.D., Wang, J.Y., Chen, T.Y. and Chien, H.Y., 2008. Application of potassium permanganate as an oxidant for in situ oxidation of trichloroethylene-contaminated groundwater: A laboratory and kinetics study. Journal of Hazardous Materials, 153(3): 919-927.

Kavanaugh, M. et al., 2003. The DNAPL Cleanup Challenge: Is There a Case for Source Depletion? USEPA National Risk Management Research Laboratory, Cincinnati, OH, USA, pp. 129.

Kim, H.-J., Phenrat, T., Tilton, R.D. and Lowry, G.V., 2009. Fe0 Nanoparticles Remain Mobile in Porous Media after Aging Due to Slow Desorption of Polymeric Surface Modifiers. Environmental Science & Technology, 43: 3824-3830.

Kim, K. and Gurol, M.D., 2005. Reaction of Nonaqueous Phase TCE with Permanganate. Environmental Science & Technology, 39(23): 9303-9308.

Kingston, J.T., Dahlen, P.R., Johnson, P.C., Foote, E. and Williams, S., 2010. Critical evaluation of state-of-the-art in situ thermal treatment technologies for DNAPL source zone treatment.

Kirschling, T.L., Gregory, K.B., Minkley, J.E.G., Lowry, G.V. and Tilton, R.D., 2010. Impact of Nanoscale Zero Valent Iron on Geochemistry and Microbial Populations in Trichloroethylene Contaminated Aquifer Materials. Environmental Science & Technology, 44(9): 3474-3480.

Kocur, C.M. et al., 2014. Characterization of nZVI Mobility in a Field Scale Test. Environmental Science & Technology, 48(5): 2862-2869.

Kocur, C.M., O'Carroll, D.M. and Sleep, B.E., 2013. Impact of nZVI stability on mobility in porous media. Journal of Contaminant Hydrology, 145(0): 17-25.

Kocur, C.M.D. et al., 2015. Contributions of Abiotic and Biotic Dechlorination Following Carboxymethyl Cellulose Stabilized Nanoscale Zero Valent Iron Injection. Environmental Science & Technology, 49(14): 8648-8656.

Kolthoff, I.M. and Miller, I.K., 1951. The Chemistry of Persulfate. I. The Kinetics and Mechanism of the Decomposition of the Persulfate Ion in Aqueous Medium1. Journal of the American Chemical Society, 73(7): 3055-3059.

Krembs, F.J., Clayton, W.S. and Marley, M.C., 2011. Evaluation of ISCO Field Applications and Performance. In: R.L. Siegrist, M. Crimi and T.J. Simpkin (Editors), In Situ Chemical Oxidation for Groundwater Remediation.

SERDP/ESTCP Environmental Remediation Technology. Springer New York, pp. 319-353.

Krol, M.M. et al., 2013. A Field-Validated Model for In Situ Transport of Polymer-Stabilized nZVI and Implications for Subsurface Injection. Environmental Science & Technology.

Krol, M.M., Sleep, B.E. and Johnson, R.L., 2011. Impact of low-temperature electrical resistance heating on subsurface flow and transport. Water Resources Research, 47(5): 1-12.

Krug, T., O'Hara, S. and Watling, M., 2010. Emulsified Zero-Valent Nano-Scale Iron Treatment of Chlorinated Solvent DNAPL Source Areas, ARLINGTON, VA.

Kueper, B., Stroo, H., Vogel, C. and Ward, C.H., 2014. Source Zone Remediation: The State of the Practice. In: B.H. Kueper, H.F. Stroo, C.M. Vogel and C.H. Ward (Editors), Chlorinated Solvent Source Zone Remediation. SERDP ESTCP Environmental Remediation Technology. Springer New York, pp. 1-27.

Lenhard, R.J. and Parker, J.C., 1987. Measurement and prediction of saturation-pressure relationships in three-phase porous media systems. Journal of Contaminant Hydrology, 1(4): 407-424.

Li, X.D. and Schwartz, F.W., 2000. Efficiency Problems Related to Permanganate oxidation Schemes. The Ohio State University, pp. 46-50.

Li, X.D. and Schwartz, F.W., 2004a. DNAPL mass transfer and permeability reduction during in situ chemical oxidation with permanganate. Geophysical Research Letters, 31(6): L06504.

Li, X.D. and Schwartz, F.W., 2004b. DNAPL remediation with in situ chemical oxidation using potassium permanganate: II. Increasing removal efficiency by dissolving Mn oxide precipitates. Journal of Contaminant Hydrology, 68(3–4): 269-287.

Liang, C., Huang, C.-F., Mohanty, N. and Kurakalva, R.M., 2008. A rapid spectrophotometric determination of persulfate anion in ISCO. Chemosphere, 73(9): 1540-1543.

Liang, C.J., Bruell, C.J., Marley, M.C. and Sperry, K.L., 2003. Thermally Activated Persulfate Oxidation of Trichloroethylene (TCE) and 1,1,1—Trichloroethane (TCA) in Aqueous Systems and Soil Slurries. Soil & Sediment Contamination, 12(2): 207.

Liao, X., Zhao, D., Yan, X. and Huling, S.G., 2014. Identification of persulfate oxidation products of polycyclic aromatic hydrocarbon during remediation of contaminated soil. Journal of Hazardous Materials, 276: 26-34.

Lide, D.R., 2005. Ionic conductivity and diffusion at infinite dilution. In: D.R. Lide (Editor), CRC handbook of chemistry and physics. CRC Press, Boca Raton, FL.

Liu, C. and Ball, W.P., 2002. Back Diffusion of Chlorinated Solvent Contaminants from a Natural Aquitard to a Remediated Aquifer Under Well-Controlled Field Conditions: Predictions and Measurements. Ground Water, 40(2): 175-184.

Liu, J., Gong, X., Song, S., Zhang, F. and Lu, C., 2014. Heat-Activated Persulfate Oxidation of Chlorinated Solvents in Sandy Soil. Journal of Spectroscopy, 2014: 5.

Liu, Y. and Lowry, G.V., 2006. Effect of Particle Age (Fe0 Content) and Solution pH On NZVI Reactivity: H2 Evolution and TCE Dechlorination. Environmental Science & Technology, 40(19): 6085-6090.

Liu, Y., Majetich, S.A., Tilton, R.D., Sholl, D.S. and Lowry, G.V., 2005. TCE Dechlorination Rates, Pathways, and Efficiency of Nanoscale Iron Particles with Different Properties. Environmental Science & Technology, 39(5): 1338-1345.

Loomer, D.B., Al, T.A., Banks, V.J., Parker, B.L. and Mayer, K.U., 2010. Manganese Valence in Oxides Formed from in Situ Chemical Oxidation of TCE by KMnO4. Environmental Science & Technology, 44(15): 5934-5939.

Mahinthakumar, G. and West, O.R., 1997. High Resulation Numerical Simulations in Support of ISCOR Experiment at Portsmouth, Oak Ridge National Laboratory, Oak Ridge, Tenn.

Masliyah, J.H. and Bhattacharjee, S., 2006a. Electrokinetic Phenomena, Electrokinetic And Colloid Transport Phenomena. John Wiley & Sons, Inc., New Jersey, pp. 221-227.

Masliyah, J.H. and Bhattacharjee, S., 2006b. Electrophoresis, Electrokinetic And Colloid Transport Phenomena. John Wiley & Sons, Inc., pp. 295-361.

Mitchell, J.K. and Soga, K., 2005. Fundamentals of Soil Behavior. John Wiley & Sons, Inc., New Jersey.

NRC, N.R.C., 2005. Contaminants in the subsurface: Source zone assessment and remediation. Committee on Source Removal of Contaminants in the Subsurface. The National Academic Press, Washington, D.C.

O'Carroll, D., Sleep, B., Krol, M., Boparai, H. and Kocur, C., 2013a. Nanoscale zero valent iron and bimetallic particles for contaminated site remediation. Advances In Water Resources, 51: 104-122.

O'Carroll, D., Sleep, B., Krol, M., Boparai, H. and Kocur, C., 2013b. Nanoscale zero valent iron and bimetallic particles for contaminated site remediation. Advances In Water Resources, 35(0): 104-122.

O'Carroll, D.M., Bradford, S.A. and Abriola, L.M., 2004. Infiltration of PCE in a system containing spatial wettability variations. Journal of Contaminant Hydrology, 73(1–4): 39-63.

O'Carroll, D.M. and Sleep, B.E., 2007. Hot water flushing for immiscible displacement of a viscous NAPL. Journal of Contaminant Hydrology, 91(3â€"4): 247-266.

O'Carroll, D. and Sleep, B., 2009. Role of NAPL Thermal Properties in the Effectiveness of Hot Water Flooding. Transport in Porous Media, 79(3): 393-405.

Pankow, J.F. and Cherry, J.A., 1996. Dense chlorinated solvents and other DNAPLs in groundwater: history, behavior, and remediation. Waterloo Press.

Parker, B.L., 1996. Effects of molecular diffusion on the persistence of dense, immiscible phase organic liquids in fractured porous geologic media.

Parker, B.L., Chapman, S.W. and Guilbeault, M.A., 2008. Plume persistence caused by back diffusion from thin clay layers in a sand aquifer following TCE source-zone hydraulic isolation. Journal of Contaminant Hydrology, 102(1–2): 86-104.

Petri, B. et al., 2011a. Fundamentals of ISCO Using Persulfate. In: R.L. Siegrist, M. Crimi and T.J. Simpkin (Editors), In Situ Chemical Oxidation for Groundwater Remediation. SERDP/ESTCP Environmental Remediation Technology. Springer New York, pp. 147-191.

Petri, B.G., Thomson, N.R. and Urynowicz, M.A., 2011b. Fundamentals of ISCO using Permanganate, In Situ Chemical Oxidation for Groundwater Remediation. SERDP/ESTCP Environmental Remediation Technology. Springer New York, pp. 89-146.

Phenrat, T. et al., 2009. Particle Size Distribution, Concentration, and Magnetic Attraction Affect Transport of Polymer-Modified Fe 0 Nanoparticles in Sand Columns. Environmental Science and Technology, 43: 5079-5085.

Poling, B.E., Prausnitz, J.M. and O'Connell, J.P., 2001. The Properties of Gases and Liquids. McGraw-Hill, Toronto.

Raychoudhury, T., Naja, G. and Ghoshal, S., 2010. Assessment of transport of two polyelectrolyte-stabilized zero-valent iron nanoparticles in porous media. Journal of Contaminant Hydrology, 118(3-4): 143-151.

Raychoudhury, T., Tufenkji, N. and Ghoshal, S., 2014. Straining of polyelectrolyte-stabilized nanoscale zero valent iron particles during transport through granular porous media. Water Research, 50(0): 80-89.

Reddy, K.R. and Karri, M.R., 2007. Electrokinetic Delivery of Nanoscale Iron Particles for In-Situ Remediation of Pentachlorophenol-Contaminated Soils, Proceedings of International Symposium on Geo-Environmental Engineering for Sustainable Development, China, pp. 74-79.

Reitsma, S. and Dai, Q.L., 2001. Reaction-enhanced mass transfer and transport from non-aqueous phase liquid source zones. Journal of Contaminant Hydrology, 49(1–2): 49-66.

Reynolds, D.A., Jones, E.H., Gillen, M., Yusoff, I. and Thomas, D.G., 2008. Electrokinetic Migration of Permanganate Through Low-Permeability Media. Ground Water, 46(4): 629-637.

Roach, N. and Reddy, K.R., 2006. Electrokinetic Delivery of Permanganate into Low-Permeability Soils. International Journal of Environment and Waster Management, 1(1): 4-16.

Robertson, T., 2009. Electrokinetic Transport of Persulfate under Voltage Gradients.

Rossberg, M. et al., 2000. Chlorinated Hydrocarbons, Ullmann's Encyclopedia of Industrial Chemistry. Wiley-VCH Verlag GmbH & Co. KGaA.

Sakulchaicharoen, N., O'Carroll, D.M. and Herrera, J.E., 2010. Enhanced stability and dechlorination activity of pre-synthesis stabilized nanoscale FePd particles. Journal of Contaminant Hydrology, 118(3-4): 117-127.

Sale, T., Parker, B.L., Newell, C.J. and Devlin, J.F., 2013. Management of Contaminants Stored in Low Permeability Zones - A State of the Science Review, SERDP/ESTCP, Alexandria, VA, USA.

Sale, T.C. et al., 2007. Unpublished Report on AFCEE Source Zone Initiative.

Sale, T.C. and McWhorter, D.B., 2001. Steady state mass transfer from single-component dense nonaqueous phase liquids in uniform flow fields. Water Resources Research, 37(2): 393-404.

Saleh, N. et al., 2008. Ionic Strength and Composition Affect the Mobility of Surface-Modified Fe 0 Nanoparticles in Water-Saturated Sand Columns. Environmental Science and Technology, 42: 3349-3355.

Santos, A.M., Vindevoghel, P., Graillat, C., Guyot, A. and Guillot, J., 1996. Study of the thermal decomposition of potassium persulfate by potentiometry and capillary electrophoresis. Journal of Polymer Science Part A: Polymer Chemistry, 34(7): 1271-1281.

Sarathy, V. et al., 2008. Aging of Iron Nanoparticles in Aqueous Solution: Effects on Structure and Reactivity. The Journal of Physical Chemistry C, 112(7): 2286-2293.

Schnarr, M. et al., 1998. Laboratory and controlled field experiments using potassium permanganate to remediate trichloroethylene and perchloroethylene DNAPLs in porous media. Journal of Contaminant Hydrology, 29(3): 205-224.

Schrick, B., Hydutsky, B.W., Blough, J.L. and Mallouk, T.E., 2004. Delivery Vehicles for Zerovalent Metal Nanoparticles in Soil and Groundwater. Chemistry of Materials, 16: 2187-2193.

Schroth, M.H., Oostrom, M., Wietsma, T.W. and Istok, J.D., 2001. In-situ oxidation of trichloroethene by permanganate: effects on porous medium hydraulic properties. Journal of Contaminant Hydrology, 50(1–2): 79-98.

Seyedabbasi, M.A., Newell, C.J., Adamson, D.T. and Sale, T.C., 2012. Relative contribution of DNAPL dissolution and matrix diffusion to the long-term persistence of chlorinated solvent source zones. Journal of Contaminant Hydrology, 134–135: 69-81.

Shackelford, C.D. and Daniel, D.E., 1991. Diffusion in Saturated Soil. I: Background. Journal of Geotechnical Engineering, 117: 467-484.

Shapiro, A.P. and Probstein, R.F., 1993. Removal of contaminants from saturated clay by electroosmosis. Environmental Science & Technology, 27(2): 283-291.

Shariatmadari, N., Weng, C.-H. and Daryaee, H., 2009. Enhancement of Hexavalent Chromium [Cr(VI)] Remediation from Clayey Soils by Electrokinetics Coupled with a Nano-Sized Zero-Valent Iron Barrier, Environmental Engineering Science, pp. 1071-1079.

Siegrist, R., Crimi, M. and Brown, R., 2011. In Situ Chemical Oxidation: Technology Description and Status. In: R.L. Siegrist, M. Crimi and T.J. Simpkin (Editors), In Situ Chemical Oxidation for Groundwater remediation. SERDP/ESTCP Environmental Remediation Technology. Springer New York, pp. 1-32.

Siegrist, R.L. et al., 2008. Chemical Oxidation for Clean Up of Contaminated Ground Water

Methods and Techniques for Cleaning-up Contaminated Sites. NATO Science for Peace and Security Series C: Environmental Security. Springer Netherlands, pp. 45-58.

Sleep, B.E., Sehayek, L. and Chien, C.C., 2000a. A Modeling and experimental study of light nonaqueous phase liquid (LNAPL) accumulation in wells and LNAPL recovery from wells. Water Resour. Res., 36(12): 3535-3545.

Sleep, B.E., Sehayek, L. and Chien, C.C., 2000b. Modeling wells in variably saturated soil with wellbore fluid gravity segregation. Advances In Water Resources, 23(7): 689-697.

Sleep, B.E. and Sykes, J.F., 1993. Compositional simulation of groundwater contamination by organic compounds: 1. Model development and verification. Water Resour. Res., 29(6): 1697-1708.

Stookey, L.L., 1970. Ferrozine-A New Spectrophotometric Reagent for Iron. Analytical Chemistry, 42(7): 779-781.

Stroo, H.F. and Ward, C.H., 2010. In Situ Remediation of Chlorinated Solvent Plumes. SERDP and ESTCP Remediation Technology Monograph Series. Springer Science + Business Media, LLC, New York, NY, USA.

Struse, A., Siegrist, R., Dawson, H. and Urynowicz, M., 2002. Diffusive Transport of Permanganate during In Situ Oxidation. Journal of Environmental Engineering, 128(4): 327-334.

Thepsithar, P. and Roberts, E.P.L., 2006. Removal of Phenol from Contaminated Kaolin Using Electrokinetically Enhanced In Situ Chemical Oxidation. Environmental Science & Technology, 40(19): 6098-6103.

Tiraferri, A. and Sethi, R., 2009. Enhanced transport of zerovalent iron nanoparticles in saturated porous media by guar gum. Journal of Nanoparticle Research, 11(3): 635-645.

Tiraferri, A., Tosco, T. and Sethi, R., 2011. Transport and retention of microparticles in packed sand columns at low and intermediate ionic strengths: experiments and mathematical modeling. Environmental Earth Sciences, 63(4): 847-859.

Torkzaban, S., Bradford, S.A., van Genuchten, M.T. and Walker, S.L., 2008. Colloid transport in unsaturated porous media: The role of water content and ionic strength on particle straining. Journal of Contaminant Hydrology, 96(1–4): 113-127.

Tosco, T., Petrangeli Papini, M., Cruz Viggi, C. and Sethi, R., 2014. Nanoscale zerovalent iron particles for groundwater remediation: a review. Journal of Cleaner Production, 77(0): 10-21.

Tosco, T. and Sethi, R., 2010. Transport of Non-Newtonian Suspensions of Highly Concentrated Micro- And Nanoscale Iron Particles in Porous Media: A Modeling Approach. Environmental Science & Technology, 44(23): 9062-9068.

Tosco, T., Tiraferri, A. and Sethi, R., 2009. Ionic Strength Dependent Transport of Microparticles in Saturated Porous Media: Modeling Mobilization and Immobilization Phenomena under Transient Chemical Conditions. Environmental Science & Technology, 43(12): 4425-4431.

Tratnyek, P.G., Johnson, R.L., Lowry, G.V. and Brown, R.A., 2014. IN SITU Chemical Reduction For Source Remediation. In: H.B. Kueper, F.H. Stroo, M.C. Vogel and H.C. Ward (Editors), Chlorinated Solvent Source Zone Remediation. Springer New York, New York, NY, pp. 307-351.

TSH, 2007. Detailed Testing Program: Highbury Complex, London, ON. Project No. 52-27811, Defence Construction Canada, London, ON.

Tsitonaki, A. et al., 2010. In Situ Chemical Oxidation of Contaminated Soil and Groundwater Using Persulfate: A Review. Critical Reviews in Environmental Science and Technology, 40(1): 55-91.

Tufenkji, N. and Elimelech, M., 2004. Correlation Equation for Predicting Single-Collector Efficiency in Physicochemical Filtration in Saturated Porous Media. Environmental Science and Technology, 38(2): 529-536.

Vecchia, E.D., Luna, M. and Sethi, R., 2009. Transport in Porous Media of Highly Concentrated Iron Micro- and Nanoparticles in the Presence of Xanthan Gum. Environmental Science & Technology, 43(23): 8942-8947.

Vermeulen, F. and McGee, B., 2000. In-Situ Electromagnetic Heating for Hydrocarbon Recovery and Environmental Remediation. Journal of Canadian Petroleum Technology, 39(8): 24-28.

Waldemer, R.H. and Tratnyek, P.G., 2005. Kinetics of Contaminant Degradation by Permanganate. Environmental Science & Technology, 40(3): 1055-1061.

Waldemer, R.H., Tratnyek, P.G., Johnson, R.L. and Nurmi, J.T., 2007. Oxidation of Chlorinated Ethenes by Heat-Activated Persulfate: Kinetics and Products. Environmental Science & Technology, 41(3): 1010-1015.

Wei, Y.-T. et al., 2010. Influence of nanoscale zero-valent iron on geochemical properties of groundwater and vinyl chloride degradation: A field case study. Water research, 44(1): 131-140.

Weng, C.-H., Yuan, C. and Tu, H.-H., 2003. Removal of Trichloroethylene from Clay Soil by Series-Electrokinetic Process. Practice Periodical of Hazardous, Toxic, and Radioactive Waste Management, 7(1): 25-30.

West, M.R., Grant, G.P., Gerhard, J.I. and Kueper, B.H., 2008. The influence of precipitate formation on the chemical oxidation of TCE DNAPL with potassium permanganate. Advances in Water Resources, 31(2): 324-338.

West, M.R. and Kueper, B.H., 2012. Numerical simulation of DNAPL source zone remediation with in situ chemical oxidation (ISCO). Advances In Water Resources, 44(0): 126-139.

Wu, M.Z., Reynolds, D.A., Fourie, A. and Thomas, D.G., 2013. Optimal Field Approaches for Electrokinetic In Situ Oxidation Remediation. Groundwater Monitoring & Remediation, 33(1): 62-74.

Xu, M. et al., 2015. Degradation of carbon tetrachloride in aqueous solution in the thermally activated persulfate system. Journal of Hazardous Materials, 286(0): 7-14.

Yan, Y.E. and Schwartz, F.W., 1999. Oxidative degradation and kinetics of chlorinated ethylenes by potassium permanganate. Journal of Contaminant Hydrology, 37(3-4): 343-365.

Yan, Y.E. and Schwartz, F.W., 2000. Kinetics and Mechanisms for TCE Oxidation by Permanganate. Environmental Science & Technology, 34(12): 2535-2541.

Yang, G.C.C. and Yeh, C.-F., 2011. Enhanced nano-Fe3O4/S2O82− oxidation of trichloroethylene in a clayey soil by electrokinetics. Separation and Purification Technology, 79(2): 264-271.

Yeung, A.T., 2011. Milestone developments, myths, and future directions of electrokinetic remediation. Separation and Purification Technology, 79(2): 124-132.

Yuan, S., Liao, P. and Alshawabkeh, A.N., 2013. Electrolytic Manipulation of Persulfate Reactivity by Iron Electrodes for Trichloroethylene Degradation in Groundwater. Environmental Science & Technology, 48(1): 656-663.

Yukselen-Aksoy, Y. and Reddy, K., 2013. Electrokinetic Delivery and Activation of Persulfate for Oxidation of PCBs in Clayey Soils. Journal of Geotechnical and Geoenvironmental Engineering, 139(1): 175-184.

Yukselen-Aksoy, Y. and Reddy, K.R., 2012. Effect of soil composition on electrokinetically enhanced persulfate oxidation of polychlorobiphenyls. Electrochimica Acta, 86(0): 164-169.

Zhang, H. and Schwartz, F.W., 2000. Simulating the in situ oxidative treatment of chlorinated ethylenes by potassium permanganate. Water Resources Research, 36(10): 3031-3042.

Zhang, W.-x., 2003. Nanoscale iron particles for environmental remediation: An overview. Journal of Nanoparticle Research, 5: 323-332.

Zhang, W. et al., 2010. Colloid Transport and Retention in Unsaturated Porous Media: Effect of Colloid Input Concentration. Environmental Science & Technology, 44(13): 4965-4972.

Zhao, D. et al., 2013. Effect and mechanism of persulfate activated by different methods for PAHs removal in soil. Journal of Hazardous Materials, 254–255: 228-235.

8   Appendix B: Supplementary Material for "Electrokinetic-Enhanced Permanganate Delivery and Remediation of Contaminated Low Permeability Porous Media"
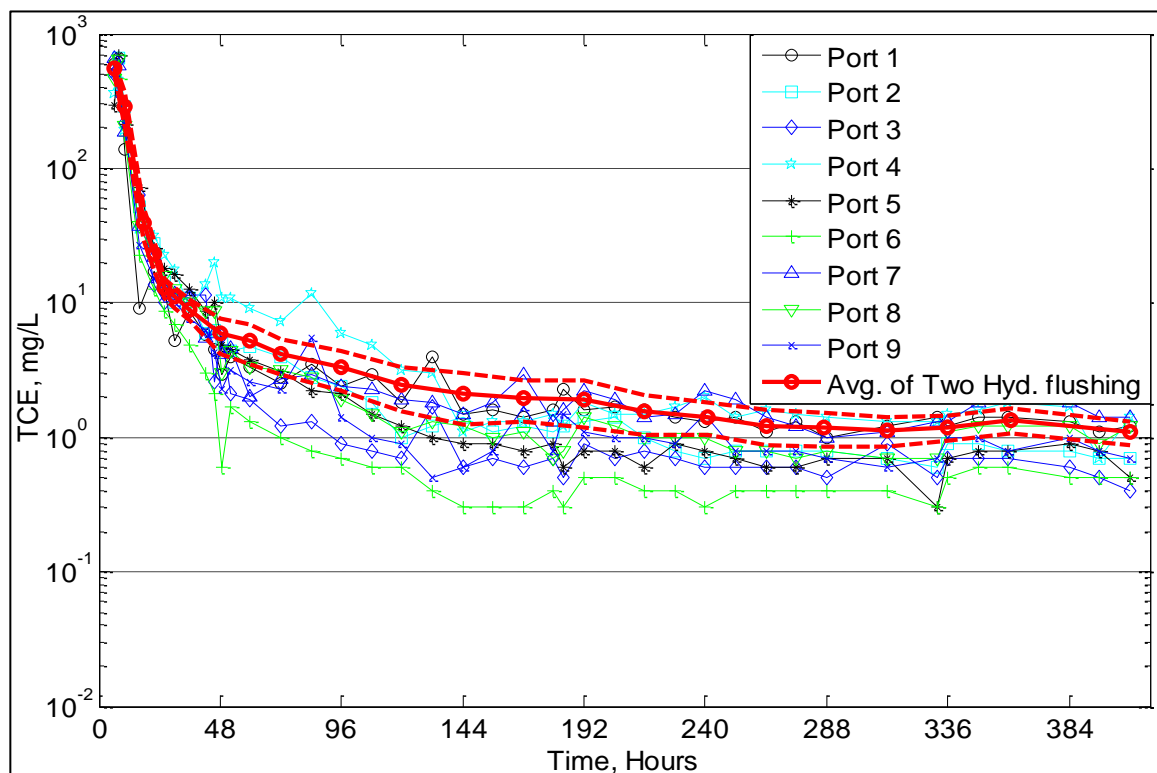

Figure 8.1: TCE concentration at different sampling ports (P1 to P9). The average TCE concentration represents the average of two control experiments (hydraulic flushing(Pre-EK) and hydraulic flushing:1) with the associated 95% confidence interval. TCE concentrations are averaged over 18 measurements per sampling time (i.e. TCE concentrations from 9 locations for each hydraulic flushing experiment per sampling time). Only time steps that were common in all two hydraulic flushing experiments were taken in averaging TCE concentrations.
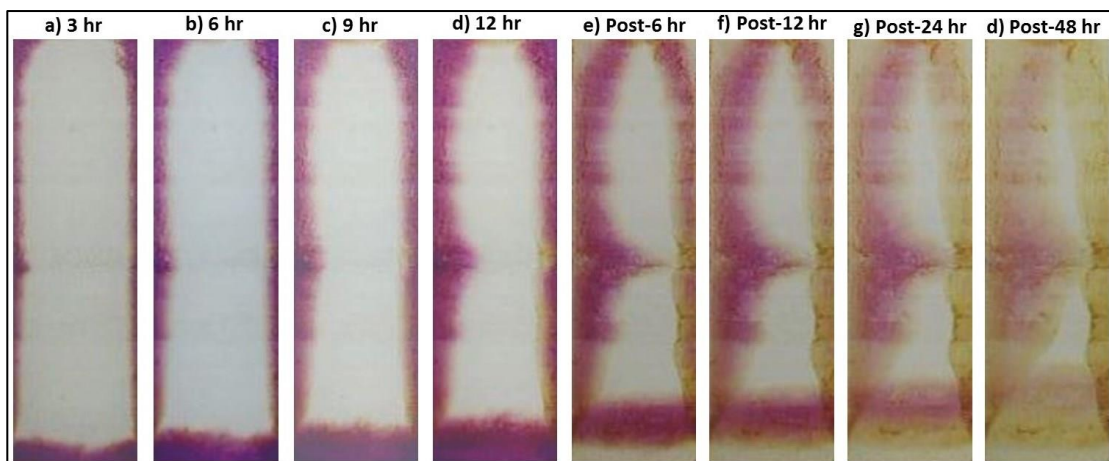
Figure 8.2: Images showing PM migration in Silt-1 at different times during the ISCO (Pre-EK) experiment. "Post" refers to the DI flushing phase following 12 hrs of PM injection. The same images were used for image analysis (Figure 8.10).
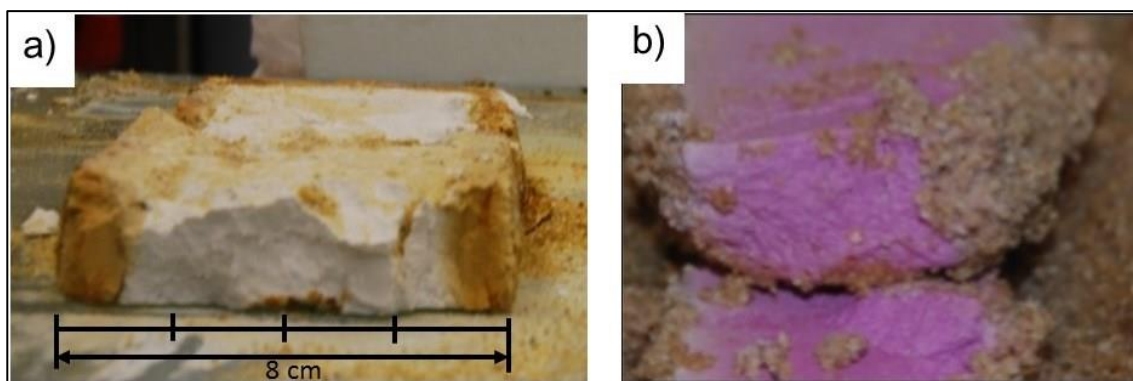

Figure 8.3: Cross-section of silt layers from a) ISCO only experiment and b) ISCO+EK; these experiments are not listed in Table 4-1.
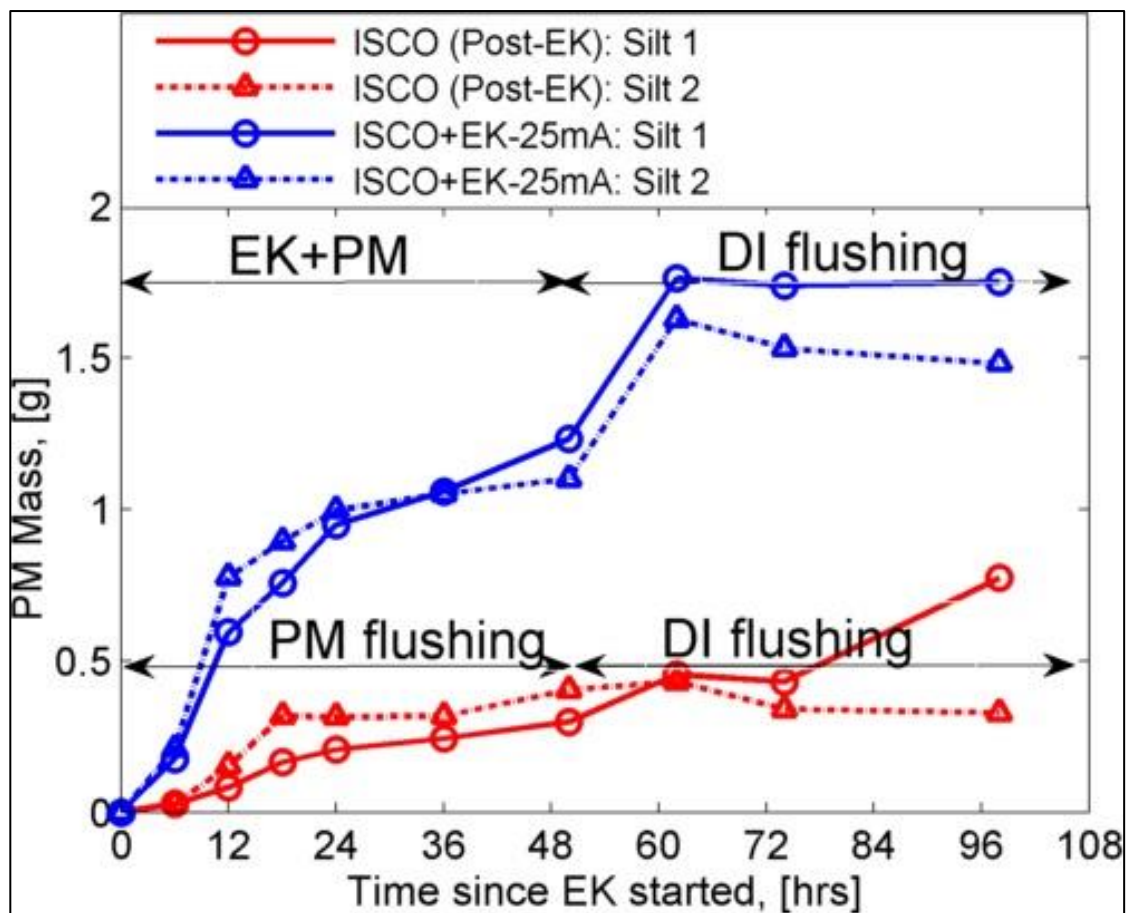
Figure 8.4: PM mass delivered into the silt layers as approximated from image analysis on photographs taken during ISCO+EK-25mA (Phase 4) and ISCO(Post-EK) (Phase 4) experiment.
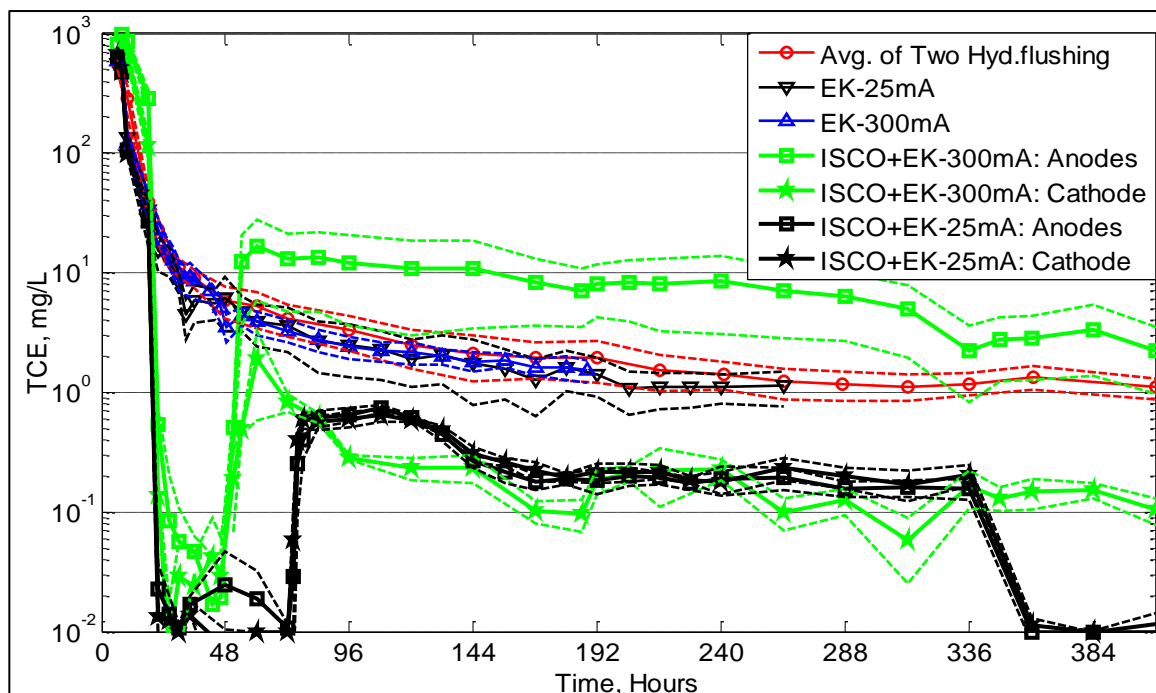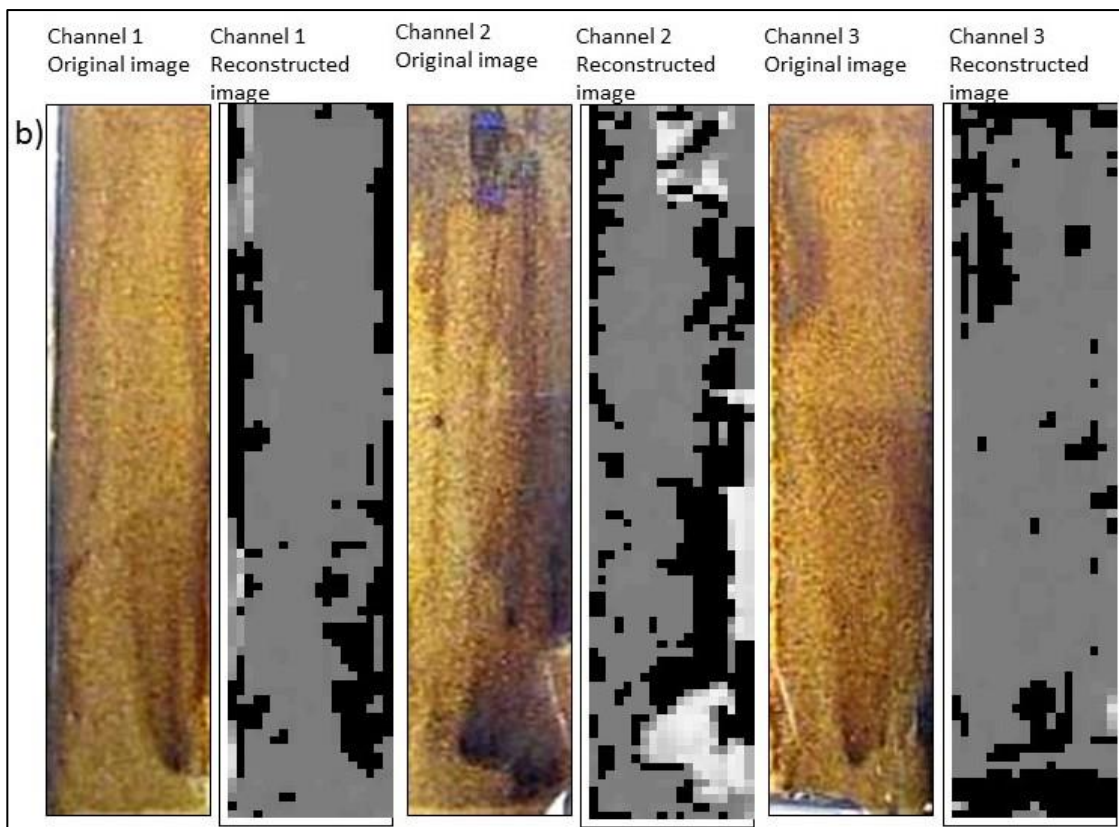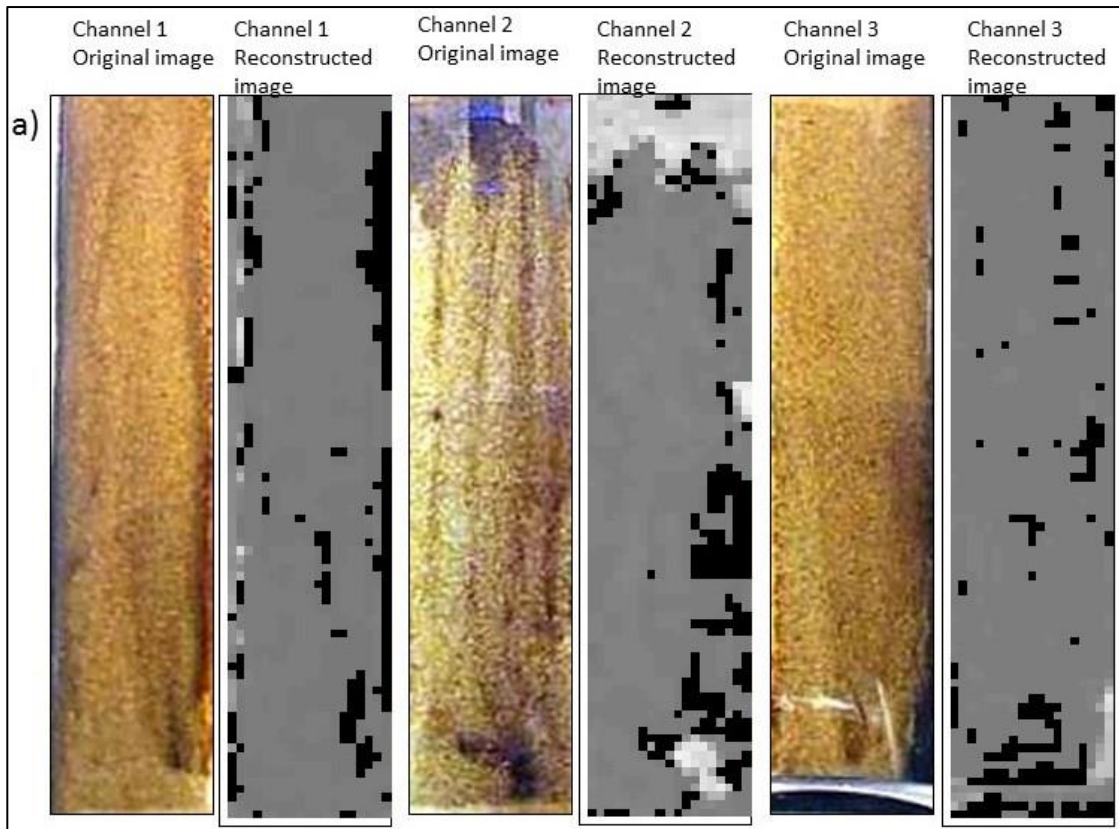
Figure 8.5: Observed mean and 95% CI of TCE concentrations of the two hydraulic flushing experiments (hydraulic flushing (Pre-EK) and hydraulic flushing:1), EK-25mA, EK-300mA, and ISCO+EK-300mA and ISCO+EK-25mA-average of Anode locations (with 95% CI), and ISCO+EK-300mA-Cathode location (95% CI).
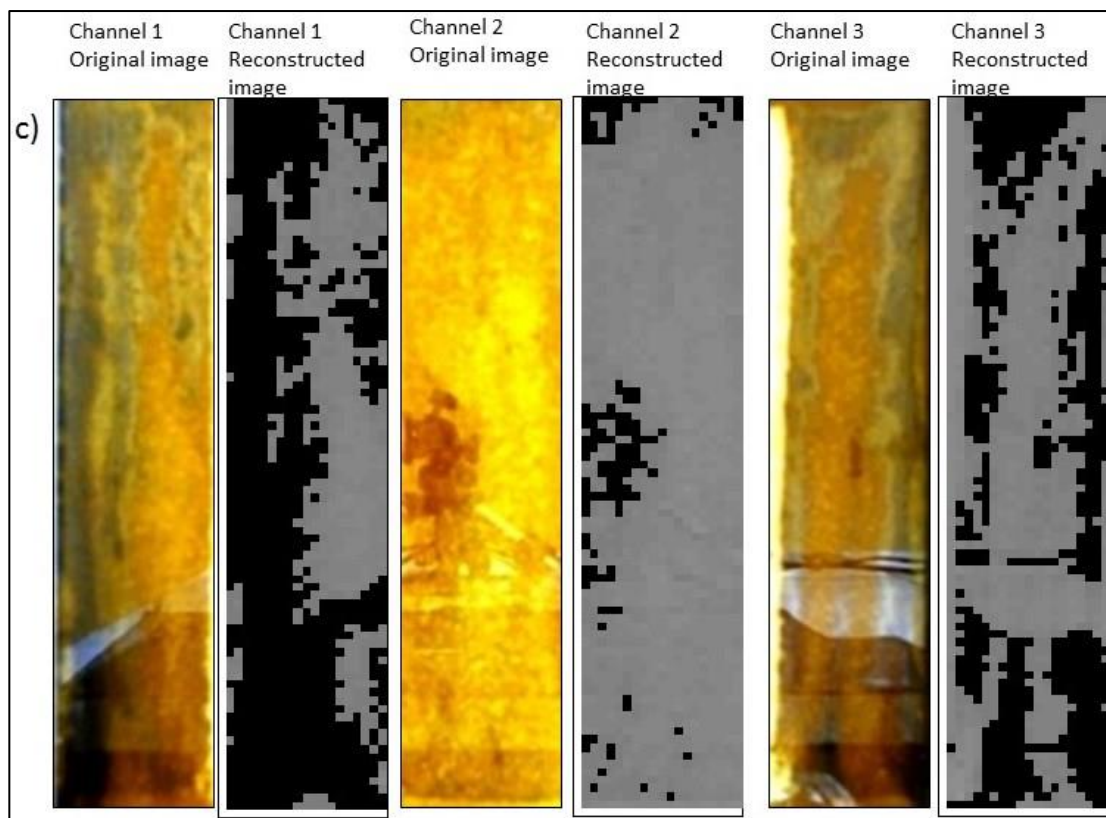
Channel 1 Original image   Channel 1 Reconstructed image   Channel 2 Original image   Channel 2 Reconstructed image   Channel 3 Original image   Channel 3 Reconstructed image

Figure 8.6: Original and reconstructed images to identify MnO$_{2(s)}$ impacted areas within channels 1, 2, and 3 for a) ISCO+EK-25mA – Phase 4; b) ISCO+EK-25mA – Phase 7; and c) ISCO+EK-300mA experiments.
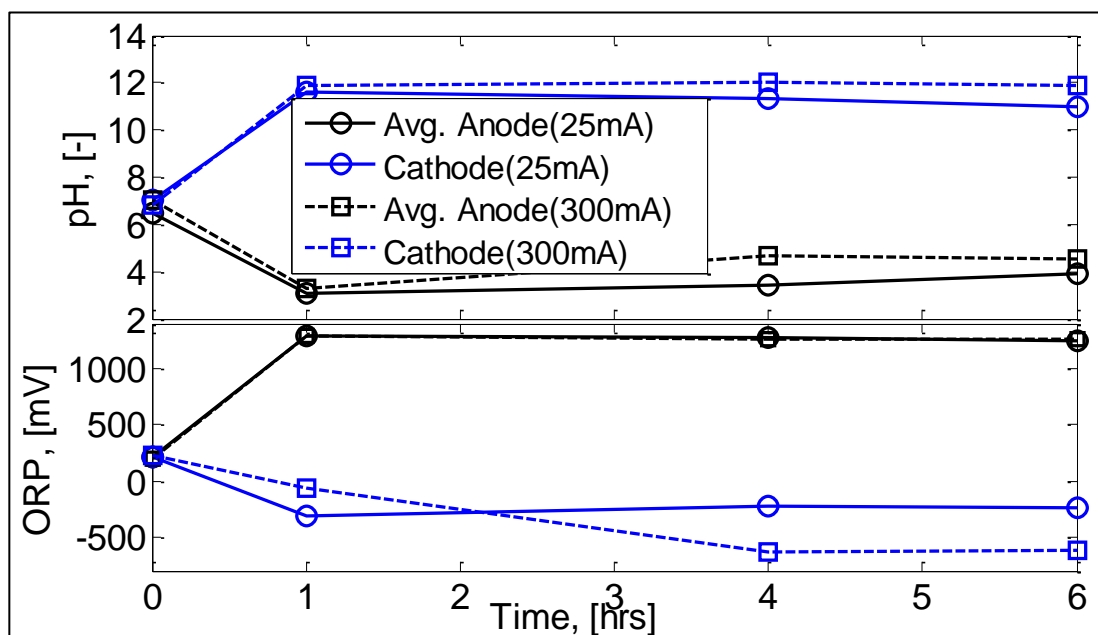

Figure 8.7: Independently measured ORP and pH values measured during EK-pH/ORP experiment at 25 and 300 mA currents.

8.1   Image Analysis

A series of PM flushing (at 0, 5 and 30 g/L) experiments were conducted after the ISCO (Post-EK) experiment using the same setup (sand packing "a") and continuous photographs were taken during these flushing experiments. The main objective of this series of experiments was to generate a set of calibration equation(s) that could be used to approximate the PM concentration or mass within the silt layers during ISCO(Pre-EK), ISCO(Post-EK) and ISCO+EK-25mA experiments. It is important to note here that $MnO_{2(s)}$ precipitated at the periphery of the silt layers (Figure 4.2a-b, Figure 8.2). It was not possible to quantify PM concentrations in zones of precipitate formation by image analysis since the $MnO_{2(s)}$ interfered with PM detection. Therefore, it was first necessary to identify and separate zones in silt layers where $MnO_{2(s)}$ formed.

8.2   Developing Calibration Curves

Step 1: Fresh PM solution of 0, 5 or 30 g/L was prepared. PM solution was injected through the inlet located at the bottom of the sandbox (Figure 4.1a, b). Five (5) pore volumes of PM solution were flushed through the dry sandbox (i.e., both the coarse and silt layers were dry). PM solution imbided into the dry silt; thus, it was expected that PM concentration should be uniform throughout the silt layer. Continuous photographs were taken during the flushing event, referred to as "Calibration" images.

Step 2: From these set of calibration images, the region of interest (i.e., Silt-1 and Silt-2) was cropped for image analysis. In addition, a "clean" image, taken before flushing any solution (i.e., before hydraulic flushing(Pre-EK) experiment) through the sandbox, and was used as a reference to determine any change (such as $MnO_{2(s)}$, PM solution) in the silt layers.

Step 3: Initial image analysis using the 0 g/L PM calibration images (i.e., the background images) showed that the $MnO_{2(s)}$ precipitates were best identified by the "intensity" value of Hue-Saturation-Intensity (HSI) image format while PM impacted areas (using 5 g/L flushed images) were best identified by the "blue" value in the Red-Green-Blue (RGB)

image format. Therefore, HSI and RGB formats of the cropped images were used for $MnO_{2(s)}$ and PM concentration analyses.

Step 4: Each silt layer (from clean, background or 0, 5 and 30 g/L PM flush, Figure 8.8a-d) was divided into 68x20 blocks where each block consisted of 4x4 pixels of a given cropped image. Therefore, each of the blocks contained the average "intensity" or "blue" value of 4x4 pixels.

Step 5: Identify areas where visible $MnO_{2(s)}$ formation was observed in the calibration images. For example, areas impacted by $MnO_{2(s)}$ in the background (i.e., 0 g/L PM) image can be located by comparing two images as shown in Figure 8.8a and Figure 8.8b. "Intensity" based clean (Figure 8.8a) and background (Figure 8.8b) images were subtracted to identify the changes in intensity values and therefore $MnO_{2(s)}$ location. A threshold value for the subtracted image matrix was used to identify $MnO_{2(s)}$ impacted area ($MnO_{2(s)}$ area is represented by the dark color in Figure 8.8e).

Step 6: The "blue" value from the background image was subtracted from the 5 g/L PM flushed image. The resulting matrix (68x20 blocks) contains the changes in each block due to 5 g/L PM flushing. $MnO_{2(s)}$ impacted areas were taken out from further analysis. A reconstructed image after the subtraction and excluding $MnO_{2(s)}$ areas is shown in Figure 8.8f.
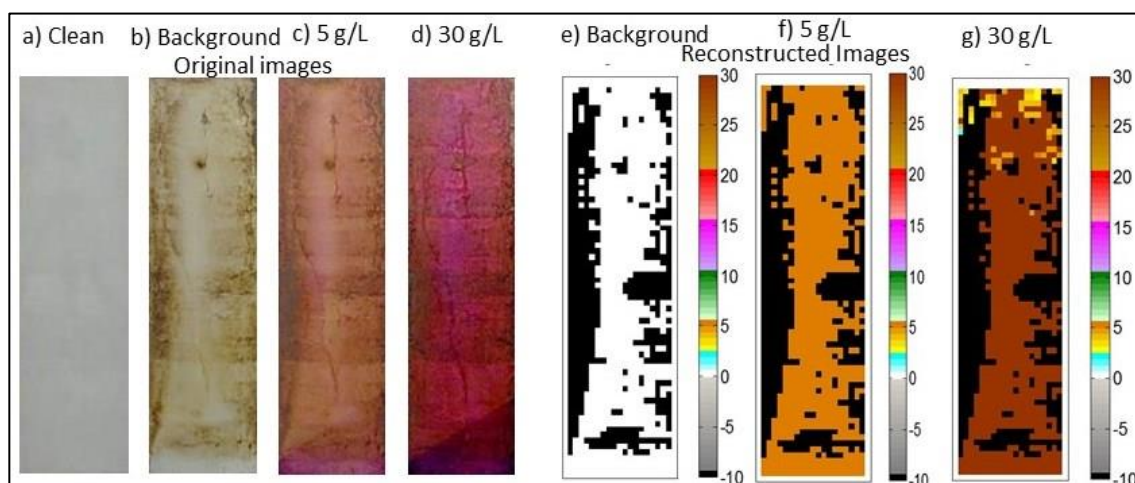

Figure 8.8: Cropped Silt-1 layer images used in analysis showing a-d) original image; e-g) reconstructed images after the image analysis. The negative PM concentration (-10 g/L) in

the color bar represents the areas with $MnO_{2(s)}$ precipitates; 0 to 30 g/L in the color bar represents image analysis calibrated PM concentration.

Step 7: A calibration curve of the difference in "blue" values between the 0 and 5 g/L PM concentration images vs PM concentration was developed for each block (68x20 blocks). Blocks with negative slopes were excluded from further analysis.

Step 8: Step 7 was repeated but for differences in "blue" values between 5 and 30 g/L images. This generated a second set of calibration curves for PM concentrations between 5 and 30 g/L. A reconstructed image is shown in Figure 8.8f,g for 5 and 30 g/L PM flushing.

These two sets calibration equations can be used to determine PM concentrations in silt layers from the photographs taken during ISCO+EK-25mA, and ISCO(Post-EK) experiments.

8.3 Determining PM concentration from photographs taken during ISCO(Post-EK) or ISCO+EK-25mA experiments

This section describes the process of determining PM concentrations from the photographs taken during ISCO+EK-25mA, ISCO(Pre-EK) and ISCO(Post-EK) experiments utilizing the sets calibration curves developed in the preceding section.

Step 1: Any image under consideration, from ISCO+EK-25mA, ISCO(Pre-EK) and ISCO(Post-EK) experiments, was cropped to extract only the silt layers (Silt-1 and Silt 2). Similar to calibration images as described in Step 4 of Section 8.3 each silt layer was divided into 68x20 blocks where each block consisted of 4x4 pixels of a given cropped silt layer. Therefore, each of the blocks contained the average "intensity" or "blue" value of 4x4 pixels.

Step 2: $MnO_{2(s)}$ impacted areas within the image under consideration were identified. For this, Step 5 of Section 8.3 was followed; however, a different background image (an image taken at the initiation, i.e., time = 0 hrs, of the experiment under consideration) was used instead of 0 g/L PM flushing image.

Step 3: To obtain the PM concentration in the images taken during the ISCO(Pre-EK), ISCO(Post-EK) or ISCO+EK-25mA experiments, a target image was selected. The "blue" value from the background image was subtracted from this target image. The resulting matrix (68x20 blocks) contains the changes in each block due to PM that has infiltrated into each block. $MnO_{2(s)}$ impacted areas were taken out from further analysis. The calibration equation corresponding to each block was then utilized to calculate the PM concentration in each block. Select reconstructed images are shown in Figure 8.9a,b for two experiments (ISCO(Post-EK) or ISCO+EK-25mA) along with original photographs of the corresponding silt layer.
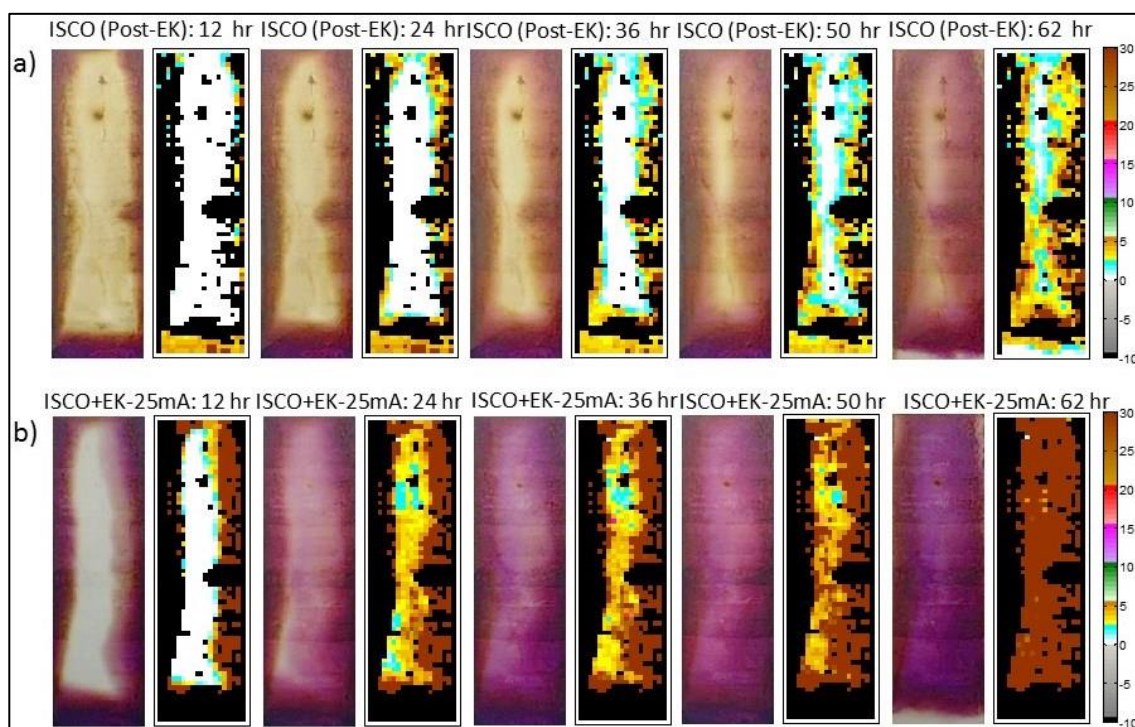

Figure 8.9: Calibrated PM concentration using image analysis for ISCO(Post-EK) and ISCO+EK-25mA experiments (Phase 4, Silt-1) at different times. Timescale in hrs represents the time since PM/ PM+EK application started. The negative PM concentration (-10 g/L) in the color bar represents the areas with $MnO_{2(s)}$ precipitates; 0 to 30 g/L in the color bar represents image analysis calibrated PM concentration.

8.4 Determining PM concentration from photographs taken during ISCO(Pre-EK) experiments

The PM flushing experiments (i.e., 0, 5 and 30 g/L) used to generate calibration curves were conducted after the ISCO+EK-25mA and ISCO(Post-EK) experiments; therefore, the silt layers were impacted by the $MnO_{2(s)}$ precipitate formed during these two experiments. Given that the ISCO(Pre-EK) experiment was conducted before the ISCO+EK-25mA and ISCO(Post-EK) experiments the silt layers had no $MnO_{2(s)}$ precipitate at the initiation of this experiment. Therefore, the background image for this experiment was very similar to the "clean" image. A new set of calibration equations (for each of the 68x20 blocks) was therefore generated including the $MnO_{2(s)}$ impacted areas in the other calibration images. This new set of calibration equations was used to reconstruct ISCO(Pre-EK) images (Figure 8.10).
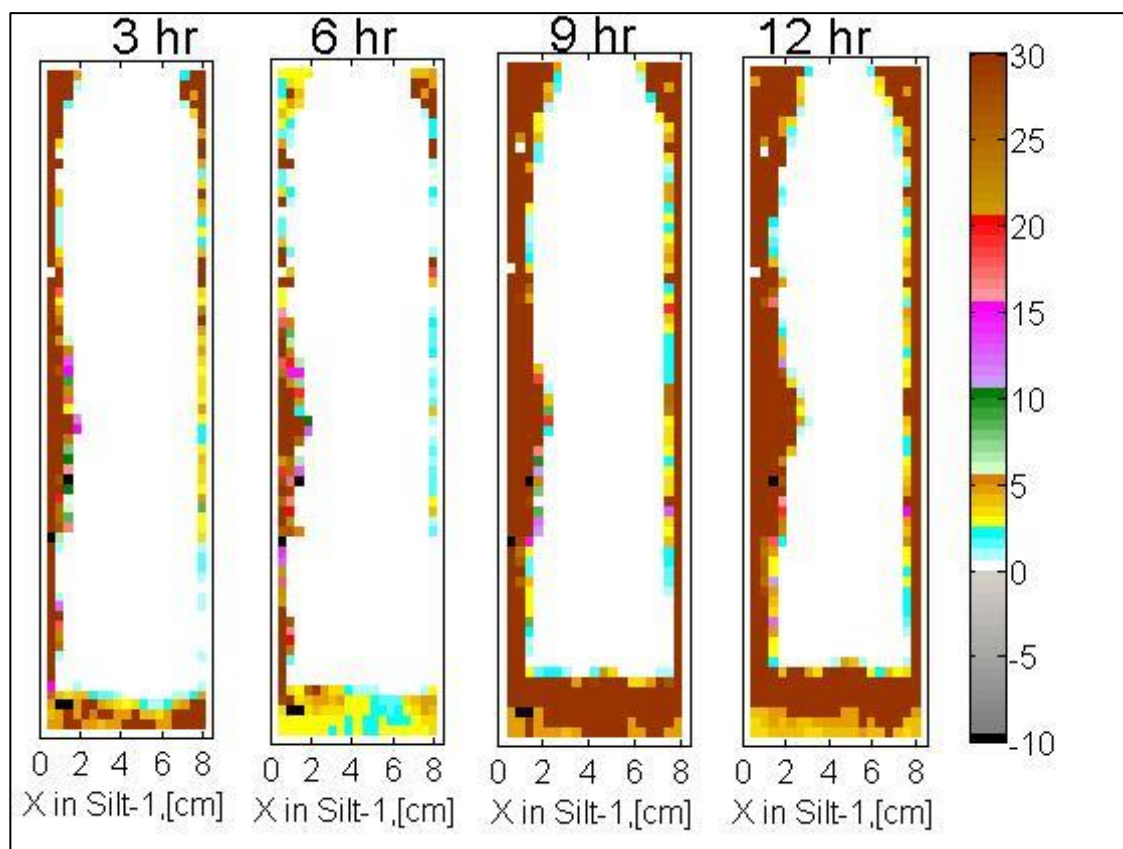

Figure 8.10: Calibrated PM concentration using image analysis for ISCO(Pre-EK) experiments (Silt-1) at different times. Timescale in hrs represents the time since PM application started. Original images are shown in Figure (8.2). The negative PM

concentration (-10 g/L) in the color bar represents the areas with $MnO_{2(s)}$ precipitates; 0 to 30 g/L in the color bar represents image analysis calibrated PM concentration.

8.5 Determining MnO2(s) area from photographs taken during ISCO+EK-25mA and ISCO+EK-300mA experiments

This section describes the process of determining $MnO_{2(s)}$ impacted area coverage within the coarse sand layers (i.e., Channel 1, 2 and 3) from the photographs taken during ISCO+EK-25mA, ISCO+EK-300mA experiments utilizing the similar image analysis concept developed in the preceding section. However, identification of $MnO_{2(s)}$ impacted area in these channels were affected by several factors (e.g., lighting, reflection etc.). Therefore, percentage of each channel impacted by $MnO_{2(s)}$ precipitates was approximated by comparing photographs taken at the beginning and end of each aforementioned experiments.

Step 1: A similar approach described steps 1 and 2 of section 2.2 in this supporting information document was used to identify possible $MnO_{2(s)}$ locations within the Channels 1, 2 and 3. However, 20×89 blocks per channel were used for $MnO_{2(s)}$ analysis instead of 20×68 blocks used for PM concentration analysis.

Step 2: Number of blocks per channel covered with $MnO_{2(s)}$ was counted once a reasonable match was obtained by changing the threshold value for each channel. Number of $MnO_{2(s)}$ were divided by total number of blocks (i.e., 20×89) to estimate the percentage of area in each channel that was impacted by $MnO_{2(s)}$ precipitates. Original and reconstructed images are shown in Figure 8.6 for these two experiments.

9 Appendix C: Supplementary Material for "Aqueous PCE Remediation in Silt via Persulfate Delivered by Electrokinetics and Activated by Electrical Resistance Heating: Proof of Concept"

9.1 Electroosmosis Induced Mass Transport

$Electroosmotic\ Flow\ Rate, Q_{EO} = k_{EO} * i_e * A;$

where, k_{EO} is electroosmotic permeability (m²/day/volt and i_e is voltage gradient (V/m), and A is area of flow (Acar and Alshawabkeh, 1993).

EO-induced PCE migration rate =

$$Q_{EO}\left(\frac{mL}{day}\right) \times chnage\ in\ Avg.PCE\ Conc.\left(\frac{mg}{L}\right)\ during\ EK - PS\ delivery\ )$$

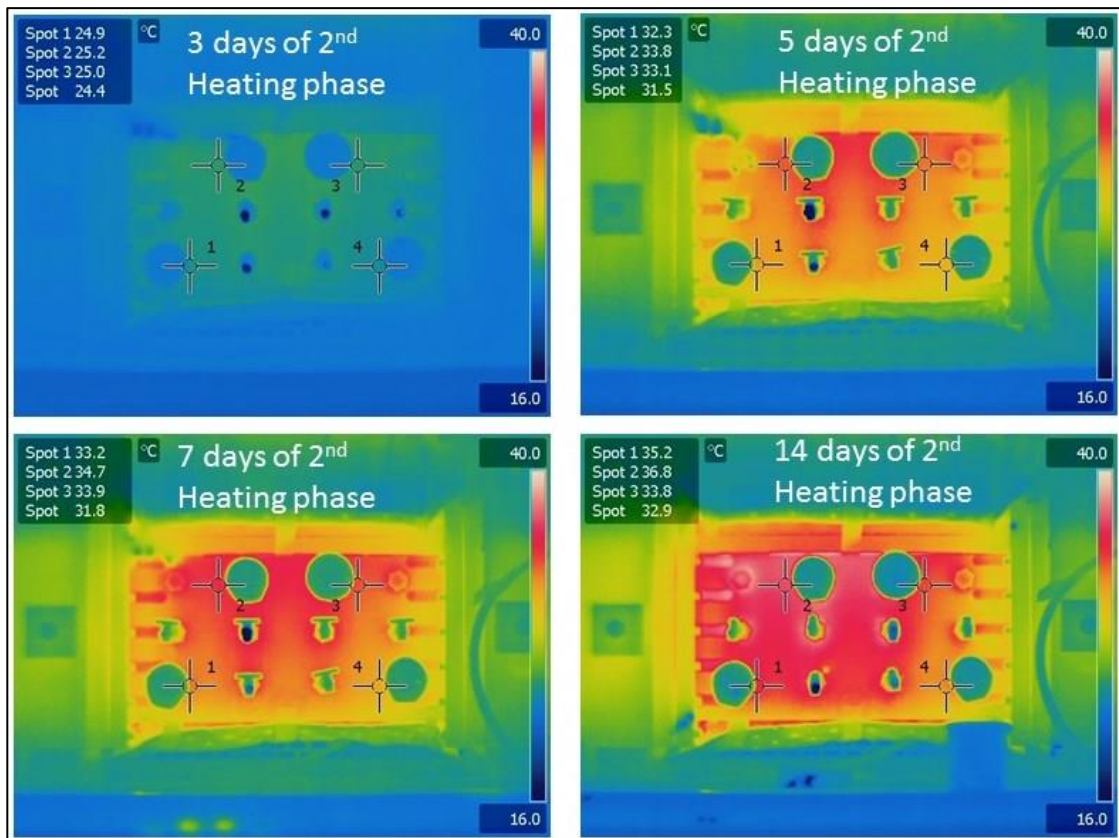(Equation 9.1)

9.2 Supporting Figures

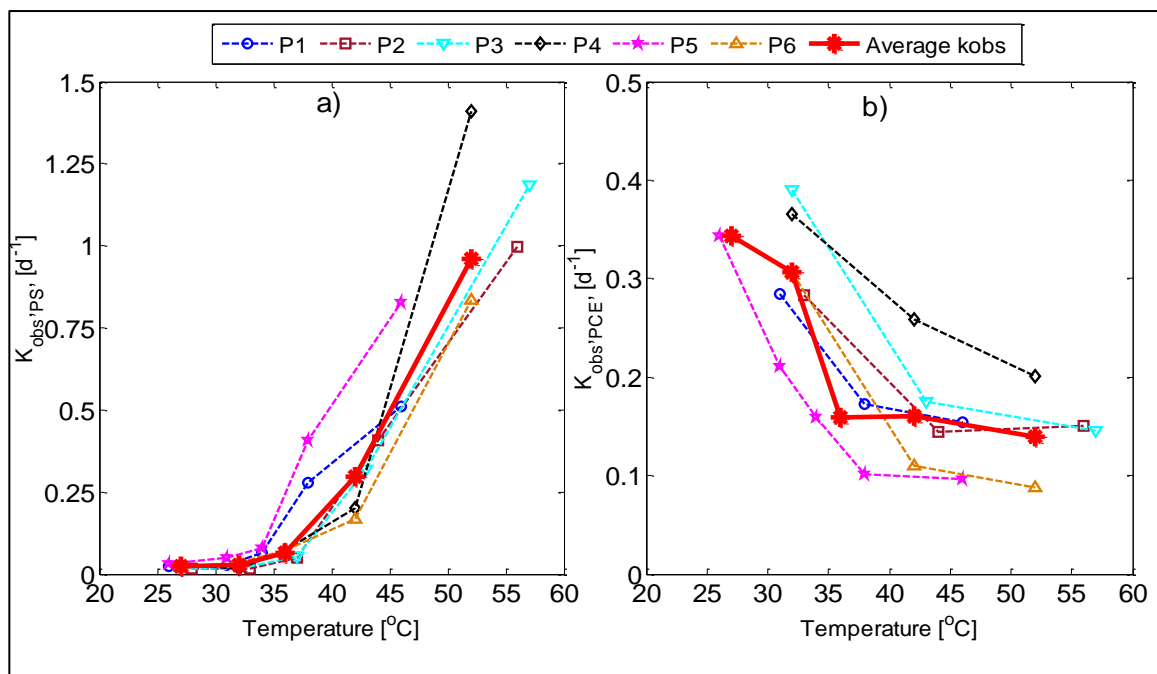Figure 9.1: Thermal images taken during 2nd Heating Period (Phase 7) using Infra-red camera.

Figure 9.2: Observed rate constants ($k_{obs,PS}$) at different temperatures and at different sampling locations a) for PS decomposition; b) for PCE degradation.
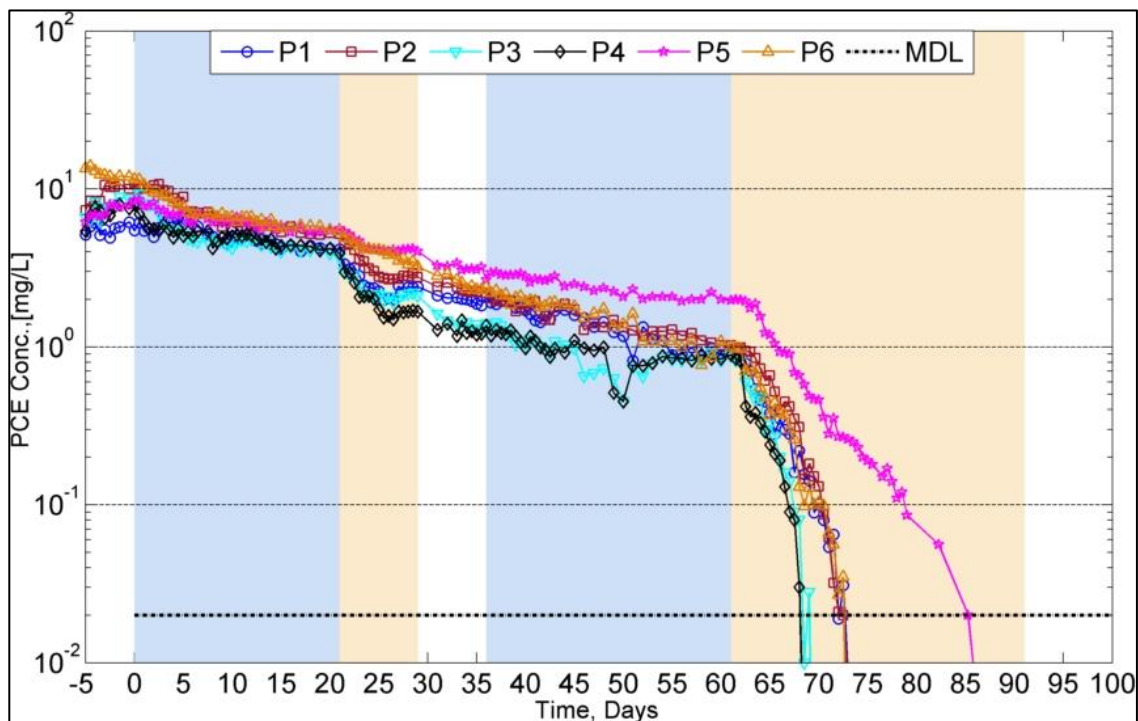

Figure 9.3: Observed PCE concentration at different locations.
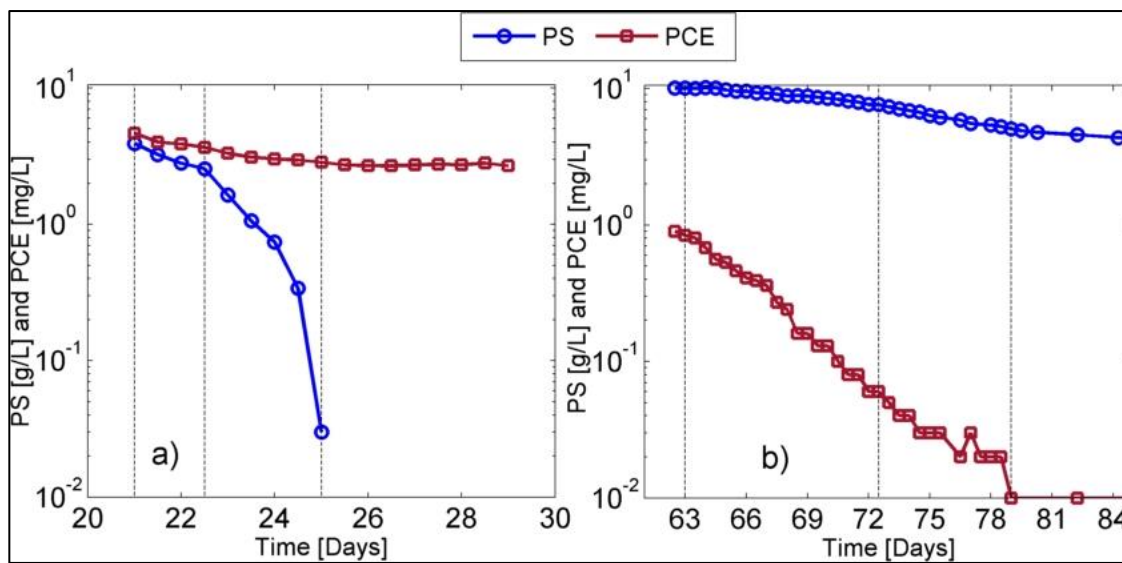
Figure 9.4: Average concentrations of PS (g/L) and PCE (mg/L) for different sampling locations at a) 1st Heating period (Phase 3); b) 2nd Heating period (Phase 7); vertical lines represent the divisions between TG1, TG2, TG3, TG4 and TG5.

10 Appendix D: Reproduction License for "nZVI Injection into Variably Saturated Soils: Field and Modeling Study"

ELSEVIER LICENSE
TERMS AND CONDITIONS

Jul 15, 2016

This Agreement between Ahmed I.A. Chowdhury ("You") and Elsevier ("Elsevier") consists of your license details and the terms and conditions provided by Elsevier and Copyright Clearance Center.

License Number	3910380545783
License date	Jul 15, 2016
Licensed Content Publisher	Elsevier
Licensed Content Publication	Journal of Contaminant Hydrology
Licensed Content Title	nZVI injection into variably saturated soils: Field and modeling study
Licensed Content Author	Ahmed I.A. Chowdhury,Magdalena M. Krol,Christopher M. Kocur,Hardiljeet K. Boparai,Kela P. Weber,Brent E. Sleep,Denis M. O'Carroll
Licensed Content Date	December 2015
Licensed Content Volume Number	183
Licensed Content Issue Number	n/a
Licensed Content Pages	13
Start Page	16
End Page	28
Type of Use	reuse in a thesis/dissertation
Portion	full article
Format	both print and electronic

Are you the author of this Elsevier article?	Yes
Will you be translating?	No
Order reference number	
Title of your thesis/dissertation	Hydrualic and Electrokinetic Delivery of Remediants for In-situ Remediation
Expected completion date	Jul 2016
Estimated size (number of pages)	200
Elsevier VAT number	GB 494 6272 12

Curriculum Vitae

Name:	Ahmed Ishtiaque Amin Chowdhury
Post-secondary Education and Degrees:	University of Western Ontario London, Ontario, Canada 2010 – 2016 Ph.D.
	The University of Western Ontario London, Ontario, Canada 2008 – 2010 M.E.Sc.
	Bangladesh University of Engineering & Technology (BUET) Dhaka, Bangladesh. 2000-2005 B.Sc. (Civil Engineering.)
Honours and Awards:	The L. G. Soderman Award Geotechnical Research Centre 2013
	NSERC-Industrial Post Graduate Scholarship With Geosyntec Consultants, Canada. 2012-2014
	The R.M. Quigley Award Geotechnical Research Centre 2010
Related Work Experience	Teaching Assistant The University of Western Ontario 2008-2014

Publications:

a. Articles published or accepted in refereed journals

Chowdhury Ahmed I. A., Krol, Magdalena M., Kocur, Christopher M.D., Boparai, Hardiljeet, Weber, Kela P., Sleep Brent E., O'Carroll Denis M., *nZVI Injection into Variably Saturated Soils: Field and Modeling Study*, (2015), Journal of Contaminant Hydrology, Vol. 183; p.16-28.

Chowdhury Ahmed I. A., O'Carroll Denis M., Sleep Brent E., Xu Yanqing (2012) *Electrophoresis Enhanced Transport of NZVI through Porous Media,* Advances in Water Resources, 40, p.71-82.

Kocur, Chris M., **Chowdhury, Ahmed I**., Sakulchaicharoen, Nataphan, Boparai, Hardiljeet K., Weber, Kela P., Sharma, Prabhakar, Krol, Magdalena M., Austrins, Leanne, Peace, Christopher, Sleep, Brent E. and O'Carroll, Denis M., *Characterization of nZVI Mobility in a Field Scale Test*, (2014), Environmental Science & Technology, Volume:48, Issue:5.

Kocur, Chris M. D., Lomheim, Line, Boparai, Hardiljeet K., **Chowdhury, Ahmed I. A.,** Weber, Kela P., Austrins, Leanne M., Edwards, Elizabeth A., Sleep, Brent E. and O'Carroll, Denis M., *Contributions of Abiotic and Biotic Dechlorination Following Carboxymethyl Cellulose Stabilized Nanoscale Zero Valent Iron Injection*, (2015), Environmental Science & Technology, Volume: 49, issue: 14.

b. Non-refereed contributions

Chowdhury, Ahmed I.A., deBoer, C., Gerhard, J.I., Reynolds, D.A., Sleep, B.E., O'Carroll, D.M., *Application of Electrokinetics for Oxidant Delivery and Complete Remediation of TCE-Contaminated Low Permeability Porous Media*, 10th International Conference on Remediation of Chlorinated and Recalcitrant Compounds, May 22- 26, 2016, Palm Springs, California, USA, (Platform presentation).

Chowdhury, Ahmed I.A., Krol, M.., Sleep, B.E., O'Carroll, D.M., *Numerical Simulation of nZVI at the Field Scale*, American Geophysical Union Fall Meeting 2014, December, 15-19, 2014, San Francisco, California, USA, (Platform presentation).

Chowdhury, Ahmed I.A., deBoer, C., Gerhard, J.I., Reynolds, D.A., Sleep, B.E., O'Carroll, D.M., E*lectrokinetics Enhanced Oxidant Delivery for In-situ Remediation of Fine-grain Porous Media*, 9th International Conference on Remediation of Chlorinated and Recalcitrant Compounds, May 19-22, 2014, Monterey, California, USA, (Poster presentation).

Chowdhury, Ahmed I. A., Kocur, C., Krol, M., Boparai, H., Peace, C., Sleep, Brent E., O'Carroll, D. M., *nZVI for Site Remediation: Field Application and Numerical Simulation*, Gordon Research Conference on Environmental Nanotechnology, June 02 – 07, 2013, Stowe, VT, USA, (Poster presentation).

Chowdhury Ahmed I. A., Kocur C, Krol M., Boparai H., O'Carroll Denis M., Sleep Brent E., (2012), *Nano-scale Zero Valent Iron (NZVI) for Site Remediation: Small-scale Field Application*, 39th Congress of the International Association of Hydrogeologists. September 17-21, 2012, Niagara Fall, Canada, (Platform presentation).

Chowdhury, Ahmed I. A., Denis M. O'Carroll, Yanqing Xu and Brent E. Sleep (2011) *Challenges and Opportunities of Electrokinetics Enhanced Delivery of Nano-scale Zero Valent Iron*, 85th Annual Symposium on Colloid and Surface Science, ACS, Montreal, June 19-22, 2011, Canada, (Platform presentation).

Chowdhury, Ahmed I. A., Kocur C, Weber Kela P., Boparai H., Krol M., Sakulchaicharoen N., Austrins Leanne, Peace Christopher, O'Carroll Denis M., Sleep Brent E., (2011), *Nano-scale Zero Valent Iron (NZVI) for Site Remediation: Field Applications*, University Consortium for Field-Focused Groundwater Contamination Research Program for Annual Progress Meeting: June 1-3, 2011, University of Guelph, Ontario, Canada, (Platform presentation).

Chowdhury, Ahmed I. A., O'Carroll Denis M., Xu Yanqing, Sleep Brent E., E*lectrokinetics Enhanced Delivery of Nano-scale Zero Valent Iron*, AGU Fall Meeting, San Francisco, CA, USA, December 13-17, 2010, (Platform presentation).

Kocur, C., **Chowdhury, A. I.A**., Boparai, H., Sakulchiacharoen, N., Krol, M., Sleep, B., Austrins, L., and O'Carroll, D., 2012. *Reactivity of nano-scale Zero Valent Iron (nZVI) Following Field Scale Injection.* In the proceedings of the 39th Congress of the International Association of Hydrogeologists. Niagara Falls, ON. Abst. Num 915.

Kocur C.M., O'Carroll D.M., **Chowdhury A.I.**, Boparai H. Sakulchiacharoen N. Weber K. Sleep B. Krol M. Austrins L. Peace C. (2011) *Nanometal particle mobility, reaction, and characterization following field scale injection*. In the proceedings of the 85th ACS Colloid & Surface Science Symposium. Montreal. Que., Canada.